Impact of transverse acoustic modes on a linearly arranged two-phase flow swirling flames

Marcos Caceres

Normandie Université

THESE

Pour obtenir le diplôme de doctorat

Spécialité Énergétique

Préparée au sein de l'INSA de Rouen Normandie

IMPACT OF TRANSVERSE ACOUSTIC MODES ON A LINEARLY ARRANGED TWO-PHASE FLOW SWIRLING FLAMES

Présentée et soutenue par
Marcos CACERES

Thèse soutenue publiquement le 29/01/2019 devant le jury composé de		
M. Franck RICHECOEUR	Professeur des Universités Ecole CentraleSupelec, laboratoire EM2C	Rapporteur
M. Laurent GICQUEL	HDR, Chercheur Senior, CERFACS	Rapporteur
M. Luc VERVISCH	Professeur des Universités INSA de Rouen Normandie, laboratoire CORIA	Examinateur
M. Toufik BOUSHAKI	Maitre de conférences Université d'Orléans, laboratoire ICARE	Examinateur
Mme. Françoise BAILLOT	Professeur des Universités Université de Rouen Normandie, laboratoire CORIA	Directrice de thèse
M. Jean-Bernard BLAISOT	Maitre de conférences, HDR Université de Rouen Normandie, laboratoire CORIA	Codirecteur de thèse

Thèse dirigée par Françoise BAILLOT et Jean-Bernard BLAISOT, laboratoire CORIA (UMR 6614 CNRS)

INSA INSTITUT NATIONAL DES SCIENCES APPLIQUÉES ROUEN

ED PSIME

coria UMR 6614

Résumé

Les besoins énergétiques de la population mondiale ne cessent d'augmenter. Les prévisions indiquent par exemple une forte croissance de la demande du secteur du transport aéronautique. La recherche de systèmes toujours plus performants et moins polluants est nécessaire. Des nouveaux concepts pour la combustion ont été mis au point et appliqués aux turbines à gaz. Parmi eux il existe ceux basés sur la combustion en prémélange pauvre ou en prémélange pauvre pré-vaporisé dans le cas où le carburant utilisé est liquide. Les nouveaux systèmes énergétiques basés sur la combustion en régime pauvre sont prometteurs pour satisfaire les futures normes d'émissions polluantes, mais ils sont plus sensibles aux instabilités de combustion qui limitent leur plage de fonctionnement et peuvent détériorer irréversiblement ces systèmes. Dans ce domaine il reste des questions à aborder. En particulier celle du comportement des flammes tourbillonnaires en combustion diphasique soumises à des perturbations acoustiques. La plupart des moteurs aéronautiques utilisent des flammes de ce type, cependant leur dynamique et leurs interactions mutuelles, quand elles subissent les effets d'une perturbation acoustique, sont loin d'être bien comprises. Ce travail aborde ces questions et apporte des éléments de compréhension sur les mécanismes pilotant la réponse de l'écoulement diphasique et de la flamme, ainsi que des éléments de validation des modèles de prédiction des points de fonctionnement instables.

TACC-Spray est le banc expérimental utilisé pour ce travail. Il a été conçu et développé au sein du laboratoire CORIA lors de ce doctorat qui s'inscrit dans le cadre du projet ANR FASMIC. Le système d'injection qui équipe ce banc expérimental reçoit trois injecteurs tourbillonnaires alimentés en combustible liquide (ici n-heptane), développés par le laboratoire EM2C. Ils sont montés en lignes dans le banc, celui-ci représentant ainsi un secteur d'une chambre annulaire. Le montage étant complexe et nouveau, un travail de développement de solutions techniques a été fait pour rendre possible l'équipement du TACC-Spray avec des capteurs de pression, température, photomultiplicateur ainsi que des diagnostiques optiques performants (e.g. LDA, PDA, imagerie à haute cadence).

Pour cette étude, le système énergétique, composé par l'écoulement diphasique et la flamme, a été soumis à l'impact d'un mode acoustique transverse excité dans la cavité acoustique. La réponse du système a été étudiée en fonction de son positionnement dans le champ acoustique. Trois bassins d'influence du champ acoustique sur le système énergétique ont été choisis, à savoir: (i) le ventre de pression acoustique caractérisé principalement par des fortes fluctuations de pression, (ii) le ventre d'intensité acoustique présentant de forts gradients de pression et vitesse acoustique, (iii) le ventre de vitesse acoustique avec de fortes fluctuations de vitesse où la fluctuation de pression est résiduelle.

L'approche de cette étude a consisté à étudier en premier lieu le système de référence en absence de forçage acoustique, les résultats sont recueillis dans la **Partie I** de ce manuscrit. En deuxième lieu le système énergétique est placé à chacune des positions d'intérêt dans le champ acoustique et la réponse de l'écoulement d'air sans combustion, la réponse de l'écoulement diphasique avec combustion et finalement celle des flammes, sont étudiées systématiquement. Les résultats de l'étude avec forçage acoustique sont

rassemblés dans la **Partie II** du manuscrit.

Des réponses axisymétriques ou dissymétriques de l'écoulement diphasique ont été observées. Elles dépendent des caractéristiques du champ de perturbation vu par le système. Le comportement de la flamme présente lui aussi ces types de réponses en concordance avec les observations de l'écoulement (pulsation de l'intensité de combustion axisymétrique et non-axisymétrique). Des effets non-linéaires issus de l'acoustique linéaire ont été aussi observés sur le comportement de la flamme. Des fonctions de transfert de flamme ont été déterminées à partir de mesures faites dans la chambre de combustion et dans le plenum d'air. Les éléments permettant de relier ces fonctions sont analysés. L'étude de la réponse de la flamme à une large gamme d'amplitudes de la perturbation de pression a permis de mettre en évidence un régime linéaire suivi par un régime de saturation observé pour la première fois dans ce type de flammes. Le mécanisme conduisant à ce régime est analysé.

Abstract

The energy needs of population around the word are continuously increasing. For instance, forecasts indicates an important grow of the request of the aeronautic transportation sector. It is necessary to continue the research efforts to get more performants and less contaminating systems. New concepts for combustion have been developed and introduced to the gas turbine industry. Among these concepts it is found technologies based on lean-premixed combustion or lean-premixed prevaporized combustion when liquid fuels are employed. These novel energetic systems, making use of lean combustion, are promising to meet the future norms about pollutant emissions, but this make them more sensitive to combustion instabilities that limit their operating range and can lead to irreversible damage. In this domain, many questions still need to be considered. In particular that of the behavior of two-phase flow swirling flames subjected to acoustic perturbations. Indeed most of aero-engines operate with this type of flames, but the dynamics and mutual interaction of these flames, as they are submitted to acoustic perturbation, are not yet well understood. This work addresses these issues and gives some understanding elements for the mechanisms driving the response of the flow and of the flame to acoustic perturbations and delivers data to validate models predicting unstable operating points.

The experimental bench employed for this work is TACC-Spray. It has been designed and developed in the CORIA laboratory during this PhD thesis which is inscribed in the framework of the ANR FASMIC project. The injections system that equips this bench is composed by three swirled injectors fed with a liquid fuel (here n-heptane), developed by the EM2C laboratory. They are linearly arranged in the bench such that this represents an unwrapped sector of an annular chamber. The setup, being new and complex, needed technical solutions developed during this work and applied then in order to equip TACC-Spray with pressure and temperature sensors, a photomultiplier as well as adequate optic diagnostics (LDA, PDA, high speed imaging systems).

In this study, the energetic system, composed by the two-phase swirling flow and the spray flame, has been submitted to the impact of a transverse acoustic mode excited within the acoustic cavity. The system response has been studied as a function of its location in the acoustic field. Three basins of influence of the acoustic field on the energetic system have been chosen, namely: (i) the pressure antinode characterized mainly by strong pressure fluctuations, (ii) the intensity antinode where important acoustic pressure and velocity gradients are present, (iii) the velocity antinode with strong velocity fluctuations where the acoustic pressure is residual.

The approach of the study presented here is to investigate in first place the energetic system free of acoustic forcing. The results concerning this first study are presented in the **Part I** of this manuscript. In second place, the energetic system is placed in each of the location of interest within the acoustic field and the response of the air flow without combustion, that of the two-phase flow with combustion and finally that of the spray flames, are systematically investigated. The results of the study under acoustic forcing are shown in **Part II** of the manuscript.

Axisymmetric or dissymmetric responses of the two-phase flow have been observed. These responses depend on the characteristics of the acoustic disturbance field seen by the system. The flame behavior shows responses congruent with those observed on the perturbed flow (axisymmetric or non-axisymmetric combustion intensity pulsation). Non-linear effects resulting from the linear acoustic are also observed on the flame behavior. Flame transfer functions have been determined from measurements performed within the combustion chamber and in the air-plenum. Elements that allow link these transfer functions are analyzed. The study of the flame response to a wide range of pressure perturbation amplitudes allows highlight a linear regime followed by a saturation regime observed for the first time in this type of flames. The mechanism leading to the saturation regime is analyzed.

Contents

Nomenclature

$< I_{OH^*} > (t)$	Sliding averaged value of the flame OH* emissions (or CH* emission if OH* is replaced by CH*) over time.
$\bar{I'}^{o}_{OH^*}$	Mean value of the flame OH* emission intensity when any acoustic forcing is applied
$\bar{I'}_{OH^*}$	Mean value of the flame OH*-emission signal during acoustic forcing
ΔP	Injection pressure in the liquid line
Δ_{probe}	Attenuation of the pressure signal
$\dot{m}_{air}$	Mass flow rate of the air
$\dot{m}_{fuel}$	Mass flow rate of the fuel
λ_b	Wavelength of the blue laser beam of LDA/PDA system
λ_g	Wavelength of the green laser beam of LDA/PDA system
ω_r	Angular frequency of the acoustic forcing
ρ_{air}	Air density
ρ_{fuel}	Liquid fuel density
σ	Surface tension of the n-heptane
θ_M	Angular position on the CCD sensor, of the first minimum of the droplet diffraction pattern
θ_{lda}	Half of the LDV laser beams intersection angle
$\varphi_p(f_0, x/L_c)$	Phase of the pressure fluctuations respect to the phase of the pressure fluctuation at $x/L_c = 0$, taken as the reference
φ_{inj}	Phase of the transfer function of the single injector
φ_{probe}	Phase shift of the pressure sensor measurement introduced by the use of the probe tube
ξ	Coordinate describing the position inside the pressure probe tube
A_0	Nozzle exit orifice area

A_{eff}	In the tomography views, is the intersection surface between the particles of interest within the flow (seeding particles or fuel droplets) and the laser sheet
a_{inj}	Distance between the injection axis of two injector
C_d	Injector discharge coefficient
d	Droplet diameter
D_{exit}	Diameter of the exit nozzle of the two-phase flow injector
e	Acoustic cavity width
f_0	Acoustic forcing frequency
f_r	Acoustic resonant forcing frequency
f_{pvc}	Characteristic frequency of the precessing vortex core
G_{inj}	Gain of the transfer function of the single injector
h_c	Acoustic cavity front walls height
h_{CP}	Convergent passage height
$I_{CH^*}^{mean}$	Mean value of the flame CH* chemiluminescence signal
$I_{CH^*}^{RMS}$	RMS value of the flame CH* chemiluminescence signal
L_c	Main dimension of the acoustic cavity
$L_{int}(t)$	The total intensity of the light scattered by the seeding particles over a series of high-speed tomography images
Q_m	Actual flow rate
Re	Reynolds number
S	Swirl number
$T(x)$	Local temperature
U_w	Speed of the propagation of the scalar information
U_b	Bulk air velocity at the injector nozzle exit
V_1	Injection inlet velocity
x_{VA}	Position along the x-axis of the velocity antinode
IAN	Intensity antinode of the 2T1L acoustic field
PAN	Pressure antinode of the 2T1L acoustic field
VAN	Velocity antinode of the 2T1L acoustic field

We	Weber number

List of Figures

Chapter 1

Introduction

1.1 Context of this work

In recent years governmental and industrial sectors have agreed upon the need for more energy-efficient combustion systems in order to protect our planet. This is to be achieved by optimizing energy systems and reducing pollutant emissions. Particularly, in the aviation sector, the High Level Group (HLG) on Aviation and Aeronautics Research of the European Commission and the Advisory Council for Aeronautics Research in Europe have set challenging goals, namely 75% fewer CO2 emissions, 90% fewer NOx emissions and 65% less flying aircraft noise by 2050 compared to 2000 levels [2]. The technology based on lean burn combustors (e.g. lean-premixed or lean-premixed prevaporized combustors) is most favored to reach the target of the NOx mitigation while limiting the formation of CO.

These energetic systems, featuring increased efficiency, promise to meet the future requirements [3]. However this technology is not free of combustion instabilities which hinder its development. Since more air is present in the injection system, the probability of activating hydrodynamic instabilities is increased. Furthermore, the probability of these hydrodynamic instabilities interacting with acoustic waves is also increased [4]. Thus, in order to eliminate them at the design stage, fundamental mechanisms leading to these instabilities must be well understood. Moreover, even today, industrial combustion systems like rocket engines, aeronautical turbines or land based turbines are subject to combustion unsteadiness, likely to interact with acoustics.

1.1.1 Gas Turbines

The propulsion or power generation rely on a gas turbine whose concept is introduced just now. The turbine defined as a device rotating by means of the action of a fluid able to produce some work was already present from the Antiquity through the use of norias and the first watermills. From the Early Middle Ages, the watermills, but also windmills, were going to be developed. In the 19th century, new concepts were introduced based on thermodynamic cycles. This is the case of the gas turbine which

operates under the Brayton cycle for which the most common working fluid is the air. The first gas turbine engines were made at the beginning of the 20th century. They are constituted with three main components through which the air passes successively: an upstream rotating compressor, a combustor used to heat and increase the thermal energy of the compressed gases, and a downstream turbine, sharing the same shaft with the compressor, where gases expand down to the exhaust pressure. This process is classically represented by a drawing as that given in Figure 1.1. According to the domain, electrical power generation or aviation, where gas turbines are used, different names are introduced. For example, in the land based applications it may be known as a *combustion turbine* or *turboshaft engine*, while in aeronautics it is know as a *jet engine*, *turbojet* or *turbofan* or a *turboprop* if used to drive a propeller.

The conception of a gas turbine can be divided into two main stages. The first one is the nominal operation point design. But an engine has to work in several conditions outside this point. This leads to the second stage, the off-design behavior study of the engine. This will provide an eventual feedback to the first stage in order to improve the original design of the jet engine components. Over the last few years the engine fan has been greatly ameliorated, with two times fewer blades. Compressors are more compact and robust. Turbines, components highly stressed by the very high temperature of hot products, are made with newer materials. However, despite these advanced material solutions, their cooling by the air issued from the compressor section, is still needed. The combustion chamber appears as the core of the gas turbine engine.

Unfortunately, the amount of pollutants formed during combustion is directly linked to the burned gases temperature in addition to the injected fuel mass. To reduce the formation and emission of the pollutants, technologies based on new research and innovation concepts were thought while keeping a high energetic efficiency and continuing to exploit liquid fuels. Among the disruptive technologies, the one based on lean burn combustors is one of the most promising to reach the objective of lessening the NOx while limiting the formation of CO. Two basic concepts are presented beneath:

- the LDI concept (Lean Direct Injection): there the fuel is injected as a liquid in the chamber where combustion is globally lean. The injectors are generally constituted of swirlers in order to improve atomization and local mixing thanks to a larger strain-rate.

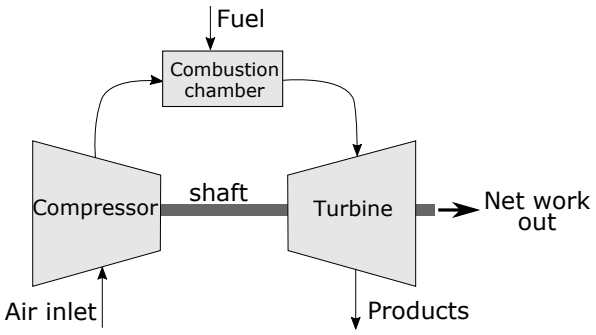

Figure 1.1: Gas turbine process schematic.

- the LPP concept (Lean Premixed Prevaporized): air and fuel are mixed before they are injected inside the combustion chamber. The lean combustion, due to an air excess, leads to a diminishing of the temperature, which tends to reduce the NOx production. When the fuel is liquid, it is prevaporized upstream the chamber and follows the process mentioned above.

Unluckily, this technology presents some drawbacks. LPP combustors operating near the lean extinction limit, they are sensitive to equivalence ratio fluctuations which can lead to extinction or flashback. They are also more sensitive to combustion instabilities, leading again to possible flashback and extinction, or structural damages. Two reasons can be mentioned:

- Lean combustion structures are more easily extinguished by turbulent fluctuations than the stoichiometric ones. The possible reignition of the flow subsequently in the chamber implies that theirs structures may become acoustic sources.
- Since more air is affected to the injection system, the probability of exciting hydrodynamic instability is also increasing. The associated structures might lead to unsteady combustion able to interact with acoustic waves and produce self-excited combustion oscillations.

Combustion-driven oscillations are thus susceptible to reduce the degrees of freedom of the engine operating domain. It is thus necessary to understand how they may appear at each development stage of the engine to minimize their impact on the operating domain.

1.1.2 Swirling flow field

Gas turbine systems largely employ swirl injectors because its favorable effects on the flow allow to stabilize a high intensity combustion process and also lead to a more efficient and clean combustion [5]. Authors in [3] present a wide review of this kind of injectors. The degree of swirl imparted to the flow is characterized by the non-dimensional swirl number S. A simplified approach consists in giving S as a global number defined as the ratio of an axial bulk angular momentum, ΩR^2 to a bulk axial velocity U_b times R where R is a characteristic radius of the injector (*e.g.* in [6]). This calculation is however too rough when transitions, as a result of the swirling process, from a flow regime to another one are investigated and/or analyzed to depict or predict the dynamic behavior of the studied system. In those cases, a more accurate relationship defining S is needed. The definition of S is the ratio of the axial "flux of angular momentum" (G_ϕ) to the axial dynalpy (G_χ) times the nozzle characteristic radius, based on local velocities calculated or measured on a characteristic surface. The "flux of angular momentum" corresponds to the convective part of the rate of change of the angular momentum [7]. The dynalpy is the sum of the convective part of the rate of change of momentum and of the pressure term [8]. Thus, S is given by the following equation:

$$S = \frac{G_\phi}{G_\chi R} \tag{1.1}$$

where the expressions of G_ϕ and G_χ are:

$$G_\phi = \int_\Sigma \rho r U_z U_\theta d\Sigma \tag{1.2}$$

$$G_\chi = \int_\Sigma \rho U_z^2 d\Sigma + \int_\Sigma p d\Sigma \tag{1.3}$$

As typically an axisymmetrical assumption is adopted and because in practice the pressure term is difficult to determine [9], the expressions of G_ϕ and G_χ are reduced to:

$$G_\phi = 2\pi \int_{r_1}^{r_2} \rho U_z U_\theta r^2 dr \tag{1.4}$$

$$G_\chi = 2\pi \int_{r_1}^{r_2} \rho U_z^2 r dr \tag{1.5}$$

and so the classical definition of S is found (Eq. 1.6):

$$S = \frac{\int_{r_1}^{r_2} U_z U_\theta r^2 dr}{\int_{r_1}^{r_2} R U_z^2 r dr} \tag{1.6}$$

Often r_1 and r_2 are defined according to geometrical considerations of the injector type, but generally, the integration is from $r_1 = 0$ to $r_2 = \infty$.

The swirling flow is characterized by a tangential velocity U_θ, leading to centrifugal effects. This creates positive pressure gradients (or a pressure deficit) in the radial direction at any axial location ($\partial p/\partial r = \rho U_\theta^2/r$) [10]. At low swirl (commonly for $S < S_{threshold}$), they give rise only to a slight axial adverse pressure gradient without any main modification of the flow. When S is $\geq S_{threshold}$, strong radial and axial pressure gradients occur near the nozzle exit. A strong coupling is set up between axial and tangential velocity components. A point is reached from which the kinetic energy of the particles flowing in the axial direction cannot surmount the axial adverse pressure gradient. This shows the appearance of the breakdown vortex phenomenon, a sudden and abrupt structural change in the core of a concentrated vortex. A qualitatively description of the physical mechanism of the vortex breakdown can be found in references [7, 11]. Upstream of breakdown, all the flows were observed to be supercritical while subcritical downstream. Several kinds of instabilities have been identified which depend on the operation conditions, *e.g.* free/confined flows, low/high Reynolds numbers, types of vortices (wing-tip or leading-edge vortices [12], ...). They led to different patterns of vortex breakdown such as nearly-axisymmetric bubble type, spiral type, and double helix type [7]. A review on this subject can be found made by O. Lucca-Negro and T. O'Doherty [13] who concluded that if many pertinent interpretations were brought up by a large studies, they could not satisfy all the observed features noted by the studies.

For turbulent flows, as those used in gas turbine combustors, the breakdown occurs for $S_{threshold}$ about 0.6; it is accompanied in the development of a so-called axial bubble, forming a central toroidal recirculation zone (CRZ). Numerical simulation by Choi *et al.* [14] in the case of reactive flows showed that parameters like the tube length, end conditions and exothermicity could delay the appearance of the CRZ compared to inert

flows by increasing the critical level of the swirl ratio of the incoming flow chosen there to describe the vortex breakdown. The flow field generated by a swirl injector features three characteristics structures:

- the central recirculation zone, situated at the exit of the injector. It acts as an aerodynamic blockage or a three-dimensional bluff body which serves to stabilize flames [15, 16].
- The precessing vortex core (PVC) and its precessing vortex layer surrounding the central recirculation zone (CRZ). The PVC is a three-dimensional unsteady asymmetric flow structure that develops when the central vortex core starts to precess[1] around the axis of symmetry at a well-defined frequency [13]. It lies on the boundary of the mean reverse flow zone between the zero velocity streamline and the separation stream-CRZ line [5]. Normally, the PVC frequency increases quasi-linearly with flow rate. A review about the role of the PVC in swirl combustion systems can be found in [16].
- the outer shear layers originated at the edge of the injector inlet orifice.

For inert or reactive flow configurations, several experimental and numerical studies investigated the structures of swirling flows, using either model swirl injectors (*e.g.* [10, 17–22]) or swirl injectors of real combustion systems (*e.g.* [23, 24]).

First, Large Eddy Simulations were performed to reproduce phenomena experimentally highlighted without combustion, examine various fundamental mechanisms dictating the flow evolution, including vortex breakdown, Kelvin–Helmholtz instability and helical instability, as well as their interactions. Calculations in inert flow configurations were made in the vicinity of a single injector exit [23] or inside a complex-geometry combustor, but still academic, supplied by a single industrial-size burner [25, 26]. The flow field exhibited well-organized motion in a low swirl-number case, in which the vortex shedding arising from shear instabilities drives acoustic oscillations. The flow structures are much more complicated with increasing swirl number with each subregime dominated by different structures and frequency contents. In particular, it was found that higher swirl velocity enhanced the central recirculating flow as well as the unsteady motion in the azimuthal direction, and subsequently suppresses the development of the streamwise instability in the outer shear-layer region [23]. Concerning the temporal evolution of the PVC, LES by Selle *et al.* [25] showed that the direction of rotation of the whole spiral, as a structure, was that of the surrounding swirling flow, but that of winding of this spiral was opposite to that of the swirl.

Secondly, LES were also carried out for flows with premixed combustion, first developing in academic chambers used for inert cases [25, 26], then in partial [27][2] or full industrial multi-injection combustion chambers [28]. In some operation conditions, it was shown that combustion could suppress structures that were present in the inert flow. Thus the PVC mode which was very strong for the cold flow, disappeared with combustion in both experiments and simulations [25]. In such complex-geometry combustors, rotating modes could appear under both cold and reacting conditions, but

[1] Relative to a conical movement around a central point

[2] Partial means a three burner sector of an annular burner

did not result from the same physical origins. If the cold flow rotating mode corresponded to the PVC process, the rotating structures observed in the reacting case was acoustically controlled. In other studies as those cited in [29], a strong PVC developed and influenced flow and flame dynamics. The interaction of the PVC and combustion instabilities has been the topic of several publications. Candel and co-workers have investigated the nonlinear interaction between the PVC and acoustic oscillations in a turbulent swirling flame for self-excited and forced thermoacoustic disturbances [30,31]. Without acoustic disturbances, the flame foot motion is piloted by the PVC, which induces heat release rate disturbances along the flame, but they cancel out in the global heat release. With acoustic disturbances, there is a coupling between PVC and helical modes characterized by a frequency which is the difference of the frequencies of the two individual mechanisms. However, self-sustained thermoacoustic instabilities in this work were concluded as not driven directly by the helical mode.

In such a context, much efforts were also devoted to investigate inert or reactive swirling flows when they underwent external disturbances. For instance, Wang *et al.* [32] showed the responses of an inert swirling flow field when periodical longitudinal oscillations were imposed to the mass flow rate at the injector entrance over a wide range of frequencies. The impressed disturbances were decomposed and propagated in two different modes because of their distinct propagating mechanisms in swirl injectors. The flow oscillation in the streamwise direction travelled in the form of acoustic waves, whereas the oscillation in the circumferential direction is convected downstream with the local flow velocity[3]. The vortex breakdown was mainly controlled by the dynamics in the core region near the axis. The dynamic response of the injector flow, however, depends significantly on the forcing frequency in terms of the acoustic admittance and the mass transfer functions. Energy can be transferred among the various structures in the flow-field under external excitations, causing highly non-uniform spatial and temporal distributions of the oscillatory flow properties at the injector exit. In another work [34], Santhosh experimentally showed how longitudinal acoustic perturbations, created upstream of the nozzle exit, could induce vortex breakdown modifications.

Durox and co-workers experimentally investigated dynamics of a swirling flame submitted to harmonic longitudinal flow rate modulations. The swirl was created by a radial swirler with movable blades that allowed changing the swirl number while keeping fixed the mass flow rate, equivalence ratio and other system parameters [35]. Their results showed that the phase of the flame transfer function between velocity perturbations at the burner outlet and heat release rate strongly depended on the swirler blade angle. Lieuwen *et al.* [36–40] studied the response of a swirling flow issued from a single burner to a transverse acoustic field in both inert or reactive conditions, but the burner presented a central bluff-body. The recirculation zone flush with the burner exit should be interpreted as a wake mechanism rather than a breakdown vortex inherent to the swirling process.

[3]This was also described experimentally and theoretically in the study of Palies *et al.* [33] in the case of an annular swirling flow.

1.1.3 Spray

1.1.3.1 Atomization and droplet characterization

Two main technologies found in the aeronautical combustors are the air blast and simplex injectors. The former one is based on the impact of drops and ligaments resulting from the primary atomization of a liquid jet, after it passes through a small orifice, on the wall of the diffuser. There they form a liquid film which is then broken up into droplets at the lip of the orifice by the air when the gas is blowing strongly enough to ensure film atomization. This basic concept is improved by adding swirl flows and multipoint injection. The other technology involves pressurized swirl injectors. The fuel, entering through swirler inlet slots, is ejected from the atomizer to form a spray with a conical hollow sheet. The flow features inside the nozzle and the liquid sheet rupture determine the characteristics of the resultant spray. The droplets size distribution is then greatly dependent on the atomizer geometry and operating conditions [41]. As for air blast injectors, some improvements can be added, for example by imparting a coaxial swirl air flow.

To finely calculate the injection, primary and secondary atomizations have to be taken into account. However, present LES simulations cannot ensure such an aim in the framework of aeronautical combustors. A method was proposed by Martinez [42] for full cone injectors and Sanjosé for hollow cone injectors [43]. There liquid and gaseous velocity profiles can be imposed at the injector exit from profiles obtained farther downstream, which avoids simulating both atomizations. The Fuel Injection Model by Upstream Reconstruction (FIM-UR) and its modified version, explained by Hannebique in [44], are proposed either by means of the Lagrangian formalism or the Eulerian formalism to predict the profiles of the different aerodynamic quantities (flow and spray). The improvement of that model is still a work-in-progress. Therefore, the experimental description of sprays appears as essential to participate in simulations validation, but also to highlight the fundamental physical mechanisms and to propose their modelling.

To do that, basic quantities are introduced (see [45]). Usually, sprays are described by mean of droplets diameters $D_{ab}^{a-b} = \frac{\int_{D_m}^{D_0} D^a (dN/dD) dD}{\int_{D_m}^{D_0} D^b (dN/dD) dD}$, where dN/dD is a number distribution function that gives the number of particles of a given diameter D. No universal functions are found. Some empirical functions are most frequently used when drop size data are analyzed: Nukiyama and Tanasawa, Rosin-Rammler and modified Rosin-Rammler functions. But also, if needed, drop size distributions may be represented by a mathematical function such as normal or log-normal distributions. Two diameters are commonly used:

- **(i)** the length diameter D_{10} is the linear average values of all the drops in the spray;
- **(ii)** the Sauter Mean Diameter D_{32} is the diameter of the drop whose ratio of volume to surface area is the same as that of the entire spray. It controls the evaporation rate.

In addition, Hannebique [44] made simulations with the FIM-UR modeling in the

configuration of a hollow conical polydisperse spray. He showed that the smallest droplets stayed in the center of the cone while the biggest ones were radially located at the periphery of the spray.

Many studies have been addressed in the case of swirling spray flow in order to evaluate liquid injectors performance, swirler configurations (axial or radial), droplets interaction with the air flowfield, both in inert or reactive conditions. For instance, in a recently work [46], Rajamanickam and Basu presented a detailed investigation of the spray generation process of a hollow cone liquid sheet and the evolution of the liquid sheet in the spatial domain of the swirling gas field coflow, by means of a combined POD analysis of the air-flow with shadowgraphy of the liquid-phase. Another group of works have been interested on the response of the swirl spray flow to external excitations in the form of imposed harmonic modulations of the flow rate. A quite extensive review on this subject can be found in [3].

In swirling two-phase flows, liquid particles may interact with the gaseous dynamics. The capability of particles in a disperse phase to accurately trace the gas dynamics is characterized by the Stokes number, S_t defined as the ratio of a characteristic time of a particle (or droplet) τ_p to a characteristic time of the flow τ_f. τ_p is based on the particle drag coefficient $C_d(Re_p)$ where Re_p is the Reynolds number characteristic of the particle, built with the velocity of the particle relative to the gas velocity ($Re_p = \frac{D_p|u_p-u_g|}{\nu_p}$). It is expressed by the following relationship: $\tau_p = \frac{4}{3}\frac{\rho_p}{\rho_g}\frac{D_p^2}{C_d|u_p-u_g|}$. In the Stokesian drag regime, $\tau_p = \frac{\rho_p D_p^2}{18\mu_g as}$. Otherwise, some correlations $C_d(Re_p)$ can be found in the literature (for example see [44]). In [47], simulations for a liquid monodisperse spray injected in a swirling gas jet showed that in the presence of a vortex breakdown different features were observed depending on the droplet size distribution. When small droplets (diameters ranging from 15 to 25 μm) were injected (Stokes number lower than one), the central recirculation zone was more intense in the liquid phase field and the liquid velocity profiles were closer to the gaseous ones. On the other hand, bigger droplets (diameters higher than 25 μm) had a more ballistic behavior. This led to only positive liquid velocity profiles with no longer indication on the presence of the central recirculation zone in the gas. The Stokes number value appears as a true indication to trace the flow even with a CRZ.

Despite the numerous works found in the latter review, their scope is still limited. A lack of data is encountered in the case of swirling spray flows perturbed by a transverse acoustic field. By means of LES, Ghani [29] succeeded in capturing transverse 1T-1L and 2T modes in a swirled liquid kerosene/gaseous air combustor comprising a single burner for which the flame was slightly lifted from the pilot injector. He showed that acoustic modes interacted with hydrodynamic modes of the flow and especially, the PVC. The strongest resonances were obtained when the frequency of the PVC (which changed with flow rate) matched the frequency of the 1T-1L transverse mode of the chamber. However, to our knowledge, it is not found *detailed* experimental data of the spray behavior submitted to a transverse acoustic field, and even less in the case of multiple swirl injectors configuration. In such a context the present work aims to participate in filling this lack by providing experimental data of an inert swirling flow and a reactive two-phase swirling flow, both undergoing the impact of a transverse

acoustic field in the case of multiple swirl injectors.

1.1.3.2 Droplet evaporation models

In liquid fueled combustors it is essential to describe not only spray characteristics, but also evaporation ones, since both phenomena play a major role in triggering two-phase combustion instabilities. An example is reported by [48]: a gas turbine burner was used with gaseous fuel and no combustion instabilities were observed while switching to liquid fuel exhibited large self-excited pressure oscillations. This is all the more important as the kind of sprays (dispersed or dense, monodisperse or polydisperse) directly impacts evaporation process. In particular, Hannebique [44] showed by means of 0D simulations of a Rozin-Rammler polydisperse spray and ten different monodisperse sprays that the temporal evaporation behavior of the polydisperse spray differed from that of the monodisperse ones due to the large size droplets which greatly influenced the mass evolution over time, characterized by a long evaporation time. One consequence was no mean diameters seemed to be able to correctly characterize the polydisperse spray. Nevertheless, whatever the approaches chosen to model the disperse liquid phase, the system of equations includes a term of droplet mass evaporation rate. Several models are proposed, among which some of them comprise the effects of multi-component droplets [49]. However, the complexity of most of them leads to still use evaporation models based on the Spalding mass-transfer model applied to an isolated droplet. Three basic models of that family are introduced below with their main assumptions whose a complete description can be found in [50]. These models are also essential to find physical scenarios in order to depict the behavior of data obtained from academic or more complex experiments. In the following, we are interested in the droplet lifetime (the time until the total vaporization of the droplet) rather than the droplet mass burning rate.

Model 1: Evaporation based on the mass transfer

The first one is known as the Spalding Model of mass transfer. It is based on the fuel mass transfer from zones of high concentration, typically the droplet surface, to zones of low concentration far away from the droplet surface, governed by the Fick's law where the diffusional flux of the droplet vapor is proportional to the binary diffusion coefficient D_F. The binary diffusion coefficient of fuel vapor into the environment is evaluated from the next equation:

$$D_F = \frac{7.66 \cdot 10^{-6}}{P_{gas}} \left(\frac{T_\infty}{300}\right)^{1.583} m^2 s^{-1} \tag{1.7}$$

T_∞ in Kelvin is the ambient temperature far from the droplet surface inside the combustion chamber, and P_{gas} is the ambient pressure in bar. The droplets are therefore injected within a hot ambient environment with a temperature (T_∞) higher than the fuel boil temperature $T_{boiling}$. At the injection, the temperature of the droplet is supposed to be at some fixed value below the boil temperature of the fuel. The temperature of the droplet surface at the injection is considered equal to the ambient temperature

outside the combustion chamber. It is assumed that when the temperature of the droplet surface increases, the entire droplet is instantaneously at that temperature. Heat of the environment within the combustion chamber supplies the energy necessary to vaporize the liquid fuel, and the fuel vapor then diffuses from the droplet surface to the ambient surrounding gas.

For that mass transfer model, the droplet lifetime, t_{evap} is based on the dimensionless mass transfer number, B_m defined as:

$$B_m = \frac{Y_{F,s} - Y_{F,\infty}}{1 - Y_{F,s}} \tag{1.8}$$

$Y_{F,s}$ is the mass-fraction at the droplet surface and $Y_{F,\infty}$ the mass-fraction far from the droplet surface is considered null. t_{evap} is then given by

$$t_{evap} = \frac{\rho_F D_{d,0}^2}{8\rho_{gas} D_F ln(B_m + 1)} \tag{1.9}$$

where ρ_F is the fuel density (considered constant) and $D_{d,0}$ the initial diameter of the droplet. The fuel mass fraction $Y_{F,s}$ included in the definition of B_m can be deduced from the fuel molar fraction $X_{F,s}$ at the droplet surface by:

$$Y_{F,s} = X_{F,s} \frac{MW_F}{X_{F,s} MW_F + (1 - X_{F,s}) MW_{gas}} \tag{1.10}$$

where $X_{F,s}$ is obtained from the Clausius-Clapeyron relationship:

$$X_{F,s} = \frac{P_{sat}}{P_{gas}} = exp\left[\frac{MW_F h_{f,g}}{R_u}\left(\frac{1}{T_{boiling}} - \frac{1}{T_s}\right)\right] \tag{1.11}$$

P_{sat} is the saturation pressure at T_S, MW_F the molecular weight of the fuel, $h_{f,g}$ the fuel latent-heat of vaporization, and R_u the universal gas constant. Finally, the surrounding gas density (ρ_{gas}) is evaluated considering a mean mixture molecular weight, $\overline{MW}$, for example, a mixture of air vitiated by burnt gases.

$$\rho_{gas} = \frac{P_{gas}\overline{MW}}{R_u T_\infty} \tag{1.12}$$

Model 2: Evaporation based on the heat transfer

The first model involved only mass transfer, since it is assumed that the droplet surface temperature is a known parameter. For the present model, the evaporation time is governed by the heat-transfer rate from the ambient at T_∞ to the droplet surface at $T_{boiling}$. There the entire droplet is at the temperature $T_{boiling}$. Heat, governed by the Fourier's law, is conducted from the hot environment to the liquid fuel droplet to vaporize it.

For this model, the lifetime of the droplet is calculated on the basis of the following

expression:

$$t_{evap} = \frac{\rho_F c_{p,g} D_{p,0}^2}{8 k_g ln(B_q + 1)} \tag{1.13}$$

where $c_{p,g}$ and k_g are the gas-phase specific heat and the thermal conductivity of the fuel respectively. The dimensionless heat transfer number (B_q) is defined as:

$$B_q = \frac{c_{p,g}(T_\infty - T_{boil})}{h_{F,g}} \tag{1.14}$$

with the latent-heat of vaporization, $h_{F,g}$.

Thermophysical properties are considered constant, while, in reality, they vary considerably from the gas-phase at the droplet surface to the far away surrounding gas. However, in order to deal with this, a usual standard technique is to introduce the following approximations [50]:

$$c_{p,g} = c_{p,F}(\overline{T}) \tag{1.15}$$

$$k_g = 0.4 k_F(\overline{T}) + 0.6 k_\infty(\overline{T}) \tag{1.16}$$

where the subscript F represents the fuel vapor and $\overline{T}$ is an averaged temperature defined as:

$$\overline{T} = (T_\infty + T_{boil})/2 \tag{1.17}$$

Model 3: Simple droplet combustion

This model combines the fuel mass transfer (Fick's law) and the heat transfer (Fourier's law) to describe the droplet evaporation. Equal diffusitivities for heat and mass is assumed, this is Lewis number equal to the unity:

$$Le = 1 \text{ therefore } \frac{k_g}{c_{p,g}} = \rho_{gas} D_F \tag{1.18}$$

The subscript **g** means the gas-phase (fuel vapor) film around the liquid droplet, and not the **gas** of the surrounding environment.

In that model, a diffusion flame, represented as an infinitesimally thin sheet (infinitely fast chemical kinetics), surrounds the droplet. The gas-phase region is constituted of two zones separated by the flame at the temperature T_f, a known value. The first zone is an inner layer whose temperature increases from the droplet surface temperature, T_s, to T_f. The second zone is an outer domain spreading from the flame sheet to a position far away from the droplet where the temperature is T_∞. The inner one is assumed to be a stagnant film of combustion products through which the fuel vapor diffuses.

Five main quantities are identified: the flame temperature (T_f), the flame position (r_f), the temperature at the droplet surface (T_s), the mass burning rate ($\dot{m}_F$) and the fuel vapor mass-fraction at the droplet surface ($Y_{F,s}$). The energy delivered by the flame is used to heat and vaporize the fuel droplet. Finally the energy necessary to heat the droplet from the injection temperature up to the surface temperature is assumed to be negligible, meaning that the droplet does not present thermal inertia.

This droplet burning model leads to the following droplet lifetime:

$$t_{evap} = \frac{\rho_F c_{p,g} D_{p,0}^2}{8 k_g ln(1 + B_{0,q})} \tag{1.19}$$

where the corresponding transfer number ($B_{0,q}$) is defined as:

$$B_{0,q} = \frac{\Delta h_c/\nu + c_{p,g}(T_\infty - T_s)}{h_{F,g}} \tag{1.20}$$

Δh_c is the heat of combustion per unit mass of fuel, and ν the stoichiometric air-fuel ratio. As in the case of the heat transfer model presented before, the appropriate thermophysical properties. are defined by:

$$c_{p,g} = c_{p,F}(\overline{T}) \tag{1.21}$$

$$k_g = 0.4 k_F(\overline{T}) + 0.6 k_\infty(\overline{T}) \tag{1.22}$$

The thermal conductivity k_∞ here is that of the oxyder. $\overline{T}$ is an averaged temperature defined as:

$$\overline{T} = (T_f + T_s)/2 \tag{1.23}$$

On the other hand, the Clausius-Clapeyron relationship for the liquid-vapor interface given by $\frac{dP_g}{dT} = \frac{P_g h_{f,g}}{(R_u/MW_F)T^2}$, leads to the expression:

$$P_g = A exp\left[\frac{-B}{T}\right] \tag{1.24}$$

with

$$A = exp\left[\frac{h_{f,g}}{(R_u/MW_F)T_{boil}}\right] \tag{1.25}$$

and

$$B = h_{f,g}/(R_u/MW_F) \tag{1.26}$$

The fuel mass fraction needed into the Eq. (1.28), is obtained from:

$$Y_{F,s} = \frac{B_{0,q} - 1/\nu}{B_{0,q} + 1} \tag{1.27}$$

The temperature at the droplet surface is then obtained using the following expression:

$$T_s = \frac{-B}{ln\left[\frac{-Y_{F,s} P_g MW_{pr}}{A\left(Y_{F,s} MW_F - Y_{F,s} MW_{pr} - MW_F\right)}\right]} \tag{1.28}$$

The molecular weight for the fuel is MW_F, and MW_{pr} for the products. The fuel vapor pressure is $P_g = 1$ atm. The constants A and B are the Clausius-Clapeyron constants, evaluated at T_{boil}.

First the temperature T_s is treated as a known parameter. Assuming a value for T_s,

Eqs. (1.19) and (1.20) can be evaluated. Eq. (1.28) is used to provide an improved value for T_s. Then, Eqs. (1.19) and (1.20) can be re-evaluated. The process is repeated until the convergence is obtained.

1.2 Thermoacoustic instabilities

1.2.1 Nature of the physical phenomenon

Understanding the mechanisms that control the combustion instabilities within the gas turbines or rocket engines has been a major priority for several decades. Instabilities are the result of resonant coupling mechanisms between two or more physical processes leading to damaging effects. The main objective is to guarantee the system energetic efficiency by avoiding operation ranges where instabilities could occurs. A usual approach is to classify instabilities in three main families [51]:

a- **Intrinsic instabilities:** inherent to the combustion process where chemical and thermo-diffusive effects can modify the flame propagation rate. In general, these instabilities depend upon the properties of the reactants. For example it can be mentioned the thermo-diffusive instability [52] or the Darrieus-Landau hydrodynamic instability [53].

b- **System instabilities:** involving some or even all the components of the system, from the fuel tank until the injection lines. This type of instability is characterized by pressure waves of low frequencies (from tens to some hundreds of Hz), propagating within the system components as longitudinal modes.

c- **Chamber instabilities:** known also as high frequency instabilities they are linked to the combustion chamber geometry. The pressure oscillations are coupled with the resonant modes of the combustion chamber. As a consequence, the characteristic frequencies of the instabilities are related directly to the chamber dimensions. In the case of axisymmetric chambers, the resonant modes can be standing or rotating.

Only the last family of instabilities is considered in this work

1.2.1.1 Acoustic modes within the combustion chamber

The combustion instability is linked to the resonance of the chamber the size of which gives the instability wavelengths. In practice the frequency f of such an instability has an order of magnitude of about 1 kHz and satisfies [54]:

$$f \sim \frac{c}{L_{chamber}} \tag{1.29}$$

with $c(T)$ the speed of sound, dependent on the temperature inside the chamber. $L_{chamber}$ can be: *(i)* the chamber length L defined in the flow direction. This corresponds to longitudinal acoustic modes; *(ii)* a characteristic length of the chamber

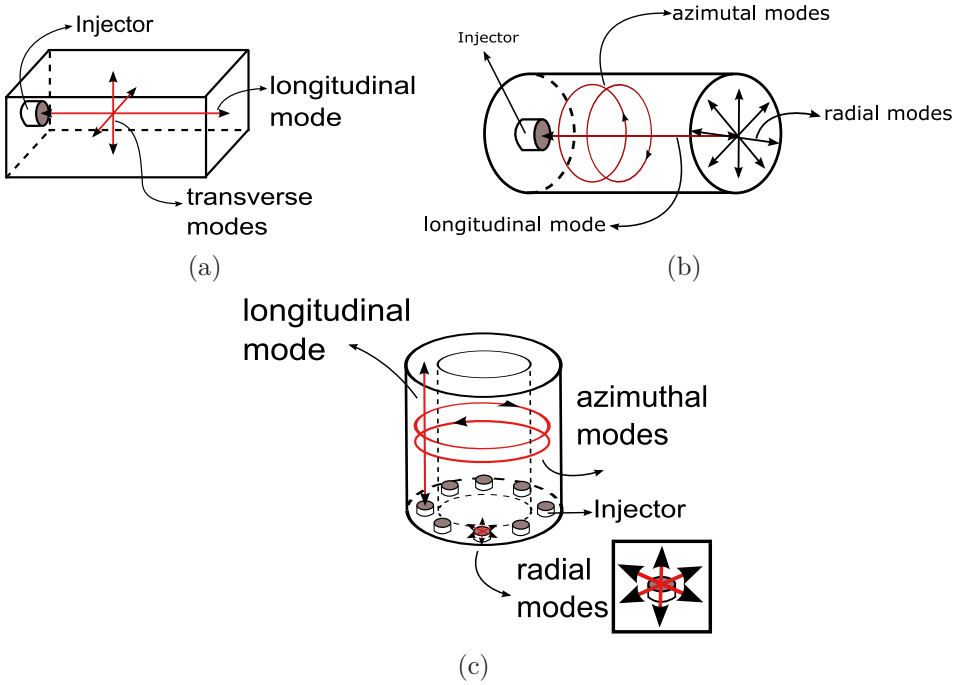

Figure 1.2: Chamber resonant modes illustrations: (a) right section, (b) circular section and (c) annular section

cross-section. For cylindrical or annular configurations this leads to spinning or standing azimuthal modes where $L_{chamber}$ is the azimuthal distance and for square configurations this leads to transverse modes; *(iii)* the width of an annular chamber or the radius of the cylindrical chamber. This leads to radial acoustic modes. This is illustrated in Fig. 1.2.

1.2.1.2 Thermoacoustic instability coupling loop

In the presence of extrinsic perturbations heat release rate (HRR) fluctuates leading to unsteady volume expansion. The flame acts as a pulsating sphere or acoustic monopole source. It generates acoustic waves corresponding to the so-called combustion noise[4]. The time fluctuation of the unsteady HRR, $\partial\dot{q}/\partial t$, appears as a source term in the acoustic pressure wave equation presented in a simple form in Eq. 1.30.

$$div\left[c^2\boldsymbol{grad}(p)\right] - \frac{\partial^2 p}{\partial t^2} = -(\gamma - 1)\frac{\partial \dot{q}}{\partial t} \tag{1.30}$$

An efficient feedback may take place between the downstream region of combustion and the jet-flow upstream of the flame, region where extrinsic perturbations are generated. As only acoustic waves are able to go back through the flow, the feedback is ensured

[4]The heat release rate unsteadiness can also generates temperature variations creating entropy waves. This leads to indirect noise or entropy noise [55]. This production of noise can participate in the occurrence of thermoacoustic instabilities. Nevertheless this issue is not studied in the present work

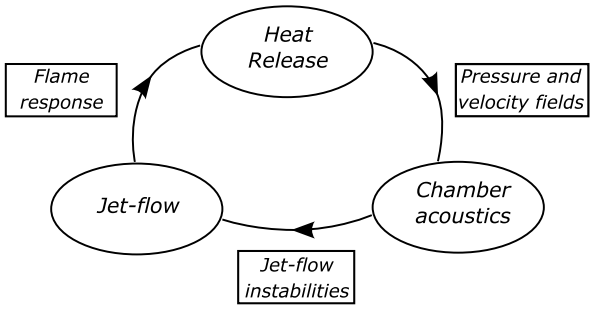

Figure 1.3: Thermoacoustic coupling loop

by these waves propagation [56]. The pressure fluctuations can participate in the development of aerodynamic perturbations, by activating intrinsic flow instabilities or by inducing flow vortical structures. These aerodynamics perturbations then produce fluctuations of the HRR. A basic model was developed by Crocco et Cheng [57] in order to link aerodynamic perturbations to the unsteady HRR, namely the $n - \tau$ model where n is the gain of the coupling and τ the time delay between the location where the perturbations is created and the location where the flame is impacted by the perturbation. Thus a coupling loop can occur which is represented by the scheme in Fig. 1.3. This coupling generates a resonant phenomenon under certain conditions, which is able to damage the chamber or blow out the combustion process.

1.2.1.3 Criterion for combustion instabilities

As mentioned above the coupling becomes dangerous as soon as an amplification of the instability can take place. The quantification of such amplification is modeled by the acoustic energy balance equation. Its local expression given per unit of volume is reported hereafter (Eq. 1.31):

$$\frac{\partial}{\partial t}\left(\frac{\rho_0}{2}\boldsymbol{u}^2 + \frac{1}{2\rho_0 c_0^2}p^2\right) = -div(p\boldsymbol{u}) + \frac{\gamma_g - 1}{\rho_0 c_0^2}p\dot{q} + \mathcal{D}_a \tag{1.31}$$

The left hand member represents the temporal fluctuations of the acoustic energy per unit volume constituted of the kinetic and potential acoustic energies. The right hand member is composed of three terms: the acoustic flux per unit area, $p\boldsymbol{u}$, the source term per unit of volume, and a damping term. To increase the acoustic energy density over time it is necessary to have a positive right hand member. For a given domain $\mathcal{V}$ (e.g. the entire of the combustor), an instability will increase over time if the following necessary condition is satisfied:

$$\int_{\mathcal{V}}\left(\int_{time} p\dot{q}dt\right)d\mathcal{V} > 0 \tag{1.32}$$

In the case of harmonic quantities modulated at the same frequency, the criterion imposes to have a positive cosine of their relative phase. This corresponds to the Rayleigh criterion.

1.2.2 Longitudinal and azimuthal mode instabilities in gas-phase combustion

Most of the times, combustion instabilities arise from the coupling between the heat release rate (HRR) with longitudinal and/or azimuthal modes developing inside annular chambers of the combustor [54, 58].

The **longitudinal modes** corresponding to the stream direction may develop as progressive waves with very low to medium frequencies. This mainly depends on the longest dimension of the chamber, but the upstream plenum may also interfere. Longitudinal modes, detected in many energy systems, have been widely studied experimentally, theoretically and numerically [59]. Their relatively low frequency range facilitating their quantification. These studies were performed in several conditions of environment and flow:

- laminar or turbulent flows,
- jet-flows with or without swirling
- acoustic fields in unconfined or confined fields
- single or multiple injectors

It has been shown that the acoustic perturbation acts on the system by inducing a convective mechanism or/and a pure acoustic mechanism. The flame responds as a low-pass filter leading in those cases to a slightly wrinkled or even unwrinkled front [60]. Experimentally, it has been highlighted that the variations of the flame front area is important in order to obtain HRR fluctuations. In particular, emission and combustion of pockets shed from the main flame front cause a strong HRR fluctuation [56].

For **azimuthal mode** studies, the same wide operation conditions and configurations, as those mentioned for the longitudinal modes, are found but the number of works is less important. In cylindrical or annular chambers, azimuthal modes may appear as spinning or standing (transverse) waves, characterized by medium to high frequencies [61, 62]. Particularly dangerous for combustor integrity, they have been systematically studied only recently due to the difficulty to quantify their space-time properties, in order to predict their triggering and growth numerically and to describe them theoretically [28, 54, 58, 63, 64]. Bourgouin *et al.* develop an experimental work on the basis of a laboratory annular chamber with multiple injectors. They showed the existence of azimuthal instabilities, resulting from two counter rotating azimuthal modes, but also of instabilities arising from the superposition of an azimuthal mode and a longitudinal mode [59, 65].

As the transverse modes are very often observed in energy systems, their properties must be well understood. Some of them have been investigated. Thus, it has been identified a particular type of coupling between the flow and azimuthal instabilities where transverse modes induce flow-rate fluctuations. This mechanism is referred to as "injector coupling" in rocket literature [66]. An analogous injector coupling was also identified as a dominant mechanisms in annular combustors of gas turbines. For example, induced flow-rate pulsations were noted in LES calculations of a complete

helicopter combustion chamber in the presence of a spinning mode [28]. A conversion from an acoustic transverse mode of the cavity to a longitudinal mode, shown previously by Baillot and Lespinasse [67] on a laminar flame or by Lieuwen and co-workers [38,68] for a swirling flame, both forced by a transverse acoustic field, was noted in the case of self-sustained instabilities in an annular chamber [65].

1.2.3 Interest of studying in open-loop acoustic forcing

As the mechanisms involved in thermoacoustic instabilities are complex, splitting up the instability analysis into several elements occurring in the coupling loop is useful to quantify the piloting phenomena. The feedback mechanism introduced previously as the n-τ model still necessitates studies to improve instabilities understanding. In particular, fine experimental investigations are needed to build physical scenarios and validate models. Facilities have proposed to work in open-loop acoustic forcing as reported in the review article [58]. The idea of these setups is to highlight and quantify some fundamental mechanisms which cannot be obtained in industrial combustor but also in academic ones. In that way, acoustic forcing imposed on the fluid system (flow and flame) is used to investigate flow topology and its interaction with flames. An illustration of this kind of investigation is given for transverse modes obtained in a semi-opened cavity in the case of a laminar premixed inverse-conical flame reported in [67]. It is shown that at the pressure antinode (PAN) flames are mainly driven by the dynamics of the vortex arrays generated by the acoustics. A wide variety of flame responses was investigated highlighting several physical mechanisms such as subharmonic strongly rolled-up flames, elongated wrinkled flames, asymmetric wrinkling flames due to and helical mode or aperiodic fluctuating flames. At the acoustic velocity antinode (VAN) the flame response shows strong horizontal oscillating displacement. The flame front moves laterally and periodically. When the fluid system is located at the acoustic intensity antinode (IAN) where the pressure gradient is high, the flow field and the flame front become non-axisymmetric.

By means of such forcing experiments it has been also possible to develop dynamical models, known as low order models (LOM), relying on semi-analytical modelings of the feedback mechanism. Indeed, a universal model able to represent how acoustic waves can impose HRR unsteadiness is still not obtained. To overcome this difficulty, different strategies, considering the flame as compact, can be chosen. Many works have been devoted to premixed combustion in the case of longitudinal modes. Thus some of them are based on analytical approaches [69], others on numerical calculations [27,70], or on experimental methods leading to determine the flame transfer function (FTF) in the linear case [71] or the flame describing function (FDF) in the non-linear case for which the gain and phase of the FDF depend on the amplitude level of the input [72,73] from measurements, at the frequency forcing, of the imposed acoustic perturbations and the resulting global fluctuating HRR.

The obtention of the FTF or FDF is quite scarce in the case of azimuthal modes or spray flames. It can be mentioned the LES work of Ghani who proposed in the presence of azimuthal instabilities an extension of the relationship obtained for longitudinal

acoustic modes where the local heat release perturbations were driven by orthoradial velocity fluctuations and not axial velocities as assumed for longitudinal modes [29]. There the FTF for transverse modes assumed the time delay between the orthoradial velocity and the unsteady heat release was imposed as a rotating field at a pulsation ω_{PVC} imposed by the flow. On the other hand, experimental FDF were measured by Mirat et al. [74] in order to characterize acoustic responses of a swirling spray flame performed in the case of steam assisted liquid fuel injectors. The spray flames investigated featured a distinct response to a longitudinal forcing compared to those obtained for premixed swirling flames. Another investigation is presented in [1] where the method to carry out the FDF of a single spray flame issued from a simplex injector is analyzed, again in the presence of a longitudinal mode. The FDF based on velocity fluctuations gave interesting and usable results whereas the FDF measured with the acoustic pressure radiated by the flame in the chamber was inappropriate, since the pressure appeared as an output of the unsteady flame and could not be taken as an input.

Once the link of the fluctuating heat release rate to the perturbations quantities is known, the set of equations which describes the thermo-acoustic system is then closed. Several ways of modeling can be advanced. Among them two general classes of low order models are distinguished, depending on their formulation in the frequency or time domain. This is introduced in the following sections.

1.2.3.1 Time domain representation

In the time domain, the perturbed quantities, pressure, velocity and HRR, are arbitrary functions of time. This approach is appropriate when nonlinear phenomena dominate such that the fluctuations depend on two or multiple acoustic modes, or develop during a transient phase. The Green function technique is in general valid for linear stability analyses of an oscillatory flowfield while the Galerkin method is employed for the problem of nonlinear oscillations (see [54]). There are two types of time domain analysis depending on the normality or non-normality of the systems modes.

In the case of **normal modes** expansion, the approximation is valid when the frequencies and spatial variations of oscillations deviate only slightly from the solution obtained without source terms. The spatial complexity of the model is reduced by chosing the acoustic eigenmodes of a cavity as basis functions of the Galerkin expansion to represent the acoustic quantities. The method was initially conceived by Zinn and Powell (1970) [75] and explored by Culick (1988) [54]. For a single cavity system, the acoustic pressure is written as follows:

$$p(t,x) = \sum_m \eta_m(t)\Psi_m(\boldsymbol{x}) \tag{1.33}$$

where Ψ_m are the eigenmodes. The amplitudes $\eta_m(t)$ of these eigenmodes satisfy second order dynamical equations.

$$\frac{\partial^2 \eta_m}{\partial t^2} + \omega_m^2 \eta_m = S_m(t,\boldsymbol{x}) \tag{1.34}$$

The source term S_m contains the effects of the flame dynamics, the damping and the acoustic forcing.

Bourgouin [65] used an expression expanded to n acoustic cavities, where *a priori* two modes Ψ_k and Ψ_l were orthogonal:

$$p_n(t,x) = \sum_{n,m} \eta_{n,m}(t)\Psi_{n,m}(\boldsymbol{x}) \tag{1.35}$$

In that case the heat release rate depends only on delayed values of acoustic velocity such as:

$$\dot{q}' = G\bar{\dot{q}}\frac{u'(t-\tau)}{\bar{u}} \tag{1.36}$$

In the case of **non-normal modes**, Balasubramanian and Sujith [64] have investigated the role of non-normality and nonlinearity nature of thermoacoustic oscillations in a Rijke tube. A system is said to be non-normal if its eigenvectors are not orthogonal. Non-normality can lead to transient growth of oscillations before they eventually decay. Further, non-normality leads to coupling between modes. This analysis allows energy exchanges between the cavity modes.

1.2.3.2 Frequency domain representation

In the frequency domain, the pressure, velocity and HRR are considered as harmonic quantities. The angular frequency is complex $\omega = \omega_r + i\omega_i$, with $\omega_r = 2\pi f_0$ the angular frequency and ω_i the growth rate. This model does not consider transient regimes and eigenmodes do not interact with each other. The set of equations modeling the system is closed by means of the knowledge of the link between the fluctuating HRR and the perturbing quantities. This leads to a dispersion relation from which modal growth rates and modal frequencies, defining the system dynamics, are determined. Two types of frequency domain analysis have been developed depending on a linear or non-linear approach. In the linear approach the Flame Transfer Function (FTF) $\boldsymbol{F}$ relates the flame global dynamic response in terms of fluctuating HRR to a fixed modulation level of the acoustic velocity fluctuations measured at a chosen point in the flow. $\boldsymbol{F}$ is searched as function of a gain (n) and a phase shift (τ), each one as a function of the angular frequency $\omega = 2\pi f_0$ with f_0 the forcing frequency:

$$\boldsymbol{F}(\omega_r) = \frac{\dot{Q}'}{\bar{\dot{Q}}} / \frac{u'}{\bar{u}} = n(\omega_r)e^{i\tau(\omega_r)} \tag{1.37}$$

where the prime symbol represents the temporal fluctuation and $\dot{q}$ is replaced by $\dot{Q}$, a global HRR considering the flame compact with respect to the acoustic wave. But this analysis cannot predict amplitudes of oscillations at the limit cycle and can not explain mode switching and instability triggering phenomena. So as mentioned above, to include such nonlinear phenomena, the Flame Describing Function (FDF) can be used. It is a method introduced by Dowling [76], generalized by Noiray et al. [72] and improved by F. Boudy et al. [77]. In this non-linear approach, the FDF define a flame

transfer function which depends on both input frequency and perturbation amplitude. Thus, its formulation is:

$$\boldsymbol{F}(\omega_r, \frac{u'}{\bar{u}}) = \frac{\dot{Q}'}{\bar{\dot{Q}}} / \frac{u'}{\bar{u}} = n(\omega_r, \frac{u'}{\bar{u}}) e^{i\tau(\omega_r, \frac{u'}{\bar{u}})} \tag{1.38}$$

They are used as predictive tools of system instability range. Very recently, the experimental work of Gaudron [78] on laminar and turbulent premixed flames, has brought important elements in the complete modeling of the burner where self-sustained instabilities can occur.

1.2.4 Instabilities in the presence of swirl and/or two-phase flows

Even though numerical methods have become very attractive [28, 79–82], the systems generally reach statistically preferred states which are difficult to predict. Thus, experimental studies remain essential to validate models and simulations. So far, much of the research effort has been devoted to gaseous flame systems. Most of the work concerns the coupling between combustion and longitudinal modes acting on single-flame test facilities. Far fewer works involve azimuthal instabilities [36, 38, 67, 83, 84] which are the most difficult to study in laboratory scale experiments, despite them being the most detrimental in engines. Moreover, since industrial systems implicate a set of flames, the study of the response of a single flame to thermoacoustic instabilities is questionable, when the objective is to characterize combustion dynamics occurring in annular combustors [61, 62].

Only some recent investigations report simulations of thermoacoustic instabilities in annular chambers and only few well-controlled laboratory-scale experiments are dedicated to gas-phase combustion in annular combustors in the presence of azimuthal perturbations [59, 61, 62, 85–87].

Investigations into the collective interactions between adjacent flames are essential in order to correctly take into account the multiple injection system flame dynamics perturbed by the acoustic field. Even if laboratory scale annular chambers can reproduce self-excited instabilities, a detailed investigation of the flows and flames is tricky to carry out, especially due to geometrical considerations. Besides that, the control of the occurrence and the persistence of self-excited instabilities are of great difficulty, participating in the complexity of the quantification of the phenomenon.

In this context, developments involving an acoustic forcing to well control this acoustic field over large ranges of amplitudes and frequencies of fluctuations have been made. For example an open-loop method was applied successfully on a single flame system in the presence of a transverse mode [83] which enabled a detailed and fruitful experimental analysis. This approach was recently used to show that applying an azimuthal forcing to flames developing in annular chamber [88] is a promising tool, in particular for a chamber able to produce self-excited instabilities.

Another important issue of interest, for power generation and aeronautical industries, is that of the liquid-fueled-combustor flame structure, which differs from lean premixed gas-fueled combustion [89]. However studies devoted to the response of swirl-stabilized spray flames to acoustic disturbances are still scarce. It should be noted that a few calculations [28, 79, 90] and a few experimental studies in the case of forced or self-sustained turbulent reacting two-phase swirled flows powered by liquid fuelled injectors [48, 91–94] do exist in literature. The few number of investigations in this area are incapable to provide all the explanations needed to highlight the mechanisms driving thermoacoustic instabilities, in particular for liquid fuel systems comprising multiple swirling injectors.

During this work a new original experimental setup has been designed in which longitudinal and/or transverse acoustic waves can be generated to perturb three air/n-heptane flames issued from two-phase swirled flows. Forcing these flames gives us the ability to follow the evolution of fundamental quantities and to produce a fine analysis of their behavior. This will lead to an improved understanding of the mechanism of the origins of thermoacoustic instabilities.

1.3 Objective and structure of the manuscript

The experimental setup designed and used for this work belong to the group of open-loop acoustic forcing test rigs. It is called TACC-Spray, that stands for Transverse Acoustic Combustion Chamber working with multiple two-phase swirling injectors. Unlike some works (e.g. [39]), in our case there is not a centerbody at the injector outlet. The 2T1L acoustic mode created within the chamber during our experiments is suitable because it allows to study the response of the flow and flames at various position of the acoustic field. Basically, there are three positions or basins of influence: the pressure antinode (PAN), the intensity antinode (IAN) and the velocity antinode (VAN). TACC-Spray is an important evolution of the test bench done by the CORIA team for an inverted conical laminar premixed flame in the framework of the ANR MICCA project [67, 83, 95]. The counterpart is the MICCA annular chamber of the EM2C laboratory, used to examine combustion instabilities coupled by azimuthal acoustic modes in gas-phase combustion [59, 65, 96] and recently also in spray conditions [1]. Unlike most of the facilities designed for transversely forced experiments where neighboring flames interaction cannot be studied [82], TACC-Spray will allow the investigation of this phenomenon, that can lead to strong HRR pulsations, which up today was studied only in full 360 degree combustors [61].

The current ANR FASMIC project, framework where this work is inscribed, is providing experimental and numerical data about combustion thermoacoustic instabilities in the case of two-phase flow swirling flames. As we have seen in the latter section, there is a need to fulfill the lack of experimental and numeric data about this type of systems since its interest for the future clean combustion technologies.

While currently, the CORIA team has also carried out studies concerning the spray behavioral response in non-reactive conditions to strong acoustic perturbations (e.g.

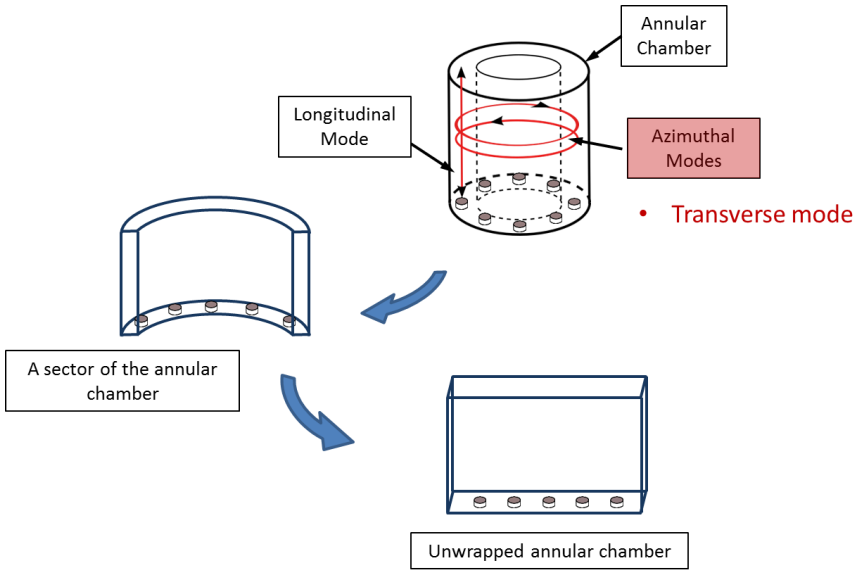

Figure 1.4: Unwrapped sector of an annular chamber designed for transversely forced experiments. Adapted from [58].

[97]), this work focuses in providing experimental data about:

1 the characterization of the two-phase flow and the spray flame;

2 the two-phase flow behavior under acoustic transverse perturbations;

3 the responses of spray flames to those acoustic transverse perturbations when they are placed in one of the three basins of influence (PAN, IAN or VAN) mentioned above.

TACC-Spray is composed of three flames linearly arranged. It represents an "unwrapped" sector of a thin-gapped annular combustor (see Fig. 1.4), the MICCA-Spray annular chamber, the adaptation of the MICCA annular chamber cited before. G. Staffelbach in [27] showed that even considering only three burners of an annular gas turbine gave information on flame stabilization that were not evidenced in the equivalent single burner simulation. This was not the case in the cold flow configuration. Accounting for the real geometry of a turbine appeared necessary in order to correctly predict the flame stabilization process. In particular the flame presence changed the burner behavior dramatically. A natural purely azimuthal mode of the set-up was excited in the reacting flow case, which cannot be evidenced in a single-burner study. The results presented in this manuscript are mainly extracted from the central flame. The manuscript comprises two main parts which are described hereafter.

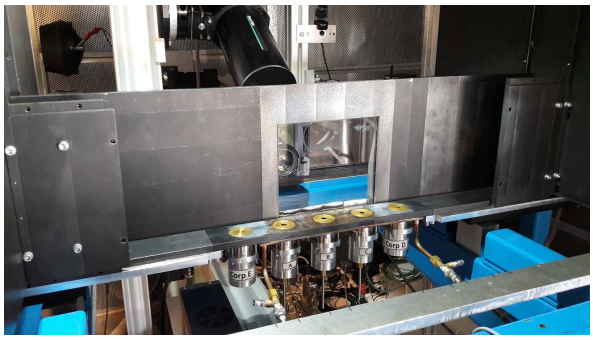

Figure 1.5: Picture of the injector system mounted in the combustion chamber. The three injectors in the center are reactive and those in the extremities are inert lines for stabilization. Front wall was removed.

Part I: TACC-Spray equipment and characterization

The first part presents the experimental bench designed and developed for this investigation as well as the post-treatment tools developed to analyze and extract valuable information about the two-phase flow and flame behaviors. This part begins with a detailed description of the experimental setup and its possible configurations. Basis measurements of temperature and acoustic pressure in the bench are described. Advanced optical diagnostics techniques used to characterize the two-phase flow properties, such as velocity field, fuel droplets sizing (e.g. LDA, PDA) and spray flow structures (visualized by high speed laser tomography) are detailed in ***chapter 2*** as well as experimental methods implemented to characterize the spray flame dynamics. These measurements are also exposed in that chapter.

In chapter 3 the injector system, composed of three identical independent burners, is introduced. The main components are presented and its implementation in the test bench is described (see Fig. 1.5). The innovative aerodynamical solution, found to stabilize the three spray flames without the help of a strong confinement by walls as usually done, is presented here. The acoustic response characteristics of a single unconfined burner, called also as independent injector[5], is also shown and explained (section 3.2).The study in that section is made in natural conditions free of forcing. The swirling air flow issued from an injector is characterized by its velocity profiles and its structures (section 3.3). Experimental velocity profiles allow to evaluate the swirl number S which indicates the swirl level imparted to the flow. In section 3.4 the atomizer performance is first characterized by means of a n-heptane spray. Then the fuel droplets sizing is measured at the injector exit. In section 3.5 the flames ignition protocol is described. The thermal behavior of the combustion chamber during the ignition process is exposed by means of temperature measurements recorded at several points in the bench. The attention is focused then in the fuel droplets behavior during combustion (section 3.6). Both fuel droplets velocity profiles and fuel droplets sizing have been investigated in a region located at the injector exit. In addition fuel droplets spatial and temporal evolution is explored in a region that extends upto several times the injector nozzle exit diameter. This is achieved by means of droplets

[5]In this work *the injector* refers to a single burner and does not refer to the atomizer.

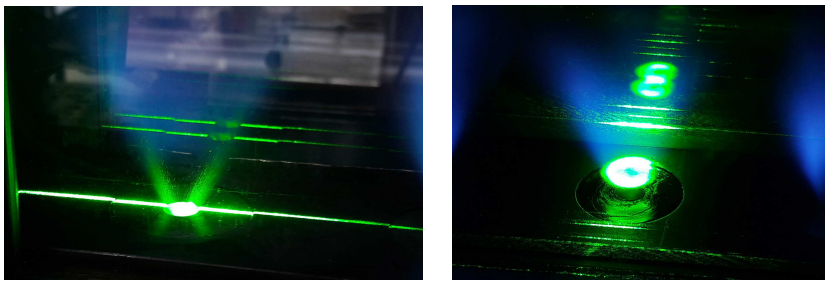

Figure 1.6: Picture of spray and flame when the laser tomographic technique is applied. Vertical view on the left and horizontal on the right.

rate measurements and spray visualizations made in vertical and horizontal high speed tomography planes (see Fig. 1.6). The spray is observed and studied by means of the time resolved views, but also by averaged views. Possible droplet evaporation mechanisms are also discussed and contrasted with the droplet rate measurements. At the end of the chapter, the three spray flames characterized without acoustics are presented. Their description will serve as a reference in the following. The central one is studied by analyzing CH* and OH* chemiluminescence emissions. The influence of operating conditions is analyzed by varying fuel flow rate, and consequently global equivalence ratio.

In ***chapter 4*** the methods developed to extract and analyze useful quantities from the recorded two-phase flow images, as well as those of the flame are presented. The high time resolution also gives the opportunity of performing class-averaged images defined on the basis of short duration sampling windows. Original post-processing methods applied to follow droplets are described.

Part II: TACC-Spray acoustic characterization and spray flame dynamics under an open-loop transverse acoustic forcing

Waves existing in self-unstable combustors can simultaneously impose different disturbances to the flames distributed inside the chamber. In particular when standing waves are present, flames modulations depend on their positions in the acoustic field. To bring fundamental elements of understanding, it has been chosen to place the system composed of the three flames at three acoustic basins of interest in the 2T1L acoustic resonant mode of the chamber: the pressure antinode (PAN), the intensity antinode (IAN) and the velocity antinode (VAN). This part is dedicated to the presentation of the results resulting from this investigation. It includes the description of the diverse responses of the spray and flames and the explanations of the underlying mechanisms that govern them. Part II is divided in four chapter.

The chapter 5, is devoted to the properties of the acoustic field. The study of the acoustic response of the combustion chamber is presented in sections 5.1 and 5.2. The experimental transverse mode is compared to numerical simulations and analytical calculations. A peculiar attention is brought to the influence of the temperature field on the acoustic response of the cavity and on the properties of the excited acoustic

mode. A development of the acoustic pressure wave in the case of non constant speed of sound is given in subsection 5.1.2. A simplified experimental procedure is proposed to validate the existence of the 2T1L acoustic mode obtained under cold conditions and then it is applied and validated under combustion condition (subsections 5.2.1 to 5.2.3).

The next two chapter present the effects of the acoustic mode on the energetic system. ***The chapter 6*** deals with the system response at the pressure antinode, while ***the chapter 7*** is concerned with the behavioral response of the system placed either at the basin of influence of IAN or at the basin of VAN. The approach in both chapters consists in investigating the swirling air flow, the spray and finally the flame response for a wide range of imposed acoustic pressure perturbations.

The aerodynamics of the air flow seeded with olive oil or DEHS particles is quantified under cold conditions by means of a LDA setup and the visualization of its main structures (sections 6.1, 7.2.1). The three velocity components are measured at the burner exit, allowing to calculate the swirl number S with and without acoustics. The same quantities as those in Part I to characterize *the spray* behavior are now quantified under forcing conditions (sections 6.3 and 7.2.2).

The flame dynamics is also quantified by means of CH* and OH* chemiluminescence global emissions (sections 6.4 and 7.3). A method using line-of-sight images of the flame gives access to its front evolution. Velocity and pressure fluctuations are simultaneously measured in the combustion chamber and within the air plenum along with the flame global CH* emissions, which allows to determine transfer functions between these quantities. This brings important elements in order to construct flame describing functions in the case of a downstream transverse forcing configuration. On the basis of results obtained at PAN, IAN and VAN locations, a mechanism of saturation is studied in the last section of chapter 7. ***The chapter 8*** summarizes the mains conclusions and gives some perspectives for future works.

Part I

TACC-Spray development and equipment

Chapter 2

Experimental setup

We introduce within this chapter a facility called the Transverse Acoustic Combustion Chamber (TACC). Inside this chamber, the combustion is achieved by the ignition of a two-phase flow, composed of liquid n-heptane atomized in a co-flow of swirling air. The resulting flame is recognized as a spray-flame and thus this experimental bench takes the name of TACC-Spray. At the conception stage of TACC-Spray it was desired to achieve a maximum of modularity, while keeping handling simple and practical. The result of this conception effort is presented below.

2.1 TACC-Spray set-up

This setup belongs to the class of open loop transverse forcing experiments. The acoustic forcing system used allows to attain important levels of acoustic pressure amplitudes. For this reason the entire setup is placed in an acoustically isolated room provided with adequate passages for electric cables and pipes. The acoustic forcing system is composed of:

- a signal generator HAMEG HM8150
- a frequency filter IMG STAGELINE
- an amplifier PEAVEY PV 900
- two compression drivers BEYMA CP850ND

A sinusoidal signal generated by the signal generator is sent to the frequency filter in order to cut off frequencies below 500 Hz so that to protect the compression drivers. The signal is then amplified by the amplifier before being sent to the compression drivers. The vibration velocity of the compression driver membrane was controlled with a POLYTEC 3000 series vibrometer. For the frequency range considered in this work, the behavior of the membranes gives an almost constant acoustic power whatever the frequency (see B).

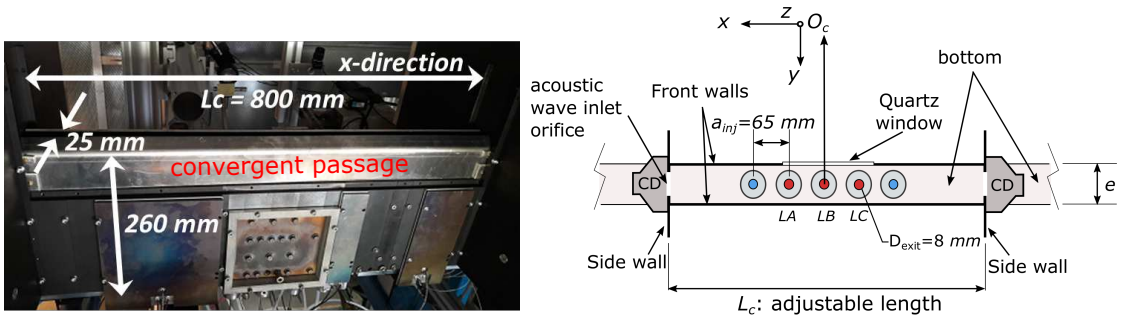

(a) (b)

Figure 2.1: (a): Characteristic dimensions of the combustion chamber. (b) Top view sketch of the cavity: compression drivers (CD), injectors: in red (fuel/air), in blue (only air).

The combustion chamber is where combustion takes place and, is also the acoustic cavity since the acoustic field created by means of the acoustic forcing system is established inside the chamber. Both expressions, combustion chamber and acoustic cavity, refer to the same part of this setup. In this manuscript the choice of one of this terminology will depend upon the context.

The Fig. 2.1 shows the setup composed of a bottom and two side and two front walls which can be moved all together relative to the bottom by a sliding mechanism. If needed, only the bottom can be moved leaving the walls fixed. Finally, for technical reason linked to optic diagnostics, the entire cavity (bottom and walls) can slide together. All the walls are made of steel as well as the bottom. The compression drivers are mounted, facing each other, on the side walls of the cavity (see Fig. 2.1(b)), on which an orifice is present to let the acoustic wave enter the cavity. These orifices have a diameter equal to 50 mm and their centers are placed at $x = \pm L_c/2$, $y = 0$, $z = 93.5$ mm.

The cavity dimensions are defined by a width e of 55 mm, front walls height h_c of minimum 200 mm and adjustable length, L_c, as it is shown in Fig. 2.1. L_c is chosen in order to force a 2T1L resonant chamber acoustic mode for a range of frequencies between 500 and 1400 Hz. Any point inside the cavity can be specified by a Cartesian coordinate system (O_c, x, y, z) where O_c is the center of the horizontal bottom plate; axis (O_c, x) is horizontal and O_c, z is the vertical ascending axis.

A convergent element of exit width equal to 10 mm has been used to reduce heat losses in the cavity. Indeed, it was verified that cold air was entrained in the cavity in combustion conditions (see Fig. 2.2(a)). To track the movement of the air, the air outside the cavity was seeded with incense smoke and illuminated by a vertical plane laser sheet perpendicular to the front walls. Thus, it has been verified that without convergent element there was an significant amount of cold air aspirated from the outside of the cavity. The convergent element avoids almost totally this aspiration (Fig. 2.2(b)). As a consequence, the use of a convergent element increases the temperature inside the cavity and homogenizes the temperature field as illustrated in Fig. 2.3, in the case where the flames are centered inside the cavity.

Attached to the bottom plate of the cavity is installed the injection system. This system is composed of three reactive injectors (fuel + air) and two non reactive (only air) at either side, that serve to stabilize the flames. The injection system characteristics are developed in section 3.1. The liquid-lines, that feed the three reactive injectors, are pressurized by a unique pump, namely the Tuthill DGS. Fig. 2.4 shows the diagram of the liquid-lines feeding system. The liquid flow rate for each line is controlled by a Coriolis mass flow meter CORI-FLOW from BRONKHORST; the air flow rate for each line is given by a mass flow meter HASTING HFM-201. Operating conditions range in $0.094 - 0.125$ g/s for $\dot{m}_{fuel}$, the fuel mass flow rate, and in $1.51 - 2.26$ g/s for $\dot{m}_{air}$, the air mass flow rate. These conditions provide a global power P of about 4.2 kW to 5.6 kW for each flame. A single quartz window, or two facing each other, if needed are assembled on the front walls allowing optical access to the injection zone. The front walls are composed of removable plates allowing us to choose the L_c distance and the position of the quartz windows depending on the zone of interest.

2.2 TACC-Spray configurations

L_c dimension is not varied continuously, but by increments corresponding to the set of removable plates that can be used for the front walls. The length of these plates goes from 20 to 200 mm. With this set of plates the maximum value of L_c that can be reached is 800 mm. It is also possible to increase the height h_c of the cavity up to 400 mm.

Each of the injectors used in the combustion chamber are fixed to the bottom plate. The distance a_{inj} between the center of these injectors can also be changed, to change the distance between flames. All the results within this manuscript have been obtained with $a_{inj} = 65$ mm. The study of a shorter distance ($a_{inj} = 40$ mm) is in progress.

In order to study the flames responses at different positions inside of the acoustic field established inside the cavity, or in order to study a zone of interest within the combustion chamber (e.g. recirculation zones), the position of the quartz windows can also be changed. Furthermore, one of the quartz windows can be replaced by a

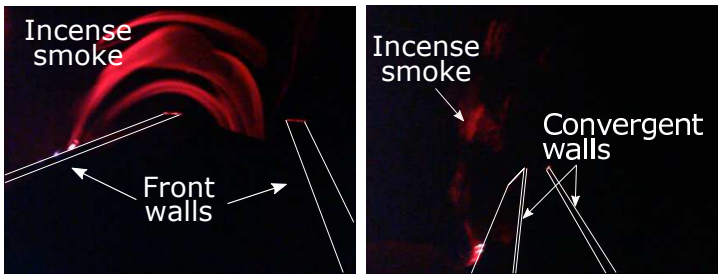

(a) (b)

Figure 2.2: Cold air traced by incense smoke: (a) entering a combustion chamber without convergent element; (b) barely entering a combustion chamber with the convergent element.

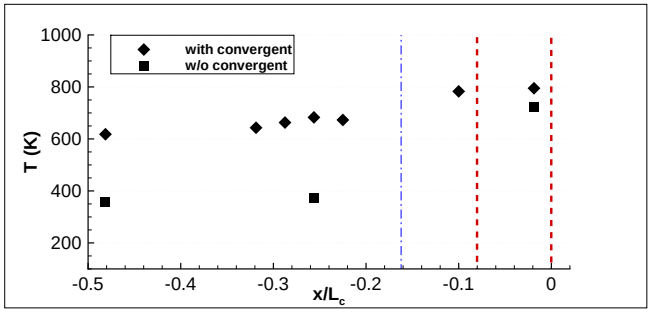

Figure 2.3: Temperatures measured in a half-cavity with the use of a top convergent. Dashed lines: positions of two injectors with flames; dot-dashed line: position of a non-reactive flow injector.

perforated plate where each perforation can receive a sensor in order to probe several points of the zone of interest (see Fig. 2.5(a)).

2.3 Measurements and diagnostics techniques

Basic instrumentation of TACC-Spray is composed of thermocouples type K and microphones B&K type 4182. In some cases, a DISA type 55M01 hot-wire is installed upstream of the injector exit in order to measure velocity fluctuations. Several optical diagnostics were also used in this study. Some diagnostics are applied simultaneously if necessary and if this was technically possible. All the measurements are synchronized with the acoustic forcing signal. Signals of pressure, chemiluminescence recorded by using a photomultiplier, and the hot-wire (when this is installed) are acquired at a sampling rate of 100 times the acoustic forcing frequency by using a National Instruments (NI) data acquisition card PCI-6123. The diagnostic setups and measurements are detailed hereafter.

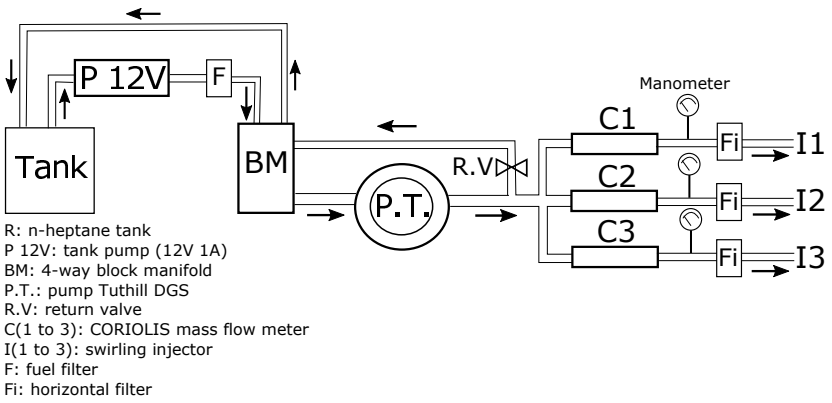

Figure 2.4: Diagram of the liquid-lines feeding system.

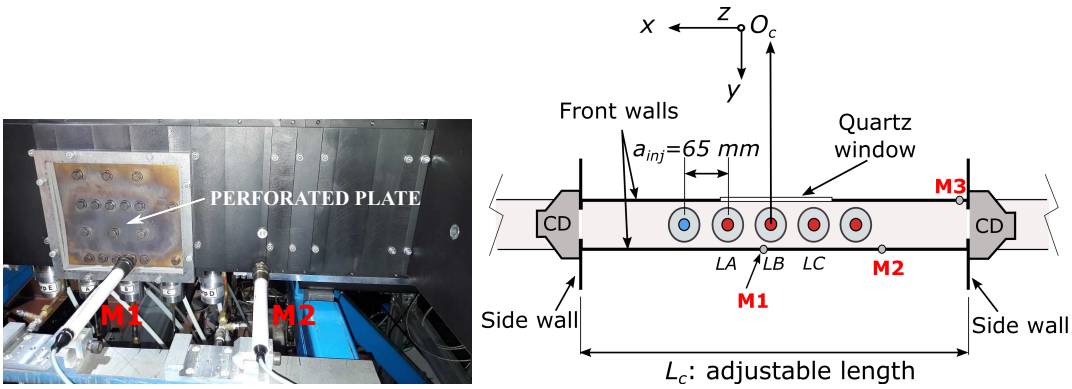

(a) (b)

Figure 2.5: (a) Picture of microphones mounted on the front wall and in a point of the perforated plate. (b) Top view of the microphones position relative to the injectors when these are in the middle of the cavity.

2.3.1 Pressure and temperature measurements

The thermocouples type K used can perform measurements from −210 to 1250°C. Here, measurements are recorded by using the ALMEMO 5690-2 acquisition system. This system has 9 channels and allows recording with a frequency up to 100 Hz. When multiple channels are used, measurements with a frequency higher than 10 Hz can perturb their precision. Measurements presented in this work are for frequencies up to 2 Hz. The microphones B&K type 4182 have a frequency response between 1 Hz and 20 kHz and they are used along with their NEXUS signal conditioner type 2690. The sensitivity for the acoustic pressure measurements was set using the signal conditioner, to 3.16 mV/Pa for pressure amplitudes lower than 1000 Pa (zero to peak) and 1 mV/Pa for higher amplitude levels.

Thermocouples and microphones are installed at various locations within the cavity. In the absence of combustion a microphone is mounted on a traverse system. The microphone access within the cavity by the top. Thus, in practice all the points within the cavity can be probed, however limited by the traverse system displacement motor, that have a step of 0.00625 mm. In this case, the temperature is constant within the cavity.

During combustion, microphones and thermocouples, passing through one of the front walls, are kept flush at the wall inner surface, at $y/e = 0.5$, and can be positioned at several (x, z)-locations (Fig. 2.5). The location of M1 is at $x/L_c = 0$, $z/h_c = 0.025$; the M2 location is at $x/L_c = -0.256$, $z/h_c = 0.025$ and the M3 location is at $x/L_c = -0.481$, $z/h_c = 0.025$.

The microphones are equipped with a stiff tube of a diameter $d_{tube} = 1.2$ mm and length $L_{tube} = 100$ mm. This is to keep the sensor away from the hot environment. The use of the tube introduces a phase shift (φ_{probe}) associated with the propagation of the acoustic wave within the probe tube at $c(T)$ the speed of sound. T is the temperature of the fluid where the sound propagates. In addition, a phase-shift of π is added due

to an intrinsic electronic inversion introduced by the microphone signal conditioner. A complex formulation is used to express the pressure temporal signal. For example, the local pressure fluctuations are denoted by the quantity $\hat{p}'(\mathbf{x},t)$ with amplitude $|P'|_{x,y,z}$. Thus pressure fluctuations $\hat{p}'(\mathbf{x},t)$ can be deduced from probe measurements, $\hat{p}'_{probe}(\mathbf{x},t)$ by the expression:

$$\hat{p}'(\mathbf{x},t) = \hat{p}'_{probe}(\mathbf{x},t)e^{i\varphi_{probe}}. \tag{2.1}$$

During combustion, the temperature field is non-uniform inside the cavity, and in consequence, the temperature at the point of measurement of pressure fluctuations must be taken into account to correctly calculate the phase shift, φ_{probe}.

2.3.1.1 Determination of φ_{probe} with and without combustion

For sake of precision, the acoustic pressure measurements (important to correctly identify the acoustic modes within the cavity) are corrected from the influence of φ_{probe}, without and with combustion. The phase shift, φ_{probe} is induced by the distance, L between the probe tube-end and the position of the probe membrane:

$$L = L_{tube} + L_m, \tag{2.2}$$

where $L_m = 13$ mm is the length of the connecting element between the probe tube and the membrane. Without combustion, the temperature (T) is constant within the cavity and within the tube. Thus, for a harmonic wave of angular frequency ω, we have:

$$\varphi_{probe} = \frac{\omega L}{c(T)} + \pi. \tag{2.3}$$

With combustion, the temperature field becomes non-uniform within the cavity as well as within the tube. Thus it is necessary to consider the speed of sound inside the tube, in order to determine the local pressure fluctuations. In order to do this, the temperature variation was assumed to be linear along the length of the probe tube (described by the coordinate ξ). Here, it is considered that $L = 113$ mm is small enough to make this assumption reasonable. For a higher value of L, knowing the temperature distribution within the probe tube is necessary. Taken this assumption into account to rewrite Eq. 2.3, we get the following expression for the phase correction:

$$\varphi_{probe} = \int_0^L \frac{\omega}{c(T(\xi))} d\xi + \pi \tag{2.4}$$

Applying the boundary conditions, $T(\xi = 0) = T(x)$ (the temperature inside the cavity at the inner wall surface), and $T(\xi = L) = T_L$ (the temperature at the sensor inner surface), we obtain:

$$T(\xi) = T(x) + \frac{(T_L - T(x))}{L}\xi \tag{2.5}$$

Substituting Eq. 2.5 into Eq. 2.4 and integrating the first term of the right hand side

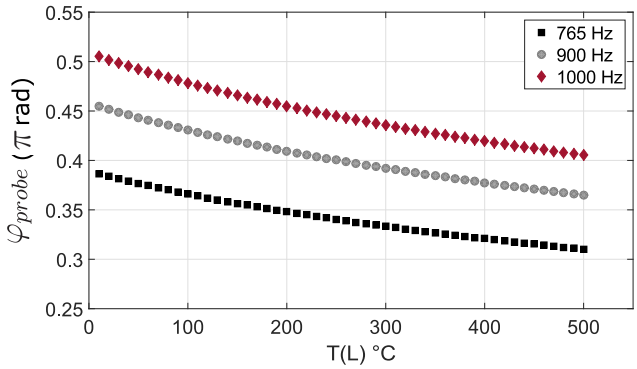

Figure 2.6: Phase shift (φ_{probe}), induced on the pressure measurements by the use of the probe tube, plotted as a function of the temperature T_L when the temperature within the cavity at the x-position is $T(x) = 500°C$.

yields to:

$$\varphi_{probe} = \frac{2\omega L}{\gamma r_{air}(T_L - T(x))}[c(T_L) - c(T(x))] + \pi \tag{2.6}$$

where γ is the adiabatic index and r_{air} is the specific gas constant. The Eq. 2.6 is under an indeterminate form when $T_L = T(x)$. To remove the indeterminacy of this equation, we made the following replacement:

$$c(T_L) = \sqrt{\gamma r_{air} T_L} \tag{2.7}$$

$$c(T(x)) = \sqrt{\gamma r_{air} T_x} \tag{2.8}$$

Then, we multiply numerator and denominator by $(\sqrt{T_L} + \sqrt{T_x})$. These steps give the final expression for φ_{probe}:

$$\varphi_{probe} = \frac{2\omega L}{\sqrt{\gamma r_{air}}(\sqrt{T_L} + \sqrt{T_x})} + \pi \tag{2.9}$$

The first term of the right hand of Eq. 2.6 is plotted in Fig. 2.6 for three different angular frequency values (ω), as a function of the temperature T_L, and considering $T(x = 0) = 500°C$. The temperature $T(x = 0)$ of this illustration is that measured at the M1 position when the central injector is at the basin of influence of PAN. As we can see from these equations, to calculate φ_{probe} it is necessary to know the temperature T_L.

The temperature at the sensor inner surface (T_L) has been measured, keeping the microphone mounting but, replacing the corp of the microphone by a thermocouple. We found values of T_L between 80°C and 90°C, when $T(x)$ was approximately equal to 500°C. To facilitate the determination of φ_{probe} in the case with combustion, since T_L is not easily available, one can wonder if it is acceptable to consider that the temperature

within the tube is constant and equal to $T(x)$, This is, using the following equation:

$$\varphi_{probe} = \frac{\omega L}{c(T(x))} + \pi \tag{2.10}$$

The precision of the φ_{probe} calculus, using Eq. 2.10 is then evaluated. For instance, the difference on the estimation of φ_{probe} between the Eq. 2.9, considering $T_L = 80°C$, and the Eq. 2.10, is in a range of 0.059π to 0.078π for the range of frequencies of Fig. 2.6. These differences represent a percentage of the acoustic forcing period in the range of 2.95% to 3.92%. This means that, using Eq. 2.10 rather than Eq. 2.9, have a low impact on the accuracy of the estimation of φ_{probe}. If a temperature lower than $T(x = 0) = 500°C$ is introduced in the two last equations, the difference between the values of φ_{probe} given by these equations is lower. In consequence, the accuracy of the estimation of φ_{probe} with Eq. 2.10 is better at lower temperatures. Because the results obtained during combustion presented in this work belong to cases with acoustic forcing frequencies from 760 to 830 Hz, the underestimation of φ_{probe} induced by Eq. 2.10 remains always lower than 4% of an acoustic forcing period. Therefore, this equation was chosen to deduce $\hat{p}'(\mathbf{x}, t)$.

2.3.1.2 Attenuation Δ_{probe} of the pressure signal

The attenuation depends on the length L_{tube} and the acoustic wave frequency (f_0). A law is obtained in [95] in cold condition for a probe length $L_{tube} = 100$ mm. This law is given by:

$$\Delta_{probe} = 20log_{10}\left(\frac{|P'|}{|P'|_{ref}}\right) = -1.1 \cdot 10^{-3} f_0 - 0.6 \tag{2.11}$$

where $|P'|$ is the pressure amplitude measured with the microphone equipped with the probe tube and $|P'|_{ref}$ is a measured reference pressure amplitude; f_0 is the frequency imposed to the compression driver. Calculation using this law gives an attenuation between -1.205 dB (13%) and -1.7 dB (18%) for frequencies between 550 and 1000 Hz. No corrections due to the attenuation have been applied to the pressure signals presented in this manuscript.

2.3.2 Laser diagnostics setup

The air-flow and spray was investigated by means of several laser-based diagnostics. Velocity profiles of the air flow within the cavity were obtained by means of a Laser Doppler Anemometry system (LDA). A high-speed laser tomography technique is used to visualize the air-flow structures and n-heptane droplet distribution. Droplet sizing at the nozzle exit was carried out by means of a laser diffraction (Malvern system) and by an imaging technique based on the transmission of a backlight diffuse-illumination, both techniques applied without combustion, without acoustic forcing and in a open field configuration. A Phase Doppler Analyzer (PDA) was used to quantify the n-heptane droplets presence and diameters within the cavity in a zone localized above the central injector, in the presence of the three flames.

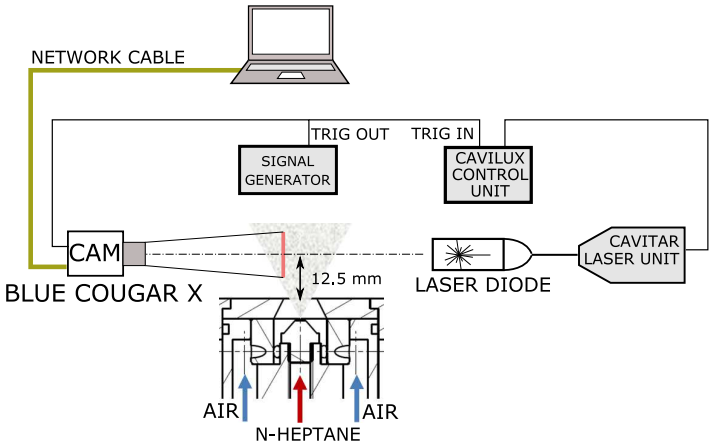

Figure 2.7: Setup of the imaging system based on backlight diffuse illumination.

2.3.2.1 Spray imaging by light transmission technique

The n-heptane spray issuing from a single injector was quantified in the presence of a swirling air flow without combustion. In order to do this, an imaging technique with backlight diffuse-illumination has been applied. This technique consists in placing the object (the spray in this case) between a continuous diffuse light source and a camera. The presence of the object between the light source and the camera causes a local decrease of light transmission and the pixels on the image corresponding to the object show a lower grey level respect to the background (see Fig. 2.9). The setup is composed of a laser diode powered by a CAVITAR laser unit (laser wavelength 640 nm, maximum pulse frequency 100 kHz, minimum pulse duration 20 ns), and a camera (see Fig. 2.7). The parameters of the laser were controlled through the Cavilux control unit. The laser diode has been synchronized with a Blue COUGAR-X camera equipped with a macroscopic lens. The synchronization of both, laser unit and camera has been made by means of the HAMEG signal generator. The signal applied is a 7 Hz and 1 volt square wave. The images obtained have 2448×2050 pixels and a resolution of 297.5 pix/mm.

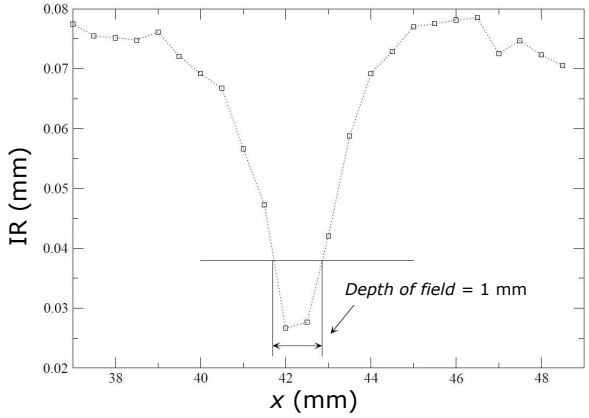

Figure 2.8: Impulse response from where 1 mm depth of field is obtained.

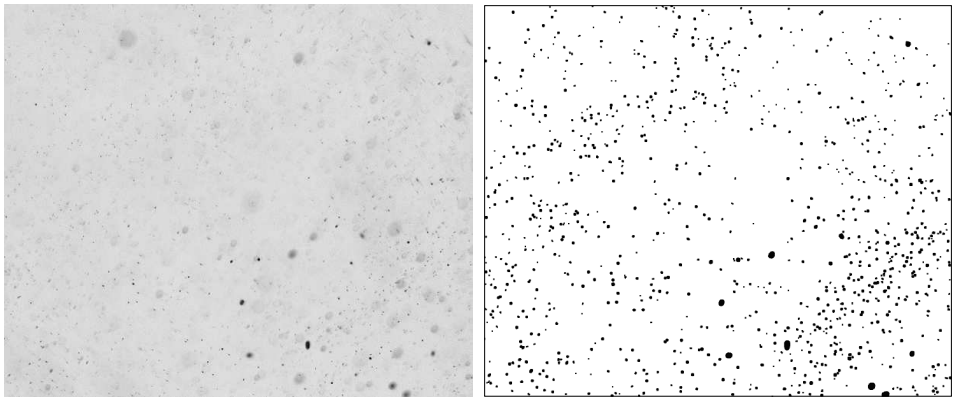

(a) (b)

Figure 2.9: Example of a normalized image (a) and the two-level image with the localized objects (b).

In addition, in order to correctly cover the spray thickness, the Point Spread Function (PSF), commonly known as impulse response (IR), has been measured (see Fig. 2.8). The PSF of an optical system is defined as the response of the imaging system to an infinitesimally small source point. It is a function of the position of the object with respect to the focus plane, and its width is minimum at the focus plane [97]. The PSF measurement gives a depth of field of 1 mm and as a consequence five parallel vertical planes separated by 1 mm have been taken. Thus, this technique is a tomographic-like measurement method, even if it is a line of sight one, thanks to the determination of the PSF width for each object. The optimal number of images have been searched for and then fixed at 100 in order to obtain statistically correct results. The spray images are first normalized with a background average image to avoid the influence of any variation of the light source on the localization of n-heptane droplets (see Fig. 2.9(a) and 2.9(b)). The localization consists in counting the droplets in a volume of section equal to that of the camera field of view: 56 mm^2. Image post-processing is performed with a software developed in [98]. The numeric droplet size distribution of the droplets and the characteristics diameters can be calculated. Their evaluation is crucial to quantify the fuel atomization and evaporation quality [99]. In particular, it is interesting to evaluate the Sauter Mean Diameter (SMD) D_{32} due to its wide utilization in spray and combustion. The SMD is a quotient of the total droplet volume divided by the total droplet surface area, and reflects both the energy content and the evaporation rate [100]. Details concerning the droplet size measurement by image processing can be found in [101]. Results obtained with this method are presented in section 3.4.2.

2.3.2.2 Laser diffraction technique

This technique is based on the analysis of the diffraction patterns of a laser beam going through the spray (forward diffraction). The principle of this technique is sketched in Fig. 2.10. The system is composed of a helium-neon laser beam (670 nm), with a diameter of about 13 mm, generated by a stabilized laser source, used to probe the droplets cloud. In our setup the center of the laser beam is positioned at $z_s = 12.5$

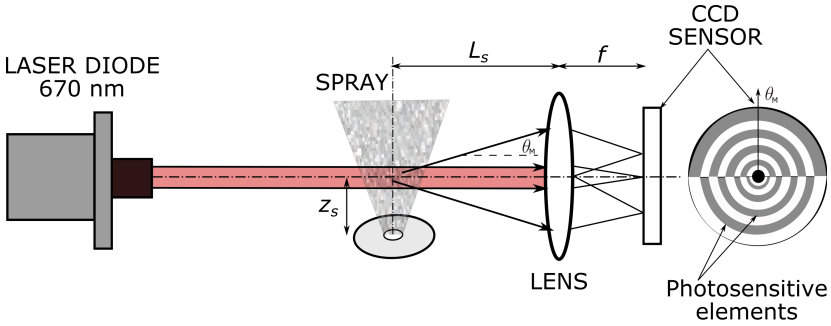

Figure 2.10: Sketch of principle of the system based on the diffraction of a laser going through the spray (Malvern system).

mm. A lens with a focal distance $f = 200$ mm, is installed in the receiver head in order to measure the light intensity diffused by the spray. The spray is positioned at a distance lower than or equal to $3f/2$ from the lens. In our setup the distance between the spray and the receiver was of 170 mm. In the receiver a CCD sensor records the diffraction patterns. This CCD is composed of a set of photosensitive elements placed concentrically.

The theory behind this technique states that the diameter of a droplet will be inversely proportional to the angular position (θ_M), on the CCD sensor, of the first minimum (referred to the light intensity) of the droplet diffraction pattern. This is then extended to analyze an entire spray. The system gives a volumic droplet size distribution integrated over a volume generated by the intersection of the laser beam and the spray. For our system this volume has a section of about 132 mm^2, which is that of the laser beam. Data has been processed with the INSITEC RT Sizer software of Malvern Instruments. Characteristic diameters are calculated and in particular the SMD diameter because its interest to quantify the quality of the atomization. Results are discussed in section 3.4.2. Further details on this technique can be found, for instance, in reference [102].

2.3.2.3 Laser Doppler Velocimetry and Phase Doppler Particle Analyzer

The Laser Doppler Anemometry (LDA) technique requires the seeding of particles in the fluid when the gaseous phase is studied. To quantify the n-heptane droplet velocities, rate and diameters a Phase Doppler Analyzer (PDA) technique is applied. The LDA/PDA system principle is sketched in Fig. 2.11. It is composed of a 4W argon-ion laser source. From this source two wavelengths in the visible spectrum (390 to 700 nm) are selected and carried to the transmitting probe through a fiber. A beam splitter is used in order to obtain two coherent laser beams from each single laser beam. The laser beams are focused by a lens with focal-length of 500 mm that equips the transmitting head. The beam spacing is 50 mm and the beam half-angle is 2.862°. The measurement volume obtained by the intersection of the two laser beams from each single one is $dx \cdot dy \cdot dz = 0.149 \cdot 0.149 \cdot 2.981 = 0.066$ mm^3. The two blue laser beams at $\lambda_b = 488$ nm measure the vertical velocity and the two green laser beams at $\lambda_g = 514$ nm measure the radial or azimuthal velocity component depending upon the position of the measurement volume into the flow. The interference of the two laser

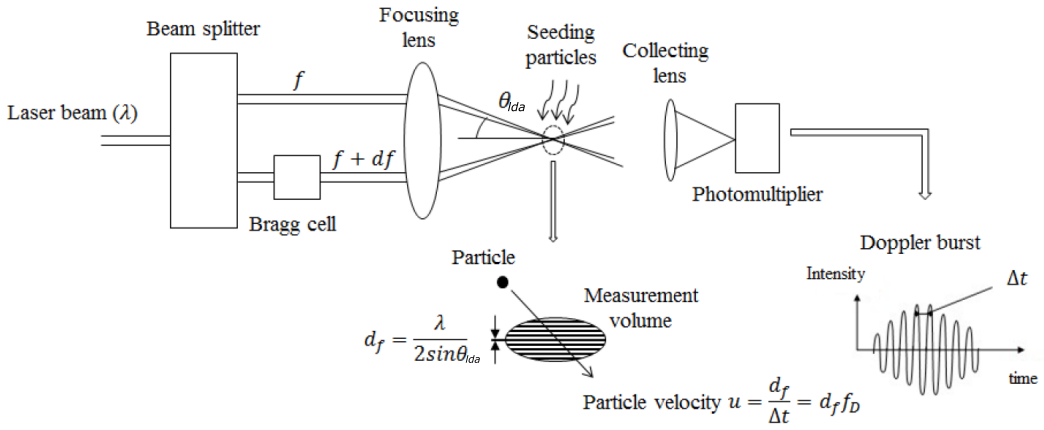

Figure 2.11: Sketch of the LDA/PDA system principle [97].

beams creates fringes of high light intensity. The distance between two consecutive fringes (d_f) is defined by the wavelength of the laser light and the angle θ_{lda} (half of the LDV laser beams intersection angle) as $d_f = \lambda/2sin\theta_{lda}$. As the particle traverses the fringes the scattered light fluctuates in intensity at a frequency called Doppler frequency (f_D). The scattered light is collected by a photomultiplier that equips the receiving probe, which produces an electrical current proportional to the light flux, called Doppler burst. The system signal processor determines the Doppler frequency of each particle. A Bragg cell produces a slight frequency shift (df) on one of the two beams (see Fig. 2.11), making the fringes pattern moves at a constant velocity. This allows to determine the direction of the particle velocity. Two particles with the same velocity, but moving in opposite directions, will produce a measured frequency given by $f_m = df \pm f_D$, with the sign depending on the direction of the particle. Finally, the particle velocity is obtained as $V = d_f(f_m - df)$. The receiving probe is mounted to face the transmitting probe and collects the light scattered by the particles passing through the measurement volume. In the PDA system the receiving probe is put in FIBER mode having a scattering angle of 30° and focal length of 310 mm.

Velocity profiles of the air flow were obtained by means of the LDA system. In order to achieve the measurements using this technique, the air was seeded upstream by DEHS droplets of diameter $d_p < 5$ μm and density $\rho_p = 912$ kg/m^3. The Stokes number, S_t, is introduced to evaluate how the seeding is able to follow the air flow dynamics. It is defined by $S_t = \tau_{DEHS}/\tau_{air}$ with $\tau_{DEHS} = \rho_p d_p^2/18\mu_{air}$ (with $\mu_{air} = 1.8 \cdot 10^{-}5$ kg(ms)$^{-1}$) and $\tau_{air} = D_{exit}/U_b$. Since S_t is lower than 0.25 for typical operation conditions, the use of this tracer is satisfactory to investigate air flow properties. For this illustration, the physical properties are taken at $T_{ref} = 293$ K. As an example, the velocities measured at a plane $z = 3$ mm, above the middle injector is shown in Fig. 2.12.

When the disperse phase is studied by using the PDA system, no seeding is required since we are interested in n-heptane droplets. Radial profiles of the droplet Sauter mean diameter (d_{32}) and mean arithmetic diameter (d_{10}) corresponding to various z-positions have been calculated. Vertical and radial velocity profiles of n-heptane droplets were also obtained in this mode and a variable Stokes number as function of

n-heptane droplet mean arithmetic diameter d_{10} has been introduced. The results of these measurements will be discussed in chapter 3.

2.3.2.4 High-speed Laser Tomography technique

Visualization of the swirling flow has been performed by means of a high-speed laser tomography technique in order to study its structure and temporal evolution. This technique has been applied in two cases:

- on the gaseous phase, seeded with DEHS particles and without liquid (n-heptane) injection,
- on the spray with combustion

The n-heptane droplets, olive oil or DEHS particles, depending on the case, were illuminated by a horizontal or vertical laser sheet created with an adapted optic lens array. The laser source is a COHERENT Genesis MX series continuous wave ($\lambda_g = 514$ nm) with 1.1 W of output power. The scattered light from the flow tomography cuts made by the laser sheet are recorded by means of a V2512 Phantom camera. This camera has a 28 micron pixel size and 12-bit depth. It was equipped with a lens with focal-length of 200 mm (f/8 and f/4 for horizontal and vertical tomography respectively) and 20 mm extension tube. Some vertical tomographic views have been obtained also with a Photron FASTCAM SA5 camera. Its pixel size is of 20 micron and capture image with 12-bit depth. It was equipped with a lens with focal-length of 200 mm (f/4).

Obtaining horizontal tomographic views in our experimental setup was challenging. The camera for this setup can not be installed vertically over the flow because it must not receive seeding particles, fuel droplets or burned gases from combustion. Thus, the camera was installed outside of the flow, inclined at 45° from the x-y plane and it was equipped with a Scheimpflug mount inclined at 20° with respect to the camera (see

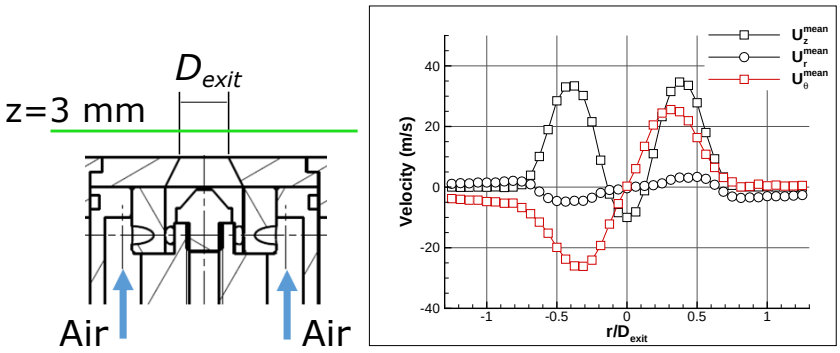

(a) (b)

Figure 2.12: (a) Side view of the plane of measurements by LDA at $z = 3$ mm above the nozzle exit plane and (b) mean velocity profiles of the seeded swirling air jet issued from the middle injector: U_z^{mean} (vertical), U_r^{mean} (radial), U_θ^{mean} (azimuthal), for $\dot{m}_{air} = 1.72$ g/s ($U_b = 28.6$ ms^{-1}) and $S = 0.68$.

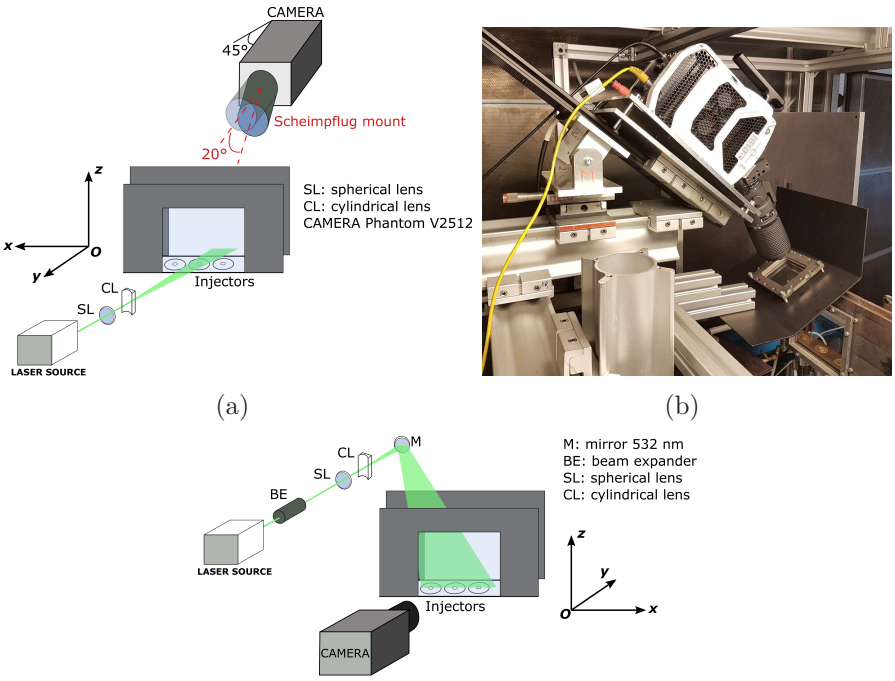

Figure 2.13: (a-b) Setup of the horizontal and (c) vertical laser tomography technique.

Fig. 2.13(a)). This setup is very sensitive to the camera inclination angle, in particular due to the presence of the quartz window of the cavity. The focus process needed a fine positioning system for the camera and the lens Scheimpflug mount, specially made for this setup. Even with the camera installed outside the flow, a protection system consisting in a steel screen with a quartz window was employed (see Fig. 2.13(b)) to avoid seeding particles impinging on the camera and lens or avoid their exposition to high temperature. Images in the x-y planes was captured for positions from $z = 1.5$ to 8.5 mm. In this setup, the camera was set to record images of 768×768 pixels with a spatial resolution of 0.031 mm/pixel at 35 kfps. The exposure time is 10 μs.

For the vertical views, the camera is positioned perpendicular to the x-z plane and the vertical laser sheet intersects the flow at $y = 0$ (see Fig. 2.13(c)). In this setup the V2512 camera was set to record images of 976×1024 pixels with a spatial resolution of 0.036 mm/pixel, at 20 kfps. When the FASTCAM SA5 camera was used it was set to record images of 704×520 pixels with a spatial resolution of 0.042 mm/pixel, also at 20 kfps. For this setup, in the case of both cameras, the exposure time is fixed at 40 μs.

2.3.3 Flame front light emissions measurements

The flame dynamics is characterized through the analysis of the emission signal of OH* and CH* radicals. The emission signal, noted $I'_{OH^*}(t)$ or $I'_{CH^*}(t)$, is considered to be an indicator of the combustion intensity. In the absence of soot, this signal can be directly linked to the heat release rate of the combustion [74]. The time-resolved emission

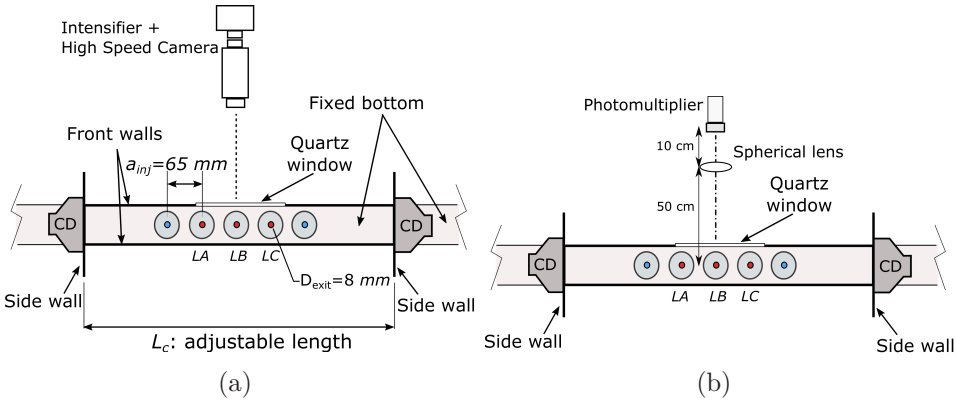

Figure 2.14: Top view of the cavity with (a) a light intensifier plus a high speed camera; (b) a photomultiplier (PM) equipped with an interference filter.

signals are registered by a photomultiplier (PM) HAMAMATSU H6779 equipped with an interference filter centered at $\lambda = 325$ nm with a full width at half maximum (FWHM) of 95 ± 2 nm for OH* or centered at $\lambda = 430$ nm with a FWHM of 20 ± 2 nm for CH*. The PM gain is adjusted to $0.435 \cdot 10^5$ and $0.600 \cdot 10^5$ for OH* or CH* chemiluminescence emissions respectively (Fig. 2.14(b)) in order to reach similar signal levels with both filters. The time response of this PM is 0.78 ns.

The middle flame is imaged on the PM by using a UV-spherical lens. A high speed camera, Phantom V10, providing a 12-bit grey scale resolution is used to record flame motions. A LAMBERT HICATT 25 Instrument image intensifier is mounted (see fig.

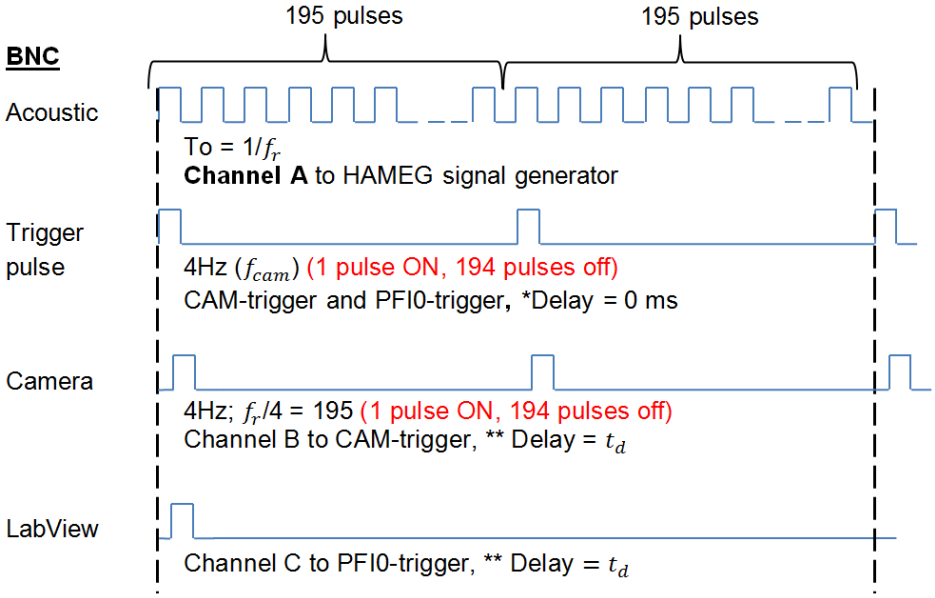

Figure 2.15: Synchronization diagram between the external harmonic excitation (acoustic forcing) and images acquisition with the PIMAX4 camera. Illustration for a case with $f_r = 780$ Hz and $f_{cam} = 4$ Hz. *Delay with respect to the acoustic forcing. **Delay (t_d) with respect to the image acquisition trigger pulse, with $0 \leq t_d < 1/f_r$.

2.14(a)) with an UV-48 mm lens and an interference filter centered at $\lambda = 325$ nm to visualize OH* emissions. Intensifier gain remains constant during all experiments. The camera is set to record images of 576×1000 pixels at 2773 fps when the three flames are considered. When only the middle flame is followed, the camera sampling rate is set to 6120 fps with 576×400 pixels. The spatial resolution in both cases is 0.16 mm/pixel. The exposure time is 160 μs.

Phase-locked images synchronized with the acoustic signal were recorded with a configuration that consists of a PIMAX4 emICCD camera, an UV-48 mm lens and interference filters for OH* or CH*. This camera provides an image definition of 1024×1024 pixels with a spatial resolution of 0.088 mm/pixel. A cycle of the acoustic forcing is reconstructed using 10 equidistant time delays. For each delay a phase-averaged image is computed over 100 images. A full cycle of the flame front motion is reconstructed from these phase averaged images. The synchronization diagram between the acoustic forcing and the image acquisitions with the PIMAX4 camera, is presented in Fig. 2.15, using as illustration a case with acoustic forcing frequency $f_r = 780$ Hz and acquisition rate $f_{cam} = 4$ Hz. The synchronization signals are delivered by a delay generator BNC Berkcley Nucleonics 575 series. The sinuous signal for acoustics is delivered by a function generator HAMEG HM 8150. A trigger pulse, with a delay t_d, is sent to the camera and to the NI acquisition card used to record pressure signals. For this illustration, the time delay is $t_d = (i-1)/(780 \cdot 10)$ s where i represents the equidistant phase-locked points from 1 to 10.

2.3.4 Main measurement instruments and diagnostic techniques

The main instruments and diagnostic techniques employed in this work to study the fluid system are listed in Table 2.1.

Table 2.1: Table summarizing diagnostics and measurements techniques applied in this work.

Physical property	***Applied to***	***Instrument / Diagnostic***
Acoustic pressure	the cavity or air plenum	Microphones
Temperature	outer walls/cavity inside	Thermocouples
Size distribution	n-heptane droplets	Laser diffraction
Size distribution	n-heptane droplets	Imaging
velocity profiles	seeded injected air	LDA
Size and velocity	n-heptane droplets	PDA
Trajectory and streakline	n-heptane droplets	High-speed Tomography
CH/OH* light emission*	flame	Cameras and Photomultiplier

Chapter 3

Injection system

In this chapter we introduce the injection system that equips TACC-Spray bench. We detail the components of the injectors and the setup of these injectors in the chamber and we introduce the aerodynamic stabilization of the flame that plays the role of a soft confinement for our flames.

Using the COMSOL simulation software we study the acoustic response of a single injector and we compare the simulation results with experimental measurements using a dedicated setup.

The air-flow, in non-reactive condition and without acoustic forcing, exiting from a single injector, is characterized when the injector is placed inside the chamber with all the injectors operating. In order to do this, we use a LDA system and laser tomography views of the seeded air-flow.

Within the next section, the results of the characterization of the atomizer are present. Next to this, the spray behavior without acoustic forcing is described, by means of the results of PDA measurements and tomography views. Some basic evaporation models are also presented and we discuss about its applicability to describe the n-heptane droplets evaporation process in our case. Finally, in the last section, we introduce the two-phase flow swirling flames without acoustic forcing.

3.1 Components and assembly in the combustion chamber

The injection system consists of three independent linearly-arranged radial swirl injectors separated by a center distance $a_{inj} = 65$ mm. It is mounted on the fixed bottom of the cavity (see Fig. 3.1). By using the sliding mechanism the injection system can be placed at various specific locations of the controlled acoustic field. Each injector is composed of a plenum, a distributor and a radial swirler for the air, and a simplex atomizer for n-heptane, provided by EM2C laboratory (Fig. 3.2). The air distributor is an element with six ducts circumferentially placed and regularly spaced connected

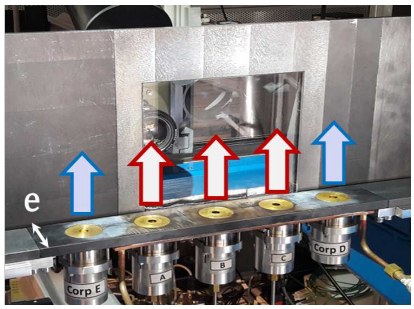

Figure 3.1: Swirling injectors system. Arrows: red indicates a two-phase flow and blue only air flow.

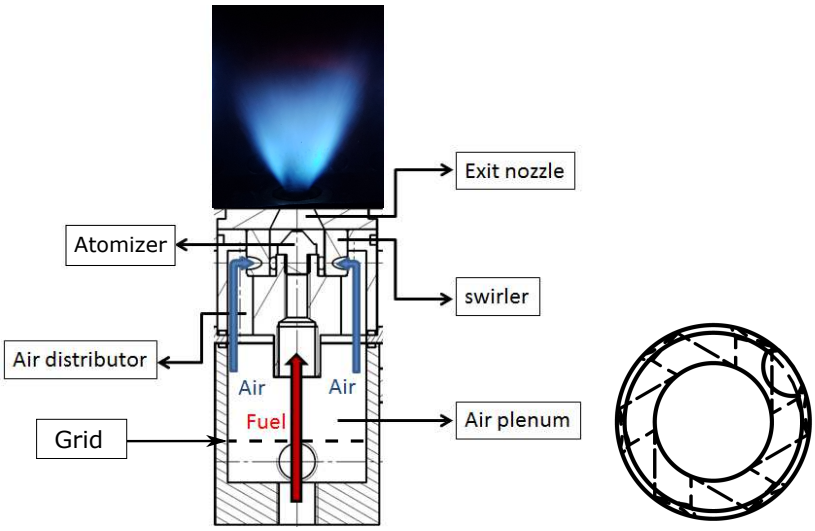

Figure 3.2: (a) Single injector components and its two-phase flow swirling flame (middle flame). (b) Cut of the radial swirler model, viewed from the top.

to the radial swirler. The swirler has also six inclined circular vanes to direct the air into the nozzle. These vanes make the air rotate in the clockwise direction, viewed from the top as it is shown in Fig. 3.2(b). Two swirlers, with circular vanes of two different diameters, have been used during this work. The results presented within this manuscript, have been obtained using the swirlers with vanes of diameter equal to 4.5 mm. The liquid fuel is transported through the air plenum, inside a linear tube of outer diameter equal to 4 mm. Then, it is injected into the swirling air-flow by means of the atomizer. The atomizer is set 5.36 mm back from the nozzle exit. The exit nozzle of the two-phase flow injector has a diameter $D_{exit} = 8$ mm. The particularity of the nozzle used for these injectors is its non-inverted cone trunk shape.

3.1.1 Aerodynamic stabilization of the flames

In an annular chamber like that studied in [62, 87, 94, 103], the overall stabilization is ensured by the fact that the swirled flames are distributed all around a circumference, each flame being surrounded by two others. The three linearly-arranged flames cannot be stabilized *a priori* due to the absence of an adequate confinement of the energetic system. To resolve this difficulty an aerodynamic solution was found, able to guarantee combustion persistence. It consists of additional swirling air jets, placed at the same center distance a_{inj} to the outer injectors (see blue arrows in Fig. 3.1). This soft confinement creates the appropriate boundary conditions to well stabilize the spray swirling flames in the cavity. Moreover the two non-reactive jets keep the flames away from side walls, preventing overheating of the compression drivers mounted on these walls. The driver performances are thus unchanged compared to ambient temperature conditions. Compared to others experimental setups in the group with open-loop acoustic forcing test-bench (e.g. [36, 104]), this stabilization solution avoids the need of a strong wall confinement and, by preventing the compression drivers overheating, reduce the complexity to drive and assess the acoustic injected into the cavity.

When the middle injector is placed at the center of the cavity, the stabilization injectors are symmetrically placed relative to this position, so at the same distance from the side walls and the stabilization injectors flow rates are identical. When the injection system is not centered within the cavity, the flame stabilization is modified. In order to keep three flames with similar shapes and sizes, the flow rate of the stabilization injectors must be adjusted in order to compensate the distance between each side wall and the respective stabilization injector. An illustration of a typical operating condition for each position considered in this work is reported in the Table 3.1 for the configuration $L_c = 0.8$ m. In this table, "non-reactive left" identifies the stabilization injector nearest to the side wall in the region $x/L_c < 0$. The reactive injectors have typically the same flow rates regardless the position of the injector system within the cavity. However, some results presented in this manuscript, correspond to cases where the reactive injectors have different flow rates.

Table 3.1: Typical flow rates operating condition

Injector	$\dot{m}_{fuel}$ (g/s)	$\dot{m}_{air}$ (g/s)	Equivalence ratio ϕ
Both non-reactive (PAN)	—	3.23	—
Non-reactive left (IAN)	—	2.58	—
Non-reactive right (IAN)	—	3.23	—
Non-reactive left (VAN)	—	2.43	—
Non-reactive right (VAN)	—	3.45	—
Reactive Middle	0.097	1.72	0.85
Reactive Sides	0.097	1.72	0.85

3.2 Acoustic response of the injectors

In this section we present the results of the modal analysis of a single injector achieved by numerical simulations with COMSOL Multiphysics and by an analytic model and also verified by experimental measurements. The study was performed without air flow. However, the influence of the air-flow on the acoustic response will be discussed. The eigenmodes are searched in order to know if there are modes able to be excited by the transverse acoustic mode that will be generated within the acoustic cavity in the frequency range of 0.5 to 1.4 kHz.

The 3D model considered for the simulation consists of the air plenum, the six ducts of the air distributor, the six vanes of the swirler and the exit nozzle. This model takes into account the presence of the atomizer, but the fuel line is not modeled. A sound hard boundary condition has been applied to all the walls (Eq. 3.1). This condition prescribes a boundary at which the normal component of the acceleration is zero:

$$\mathbf{n} \cdot \frac{1}{\rho_0} \mathbf{grad} p' = 0 \tag{3.1}$$

At the nozzle exit surface a sound soft boundary condition is applied, meaning that the acoustic pressure vanishes (see Eq. 3.2):

$$p' = 0 \tag{3.2}$$

The mesh has been created applying the physics-controlled mesh option of COMSOL (Fig. 3.3) with the size option *Fine* selected. This method adjusts the mesh element size depending on the geometric characteristics of the different regions of the model.

The origin of the Cartesian coordinate system of this model is placed at the center of the bottom section of the air plenum which is circular with a radius equal to 15 mm. A pressure probe is placed at a point defined by $(x, y, z) = (5, 0, 10)$ mm (Fig. 3.4(a)). The first seven eigenfrequencies are plotted in Fig. 3.4(b). The first eigenfrequency is

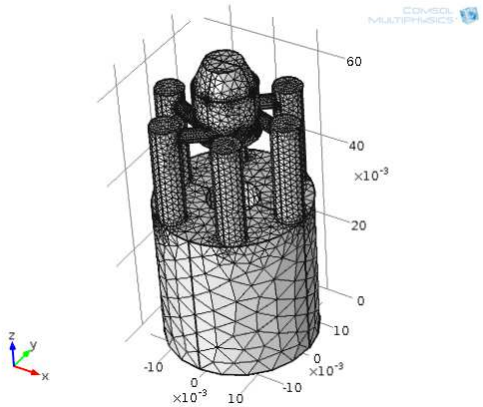

Figure 3.3: Mesh of the 3D model used to study the eigenfrequencies of the single injector.

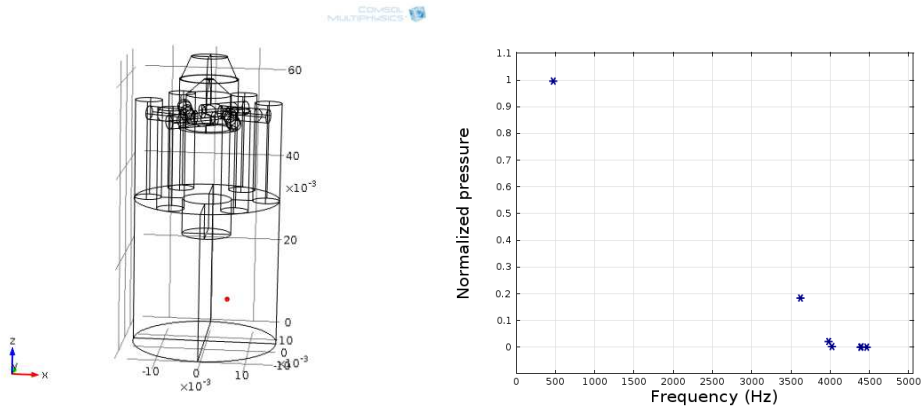

(a) (b)

Figure 3.4: (a) Position of the probe point inside the single injector geometry and (b) the normalized pressure for each of the seven eigenfrequencies. The maximum value corresponds to 472 Hz.

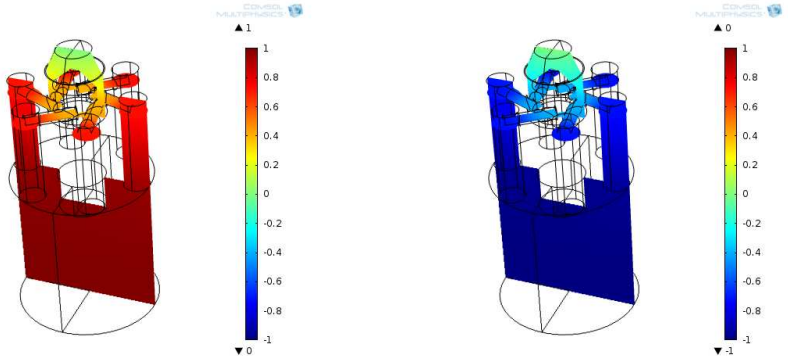

(a) (b)

Figure 3.5: Pressure field inside a single injector showing the response as Helmholtz resonator at the first eigenfrequency equal to 472 Hz: (a) at 0° and (b) 180° of a cycle.

found at 472 Hz. The other eigenmodes correspond to frequencies higher than 3.5 kHz, so outside of the frequency range of our investigation. Furthermore, the eigenmodes over 3.5 kHz are very weak compared to the first eigenmode at 472 Hz. The pressure field obtained for the eigenmode at 472 Hz is shown in Fig. 3.5. At each instant of the acoustic cycle, the acoustic pressure is uniform within the whole geometry, except near the exit of the air distributor upto the nozzle exit, where the pressure amplitude decreases to match the sound soft boundary condition. Taking as $t/T_{cycle} = 0(0°)$ the pressure field where the pressure amplitude is at its maximum, it is out-of-phase at all the points of the geometry with the pressure field at $t/T_{cycle} = 0.5(180°)$ where the pressure amplitude is at its minimum. This mode is thus identified as a Helmholtz resonator response.

The eigenfrequency of the Helmholtz resonator can be estimated by an analytical model of the injector. The single injector can thus be modeled as illustrated in Fig. 3.6, keeping the actual dimensions of the air plenum but considering an equivalent circular

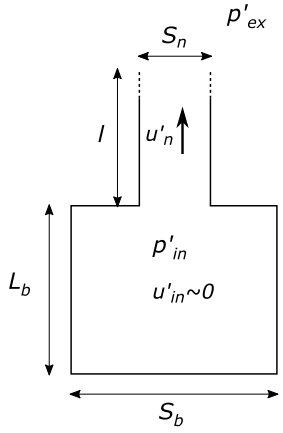

Figure 3.6: The single injector without a mean flow, represented as bottle shape, behaves as a Helmholtz resonator at $f_H = 420$ Hz.

neck of constant cross section (S_n) and diameter equal to D_{exit}, instead of the real geometry of the air distributor until the nozzle exit. The length of the neck (l) is the actual length of the injector from the air distributor until the nozzle exit. The natural resonance frequency of a Helmholtz resonator with this geometry is given by Eq. 3.3 (see appendix A.1), yielding $f_H \approx 420$ Hz. The discrepancy with the simulation can be corrected by considering an end correction to account for the contribution of the inertia of the acoustic flow just outside the nozzle exit cross section. Adding to the simulation model an end correction δ of about $0.65D_{exit}$ [105], the frequency obtained is 420 Hz.

$$f_H^2 = \frac{S_n c_0^2}{4\pi^2 S_b L_b l}. \tag{3.3}$$

The frequency response of the Helmholtz resonator is modified by the presence of a mean flow. When a mean flow is considered, a damping rate (ε) appears in the solution (see the appendix A.2). The modified resonance frequency is given by Eq. 3.4:

$$f_r = f_H \sqrt{1 - 2\varepsilon^2} \tag{3.4}$$

The condition to get an amplification of the pressure fluctuation in this case is $\varepsilon < 1/\sqrt{2}$ where the typical value of the damping rate in our experimental condition is given by:

$$\varepsilon = \frac{U_b}{2\omega_0 l} \approx 0.18 \tag{3.5}$$

for $\dot{m}_{air} = 1.72$ g/s, giving a bulk velocity based on the nozzle exit cross section $U_b = 28.6$ ms^{-1}. For this damping rate we find $f_r \approx 407$ Hz. Actually, the air-flow used in this calculation corresponds to that of the reactive injectors which has been kept virtually the same for all the experiments. In consequence, the resonance frequency is slightly modified relatively to the case without air-flow (f_H). For the non-reactive stabilization injectors, the air-flow rate is higher, the damping rate grows and the resonance frequency (f_r) decreases to around 362 Hz.

Experimental measurements of the acoustic response of the single injector were carried

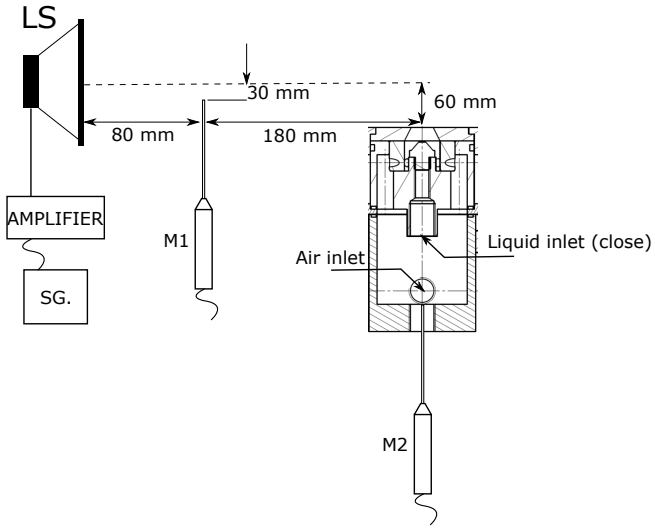

Figure 3.7: Sketch of the setup for measurements of the acoustic response of a single injector. LS: loudspeaker; SG: signal generator; M1 and M2: microphones.

out outside the combustion chamber, without confinement and without a mean flow. A sinusoidal perturbation is imposed to the nozzle exit (see Fig. 3.7). A loudspeaker, positioned 260 mm away from the injector vertical axis and with the acoustic axis 60 mm over the injector exit cross section, produces the sinusoidal perturbation with a frequency in the range 40-1100 Hz. Two pressure signals are simultaneously measured by means of two microphones. The first microphone is placed 80 mm away from the loudspeaker 30 mm below the acoustic axis. The second microphone is flush installed at the bottom of the air plenum. We define a transfer function between these two signals as follow:

$$\frac{P'_{M2}(t)}{P'_{M1}(t)} = G_{inj} e^{i\varphi_{inj}} \tag{3.6}$$

where G_{inj} is the gain and φ_{inj} the phase of the transfer function.

The Fig. 3.8 shows the response of each of the three single injectors used as reactive injectors. The gain of the transfer function (G) features a peak at 420 Hz. At this frequency, the phase plot shows a value of $\varphi_{inj} = \pi$ indicating that p'_{ex} and p'_{in} are out-of-phase. This behavior is recognized as a Helmholtz resonator. These measurements agree very well with the predictions of the simulation and the theoretical calculation.

3.3 Air-flow characteristics without acoustic forcing and without combustion

In this section, the main features of the swirling air flow obtained without acoustic forcing and without combustion are shown. Velocity profiles have been obtained by means of a LDA system, and used to calculate the swirl number S. In our case $S = 0.68$. A center recirculation zone (CRZ) has been detected, as expected for a swirl flow with $S > 0.6$, the value conventionally accepted as a threshold to get a CRZ in swirl injectors.

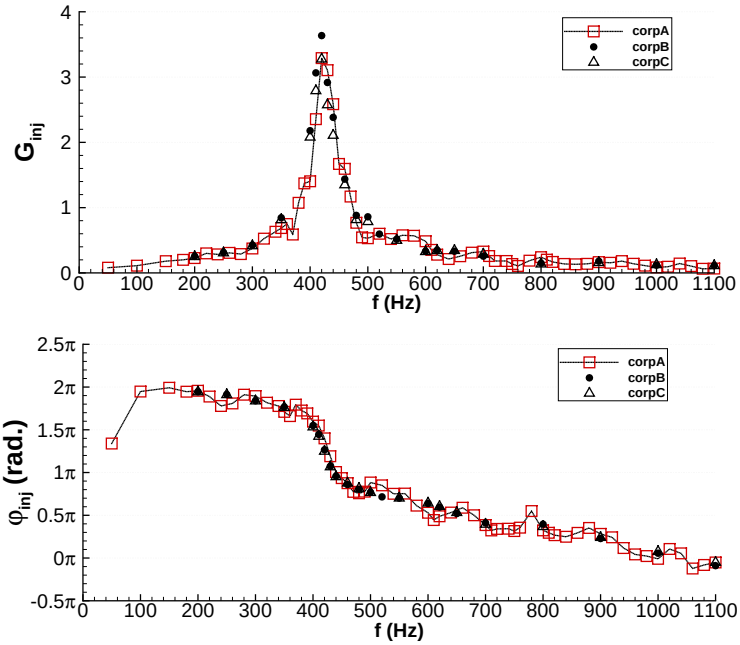

Figure 3.8: Gain and phase of the transfer function calculate from measurements made of each single injector. The peak in the Gain plot correspond to $f_H = 420$ Hz.

3.3.1 Velocity profiles measured by LDA

The mean and RMS velocity profiles (U_z, U_r, U_θ) measured at various z-positions, namely $z/D_{exit} = 0.375$, $z/D_{exit} = 0.75$ and $z/D_{exit} = 1.125$ are presented in Fig. 3.9. The mean data rate of $40,000$ droplets/s ensures the convergence of the measured mean quantities. The mean vertical velocity profile clearly presents a central recirculation zone (CRZ) at each downstream location. The azimuthal component has the same order of magnitude as the vertical component, indicating a strong swirl. The experimental swirl number S is evaluated from Eq. 3.7 at $z/D_{exit} = 0.375$ [35]. Here S equals 0.68, which is consistent with the CRZ detection. The reference radius in Eq. 3.7 is the radius of the nozzle exit $(D_{exit}/2)$.

$$S = \frac{\int_0^R U_z U_\theta r^2 dr}{R \int_0^R U_z^2 r dr} = \frac{\sum_0^R U_z(r) U_\theta(r) r^2}{R \sum_0^R U_z^2(r) r} \tag{3.7}$$

The radial expand of the CRZ estimated from the mean vertical velocity profiles goes from $r/D_{exit} \approx \pm 0.15$ and slightly increases with z until $r/D_{exit} \approx \pm 0.2$. At $z/D_{exit} = 0.375$, the maximum values of the mean vertical velocity are located at $r/D_{exit} = \pm 0.4$, and are equal to 35 m/s. This maximum decreases downstream and the location expands in the radial direction. The azimuthal mean velocity profile obtained at $z/D_{exit} = 0.375$ shows its maximum magnitudes at $r/D_{exit} = \pm 0.3$. This location almost does not change with z but the values decrease from 25 m/s to around 18 m/s. The maximum values of the radial velocity magnitude (≈ 5 m/s) are found at $r/D_{exit} = \pm 0.5$. Downstream, the location of these maximums moves outward and

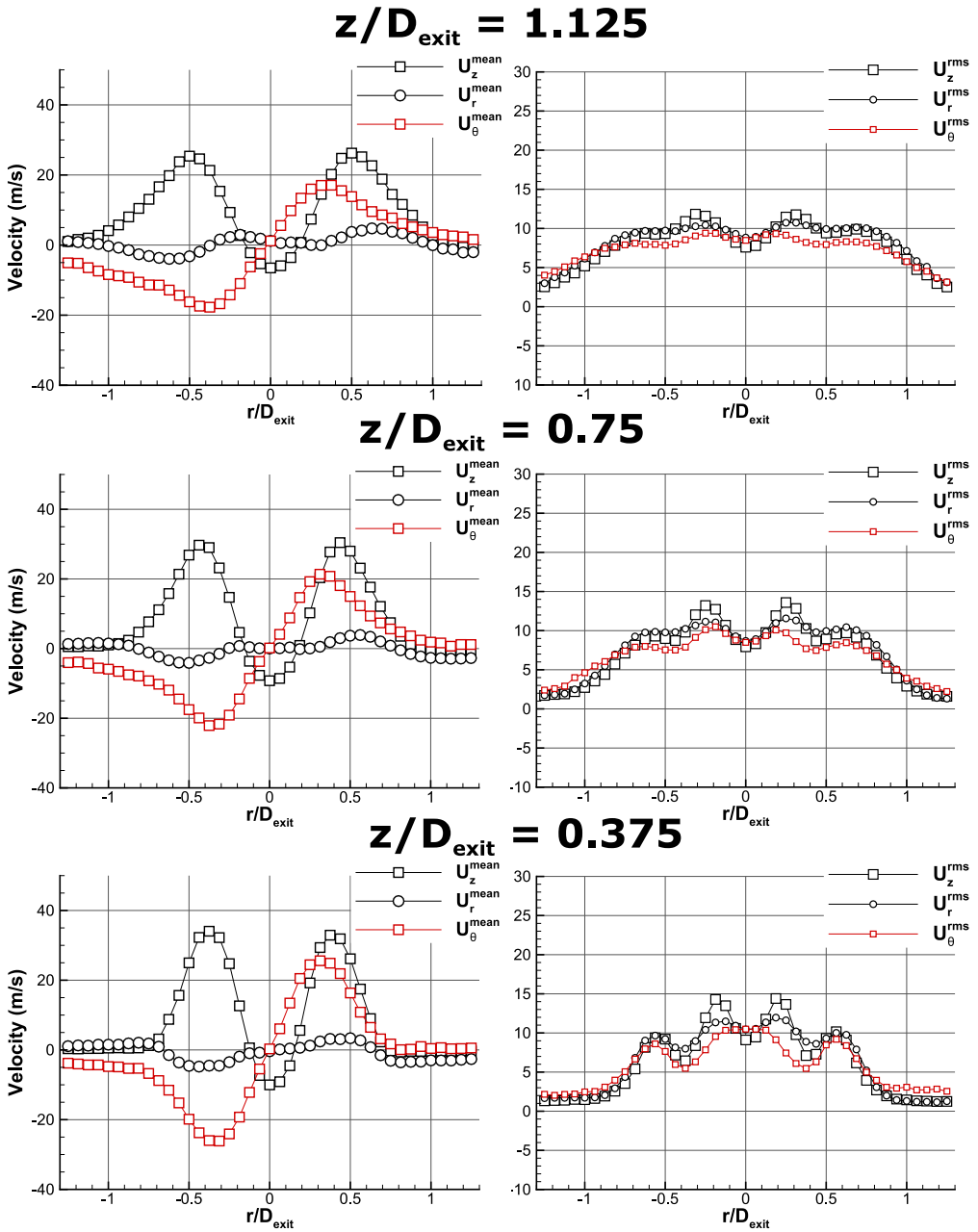

Figure 3.9: Mean and RMS velocity profiles of the seeded swirling air jet above the nozzle exit plane of the middle injector: U_z (vertical), U_r (radial), U_θ (azimuthal), for $\dot{m}_{air} = 1.72$ g/s ($U_b = 28.6$ ms^{-1}) and $S = 0.68$.

the values decrease.

The vertical, radial and azimuthal RMS velocity profiles are similar at each z position and their values decrease downstream. The maximum magnitudes for the vertical RMS profile at $z/D_{exit} = 0.375$ are found at $r/D_{exit} \approx \pm 0.2$. At $r/D_{exit} = 0$, the RMS value close to 10 m/s, is similar to the mean velocity magnitude of the CRZ meaning that at this position the velocity is not always negative and therefore the CRZ is not always established. As the CRZ is induced by the vortex-breakdown phenomenon, the

diminution of the CRZ could be linked to a disruption of the vortex breakdown or a change of its position. A second maximum of the RMS velocity magnitude appears at a radial position equal to $r/D_{exit} = \pm 0.5$ on the three velocity profiles. This is linked to the shedding of Kelvin-Helmholtz vortices formed at the orifice edge of the injector exit nozzle. The air flow structures are analyzed in more detail hereafter.

3.3.2 Air-flow structures without acoustic forcing

Averaged quantities could hide important details of what happens during a forcing cycle. If time averaged quantities were enough, performing expensive DNS simulation would not be necessary. As this is not the case, investigation of instantaneous quantities is necessary, in order to better understand the physics behind observed phenomenon, and to validate simulations.

Analyzing the high speed tomography images of the air flow without acoustics, it is possible to identify some coherent structures, both in the outer layer as in the inner layer as well. At the outer layer, Kelvin Helmholtz type vortices are shedding with a frequency, estimated from the vertical tomography views, between 2200 and 2500 Hz (see Fig. 3.10). Due to the flow swirl motion, these vortices form, in the 3dimensional space, a helical structure turning with the swirl flow. This is a known feature of swirling flows, reported in the literature (e.g. [6, 21]). At the center of the injector exit, we can also periodically observe, two elliptical dark patterns axisymmetrically formed and being convected (see the dashed ellipses on Fig. 3.10). These patterns appear to be in fact the cross-section of a double helix vortex breakdown structure which is precessing around the CRZ. This type of vortex breakdown has been found experimentally [13, 106] and by DNS simulation [18]. Crossing the information from vertical tomography views with horizontal ones, confirms the presence of a double helix. On the horizontal tomography views, recorded at $z = 3$ mm ($z/D_{exit} = 0.375$), we can identify two dark patterns turning (or precessing) in the swirl flow direction (Fig. 3.11). This is identified as the Precessing Vortex Core (PVC). The PVC frequency (f_{pvc}) can be roughly estimated counting the number of images, taken by the double pattern identified on horizontal views, to make a revolution around the injector axis. We have estimated a value for f_{pvc} between 2.25 and 2.5 kHz. This range of frequencies is representative of the characteristic frequencies of this region of the flow field found in gas-turbine swirl injectors (e.g. [32]). As the double helix turns, this explains the downstream convective-like motion of the dark pattern in the vertical views. Indeed, this pattern is not always clearly formed, indicating its quasi-steady nature. As the vortex breakdown is at the origin of the CRZ, this unsteady behavior could be analyzed studying the velocity signal in this region.

The CRZ is recognized for the negative velocities of the flow in this region as it is shown by mean velocities measured by LDA. Nevertheless, the velocity is not always negative as we can see on the velocity signal at $r/D_{exit} = 0$ in Fig. 3.12. Indeed, large positive velocities values appear irregularly with time. The frequency spectrum of this signal does not show any particular peak. From this signal, we have quantified a ratio of the number of positive values of the vertical velocity of about 13.9%

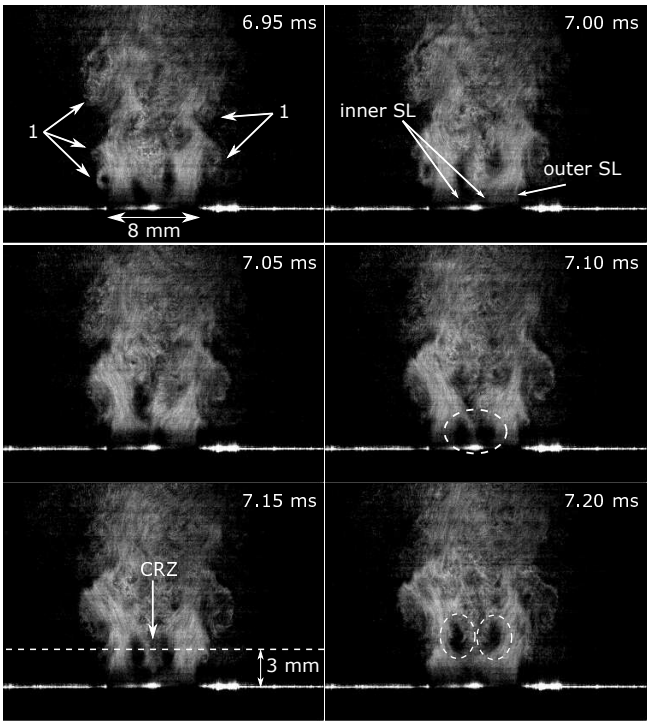

Figure 3.10: Vertical tomography views of the seeded air-flow recorded at 20 kfps, in cold condition without acoustic forcing. Kelvin-Helmholtz type vortices (1); central recirculation zone (CRZ); the dark pattern, corresponding to a cross-section of the double helix vortex breakdown, is enclosed in a dashed ellipse. Inner and outer shear layer (SL).

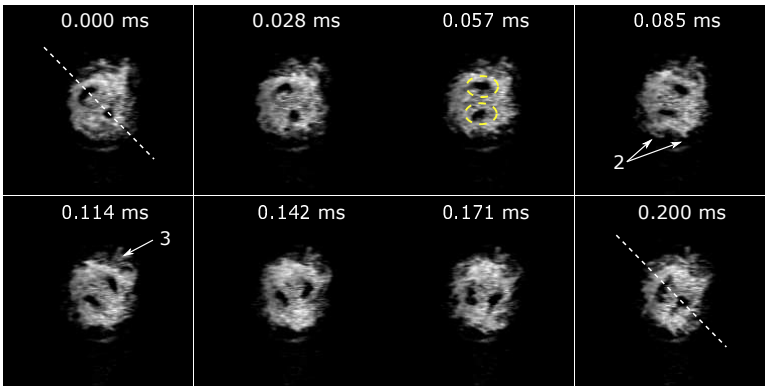

Figure 3.11: Horizontal tomography views of the seeded air-flow recorded with a high speed camera at 35 kfps, in cold condition without acoustic forcing, at the position $z = 3mm$ ($z/D_{exit} = 0.375$). Small streamwise vortices (2); small matter ejections (3); the dark pattern, corresponding to a cross-section of the double helix vortex breakdown, is enclosed in a dashed ellipse. In these views the dark pattern completes the half of a revolution.

respect to the total. These observations attest the natural unsteady character of the central recirculation zone and in consequence of the vortex breakdown occurrence. Two possible explanations for these observations can be mentioned. One is that the vortex-

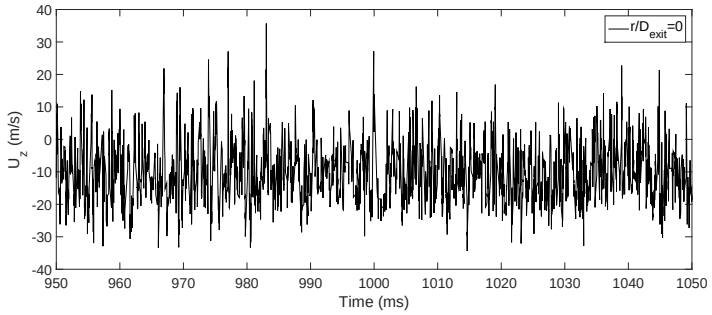

Figure 3.12: Velocity signal of the seeded air flow measured in the CRZ region ($z/D_{exit} = 0.375$, $r/D_{exit} = 0$), without acoustic forcing and without combustion.

breakdown-induced CRZ is not always well formed due to the high level of turbulence of the flow. The other explanation could be that the entire structure (CRZ), being always well formed, is radially displaced or tilted in a random way, also due to high level of turbulence. A third reason could be a combination of the two former behaviors.

On the basis of a well understanding of the swirl flow natural behavior analyzed here, we can then investigate, in our case, how acoustic forcing will modify the swirl flow field structure, in particular the vortex-breakdown-induced CRZ. It is known that acoustic forcing can change the structure of the flow field [16, 107].

This is a key element to well understand the swirling flame responses [39] in presence of acoustic perturbations. Finally, in order to conclude this section, we can say that the investigation of this case, without acoustic forcing and without combustion, can bring some useful information to validate numerical simulation models. The flow field will be investigated in chapter 6, with acoustic forcing, first without combustion and then in presence of the two-phase flow swirling flames.

3.4 Spray characterization without acoustic forcing and without combustion

In this section we present the results of the characterization of the spray, both with and without combustion but always without acoustic forcing. No seeding was introduced into the air line. First, some important operating features of the atomizers are presented.

3.4.1 Flow rate and discharge coefficient of the atomizer

The atomizers have been installed and tested[1], outside the cavity, without the swirling air flow, in order to verify if they all exhibit the same flow rate as a function of the injection pressure ΔP. The results shown in Fig. 3.13 exhibit a quasi linear dependency between the flow rate and the injection pressure, within our operating range. As ΔP tends to zero, also Q_m does, so is easy to draw a curve in $(\Delta P)^{1/2}$, which is what is expected (see Fig. 3.13). All the injectors have shown almost the same liquid flow rate for the same ΔP.

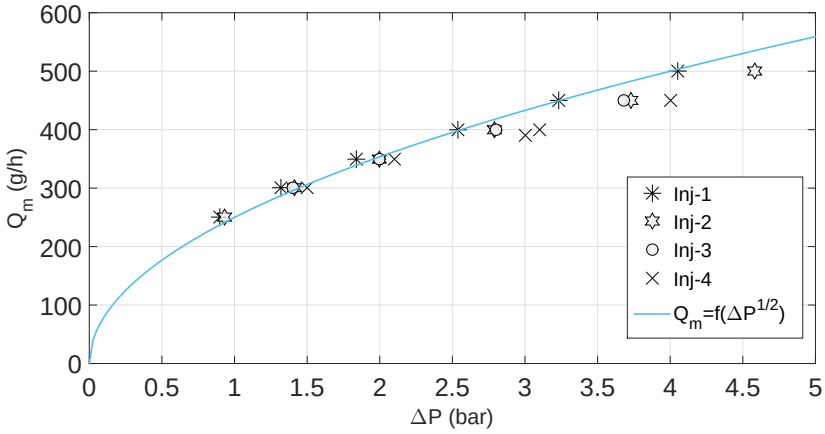

Figure 3.13: Operating points for all the injectors. Three are used for the injection system and the fourth is a backup. The solid line is the expected flow rate as a function of $(\Delta P)^{1/2}$.

The discharge coefficient C_d has been also calculated because it is a performance parameter of the atomizer. It is defined as the ratio between the actual flow rate Q_m and the theoretical one (3.8).

$$C_d = \frac{Q_m}{3.6 A_0 (\frac{2\Delta P}{\rho_{fuel}} + V_1^2)^{1/2}} \tag{3.8}$$

where the nozzle exit orifice area is A_0, ρ_{fuel} is the liquid fuel density and V_1 is the inlet velocity. The parameters A_0, ρ_{fuel}, V_1 and ΔP are in SI units. The resulting points are almost the same for all the injectors with an evolution of C_d with a mildly descending slope (Fig. 3.14).

[1]A total of four injectors have been tested. The fourth one is a backup injector

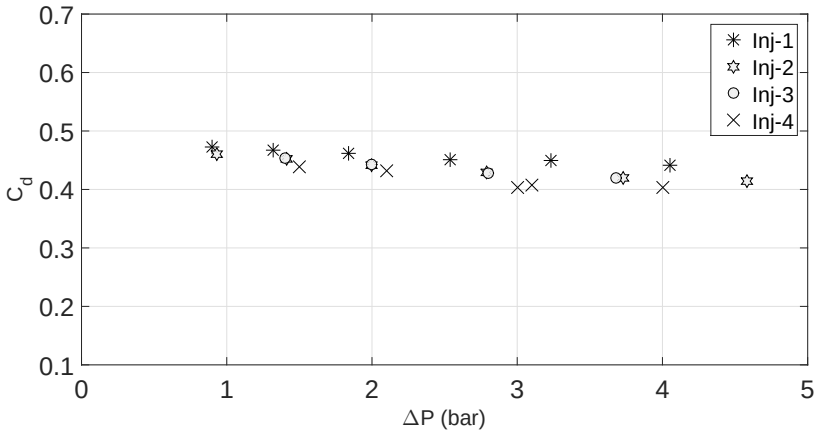

Figure 3.14: Discharge coefficients for each injector as a function of the injection pressure. Temperature of the n-heptane was constant at 293 K.

3.4.2 N-heptane droplet sizing without combustion

Droplet sizing at the nozzle exit was carried out by laser diffraction (Malvern system. See section 2.3.2.2). In addition, the spray was investigated by means of an imaging system based on backlight diffuse illumination (See section 2.3.2.1). These measurements have been carried out outside the cavity, in open field condition (without confinement). In all these tests the swirling coflow of air was present. The center of the laser beam of the diffraction technique and the center of the camera field of view are positioned at $z_s = 12.5$ mm. Both techniques give a volumic droplet size distribution from where the Sauter Mean Diameter (SMD), d_{32}, evolution is calculated as a function of the fuel flow rate ($\dot{m}_{fuel}$) with a fixed air flow rate ($\dot{m}_{air} = 1.510$ g/s), and as a function of the Weber number *We* for various ($\dot{m}_{fuel}$). The Weber number is defined as:

$$We = \rho_{air} U_b^2 D_{exit} / \sigma \tag{3.9}$$

where U_b is the bulk air velocity at the injector nozzle exit and σ is the surface tension of the n-heptane. Based on the chart of Lasheras and Hopfinger [108], the jet breakup process is at the limit between the membrane breakup (We< 300) and fiber type

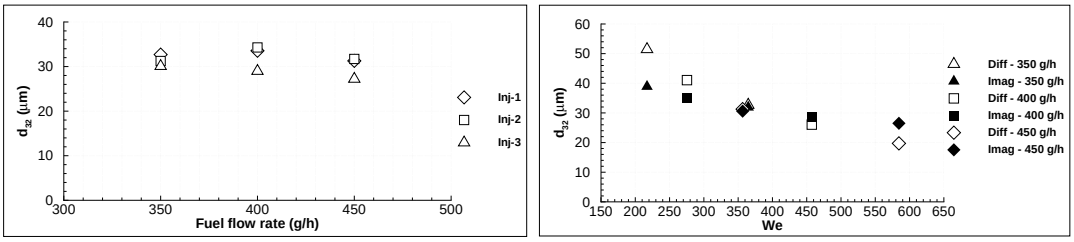

(a) (b)

Figure 3.15: (a) SMD vs. $\dot{m}_{fuel}$ measured by laser diffraction (Malvern system) for each injector for (*We*= 365); (b) SMD vs. *We*, obtained by laser diffraction and imaging for a given $\dot{m}_{fuel}$.

atomization (We> 300). The Reynolds number, defined by $Re = \rho_{air} U_b D_{exit}/\mu_{air}$ (with $\mu_{air} = 1.8 \cdot 10^{-}5$ kg(ms)$^{-1}$), falls within the range $[1 \cdot 10^4 - 2.2 \cdot 10^4]$. The Weber and Reynolds numbers are calculated with physical properties at $T_{ref} = 293$ K.

The SMD are reported in Fig. 3.15. Comparison of the results obtained by means of the two methods shows that the Sauter Mean Diameter (SMD) d_{32} is independent of the liquid flow rate $\dot{m}_{fuel}$ for a given $\dot{m}_{air}$ (Fig. 3.15(a)), and depends inversely on $\dot{m}_{air}$. SMD varies here from 50 to 20 μm for $\dot{m}_{air}$ ranging from 1.292 to 2.262 g/s. The SMD as a function of the Weber number is reported in Fig. 3.15(b). It is noted that the higher is *We* (as a consequence of a higher $\dot{m}_{air}$), the better is the injector atomization. For the higher $\dot{m}_{air}$ tested here it is found that d_{32} is between 19 and 30 μm. This is consistent with the characterization of the n-heptane d_{32} diameter made by Prieur *et al.* [94] in a single burner equipped with the same air swirler and atomizer, under cold flow conditions without confinement.

3.5 Flames ignition protocol in TACC-Spray

The chamber is equipped with a set of heating plates mounted on the external face of the front walls. They have a height of 200 mm and three different width: 50, 100 and 200 mm. They are used to preheat the cavity when starting the experiment, thus facilitating the ignition process and also avoiding the condensation of water on the walls and quartz windows. The number of heating plates depends on the cavity configuration. When spray flames are centered in the cavity, the plates are placed symmetrically to the middle of the cavity and set to 300°C. When spray flames are not centered, the heating plates are mounted on the opposite side, in order to homogenize the temperature in the cavity. In this case the heating plate temperature is set to 500°C. The ignition process begins with preheating the chamber at least during 60 minutes in order to stabilize the temperature of the wall and within the chamber. The flames ignition starts with a premixed methane/air flame used as pilot, confined by two auxiliary steel plates separated by a distance of 60 mm (see Fig. 3.16 (a)). The operating condition of this premixed flame is $\dot{m}_{air} = 1.29$ g/s (60 L/min) and $\dot{m}_{fuel} = 0.076$ g/s (7 L/min). The pilot flame can be stabilized on the central injector or on one of the side injectors, thus the ignition can start from the central injector to the sides, or from a side injector to the other side as is illustrated in the Fig. 3.16.

3.5.1 Steps to ignite one to three spray flames

Once the methane/air flame is stabilized (Fig. 3.16 (a)), the injection of n-heptane starts with a mass flow rate of about 0.1 g/s. Immediately after n-heptane flame is ignited, the methane injection is cut off and the air mass flow rate is progressively increased to approximately 1.5 g/s (Fig. 3.16 (b)). The auxiliary plate is then moved away such that the space between the two auxiliary plates covers also the next injector. The second reactive flow is auto-ignited when flow rates are set (with the same values as for the first one) leading to the second spray flame (Fig. 3.16 (c)). The auxiliary

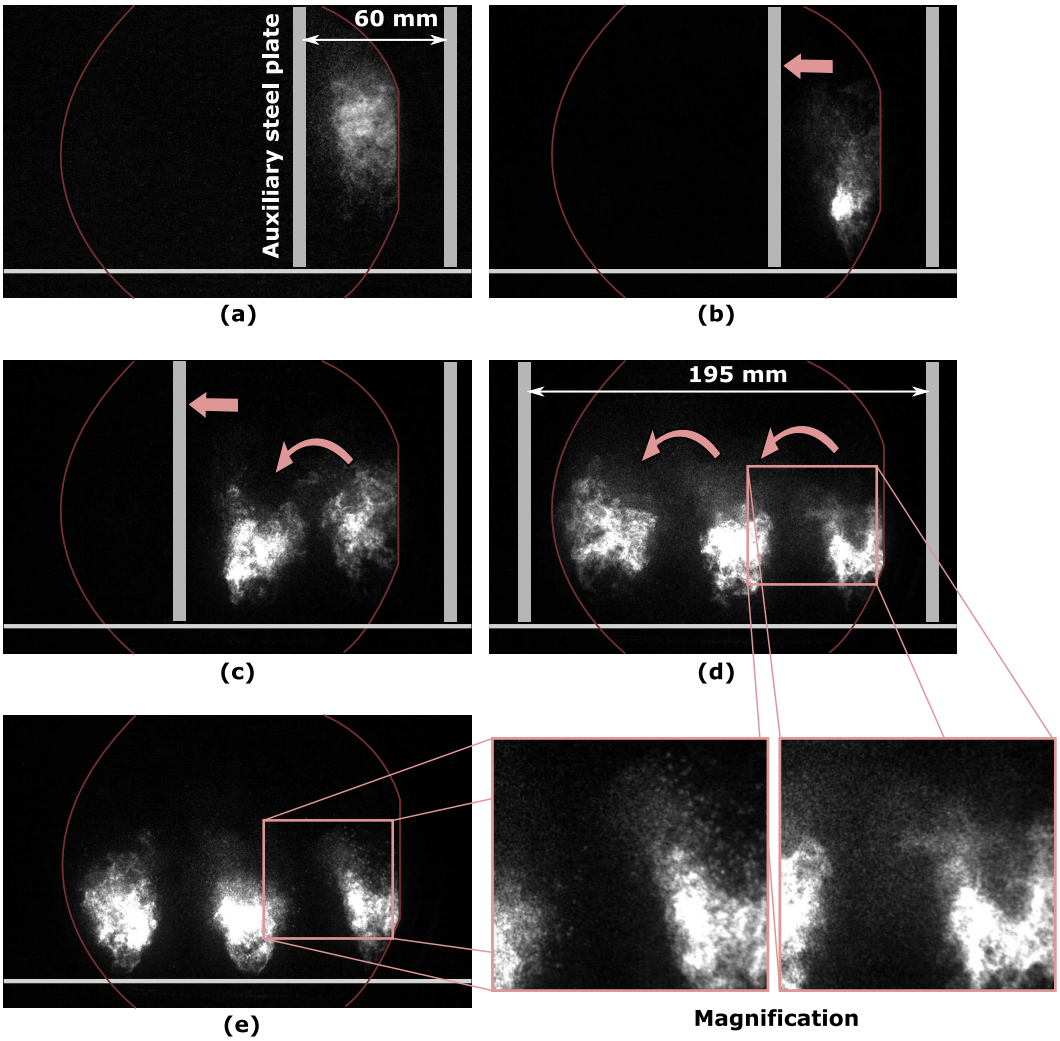

Figure 3.16: Instantaneous images of the flames fronts (CH*) during the ignition procedure, from (a) a methane/air premixed flame until (e) the three n-heptane/air flames without strong confinement. Injector system centered within the cavity (L_c = 800 mm).

plate is moved again in order to get a distance that covers the three injectors between the two auxiliary plates. The same flow rates are also set for the third injection and the third spray flame is then auto-ignited by the neighboring flame. The three spray flames are stabilized thanks to the strong confinement imposed by the auxiliary plates now separated by a distant of about 200 mm (Fig. 3.16 (d)). The next step is to set the desired nominal operating conditions on the three flames. For the example of the Fig. 3.16, the nominal operating condition for the three spray flames is $\dot{m}_{air}$ = 1.724 g/s and $\dot{m}_{fuel}$ = 0.097 g/s. Once the nominal operating condition is reached, the auxiliary plates are moved away from each other in order to introduce the additional swirling air jets. Finally, the auxiliary plates are removed from inside the cavity and then the convergent element is installed. It was noted that during this ignition process the flame fronts changed from a more smooth aspect when they are strongly confined by the auxiliary plates to a more granular aspect when the strong confinement is removed.

This seems to be due to an effect of the temperature field of the flame regions that impacts the evaporation process of the n-heptane droplets, since the temperatures are higher with the strong confinement.

3.5.2 Thermal behavior of the cavity during ignition

3.5.2.1 Temperature measurements and convergent element influence

The following illustrations are for nominal operating conditions of the side spray flames equal to $\dot{m}_{air} = 1.724$ g/s and $\dot{m}_{fuel} = 0.11$ g/s, and for the center spray flame equal to $\dot{m}_{air} = 1.724$ g/s and $\dot{m}_{fuel} = 0.108$ g/s. The spray flames are centered in the cavity which is set to $L_c = 800$ mm. Temperature measurements carried out during the ignition process are presented in Fig. 3.17. The temperature within the cavity close to the side wall ($x/L_c = -0.48$) is almost not sensitive to the presence of the flames (see Fig. 3.17). This is in particular due to the aspiration of cool air from outside of the cavity as we have seen in section 2.1. The hot gases are extracted from the acoustically isolated room by a large chimney placed over the cavity at a distance of 870 mm. This chimney is equipped with a cooling system designed to reduced the temperature of hot gases below 373 K (controlled by a thermocouple) and placed just before the exhaust system. The cooling system consists in a frame made of copper tubes with several perforations that inject fresh air within the hot gases that go within the frame. The temperature measured by the thermocouple flush mounted in the cavity wall at $(x; z)$=$(0; 5)$ mm, registers the temperature increase corresponding to the ignition of each flame (see Fig. 3.17). The temperature increases and stabilizes until the auxiliary plates were moved away again in order to introduce the aerodynamic stabilization flows. During this step the temperature at $x/L_c = 0$ decreases because the strong wall confinement was removed and fresh air enters the flame region.

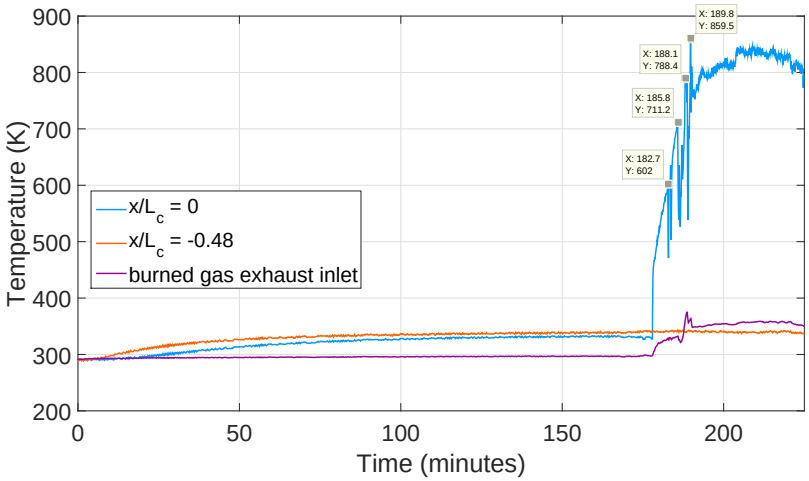

Figure 3.17: Temperature measurements during the ignition procedure and the flame stabilization without convergent element. Measurements inside the cavity are with thermocouples flush mounted in the front wall at $z = 5$ mm.

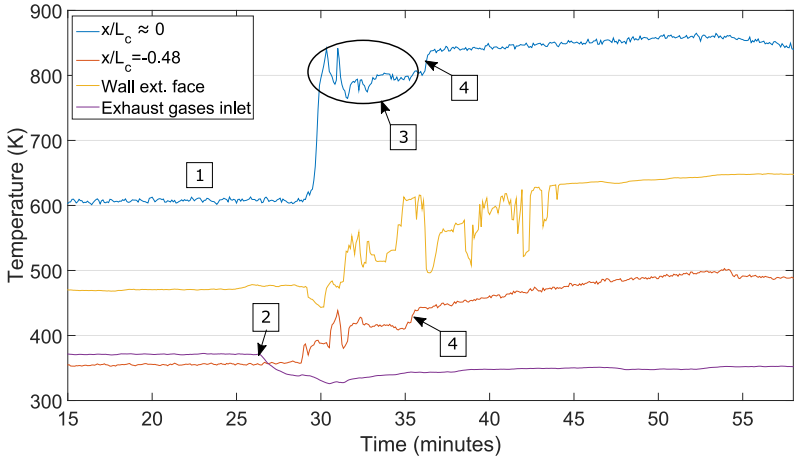

Figure 3.18: Temperature measured during an ignition sequence starting from stabilized methane/air premixed flame condition (1). The cooling system of burned gases is turned on at (2). The three n-heptane/air flames are stabilized at (3) and the convergent element is mounted at the top of the cavity at (4). The temperature of the front wall external face is measured at $(x; z)$=$(32; 40)$ mm. Measurements inside the cavity are done with thermocouples flush mounted in the front wall at $z = 5$ mm.

After removing the auxiliary plates from the cavity, the convergent element is mounted at the top of the cavity. The effect of the convergent element on the temperature within the cavity is shown in Fig. 3.18. In this plot is added the temperature measured on a wall external face of the cavity, performed by a thermocouple positioned at $(x; z)$=$(32; 40)$ mm. The plot starts when the methane flame is already stabilized (label(1)). By the label (2) the effect of the cooling system on the hot gases is indicated. The temperature of hot gases decreases and then, coinciding with the ignition of the spray flames, it increases again until a constant value lower than 373 K. The time interval corresponding to the spray flames ignition is labeled as (3) on measurements at $x/L_c = 0$. During this interval, the temperature at $x/L_c = -0.48$ and $x/L_c = 0$ stabilizes close to 400 K and 800 K respectively; the temperature at the wall external surface reaches temperatures between 500 K and 600 K. The label (4) in Fig. 3.18 indicates the moment just after the convergent element is mounted. Its effect is first registered by the temperature measurements at $x/L_c = -0.48$ because the aspiration of cool air from the outside is immediately ceased. The temperature at $x/L_c = 0$ also increases and stabilizes at $\approx$ 850 K. Finally, the wall external surface temperature stabilizes at $\approx$ 650 K, approximately 10 minutes after the installation of the convergent element. These measurements show that the temperature field within the entire cavity is augmented and also allow to determine the duration time after which the system reaches a thermal equilibrium.

3.5.2.2 Radial profile of temperature at the injector exit

The following measurements correspond to a nominal operating condition for the three spray flames equal to $\dot{m}_{air} = 1.724$ g/s and $\dot{m}_{fuel} = 0.097$ g/s. Once the thermal

equilibrium is reached, a thermocouple is installed through the front wall at the x-position of the central flame ($x = 0$) and at $z = 5$ mm ($z/D_{exit} = 0.625$). The thermocouple is moved in the y-direction coinciding with a radial direction of the central injector. Thus, several points are probed from close to the wall until near of the injector axis. Each obtained temperature value has been registered when the measurement reaches the equilibrium with a precision of about $\pm 5°$C. The radial profile of temperature obtained is shown in Fig. 3.19. As expected, the temperature towards the flame is higher than the temperature close to the wall of about two times. But the temperature suddenly decreases when the termocouple get into the spray flow, showing that the spray injection at the vicinity of the injector exit is not immediately at the temperature imposed by the flames and hot gases. This profile of temperature is linked with the position of the flame foot which fluctuates since the combustion is turbulent. But on average the flame foot, in conditions without acoustic forcing, is positioned at a higher z-position than $z = 5$ mm, the position of these measurements.

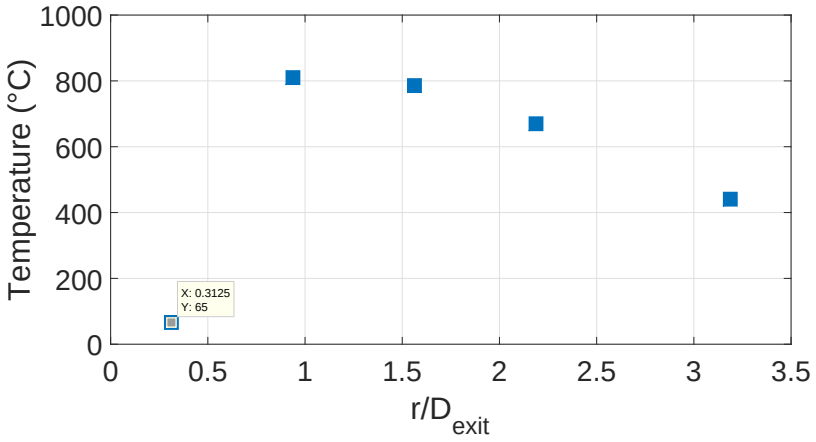

Figure 3.19: Temperature radial profile within the cavity in the y-direction coinciding with a radial direction of the central injector, at $(x; z)$=$(0; 5)$ mm, obtained with combustion.

3.6 Aerodynamic characterization of the two-phase flow during combustion

3.6.1 N-heptane droplets sizing and velocity measurements

A Phase Doppler Analyzer (PDA) was used to quantify n-heptane droplet diameters in a zone localized above the middle injector in the presence of the three flames. Several operating conditions were examined near to stoichiometric and lean-fuel equivalence ratios ϕ. Results are presented here for $\dot{m}_{air} = 1.72$ g/s, $\phi_{LB} = 0.95$ and $\phi_{LA} = \phi_{LC} = 0.97$. Fig. 3.20 shows the profiles of the n-heptane droplet diameters d_{10}, the arithmetic mean diameter, and d_{32} the Sauter Mean Diameter (SMD). Measurements were carried out at various downstream heights, $z = 3$ mm ($z/D_{exit} = 0.375$), 7.5 mm ($z/D_{exit} = 0.937$), 10 mm ($z/D_{exit} = 1.25$), 15 mm ($z/D_{exit} = 1.875$), 20 mm ($z/D_{exit} = 2.5$). The radial location of measurement points were ranging from $r/D_{exit} = -1.25$ to $+1.25$ by step of 0.0625.

The spatial distributions for diameters d_{10} and d_{32} are quite different.At $z/D_{exit} = 0.375$, the layer limited by $0.3 \leq r/D_{exit} \leq 0.7$ corresponds to the region of droplets data rate maximums. Within this layer, the diameter d_{10} is between 5 and 10 μm while d_{32} is around 20 μm. Droplets data rate measurements downstream show that this layer moves outward as z increases (Fig. 3.21(a)). The droplets data rate was at least $6,800$ droplets/s in this region. In the central region of the spray, occupied by the CRZ, data rate rapidly drops down to ≈ 600 droplets/s for measurements at $z = 3$ mm, and even lower at higher z-positions. For the z-positions considered and within the layer of droplets data rate maximums, both d_{10} and d_{32} diameter values remain in the ranges of size mentioned previously.

To evaluate the ability of n-heptane droplets to follow the air flow motion, a local Stokes number (S_t) based upon the droplet mean diameter d_{10} was estimated from Eq.3.10:

$$S_t = \frac{\rho_{fuel} d_{10}^2 U_b}{18 \mu_{air} D_{exit}} \tag{3.10}$$

This S_t is calculated assuming that the fuel density does not change at the injector exit in the presence of combustion. The air dynamic viscosity was taken at 750 K ($\mu_{air} = 3.5 \cdot 10^{-}5$ kg(ms)$^{-1}$). The variation of S_t along r-direction for $z/D_{exit} = 0.375$ is plotted in Fig. 3.21(b). It shows that droplets of $d \leq d_{10}$ should closely follow the gaseous phase.

The velocity profiles (U_z, U_r, U_θ) obtained at the injector exit ($z/D_{exit} = 0.375$) based on the n-heptane droplets (Fig. 3.22) have virtually the same aspect than the air-flow velocity profiles based on the seeded air. The radial locations of maximum magnitude values are the same than for the seeded air-flow. The maximum magnitude values of the vertical and azimuthal mean velocities are the same while the maximum magnitudes of the radial mean velocity is higher than the respective air-flow velocity (see Fig. 3.9). This difference might be ascribed to the ballistic trajectory of droplets of large diameter, that do not follow the air-flow. Even though they are less in number they

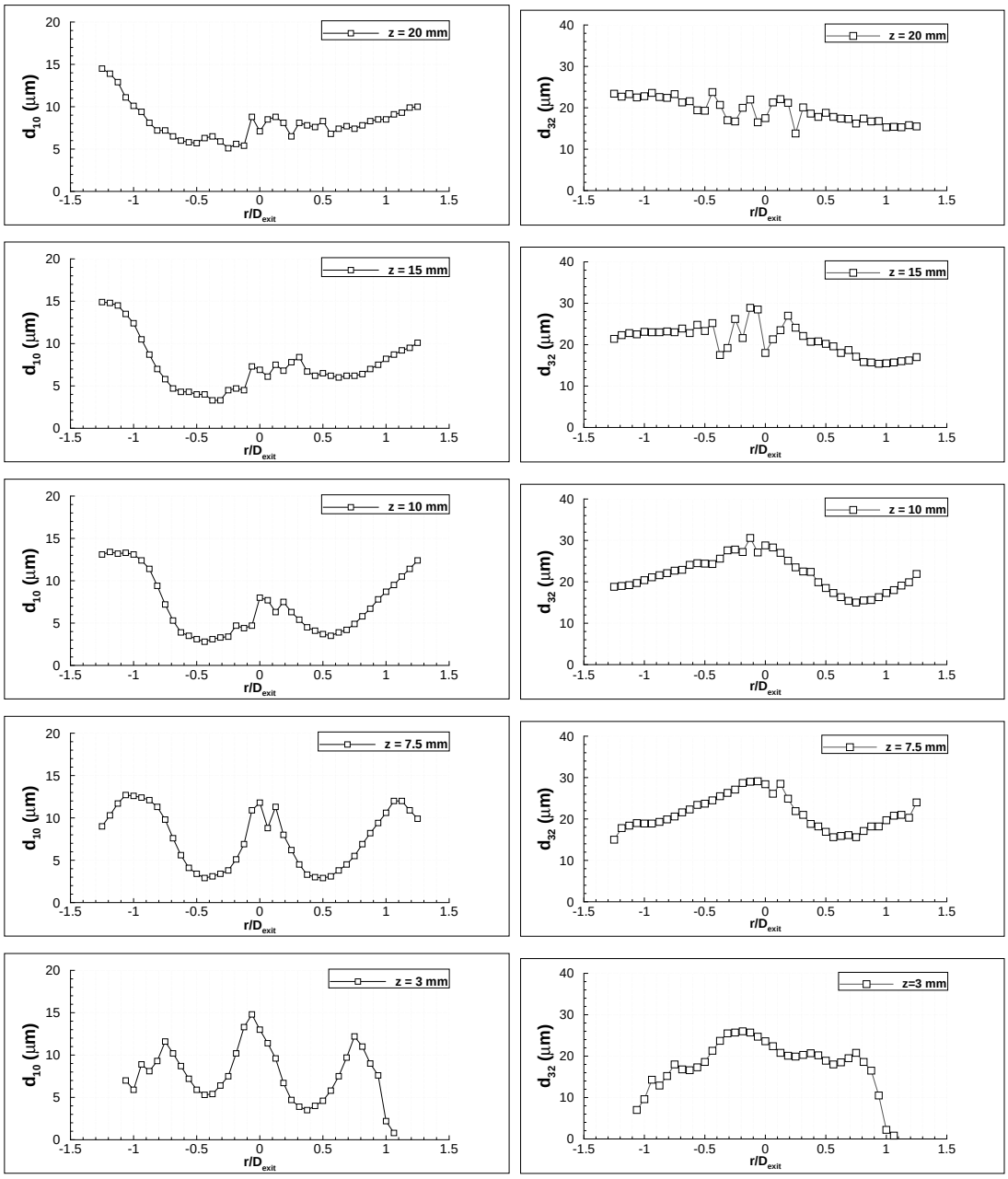

(a) (b)

Figure 3.20: N-heptane droplet diameter profiles inside the cavity with combustion: (a) arithmetic mean diameter d_{10} and (b) Sauter mean diameter d_{32} for $z = 3$ mm ($z/D_{exit} = 0.375$) to 20 mm ($z/D_{exit} = 2.5$).

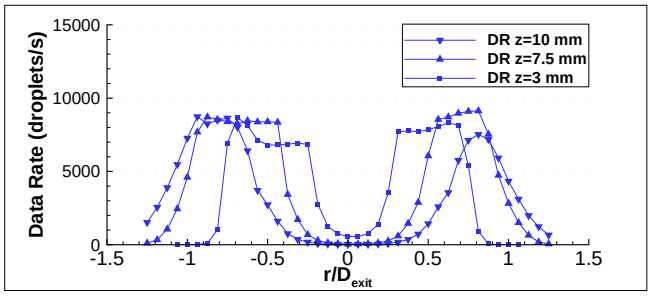

(a)

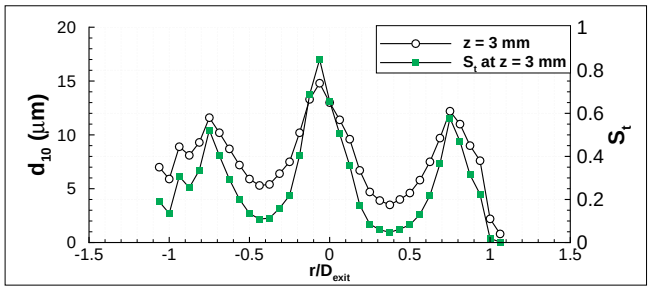

(b)

Figure 3.21: (a) Data rate (droplets/s) for $z = 3$ mm, $z = 7.5$ mm and $z = 10$ mm. (b) Plot of the local Stokes number based on d_{10} n-heptane droplets diameter at $z = 3$ mm.

influence the mean value of the velocity. The number of droplets per second measured as a function of their size will be addressed in the section 3.6.2.

Another difference is found in the center recirculation zone where the mean vertical velocity value is not negative but equal to ≈ 8 m/s, seems not to be reversed. The RMS value at this position ($r/D_{exit} = 0$) is around 10 m/s indicating that there may be negative velocity values. Once again the largest droplets affect the mean velocity value. In order to highlight this, we compare the vertical mean velocity profiles considering all the droplet sizes to the vertical mean velocity profile obtained only from droplets of size in the range of 1 to 5 μm.

We first verified that LDA and PDA measurements can be compared. The mean vertical velocity profiles of n-heptane droplets obtained by LDA and PDA are plotted in Fig. 3.23(a), for the same operating conditions. As the profiles are correctly overlapped, it is concluded that comparing the results from both techniques makes sense. In the Fig. 3.23(b) is displayed the vertical mean velocity profile of the n-heptane droplets, obtained by PDA without discriminating the size, compared to the mean velocity profile of droplets of size in the range of 1 to 5 μm. The smallest n-heptane droplets have on average a negative velocity value. Comparing this profile with that of the seeded air-flow (without combustion, see Fig. 3.23(c)) we see clearly that the maximum velocity values are the same and are located at the same radial location ($r/D_{exit} \pm 0.4$). However, the seeded air profile is always under the n-heptane droplets profile. As for this range of size, both n-heptane and DEHS droplets, correctly follow the air-flow, the difference can be attributed to the presence of combustion. With combustion, as the temperature is higher than in cool condition, the air-flow expands faster downstream.

We finish this section showing the velocity field constructed using the PDA measurements at the z positions mentioned before (z/D_{exit} = 0.375, 0.937, 1.25, 1.875, and

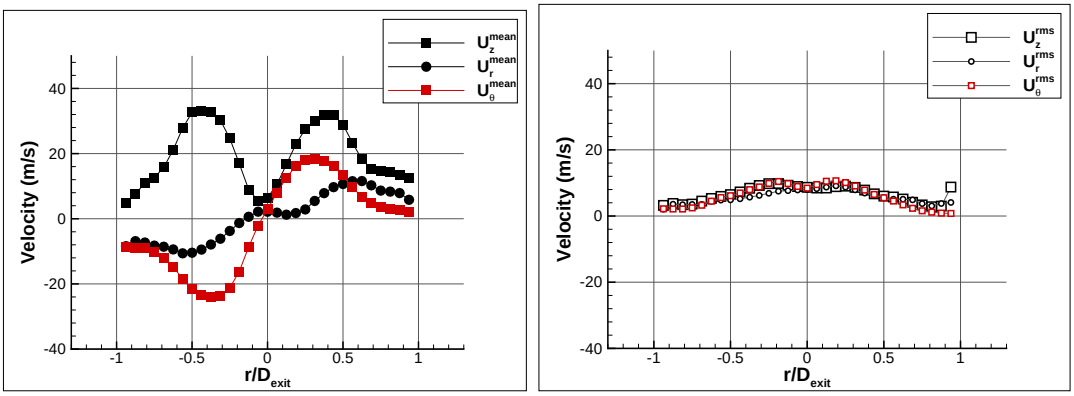

(a) (b)

Figure 3.22: Mean and RMS velocity profiles of n-heptane droplets at $z/D_{exit} = 0.375$ above the nozzle exit plane of the middle injector: U_z (vertical), U_r (radial), U_θ (azimuthal), for $\dot{m}_{air} = 1.72$ g/s ($U_b = 28.6$ ms^{-1}) and $\dot{m}_{fuel} = 0.108$ g/s.

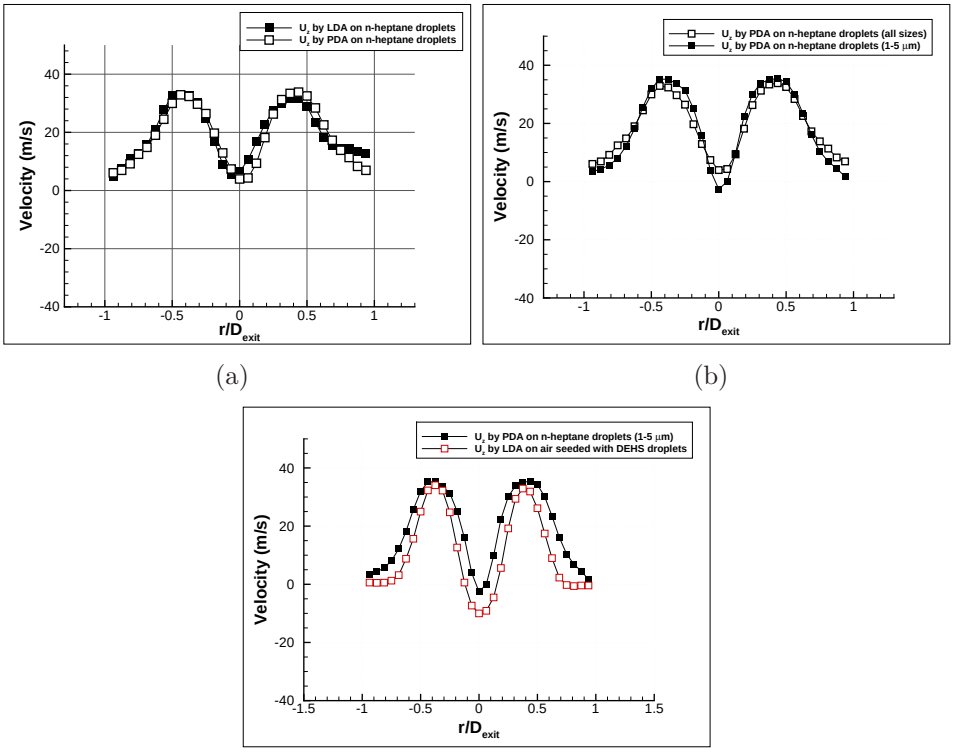

(a) (b)

(c)

Figure 3.23: U_z mean velocity profiles of n-heptane droplets: (a) comparison of the measurement technique (LDA/PDA) and (b) comparison depending on the droplets size, both for $\dot{m}_{fuel} = 0.108$ g/s and $\dot{m}_{air} = 1.72$ g/s; (c) comparison between the profile obtained by seeding the air flow (w/o combustion) and by PDA considering only the droplets of size in the range 1-5 μm.

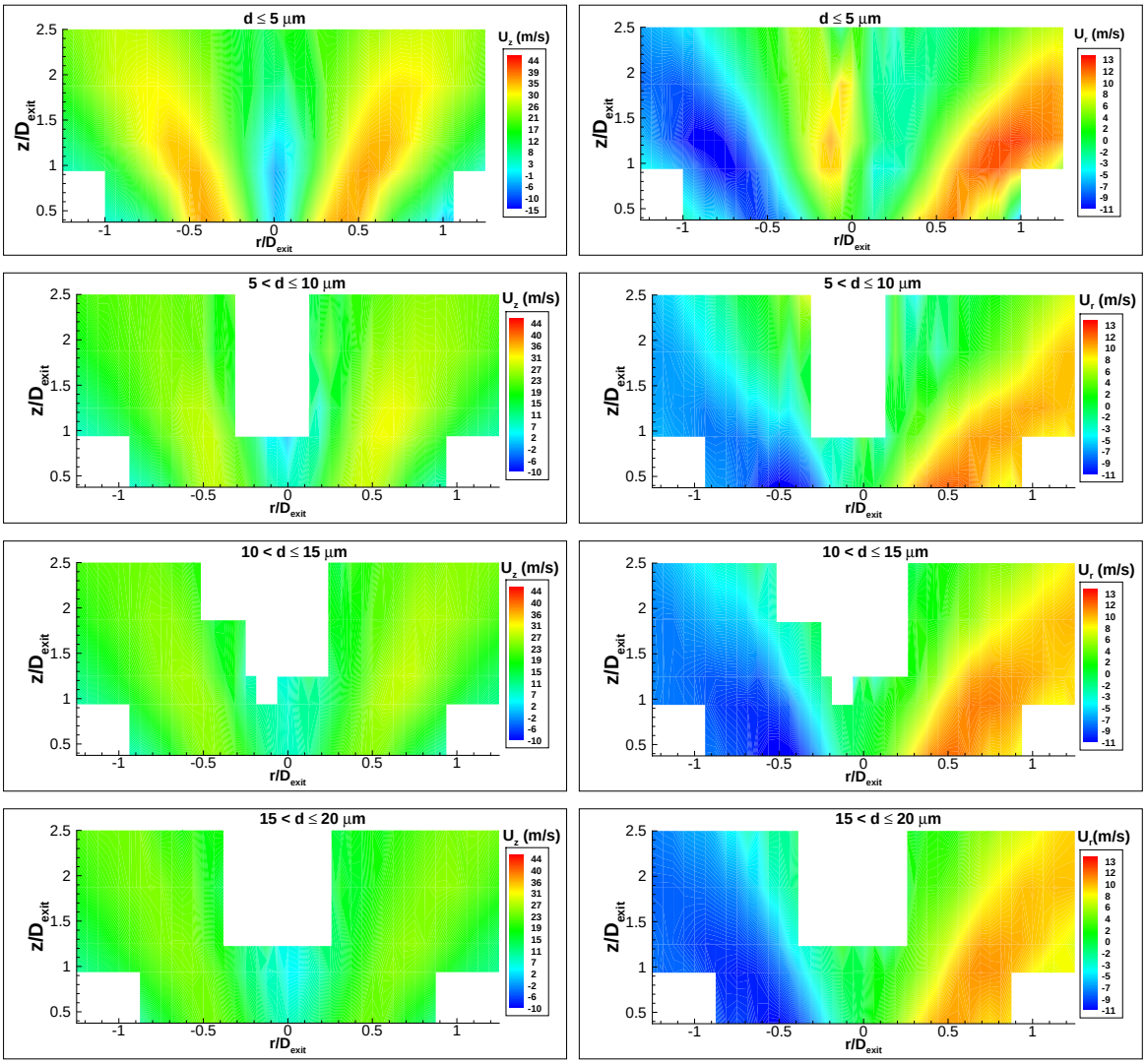

(a) (b)

Figure 3.24: N-heptane droplets U_z and U_r velocity contours obtained by PDA and sorted by droplet size groups.

2.5), with the radial step equal to $r/D_{exit} = 0.0625$ (Fig. 3.24). In these plots, the field is blank in regions with no drop counting. It is observed that the droplets with a lower size reach the higher vertical mean velocity values, while the radial mean velocities remain almost similar regardless the size of the droplets. The reversion of the flow for the smallest droplets is fairly well noted from this plots. The U_θ velocities were not measured in this case.

3.6.2 Spatial and temporal evolution of the spray

Tomographic horizontal visualizations of the flow downstream reveal that whatever the distance from the nozzle (z) the fuel spray pattern in a cross section of the flow is a donut-like pattern as usual for hollow cone sprays. For instance, this pattern is clearly seen in the averaged image, obtained from horizontal tomography views at $z/D_{exit} = 0.375$ ($z = 3$ mm), shown in Fig. 3.25(a). The size of the donut-like shape increases downstream due to the spray cone angle which is of around $48° \pm 4°$. The averaged image, obtained from vertical tomography views, shown in Fig. 3.25(b) reveals that the hollow cone is formed from the nozzle exit. Some droplets are visible within the hollow region until $z/D_{exit} \approx 0.75$ ($z = 6$ mm) but beyond this position almost no droplet is present. The droplets sizing by PDA measurement presented in the previous subsection, allow classifying the fuel droplets in four size groups of 5 μm of width, beginning from diameters (d) lower than 5 μm, until $d = 20$ μm, and one group of droplets diameters larger than 20 μm. Measurements are presented in the form of droplets data rate fields (see Fig. 3.26). The color-bar is set to the range of values for each size group in each plot. It is noted, for the size groups defined here, that the number of droplets in the spray decreases as the droplet diameter considered is larger. The maximum number of droplets per second decreases from ≈ 8000 droplets/s for $d \leq 5$ μm, to ≈ 2000, ≈ 1800 and ≈ 1500 droplets/s for diameters in the range $5 < d \leq 10$ μm, $10 < d \leq 15$ μm and $15 < d \leq 20$ μm respectively. From the Fig. 3.26 we note that the radial position of droplets depends on its size. The injection of the smallest droplets is positioned towards the center whereas the injection of the larger is positioned towards the outside, due to the ballistic trajectory of the latter. This is an important spatial property of the spray within the swirling air flow. Another property of the spray, besides the hollow cone formation, is the injection axisymmetry. Considering only the population of the smallest droplets (up to 10 μm), the corresponding data rate plots from Fig. 3.26 show that the droplets are symmetrically injected at the left and right side of the injector axis. However, the distribution of the largest droplets could be non-axisymmetric as reveals the different data rate field found at the left and right side of the injector axis, in the corresponding plots of Fig. 3.26. This can be attributed to the atomizer performance which leads to some asymmetries in the formation of a

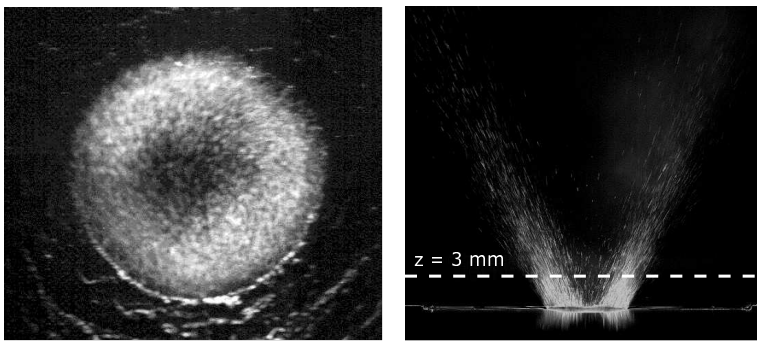

(a) (b)

Figure 3.25: Averaged images of the spray with combustion obtained by using high speed tomography views: (a) vertical view; (c) horizontal view at $z/D_{exit} = 0.375$.

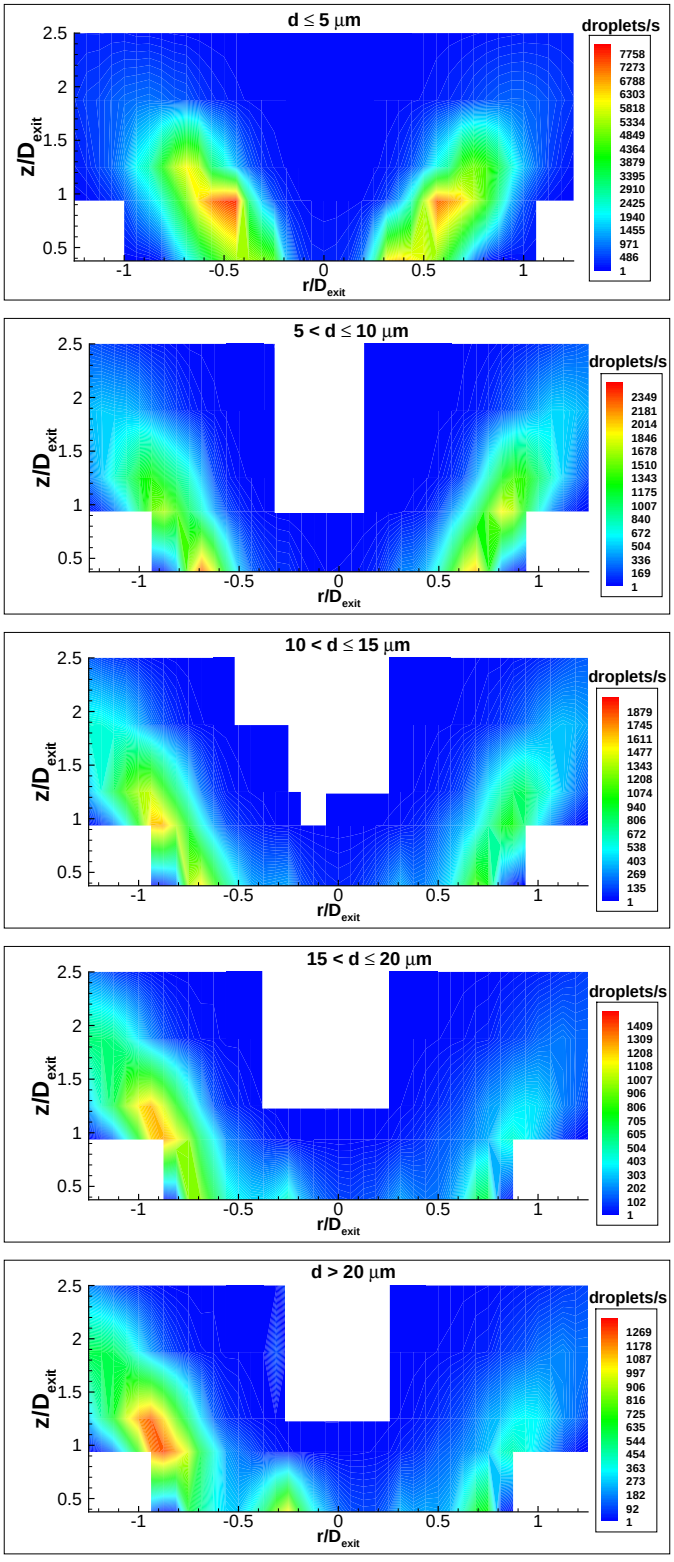

Figure 3.26: N-heptane data rate (droplets/s) contour from measurements by PDA and sorted by droplet size groups.

liquid sheet at the nozzle exit orifice that yields to a primary atomization problem. An illustration is given in the image of the Fig. 3.27. Thanks to the information given

Figure 3.27: Atomization asymmetries seen by imaging, based on backlight diffuse illumination, at the injector nozzle exit.

by the PDA measurements about the spatial distribution of the droplets relatively to their size (see Fig. 3.26), the population of droplets visualized by the laser tomography technique can be determined. An averaged image of the spray, obtained from vertical tomography views, overlaps with the PDA data rate contour of two groups as can be seen in the Fig. 3.28. Fig. 3.28(a) shows that while droplets with diameters $d \leq 5$ μm almost do not exist anymore (the data rate is lower than 10% of its maximum) beyond $z/D_{exit} = 2$ ($z = 16$ mm), in the averaged view droplets are well visible. Moreover, positions between PDA data rate contour and the averaged image does not match well. However, Fig. 3.28(b) shows the PDA data rate contour of droplets with diameters larger than 20 μm, matches quite well with the positions of the droplets in the averaged image. The data rate is still high ($\approx$ 40% of its maximum) at the limit positions of

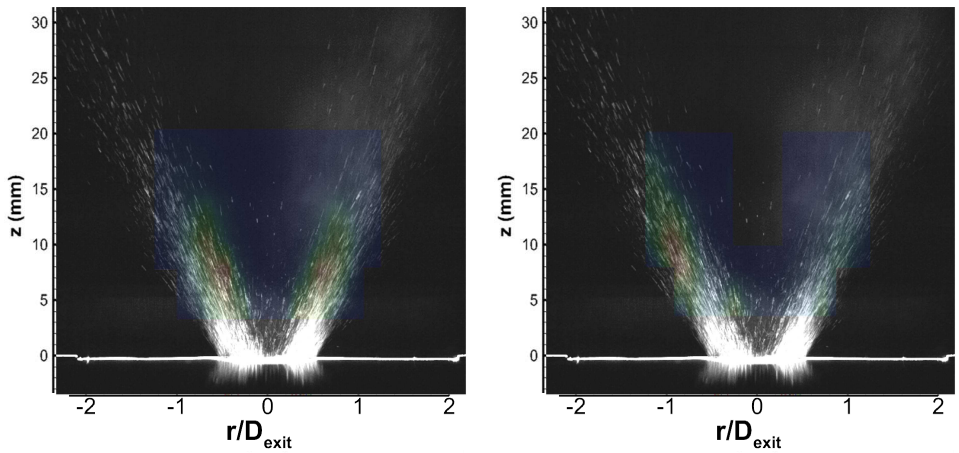

(a) (b)

Figure 3.28: PDA data rate contour of droplets with (a) diameters $d \leq 5$ μm and (b) higher than 20 μm, superposed to an averaged image of the spray obtained by using high speed tomography views. Both PDA data rate and averaged image are with combustion.

the contour plot indicating that droplets larger than 20 μm will be visible in the spray averaged image at this position and even beyond. This means that the tomography views are mainly representative of large droplets as the intensity of the light scattered by a droplet is proportional to the square of its diameter.

3.6.2.1 Results of the application of evaporation models to our case

One could wonder if it is normal to still visualize fuel droplets far away from the nozzle exit considering the presence of the flame. In order to bring a response to this question, three basic single droplet evaporation models[2] (see section 1.1.3.2) were applied to our experimental conditions (injection temperature $T_s \simeq 298$ K and environment within the combustion chamber at a temperature $T_\infty = 713$ K) to obtain an estimation of the droplet lifetime as a function of the initial diameter of the n-heptane droplet (Fig. 3.29(a)). In our case the n-heptane boil temperature is $T_{boil} = 371$ K. The first model applied, based on the mass transfer, predicts lifetime values several times higher than the two others. The two others, based on the heat transfer and on the droplet combustion respectively, predict lifetime values close to each other.

The evaporation distances predicted by the models have been calculated, using the droplet lifetime and the mean vertical velocity by range of droplets size, obtained by PDA (Fig. 3.29(b). Experimental evaporation distance can be estimated from PDA data rate measurements (see Fig. 3.26). Then it can be compared the experimental distances, as a function of the size groups, to the evaporation distance predicted by the three models (see Fig. 3.29(b)). It is noted that model 1 overestimates the droplet lifetime and in consequence also the evaporation distance. For instance, the model predicts that fuel droplets with a diameter $d = 10$ μm will be present until 60 mm while the PDA data rate indicates that droplets in the diameter range $5 < d \leq 10$ μm do not exist (data rate lower than 10% of its maximum) beyond $z = 19$ mm ($z/D_{exit} = 2.4$). In the case of the model 3, it underestimates the lifetime of the droplet and so the evaporation distance. Indeed, this model represents a very vigorously evaporation caused by the assumption of the flame present surrounding the droplet. Relative to measurements, droplets with a diameter $d = 10$ μm will be evaporated quite faster, being totally evaporated at 4.3 mm. However, the model 2 predicts an evaporation distance of about 12 mm for droplets with a diameter $d = 10$ μm. This is a no so far prediction compared to the experimental data. The model 2 based on the heat transfer works well for droplets larger than $d = 5$ μm.

Using the evaporation model based on the heat transfer (model 2), we have calculated the droplet lifetime and the evaporation distance as a function of, not only the droplet initial diameter, but also as a function of the environment temperature (T_∞). Results are reported on Fig. 3.30. We note that this model predicts the presence of droplets of size equal or higher than 20 μm beyond a distance of 20 mm, even with temperatures up to 1000 K. Hence, the predictions of the model 2 seem to be verified by the vertical tomography views of the spray, since we expect to still find droplets beyond $z = 20$

[2]More advanced models exist, which are not used in this work, where the evaporation and combustion of multiple droplets are considered (e.g. [49, 109])

mm (see Fig. 3.28).

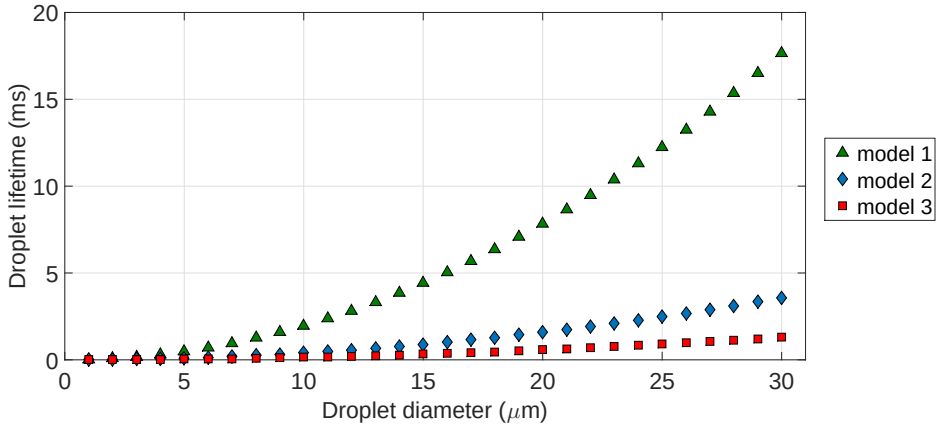

(a)

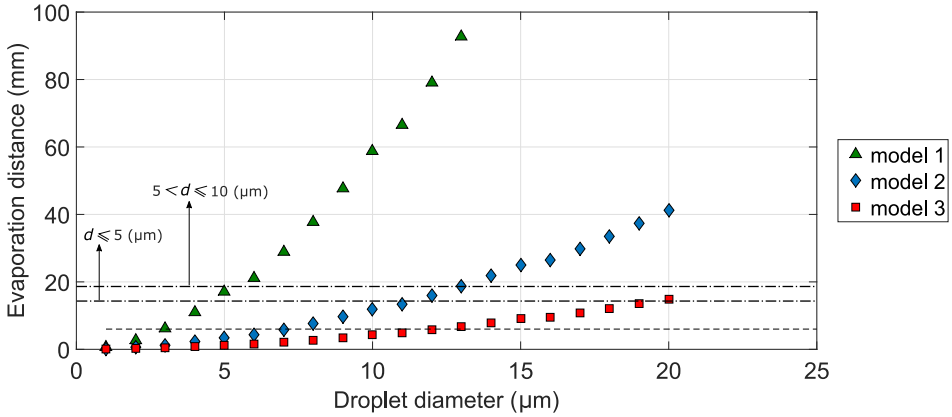

(b)

Figure 3.29: Comparison of droplet evaporation models: (a) lifetime and (b) evaporation distance of n-heptane droplet depending on its diameter.(—) flame foot position. (- ·) Experimental evaporation distance.

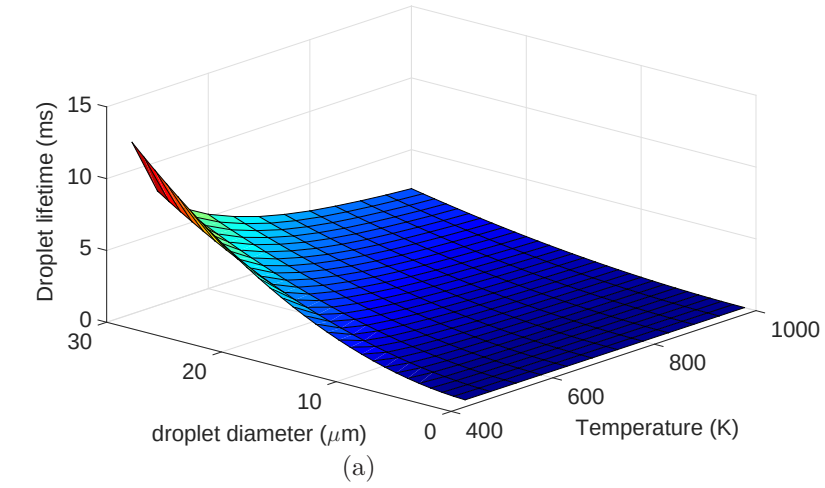

(a)

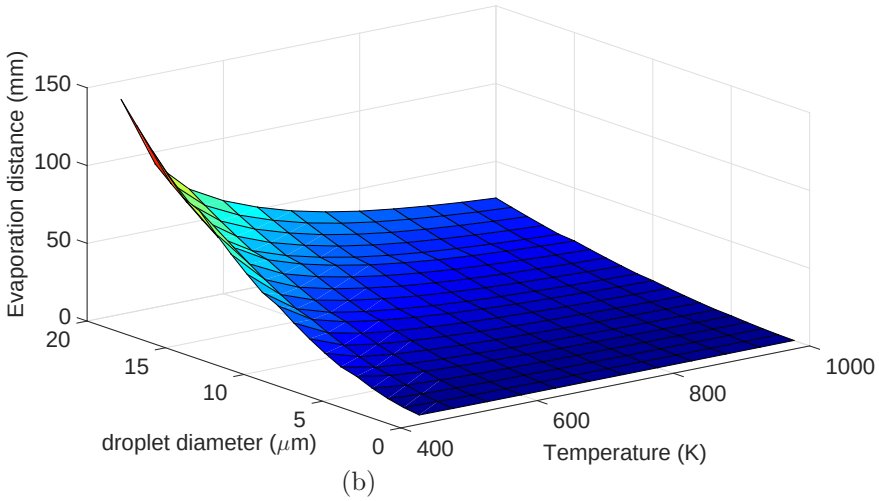

(b)

Figure 3.30: Droplet lifetime and evaporation distance calculated with the Heat Transfer model as a function of the droplet diameter and the surrounding temperature far from the droplet (T_∞).

3.6.2.2 Fluctuation of the fuel feeding system

From the high speed horizontal tomography views of the spray we can obtain a signal related to the amount of droplets over time (the procedure is explained in chapter 4). An example of such a signal for a case without acoustic is shown in Fig. 3.31(a). We note a slight low frequency modulation over time. This modulation is even not detectable only observing the tomography views. The Power Spectral Density (PSD) of this signal we found a small peak at 40 Hz that can corresponds to the slight modulation. The small modulation is ascribed to our feeding pump Tuthill DGS (P series) that works at 60% of its maximum rotation speed (4000 RPM) to provide the fuel flow rate. This rotation speed (2400 RPM) correspond to a frequency of 40 Hz.

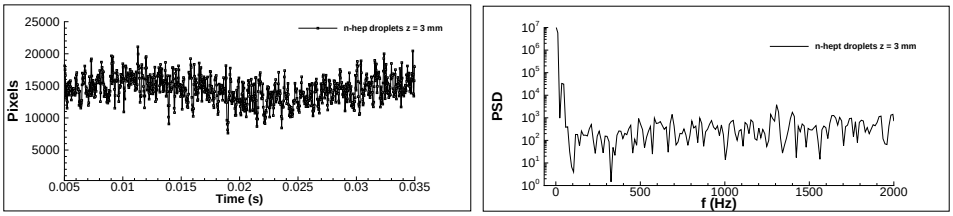

(a) (b)

Figure 3.31: (a) Spray signal in number of pixels and (b) its PSD showing no particular pic. Signal obtained from high speed horizontal tomography images of the droplets at $z/D_{exit} = 0.375$. $\dot{m}_{fuel} = 0.097$ g/s and $\dot{m}_{air} = 1.72$ g/s.

3.7 The swirling flames without acoustic forcing

In this section we present the main characteristics of the swirling flames and their chemical structure, without acoustic forcing deduced from the flame emission, OH* and CH* chemiluminescence signals. The signal $I'_{OH^*}(t)$ from the middle flame recorded by the photomultiplier, is characterized by an average value $\bar{I'}^{o}_{OH^*}$ of 2.14 (a.u.) while its PSD does not show any significant peak (Fig. 3.32).

Images from the OH* chemiluminescence signal are used to analyze the flame fronts. High speed images are recorded with a Phantom V10 camera. The high speed image sequences are averaged in order to obtain the mean spatial shape of flames. Fig. 3.33 shows an averaged image of the three swirling flames, calculated over 1000 views recorded at 2773 fps. Flames are slightly lifted around 8 mm above the nozzle exit. They have a V-shape, due to the hollow cone spray, and a similar height. The flame angle (θ_{outer}), measured from the outer contour of the flame front, is of about 60 ± 2 degrees, for the three flames. These features show that the flames are alike, as is observed in an annular chamber (e.g. [94]). In consequence, this supports the fact that our setup (three swirling flames linearly arranged) can well model a sector of an annular chamber.

In order to estimate the real shape of the flame, an Abel transform of the OH* chemiluminescence mean image of the central flame is presented on Fig. 3.34 (left), displayed in false color. A half of the flame front averaged image is deconvoluted and mirrored to form the entire deconvoluted OH* emission image of the flame. The highest OH* emission intensities are located just downstream the liftoff position of the flame. It is worth noting that the averaged image and its corresponding Abel transform represents the most statistically-probable flame shape. The instantaneous flame images do not show a flame front with a well formed V-shape, mainly due to turbulence, as illustrated in Fig. 3.34 (right). The CH* chemiluminescence of the central flame has been recorded, using the Princeton Instrument PIMAX 4 intensified camera, equipped with the appropriate interferential filter. Three operating points have been analyzed, corresponding to three different equivalence ratios.

The average images obtained for these three points are presented in Fig. 3.35. The

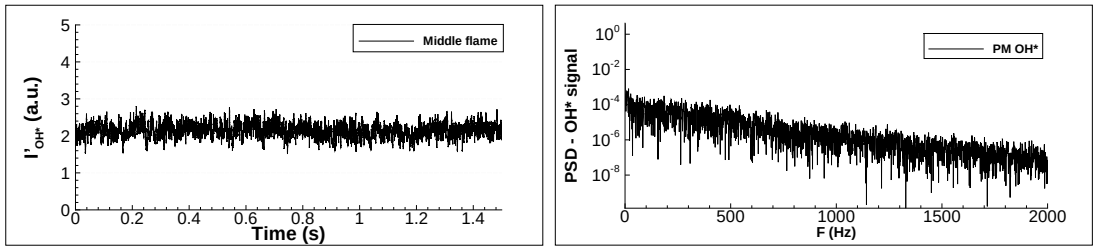

(a) (b)

Figure 3.32: (a) Flame OH* emission recorded by the PM in the case without acoustic forcing and (b) its corresponding PSD spectrum. $\dot{m}_{fuel} = 0.108$ g/s and $\dot{m}_{air} = 1.72$ g/s.

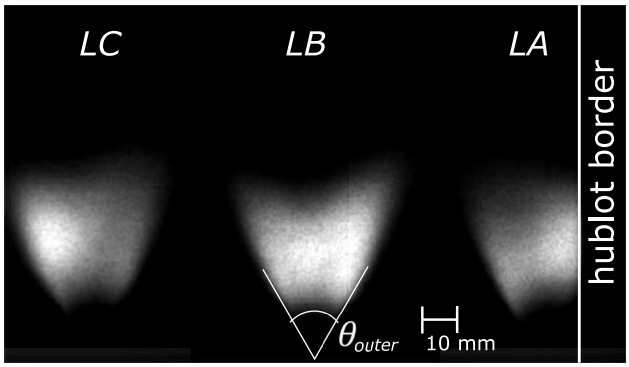

Figure 3.33: Averaged image of flames filtered for OH* without acoustic forcing. $\phi_{LB} = 0.95$ for $\dot{m}_{fuel} = 0.108$ g/s and $\dot{m}_{air} = 1.72$ g/s, total power $P \approx 14$ kW. Flame angle $\theta_{outer} = 60 \pm 2$ degrees.

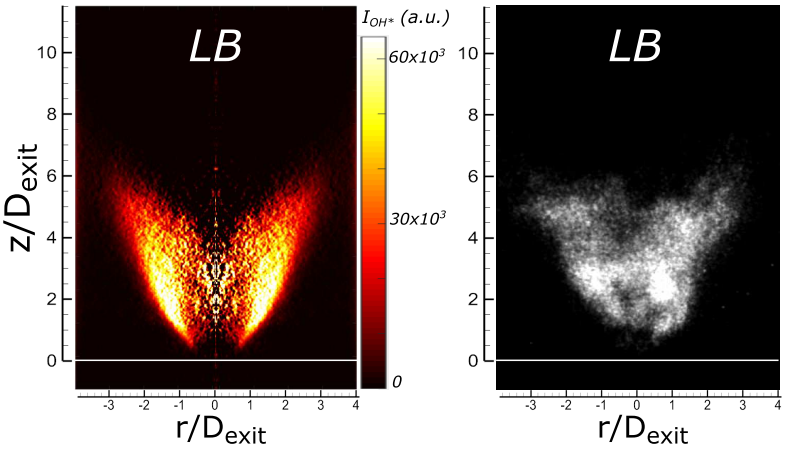

Figure 3.34: Abel transform (false colors) of the central flame averaged image, filtered for OH* (left), and an instantaneous OH* flame front image (right), both without acoustic forcing. $\phi_{LB} = 0.95$ for $\dot{m}_{fuel} = 0.108$ g/s and $\dot{m}_{air} = 1.72$ g/s.

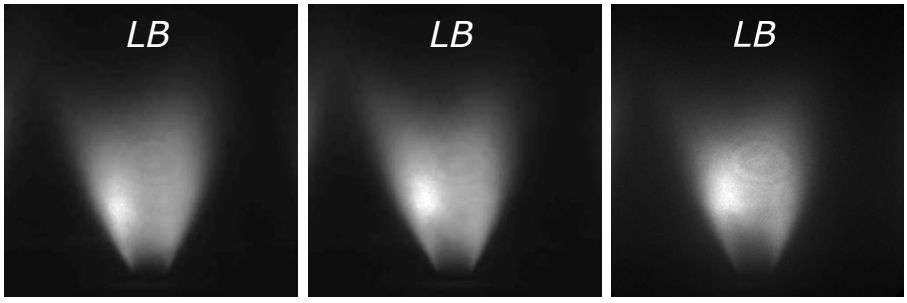

(a) $\phi_{LB} = 0.85$ (b) $\phi_{LB} = 0.90$ (c) $\phi_{LB} = 0.95$

Figure 3.35: Averaged images of the central flame (LB) filtered for CH*:(a) $\phi_{LB} = 0.85$ for $\dot{m}_{fuel} = 0.097$ g/s and $\dot{m}_{air} = 1.72$ g/s, power $P = 4.3$ kW; (b) $\phi_{LB} = 0.90$ for $\dot{m}_{fuel} = 0.105$ g/s and $\dot{m}_{air} = 1.72$ g/s, $P = 4.7$ kW; (c) $\phi_{LB} = 0.95$ for $\dot{m}_{fuel} = 0.108$ g/s and $\dot{m}_{air} = 1.72$ g/s, $P = 4.8$ kW. Flame angle $\theta_{outer} = 52 \pm 2$ degrees.

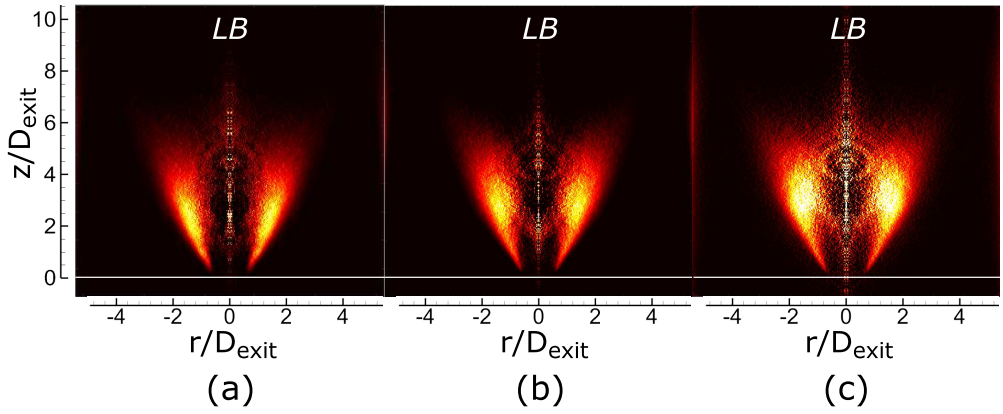

Figure 3.36: Abel transform of the central flame averaged image (false colors), filtered for CH*, at three different operating points without acoustic forcing: (a) $\phi_{LB} = 0.85$, (b) $\phi_{LB} = 0.90$ and (c) $\phi_{LB} = 0.95$.

V-shape is well defined. The flame angle based on the outer edge of the averaged flame front is almost the same for the 3 operating points, i.e. $\theta_{outer} = 52 \pm 2$ degrees. However, Abel transforms of these images show a shift of the position and an increase of the maximum CH* intensity as the equivalent ratio grows (see Fig. 3.36). For the equivalent ratio equal to 0.90, the flame starts to turn to a M-shape, the "M" being formed at the base of the flame. For $\phi_{LB} = 0.95$ the M-shape is more clearly defined.

An opening angle (θ_{int}^{max}) is defined on Abel transforms of CH* or OH* images as the angle formed by two lines drawn on each side of the flame deconvoluted image. Each line connects the lowest point of the flame foot to the region of maximum emission intensity. This definition makes this angle smaller than θ_{outer}. The angle θ_{int}^{max} diminishes when the equivalence ratio grows as illustrated in Fig. 3.37 whereas it was previously observed that θ_{outer} remains virtually unchanged.

In order to study the chemical structure of the flame, Abel transforms of CH* and OH*

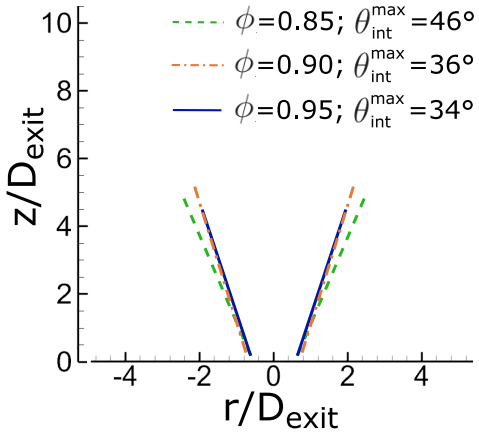

Figure 3.37: Comparison of the flame open angles (θ_{int}^{max}) measured from the Abel transform of the central flame averaged images, filtered for CH*, at three different equivalence ratios (ϕ) without acoustic forcing.

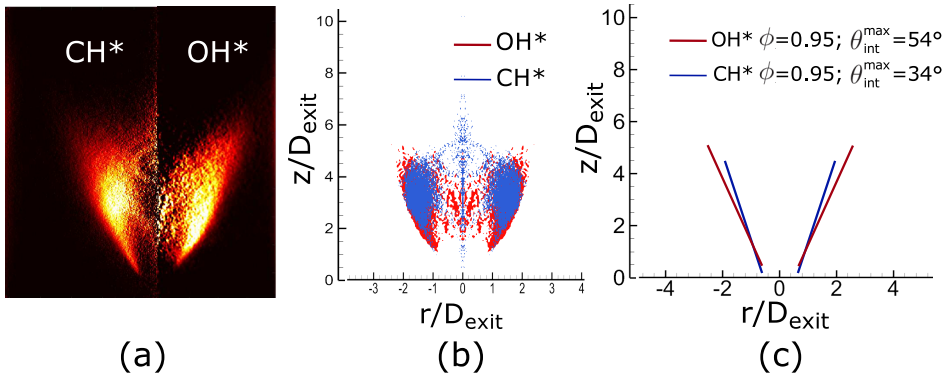

Figure 3.38: (a) Abel transform of the CH* and OH* chemiluminescence, (b) maximum radical emission intensity areas, (c) flame angles (θ_{int}^{max}). Without acoustic forcing.

emission images are compared for the same operating point $\phi_{LB} = 0.95$ in Fig. 3.38. We note first that the shape of the outer contours are similar, but the regions of maximum emission intensity are not situated at the same place. While the OH* maximum region begins from the flame foot, the CH* maximum appears farther downstream, at a higher z-position. However, the flame foot position is farther downstream for OH* emissions than for CH*.

The Abel transformed images of OH* and CH* emissions have been segmented to determine the regions corresponding to emission larger than 50% of the maximum emission. This regions are superimposed in Fig 3.38(b). The region for OH* (in red) is larger than for CH* (in blue) which indeed appears as embedded in the OH* area. The flame angle, based on the maximum of the CH* emission intensity, is smaller than for OH* (see Fig. 3.38(c)).

Chapter 4

Images analysis methods

The images recorded by low-speed and high-speed cameras presented in section 2.3, are post-processed in order to enhance the visualization of the observed system behavior in the space and time domain. Views from low-speed camera give access to instantaneous insights and as they are not resolved in time, they can however serve to perform a reconstruction of a mean behavior by means of phase-averaged images. From the high speed images we can extract signals that could be analyzed in the frequency or time domain. By taking advantage of the high time resolution, it is possible to reconstruct a mean behavior by classifying the views into windows of short time duration and then computing the average of each class. Thus, high-speed images contain the spatial and temporal information of:

- the response of flame emissions in the case of the flame front visualization;
- the seeded-air behavior in non-reactive conditions or during combustion;
- the n-heptane droplet behavior during combustion.

Some physical properties are defined from these signals. For the investigation of the flame response, the signals obtained from the flame front visualizations represent the evolution of radicals (OH* or CH*) chemiluminescence emissions. These emissions are directly linked with the intensity of the combustion over time. In the case of the fuel droplet visualization, the number, positions, dispersion and the number density per surface area of droplets has been evaluated. In the case of the views of the seeded-air without combustion, the structures of the perturbed or unperturbed air-flow was localized and followed, during acoustic forcing. On the other hand, when we analyze the seeded-air during combustion, a procedure to discriminate between the fuel droplets and the seeded droplets that trace the gaseous phase (the air) was implemented. Once this is made, we can extract the evolution of the seeded-air volumetric flow rate, separately from the liquid injection evolution.

By analyzing in particular the high-speed images of the two-phase flow, we can reconstruct the spray behavior during combustion and acoustic forcing. As a consequence, it is possible to provide valuable information to correctly understand the fuel droplets spatial structuring and temporal development, with and without the acoustic perturba-

tion. For this task, the visualization of the air-flow structures formation and development, in particular during acoustic perturbations, is essential. A better understanding of the flame response to acoustic perturbations, relies on a correct investigation of the behavior of the spray. The main details behind the post-processing of these images, are described hereafter.

4.1 Definition of the class-averaged images

The definition of a class-averaged image is inspired from the principle of the phase-average analysis. For that reason, before defining what we have named class-average image, we briefly recall the principle of phase-averaged images, in the case of image recording synchronized with an external harmonic excitation (for instance the acoustic forcing) signal at the frequency f_r. We first consider the case where the acquisition rate of the camera (f_{cam}) is much lower than f_r (this is the case of the ICCD camera PIMAX4). The limits of each cycle of the observed phenomenon can be determined using as a reference the signal corresponding to the external excitation. The camera is synchronized in order to make an acquisition at a particular phase of the cycle. As $f_{cam} \ll f_r$, the images can be recorded at each f_r/f_{cam} cycle (see Fig. 4.1 (a)). By changing the time delay (t_d, lower than $1/f_r$) between the reference phase of the external signal and the trigger of the camera, the observed phenomenon is explored within a cycle. Thus, gathering the images recorded with the same time delay, i.e. for the same phase, and calculating the average of them a phase-averaged image is obtained. The illustration in Fig. 4.1(a) presents a reconstruction of a cycle with three points per cycle and three images per point. In order to correctly reconstruct the phenomenon, the total number of images (N_t) per point and the number of points per cycle, must be high enough.

When the acquisition rate is higher than the external excitation frequency, $f_{cam} \gg f_r$, as is the case of high-speed cameras, and when f_{cam} is a multiple of f_r, several images can be recorded during a cycle, and in the successive cycles the same number of images will be recorded at the same phase delay. Thus, it is still possible to obtain a phase-averaged image for each set of images recorded at the same phase. The illustration presented in Fig. 4.1(b) shows how three phase-averaged images are obtained from seven successive cycles and three images per cycle. The number of images per cycle (i.e. is the number of points for the reconstruction) is f_{cam}/f_r.

For the case ($f_{cam} \gg f_r$) where f_{cam} is not a multiple of f_r, we can not directly overlap the recorded cycles of the observed phenomenon. Instead of this, we have defined the class-averaged images. In order to explain this, we take as example, a series of N_t high-speed images. The total acquisition time (N_t/f_{cam}), divided by the acoustic forcing period ($T_{cycle} = 1/f_r$), gives the total number of cycles recorded (N_{cycle}). Moreover, the number of images (m) recorded during each forcing cycle is approximately[1] equal to f_{cam}/f_r. Here, we divide a cycle of the acoustic forcing in a number N_w of time windows (or phase classes). The size of each time windows is $T_w = T_{cycle}/N_w$. Within

[1]Remember that f_{cam}/f_r is not integer because f_{cam} is not a multiple of f_r.

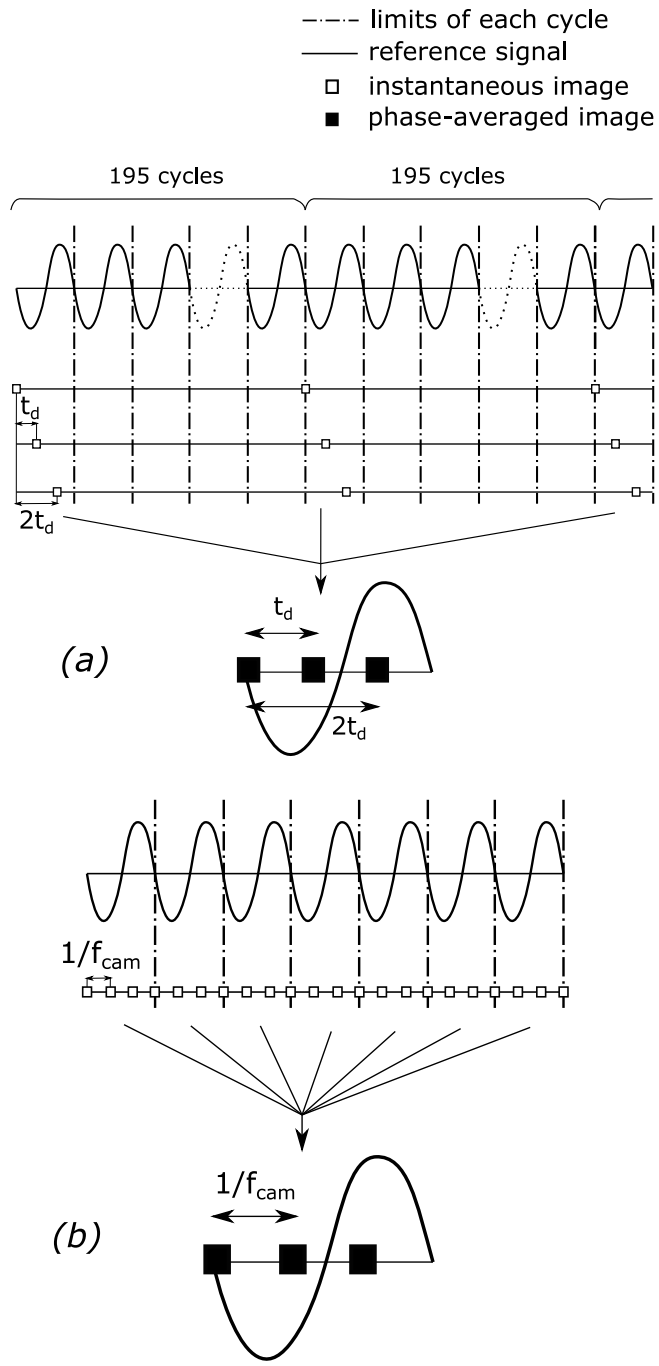

Figure 4.1: Phase-averaged images reconstruction technique: **(a) low-speed camera** ($f_{cam} \ll f_r$) illustrated for a case with $f_r = 780$ Hz and $f_{cam} = 4$ Hz, giving a ratio of 1 image acquisition over 195 cycles. The image acquisition trigger delay is t_d; **(b) high-speed camera** ($f_{cam} \gg f_r$), f_{cam} is a multiple of f_r. Three phase-averaged images are obtained from seven successive cycles and three images per cycle.

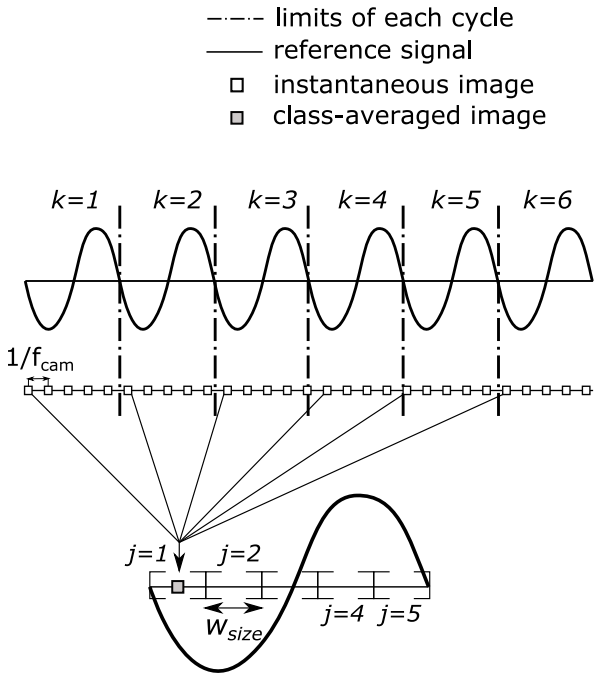

Figure 4.2: Class-averaged images reconstruction technique, with $f_{cam} \gg f_r$ and f_{cam} is not a multiple of f_r. After classify the images that enter in the first temporal window, a class-averaged image is calculated.

each time window we classify all the images of the considered series, according to their acquisition time (t_i). Thus, the image i with a time $t_i = (i-1)/f_{cam}$, is classed within the j^{th} windows if its acquisition time is such that:

$$T_w \cdot (j-1) \leq (t_i - (k-1) \cdot T_{cycle}) < T_w \cdot j \tag{4.1}$$

In the Eq. 4.1 the counter i ($1 \geq i \leq N_t$) represents the image that is currently processed and j ($1 \geq j \leq N_w$) indicates the time window number. Finally, the counter k ($1 \geq k \leq N_{cycle}$) indicates the cycle to which the image i belongs. In consequence, k goes from $k = 1$ to $k = N_{cycle}$. When all the images are classified within its respective temporal class, a mean image is calculated with the images within each class, giving the class-averaged image. Finally, we are able to reconstruct the observed phenomenon behavior over a cycle with the N_w class-averaged images. An illustration of this technique is presented in Fig. 4.2, where a cycle is reconstructed by considering five temporal windows.

This type of image averaging smooths the observed phenomenon within the temporal window. The incidence of this smoothing depends on the size of T_w relative to the size of T_{cycle}. For $N_w = 24$ the smoothing span over 4.17% of T_{cycle}, leading to the same relative uncertainty over the frequency range. Moreover, this averaging acts as a low-pass filter. Thus, a phenomenon at $f_r = 540$ Hz, will be characterized with an accuracy of 20 Hz and with a low-pass filter of about 12.5 kHz. However this cut-off frequency is far from the frequency range investigated (0.5 to 1.5 kHz).

In the case of high speed images of the flame front recorded with the Phantom V10

camera, we have chosen $N_w = 24$. For the reconstruction of a cycle of the acoustic forcing of the n-heptane droplets visualized by means of high speed horizontal tomography views, we have chosen $N_w = 20$. For all of the reconstruction made using high speed vertical tomography views we have taken $N_w = 50$.

4.2 Post-processing of horizontal tomography images

4.2.1 Identification of the effective flow region in tomography images

Tomography images are formed by the light scattered (Mie-scattering) by the droplets illuminated by the laser sheet. The width of the laser sheet is of about 500 μm. The size of the seeding particles is between 1 and 5 μm while about 9% of the fuel droplets has a size larger than 20 μm.

The effective flow region visualized in the tomography views with the air flow seeded, is the intersection surface between the seeded flow and the laser sheet. In the case of horizontal views the images can be binarized and the effective flow region area is quantified in a number of pixels in the resulting two-level image (Eq. 4.2). The subscripts j and k indicate the pixel position in the image.

$$A_{eff} = \sum n_{j,k}^{pix} \tag{4.2}$$

Thus, from a series of images, a signal $A_{eff}(t)$ over time can be obtained, i.e. the evolution of the effective flow region area. This signal is an indicator of the presence of droplets.

The total intensity of the light scattered by the seeding particles ($L_{int}(t)$) over a series of images is an indication of the evolution of the seeding particles concentration into the laser sheet. It is linked to the number of droplets in the effective flow region area. It is obtained as the addition of the grey-intensity level of all the pixels that form the flow region area (Eq. 4.3).

$$L_{int} = \sum I(n_{j,k}^{pix}) \tag{4.3}$$

These signals are computed within a region of interest (ROI) defined in each image of a series. Some illustration are given in Fig. 4.3. In this figure, views (a) and (b) are used for the computation of L_{int} while the view (c) was binarized to compute A_{eff}. The geometry of the ROI depends on the location of the injection, i.e. PAN, VAN or IAN. For instance, when the disturbance field is axisymmetric, typically at the basin of the pressure antinode, the ROI can be circular or rectangular, in this case dividing the image horizontally and taking into account for example the top half part. However, when the air flow is placed at the intensity antinode, the ROI is a circle that takes into account the whole effective flow region (Fig. 4.3(a)). When the air-flow is affected by the non-axisymmetric disturbance field in the basin of the velocity antinode, the ROI

is composed of two rectangular regions on the left and right sides of the injector axis (Fig. 4.3(b)).

When the seeded air-flow is investigated in combustion condition the Mie scattering signal is constituted of two components, i.e. the signal produced by the seeding droplets for the analysis of the air-flow and an additional signal produced by the n-heptane droplets (Fig. 4.4 (a)). In this case, the tomography views must be processed in order to separate the two signals and determine the surface area corresponding only to the seeding particles. The image is thus segmented in order to separate the n-heptane droplets from the seeding particles. The fuel droplets are identified thanks to the fact that the light intensity scattered by these droplets is higher than the light intensity scattered by the seeding particles and also well localized, i.e they are identified as bright spots in the image (Fig. 4.4 (a)). A peak extraction base on image opening (morphological operator [110]) is applied to get an image of the fuel droplets only (Fig. 4.4 (b)). This is done with the open-source image processing software Fiji [111]. This image is subtracted from the original image. To the pixels within the hole left at the position of each droplet (see magnification, Fig. 4.4 (c1)), is assigned a mean value based on the value of the pixels in its neighborhood (Fig. 4.4 (c2)). Then, this image is segmented and labeled. The labeled objects found are sorted depending on their area the smallest ones (number of pixels lower than of about 2000) being rejected. The pixels of the retained objects are set to one and surrounding pixels are set to zero to get a mask image (Fig. 4.4 (d)). This mask, is applied to the image with the holes covered to get only the signal from the seeding particles and thus the pattern of the seeded air-flow with the original dark zones in its center (Fig. 4.4 (e)). In this image, the fuel droplet signal has been replaced by an estimate of the seeding particle signal. However, the integrated intensity $L_{int}(t)$ delivered by these image was subject to some discrepancies and the area count corresponding to the seeding particles $A_{eff}(t)$ was preferred to analyze the air-flow pattern.

Finally, in the case of the horizontal tomography views of the n-heptane droplets without seeding the air flow, the effective flow region is the intersection of the fuel droplets with the laser sheet. In this case the signal $A_{eff}(t)$, computed within the corresponding ROI, is linked to the number of droplets that passes through the laser sheet, even

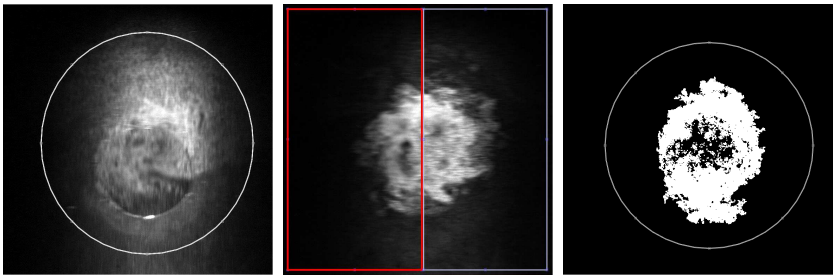

(a) (b) (c)

Figure 4.3: Illustrations of the region of interests (ROI) in the case of the seeded air (w/o combustion) placed at the basin of the intensity antinode (a), at the basin of the velocity antinode (b). ROI in the case of the seeded air (during combustion) placed at the pressure antinode (c).

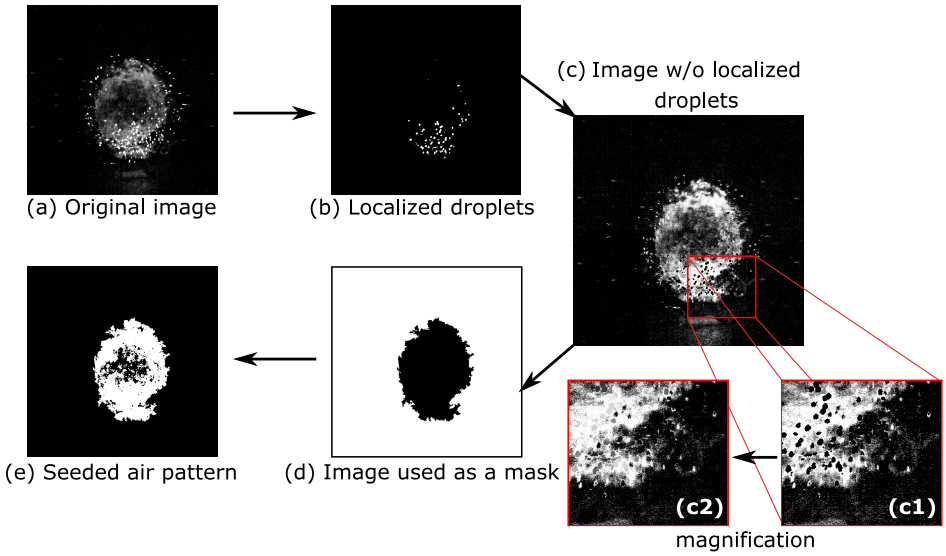

Figure 4.4: Intermediate views of the process to detect the seeded-air pattern during combustion.

though the intensity of a pixel cannot be assimilated as the signal of one droplet. Indeed, a bright spot in the image can cover several fuel droplets. As the light scattered by the droplets generates a good contrast in the tomography views, they are easily localized by applying morphological operators to the images.

4.2.2 Droplets number density

The n-heptane droplet number density is computed by using the horizontal tomography views of the spray without seeding particles into the air-flow and during combustion. The droplet number density is calculated within a rectangular ROI defined in a radial direction perpendicular to the acoustic axis, on the top side of the image (see Fig. 4.5). The ROI height is adjusted to fit the radial expand of the zone covered by the considered droplets (Fig. 4.5). The density is estimated only from top side, assuming that the spatial distribution of the droplets, in horizontal views, is axisymmetric about the injector axis. Despite some asymmetries introduced by the injection, this assumption is verified in average as we have shown in the section 3.6.2. Moreover, when the injector considered is positioned at the basin of influence of the pressure antinode, the acoustic disturbance at this location is also axisymmetric. For the present work, the droplet number density was estimated without acoustic forcing and with acoustic forcing only in the case of the central injector positioned at the pressure antinode. The 2D fuel droplets number density is estimated by the ratio of the active pixels (corresponding to the light scattered by the fuel droplets) to the area of the rectangular ROI.

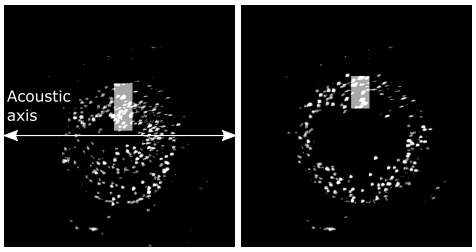

Figure 4.5: Tomography views of the droplets at $z/D_{exit} = 0.1875$, for two different instants of the acoustic perturbation, with the injector positioned at the pressure antinode. The droplet number density is calculated in a rectangular region of interest (ROI) marked in grey on the images. The ROI is adapted to follow the position of the droplets.

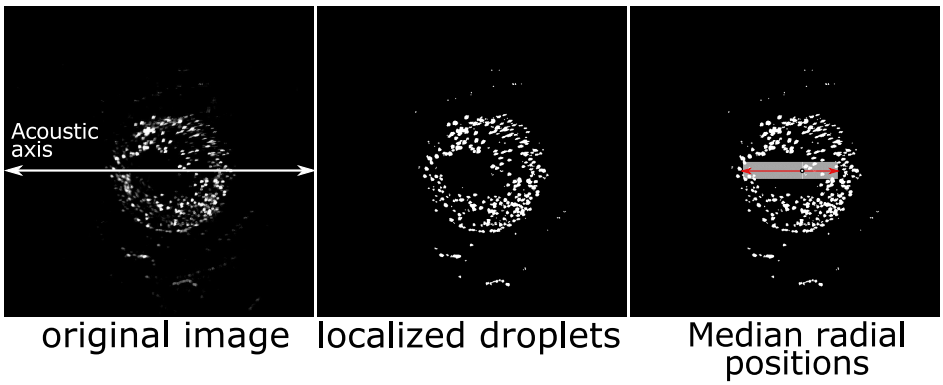

Figure 4.6: Example of tomography view of the droplets at $z/D_{exit} = 0.1875$, from where the mid value of the droplets radial position is calculated.

4.2.3 Spatial distribution of fuel droplets

The distribution of the fuel droplets in the spray gives rise to a "donuts" shape on the images obtained with the horizontal tomography visualizations, as can be seen in Fig. 4.6. The spatial distribution of the fuel droplets is estimated by determining r_d^{mid}, the mid radius of the donuts shape, and δ_r, the mean deviation from this mid radius. Two rectangular ROI are defined on the left and right sides of the injector axis, centered on the acoustic axis, with height about 1.33 mm ($\approx 0.166 \cdot D_{exit}$). The mid radius of the droplet spatial distribution (r_d^{mid}) is defined by Eq. 4.4 where r_d^{first} and r_d^{last} are respectively, the position of the first and last droplet within a defined ROI, from the center of the donuts, along a radial direction. The term "mid" is employed because the calculated position is situated in the middle of the segment defined by r_d^{first} and r_d^{last}.

$$r_d^{mid} = 0.5 \cdot (r_d^{first} + r_d^{last}) \tag{4.4}$$

In Fig. 4.6 the distance from the injection axis to the mid radial position is indicated with a shaded region and two red arrows.

The deviation from the mid radial position (δ_r) is defined by Eq. 4.5. The sign of δ_r determines whether most of the droplets are positioned inward ($\delta_r < 0$) or outward

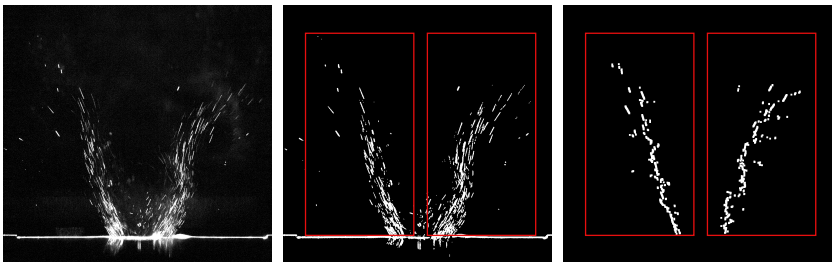

(a) (b) (c)

Figure 4.7: Illustration of the processing of the high speed vertical tomography views of the n-heptane droplets: original view (a), localized droplets and the ROI considered (b), calculated radial mid positions forming the skeleton of the spray (c).

($\delta_r > 0$) of the mid radius.

$$\delta_r = \frac{\sum_{ROI}(r_d^i - r_d^{med})}{N} \tag{4.5}$$

Here i indicates the position of each droplet in the ROI, N is the number of pixels involved in the calculation and linked with the number of droplets. The mid value of the droplets radial positions and its deviation are calculated for the cases where the central injector is positioned at the basin of influence of pressure antinode and the intensity antinode defined in chapter 5.

4.3 Post-processing of vertical tomography images

4.3.1 Streaklines of fuel droplets

The cloud of fuel droplets is obtained by performing morphological operations as it has be done in section 4.2.1. In this case the air-flow is not seeded. The mid streaklines of the fuel droplet spray are determined by computing row by row the mid radius of the spray cloud. The left and right sides of the spray are treated separately in order to obtain the left streakline and the right streakline. The mid value of the droplet radial positions is calculated on the two-level images. For each row, detecting the first and the last droplet in the row is searched within a region of interest defined on each side of the injector axis (Fig. 4.7(b)). The mid radius position is defined as the mean between radial position of the first and the last droplet. Assembling these mid radial position, for all the rows, leads to the skeleton of the spray cloud as shown in Fig. 4.7(c). The skeleton images over time are classified in temporal classes (see section 4.1) and the images of each temporal class are gathered together. The location points are then fitted by polynomials to determine the mean streakline corresponding to a given phase relative to the acoustic forcing. Then, these streaklines deduced from the class-averaged images are used in order to perform the reconstruction of the fuel droplets behavior during a full cycle of the acoustic perturbation.

The polynomial fit was made to optimize the representation of the motion of the fuel droplets during the acoustic perturbation. It was found that using a fourth degree

curve better represents the positions points. This is illustrated in Fig. 4.8, where different fitted lines are represented.

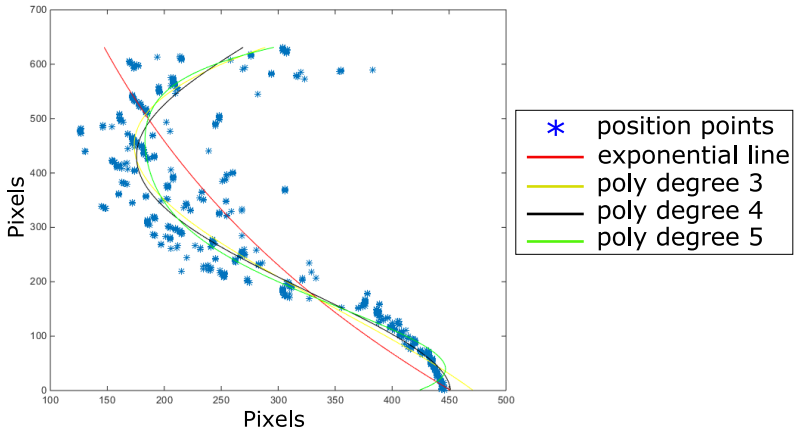

Figure 4.8: An example of some position lines fitted to represent the droplets positions. From these tests, a polynomial line fitting of 4^{th} degree have been chosen.

Part II

TACC-Spray with an open-loop transverse acoustic forcing

Chapter 5

Acoustic characterization of TACC-Spray

The chamber was built to be used as an acoustic cavity tuned to its second resonant transverse mode (2T1L). In order to guarantee the presence of this transverse mode within the cavity, simulations were performed with the software COMSOL Multiphysics. These simulations were used to support the design phase and to help interpret the experimental results. Fig. 5.1 shows an illustration of the simulated acoustic field corresponding to the 2T1L resonant acoustic mode within the cavity. The main characteristics of the 2T1L acoustic mode, obtained in cold condition, serve to subsequently verify if this mode is well excited in combustion conditions. The 2T1L acoustic mode presents three locations of interest along the x-direction, parallel to the acoustic axis, are of our interest: the Pressure Antinode **(PAN)** situated at $x/L_c = 0$, the Velocity Antinode **(VAN)** situated at the basin of pressure minima ($x/L_c \approx \pm 0.25$), and the Intensity Antinode **(IAN)** situated at a region where the acoustic velocity and the acoustic pressure, both present a strong gradient ($x/L_c \approx \pm 0.125$ and $x/L_c \approx \pm 0.375$).

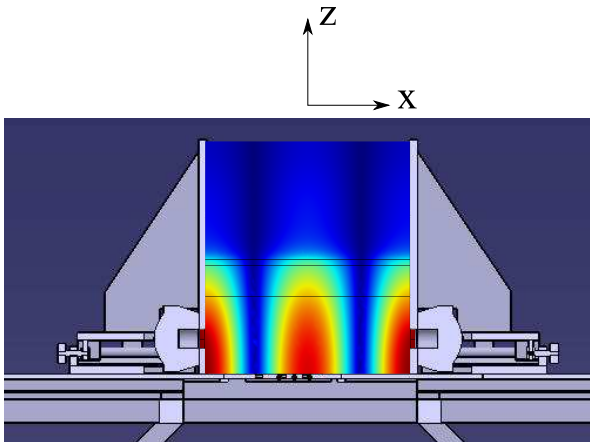

Figure 5.1: Illustration of a simulated acoustic field of the resonant cavity, in a plane situated at $y/e = 0$. Dark red and blue correspond to high and low values of the acoustic pressure amplitude respectively.

These locations represent specific acoustic conditions to which spray and flames can be confronted within a real turbine combustor. The section 5.1 presents the modeling of the acoustics in the cavity, the section 5.2 presents the experimental and numerical validation of the 2T1L mode. In subsection 5.2.2 the case with combustion, and the injection placed at PAN, is considered under an uniform temperature field condition. In subsection 5.2.3, a non-uniform temperature field is considered with the injection system is located at PAN, VAN and IAN.

5.1 Modeling of the acoustic pressure in the TACC-Spray chamber

The response of the cavity to a mono-frequency excitation has been simulated with the software COMSOL, and characterized also by an analytic study. In COMSOL, acoustic wave propagation is modeled by equations from the linearized fluid dynamics. The physic quantities, as the pressure or the fluid density, are expressed as the addition of a mean part (Ψ_0) plus an fluctuating part (ψ):

$$\Psi = \Psi_0 + \psi. \tag{5.1}$$

Only the fluctuating part of the quantities (except ρ) will be considered in the following. The mean pressure will be taken as the atmospheric pressure and the mean velocity will be set to null as swirl air flows are not considered in this part[1].

The aim of the simulation and also of the analytic calculation, is to help the recognition of the second resonant transverse mode (2T1L) from the experimental characterization of the chamber. The numerical geometry of the cavity includes the convergent element, as is described in section 2.1. Each compression driver is represented as a cylinder of length 20 mm and radius 24 mm, placed horizontally. The cylinders are closed on one side and open on the other side connected to the acoustic cavity. A wide air volume, extending beyond the cavity boundaries, is considered in the geometry in order to prevent side effects at these boundaries. The mesh for this geometry has been created applying the physics-controlled mesh option of COMSOL (see Fig. 5.2(a)).

Simulations in cold condition have been performed taking the same temperature (ambient temperature equal to 293 K) for the volume of air outside of the cavity as well as for the volume of air inside the cavity. When hot conditions were considered, only the temperature field of the volume inside the cavity was modified. Two cases were considered for the hot conditions. For the first case a constant temperature ($\overline{T}$) is set in the cavity such that the peak of the frequency response obtained numerically corresponds to the peak obtained experimentally. For the second case, in order to be as close as possible to the real conditions, we have defined a simplified but variable temperature field as a function of the flame locations within the acoustic cavity. The temperature field was defined by using temperature measurements, for three different flame locations within the cavity, i.e. central flame at PAN, VAN or IAN.

[1]All the numeric results presented in this work correspond to pure acoustic simulations

5.1.1 Boundary conditions

The Sound Hard Boundary condition is applied to all the walls of the acoustic cavity. The surfaces affected by this boundary condition are shown in Fig. 5.2(b). This condition prescribes a boundary at which the normal component of the acceleration is zero:

$$\mathbf{n} \cdot \frac{1}{\rho_0} \mathbf{grad} p = 0 \tag{5.2}$$

The impedance boundary condition is applied to the surfaces of the large volume of air outside of the acoustic cavity. These surfaces are shown in Fig. 5.2(c). This conditions is a generalization of the Sound Hard (and Soft) boundary condition, so in our case is formulated as follows:

$$\mathbf{n} \cdot \frac{1}{\rho_0} \mathbf{grad} p = -\frac{i\omega p}{Z_i} \tag{5.3}$$

where Z_i is the acoustic input impedance of the external domain and is equal to $Z_i = \rho_0 c$ (c is the speed of sound). Here the air impedance value at ambient temperature was used, i.e. $Z_i = 1.2 \cdot 343 = 411.6$ [Pa · s/m].

The acoustic sources are introduced by imposing a normal acceleration boundary condition on the closed side of the cylinders that represent the compression drivers. Thus, this boundary condition represents the external source term. The assumption here is that the velocity $\mathbf{v}$ of the fluid (air in this case) is equal to the velocity $\mathbf{w}$ of the external

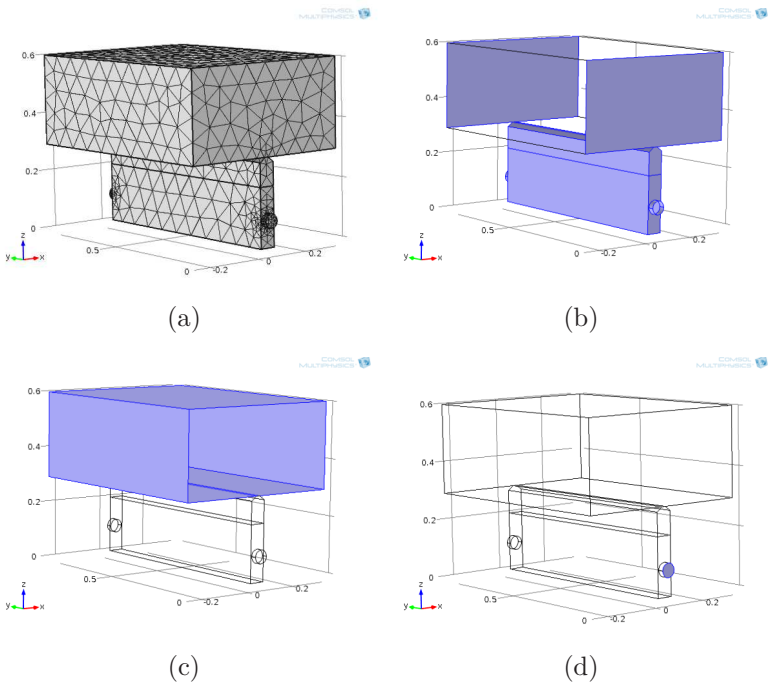

(a) (b) (c) (d)

Figure 5.2: Geometry of the acoustic cavity model: (a) mesh, (b) faces with a sound hard boundary condition, (c) faces of the outside air volume with an impedance boundary condition and (d) one of the two opposite faces with a normal acceleration as boundary condition, representing the mono-frequency acoustic forcing.

acoustic source (a membrane) in contact with it. This is expressed as:

$$\mathbf{v} \cdot \mathbf{n} = \mathbf{w} \cdot \mathbf{n} \tag{5.4}$$

Then, applying the temporal derivative on both sides of Eq. 5.4 yields Eq. 5.5:

$$\frac{\partial \mathbf{v}}{\partial t} \cdot \mathbf{n} = \frac{\partial \mathbf{w}}{\partial t} \cdot \mathbf{n} \tag{5.5}$$

Substituting the left hand side of Eq. 5.5 with Euler equation:

$$\frac{\partial \mathbf{v}}{\partial t} = -\frac{1}{\rho}\mathbf{grad}p \tag{5.6}$$

yields the normal acceleration boundary condition:

$$-\frac{1}{\rho_0}\mathbf{grad}p \cdot \mathbf{n} = a_n \tag{5.7}$$

The pressure wave (p) created by the source is determined by the normal acceleration input. Considering a progressive wave with an amplitude equal to A, the pressure wave is:

$$p = \frac{\rho_0 c}{\omega} A e^{i(\omega t - kx)} \tag{5.8}$$

with k the wave number. The acoustic power injected in the cavity, by the inlet orifice of surface S, is then:

$$W = \frac{p \cdot p^*}{\rho_0 c} S = \frac{\rho_0 c A^2}{\omega^2} S \tag{5.9}$$

where the asterisk indicates the complex conjugate. Thus, in order to obtain a constant power input regardless the frequency, the amplitude A entered as boundary condition, is set proportional to ω (about this, see also section 2.1).

5.1.2 Acoustic pressure wave equations without combustion

The development of the equations considered in COMSOL is presented beneath. The gaseous system, the air in the following, is constituted of a single species in the absence of chemical reactions. The gas is assumed as a calorically perfect gas with constant thermal properties (specific heats, thermal conductivity λ_c, etc.). Thus, the gas enthalpy per unit mass h is:

$$h = c_p T + const. \tag{5.10}$$

where the constant term contains the enthalpy of formation of the species per unit mass. Here, we are interested in the effects of the temperature field on the acoustic wave propagation. The expression of the wave equation written for the acoustic pressure is obtained as follows.

First, we consider the balance equation of the enthalpy per unit mass (Eq. 5.11) given

by:

$$\rho\frac{dh}{dt} = \frac{dP}{dt} - div(-\lambda_c \mathbf{grad}T). \tag{5.11}$$

By using Eq. 5.10 it can be rewritten as:

$$\frac{1}{T}\frac{dT}{dt} = \frac{1}{T}\left[\frac{1}{\rho c_p}\frac{dP}{dt} + \frac{1}{\rho c_p}div(\lambda_c \mathbf{grad}T)\right] \tag{5.12}$$

In parallel, the ideal gas law $P = r_g T\rho$, is introduced with r_g the specific gas constant. By performing its material derivative, the following expression is obtained:

$$\frac{1}{P}\frac{dP}{dt} = \frac{1}{\rho}\frac{d\rho}{dt} + \frac{1}{T}\frac{dT}{dt} \tag{5.13}$$

Substituting for the temperature term from Eq. 5.13 and for the density term from the mass conservation equation $((1/\rho)(d\rho/dt) + div\boldsymbol{v} = 0)$ into Eq. 5.12 gives:

$$\frac{1}{P}\frac{dP}{dt} + div\mathbf{v} = \frac{r_g}{c_p P}\frac{dP}{dt} + \frac{r_g}{c_p P}div(\lambda_c \mathbf{grad}T) \tag{5.14}$$

From the thermodynamic relations $c_p - c_v = r_g$ and $\gamma_g = c_p/c_v$, the following classical relationship is obtained:

$$\frac{r_g}{c_p} = 1 - \frac{1}{\gamma_g} \tag{5.15}$$

Using this result leads to:

$$\frac{1}{\gamma_g P}\frac{dP}{dt} + div\mathbf{v} = \left(1 - \frac{1}{\gamma_g}\right)\frac{1}{P}div(\lambda_c \mathbf{grad}T) \tag{5.16}$$

Secondly, by considering the Euler equation for a perfect fluid along with the ideal gas law, the momentum equation can be expressed as:

$$\frac{d\mathbf{v}}{dt} = -\frac{1}{\rho}\mathbf{grad}P = -\frac{r_g T}{P}\mathbf{grad}P = -\frac{c^2}{\gamma_g}\mathbf{grad}\left[ln(P)\right] \tag{5.17}$$

where c is the speed of sound. Assuming that the Mach number M is very small ($M \ll 1$) and that $\boldsymbol{v} = \boldsymbol{v_0} + \boldsymbol{v_1}$, with the unperturbed state velocity field $\boldsymbol{v_0} = \mathbf{0}$, the material derivative is reduced to its accumulation term:

$$\frac{d}{dt} \equiv \frac{\partial}{\partial t} \tag{5.18}$$

Taking into account the latter hypothesis, Eq. 5.16 and Eq. 5.17 can be rewritten as follows:

$$\frac{1}{\gamma_g}\frac{\partial ln(P)}{\partial t} + div\mathbf{v} = \left(1 - \frac{1}{\gamma_g}\right)\frac{1}{P}div(\lambda_c \mathbf{grad}T) \tag{5.19}$$

$$\frac{\partial \mathbf{v}}{\partial t} + \frac{c^2}{\gamma_g}\mathbf{grad}\left[ln(P)\right] = 0 \tag{5.20}$$

Calculating the time derivative of Eq. 5.19 and the divergence of Eq. 5.20, yields the following equations:

$$\frac{1}{\gamma_g}\frac{\partial^2 ln(P)}{\partial t^2} + \frac{\partial}{\partial t}\left(div\mathbf{v}\right) = \left(1 - \frac{1}{\gamma_g}\right)\frac{\partial}{\partial t}\left[\frac{1}{P}div(\lambda_c \mathbf{grad}T)\right] \tag{5.21}$$

$$div\left(\frac{\partial \mathbf{v}}{\partial t}\right) + div\left\{\frac{c^2}{\gamma_g}\mathbf{grad}\left[ln(P)\right]\right\} = 0 \tag{5.22}$$

The term in the right hand of Eq. 5.21 can be neglected, as given by the dimensional analysis proposed by Kotake [112]. So performing the difference between Eq. 5.21 and Eq. 5.22 leads to:

$$\frac{1}{\gamma_g}\frac{\partial^2 ln(P)}{\partial t^2} - div\left\{\frac{c^2}{\gamma_g}\mathbf{grad}\left[ln(P)\right]\right\} = 0 \tag{5.23}$$

Pressure P is linearized as the sum of the uniform unperturbed-state pressure (P_0) and small terms of higher order of magnitude such that:

$$P = P_0 + p(x,t) + O(2) \text{ with } p \ll P_0 \tag{5.24}$$

The acoustic pressure perturbation $p(x,t)$ characterizes the acoustic wave relative to the initial state of the gas through which it propagates. These latter considerations about pressure implies that:

$$ln(P) = ln(P_0) + \frac{p}{P_0} \tag{5.25}$$

By means of Eq. 5.25, Eq. 5.23 can be rewritten as:

$$\frac{\partial^2 p}{\partial t^2} - div\left[c^2\mathbf{grad}\left(p\right)\right] = 0 \tag{5.26}$$

Eq. 5.26 is the expression of the wave equation given for the acoustic pressure fluctuations in the presence of whatever temperature fields. In the case of a uniform temperature field, the speed of sound is constant ($c = c_0$) and the wave equation is simplified as:

$$c_0^2\Delta p - \frac{\partial^2 p}{\partial t^2} = 0 \tag{5.27}$$

If the temperature field varies in space according to the function $T = T(x)$, the speed of sound is not constant anymore and evolves as $c = c_0(T(\boldsymbol{x}))$. The acoustic pressure wave equation is therefore given by:

$$\mathbf{grad}p \cdot \mathbf{grad}c_0^2 + c_0^2\Delta p - \frac{\partial^2 p}{\partial t^2} = 0 \tag{5.28}$$

The first term of the left hand of Eq. 5.28 is thus introduced in COMSOL as a monopole source term when a variable temperature field is considered. Depending on operating conditions, equations Eq. 5.27 or Eq. 5.28 have been numerically solved with COMSOL for harmonic pressure fluctuations with angular frequencies $\omega = 2\pi f_0$ in order to evaluate the acoustic response of the cavity.

5.2 Experimental and numerical cross-validation of the 2T1L mode within the cavity

The characteristics of the 2T1L resonant transverse standing acoustic field were described in previous works [67, 83], for a semi-open cavity, where the environment was unmodified by combustion. For $f_0 = f_r$, with $f_0 = \omega/2\pi$ the variable forcing frequency and f_r the frequency of the resonant mode, there exists a pressure antinode (PAN) at $x = 0$, where the phase of the pressure fluctuation is taken as the reference ($\varphi_p(f_0, 0) = 0$). Two velocity antinodes (VAN), associated to the pressure minima are placed at $x_{VA} \approx \pm L_c/4$. The phase of the pressure fluctuations $\varphi_p(f_r, x)$ around x_{VA} evolves continuously from 0 to π with $\varphi_p(f_r, x_{VA}) = 0.5\pi$ [95].

The range of forcing frequencies (f_0) is set from 0.5 to 1.4 kHz in this study. The aim is to excite the second transverse acoustic resonant mode of the cavity (2T1L) with combustion. In order to achieve this, an experimental procedure has been developed to set and recognize the 2T1L mode. This procedure requires the definition of a normalized pressure amplitude which is introduced as follows:

$$\frac{|P'|_{x,y,z}}{|P'|^{ref}_{x_i,y_i,z_i}} \tag{5.29}$$

The term $|P'|$ represents the zero to peak acoustic pressure amplitude. The term $|P'|^{ref}_{x_i,y_i,z_i}$, used for normalization in Eq. 5.29, may refer to the pressure value at a specific reference location, like the center of the cavity, or it may refer to a specific reference pressure, like a point of maximum or minimum pressure in the cavity. This will be specified where it is needed. Some specific probe positions (x_i, y_i, z_i) are:

$$(x_i, y_i, z_i) = \begin{cases} (x_1; y_1; z_1) = (0; 0; 0.025h_c) \text{ (center of the cavity, PAN)} \\ (x_1; y_2; z_1) = (0; 0.5e; 0.025h_c) \text{ (center of the cavity on the wall, PAN)} \\ (x_2; y_2; z_1) = (0.256L_c; 0.5e; 0.025h_c) \text{ (VAN location on the wall)} \end{cases} \tag{5.30}$$

The procedure is first validated without combustion and then applied to the case with the three spray flames. The simulations results in cold condition (without combustion) as well as in hot condition (representing the case with combustion) are corroborated by the experimental measurements.

5.2.1 Results without combustion

The procedure is presented through some representative examples. To find the resonant modes of the cavity, the frequency forcing f_0 is varied progressively in the range mentioned before, whilst measuring the acoustic pressure amplitude at the center of the cavity ($x = x_1$) and at the location of the velocity antinode noted x_{VA}, i.e. $|P'|_{x_1,y_1,z_1}$) and $|P'|_{x_{VA},y_1,z_1}$). The phase $\varphi_p(f_0, x = x_{VA})$ of the pressure signal at x_{VA} is defined relatively to the pressure signal at $x = x_1$ that serves as the reference ($\varphi_p(f_0, x_1) = 0$). Knowing the theoretical profile of the pressure field in the cavity, the x_{VA} location is chosen to be in the basin of pressure minima, namely $x_{VA} \approx x_2 = 0.256L_c$, when the 2T1L mode is established. The measurements have been carried out for several cavity lengths L_c. Fig. 5.3(a) shows an example at ambient temperature for $L_c = 0.8$ m. For the normalized pressure amplitude $|P'|_{x_1,y_1,z_1}/|P'|^{max}_{x_1,y_1,z_1}$ (■), the supscript "max" refers to the maximum value obtained in the frequency range of investigation. In Fig. 5.3(a) a maximum of pressure ($|P'|^{max}_{x_1,y_1,z_1}$) is found for $f_0 = 600$ Hz. At the same time and for the same frequency, at x_2, a minimum of pressure is found ($|P'|^{min}_{x_{VA},y_1,z_1}$) while the phase is $\varphi_p = 0.5\pi$ (Fig. 5.3(b)). According to these features, the highest pressure peak measured in the present frequency range can be recognized as the 2T1L resonant mode of the cavity, this is $f_r \approx f_0 = 600$ Hz.

A more complete identification of the 2T1L mode can be done by considering Power Spectral Density (PSD) at particular locations in the cavity. An example is given in Fig. 5.4 for $L_c = 0.34$ m and a frequency of the resonant mode identified at $f_r = 1020$ Hz. Experimental and numerical results are superimposed as illustrated in Fig 5.4 and serve as a cross-validation of the resonant mode identification. In addition to simulations, Fig. 5.4(a) presents experimental data for $|P'|_{x,y_1,z_1}$ obtained along the x-axis ($y = y_1$), normalized by $|P'|^{max}_{x_1,y_1,z_1}$, as well as the Power Spectral Density (PSD) in two points, i.e. where pressure oscillations are maximum ($x = x_1$, middle of the cavity) and minimum ($x_{VA} = x_2$, close to a quarter length of the cavity from the origin). The spectral intensity at the mid point shows a clear response of the pressure fluctuations at the resonant frequency f_r, whereas the first harmonic is quite negligible. Close to x_2, the spectral intensities at f_r and $2f_r$ are still observed, but they are both quite negligible. Also, it was verified that signals on both sides of a minimum were

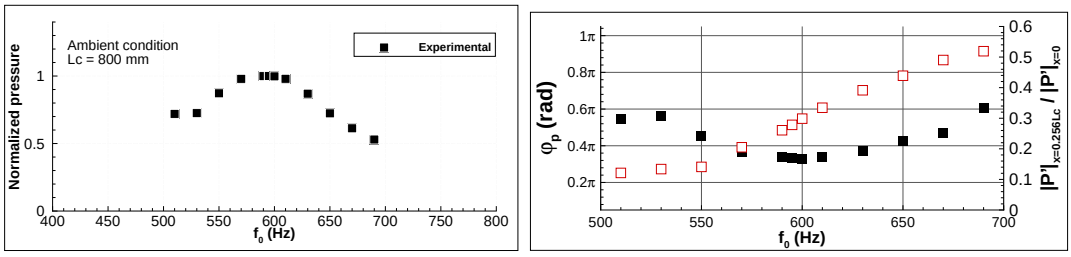

(a) (b)

Figure 5.3: (a) Normalized pressure $|P'|_{x_1,y_1,z_1}/|P'|^{max}_{x_1,y_1,z_1}$ (■). The f_r is almost equal to $f_0 = 600$ Hz; (b) normalized pressure at $x_{VA} = x_2$: $|P'|_{x_{VA},y_1,z}/|P'|_{x_1,y_1,z_1}$ (■) with phase lag $\varphi_p(f_0, x_{VA})$ (□). $L_c = 0.8$ m, without combustion, without convergent element.

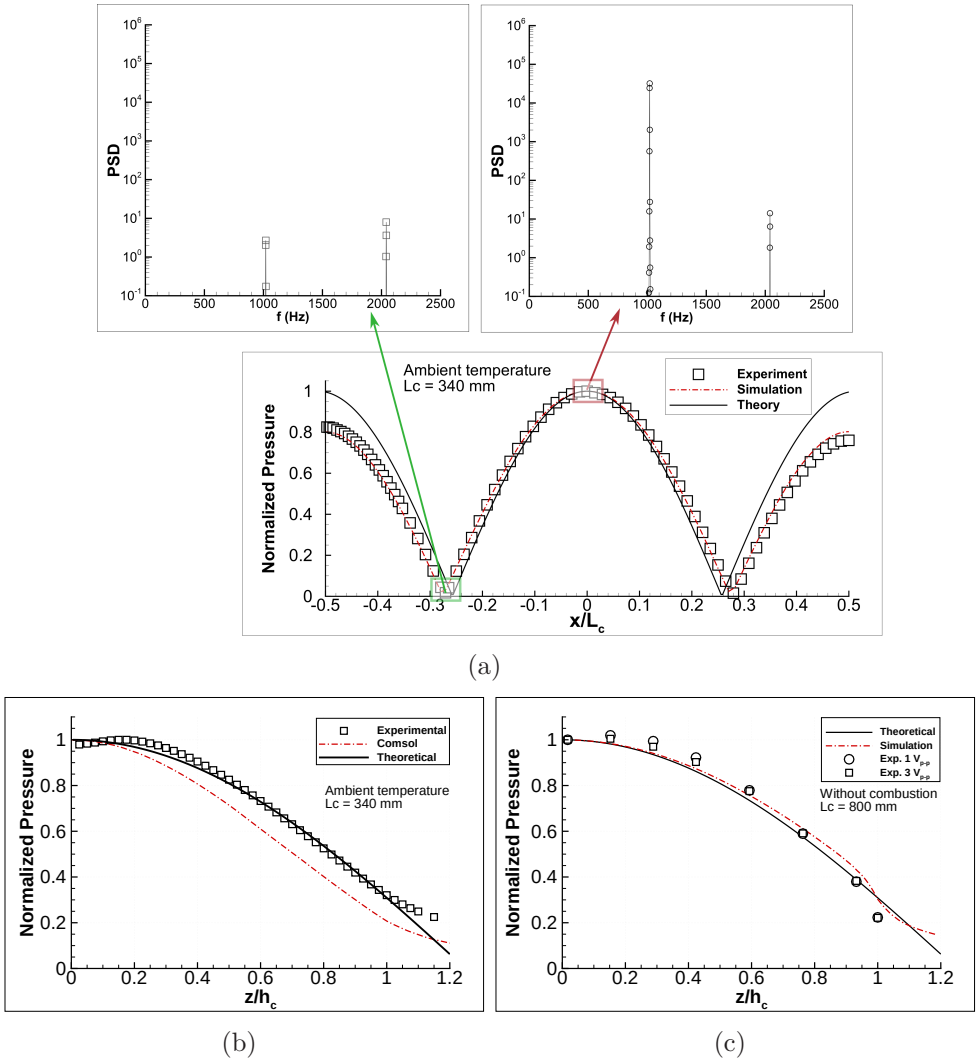

Figure 5.4: Pressure amplitude measured along: (a) x-axis (y_1, z_1, w/o convergent element) characteristic of a second order standing acoustic field; (b) without convergent element, and (c) with convergent element, both along z-axis (x_1, y_1) and showing a profile characteristic of a quarter wavelength resonator behavior. Figures (a) and (b): $f_r = f_0 = 1020$ Hz, $L_c = 0.34$ m. Figure (c): $f_r = f_0 = 555$ Hz, $L_c = 0.80$ m.

out-of-phase. This is consistent with the main characteristics of a second transverse mode of the cavity. These results indicate that the variation along x is associated with a standing wave.

Results extracted from acoustic pressure measurements performed along the z-direction ($x = x_1$, $y = y_1$) indicate that the variation is caused by a superimposition of a quarter wavelength resonator behavior. Measurements along the z-direction have been carried out with and without the convergent element and the results are reported in Fig. 5.4(c) and 5.4(b) respectively. These figures show that the quarter wavelength behavior is maintained in both cases, indicating that the presence of the convergent element does not modify the acoustic boundary condition at the top of the cavity. For the case with convergent element, two acoustic forcing levels have been tested: one for a pressure

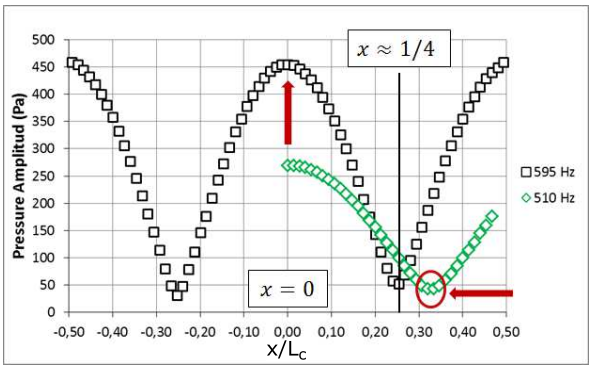

Figure 5.5: Acoustic pressure field evolution when f_0 approaches f_r.

amplitude of 620 Pa, and the other one for a maximum pressure amplitude of 1470 Pa, both at $(x, y, z) = (x_1, y_1, z_1)$. The quarter wavelength mode is well excited in both cases, regardless the acoustic forcing level. For the same L_c, when the convergent element is added at the top of the cavity, the 2T1L mode resonant frequency decreases compared to the case without it, since the cavity height is higher. Measurements along the z-direction also indicate that the pressure amplitude is virtually constant up to $z/h_c = 0.3$, which is a distance greater than the height of the flames[2] (of about $z/h_c = 0.24$ corresponding to $z/D_{exit} = 6$). Moreover, it has been verified that $|P'|_{x_i,y,z_1}$ is constant in the y-direction for any given pair of coordinates (x_i, z_i).

Additionally, simulation data with and without convergent element, well match with experimental data and corroborate the recognition of the 2T1L mode (see Fig.5.4). The discrepancy close to $x/L_c = \pm 0.5$, in the illustration case of Fig. 5.4(a), comes from the presence of the compression drivers mounted on the side walls, which deviates the response from a pure closed resonator in the x-direction.

To fully complete the acoustic mode identification, the theoretical acoustic pressure amplitude, characterizing the mode 2T1L, whose frequency is expressed by Eq. 5.31, is compared to the above-mentioned experimental and numerical data. Wavenumber components k_x, k_y, k_z in Eq. 5.31 are defined by $m_x = 2$, $m_y = 0$ and $m_z = 0$, respectively. The theoretical frequency obtained, taking $c_0 = 343$ m/s, for the case with $L_c = 0.8$ m and without convergent element ($h_c = 0.2$ m, $h_{CP} = 0$) is $f_{2,0,0} = 606$ Hz, while experimentally we have found f_r between 590 and 600 Hz. For the same L_c and with convergent element ($h_c + h_{CP} = 0.26$ m) we find $f_{2,0,0} = 541$ Hz while experimentally we have found f_r in the range of 540 to 555 Hz.

$$f_{m_x,m_y,m_z} = c_0(T)\left[\left(\frac{m_x}{2L_c}\right)^2 + \left(\frac{m_y}{2e}\right)^2 + \left(\frac{2m_z+1}{4(h_c+h_{CP})}\right)^2\right]^{1/2} \tag{5.31}$$

The theoretical solution presented in Fig. 5.4 (solid lines) agrees satisfactorily well with experimental data, confirming that the excited mode is the 2T1L of the cavity leading to the generation of the associated transverse standing wave. The addition of the convergent element at the top of the cavity does not change the **open** boundary

[2]A discussion about the flame compactness is presented in section 5.3

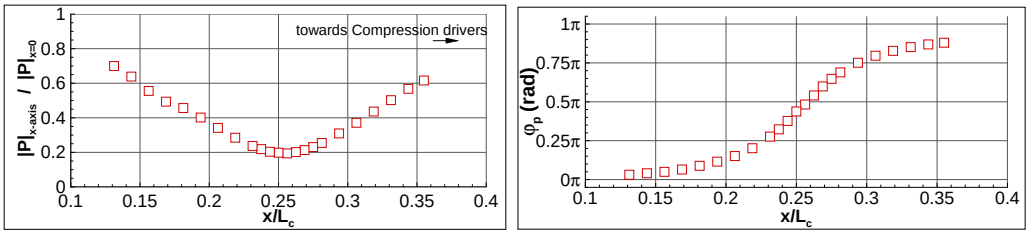

(a) (b)

Figure 5.6: Acoustic pressure field measured in the near vicinity of the pressure minimum along the line $y/e = 0, z/h_c = 0.025$: (a) pressure amplitude reduced by the maximum: $|P'|_{x,y,z}/|P'|^{max}_{0,y,z}$; (b) phase lag $\varphi_p(f_r, x/L_c)$. $f_r = 600Hz$, case without combustion, $L_c = 0.8$ m.

condition considered for the analytic solution.

In the present study it has been noted that when the forcing frequency f_0 is varied by approaching f_r (the 2T1L mode resonant frequency), the minimum of the pressure amplitude moves its position (x_{min}) toward $x/L_c = 0.25$ while the pressure amplitude $|P'|_{x_1,y_1,z_1}$ in the center of the cavity grows up to $|P'|^{max}_{x_1,y_1,z_1}$. This is indicated by the red arrows in Fig. 5.5, reporting an illustration of this behavior for the cavity set to $L_c = 0.75$ m. During the pressure minimum's displacement, its phase always satisfies $\varphi_p(f_0, x_{min}) = 0.5\pi$.

To simplify the search and identification of the 2T1L mode, the study can be carried out in the frequency domain. $|P'|_{x_1,y_1,z_1}$ is measured in the center of the cavity while the phase ($\varphi_p(f_0, x)$) of the pressure fluctuations is measured at a point of coordinate x chosen in the vicinity of $x = 0.25L_c$ ($y = y_1, z = z_1$), located in the basin of the pressure minima, as f_0 is varied. The profile of $|P'|_{x_1,y_1,z_1}$ versus f_0 shows a maximum at $f_0 = f_r$ while the profile of the phase passes from 0 to π. In consequence, identifying a 2T1L mode is possible, provided that the two following conditions are satisfied as f_0 is varied:

1- f_0 is considered as the resonance frequency f_r when the pressure amplitude measured at $x = 0$ is maximum ($|P'|_{x_1,y,z} = |P'|^{max}_{x_1,y,z}$).

2- the phase of the pressure fluctuations ($\varphi_p(f_0, x)$) measured at any fixed point in the vicinity of $x = 0.25L_c$ (the basin of pressure minima) must vary from 0 to π.

This procedure has been corroborated with the example presented previously in Fig. 5.3. Once the frequency f_r is determined, the position of the velocity antinode (x_{VA}) can be identified by studying the response of the pressure fluctuations in the spatial domain, namely in the vicinity of $x = 0.25L_c$. It is localized where the pressure amplitude is minimum[3] with $\varphi_p(f_r, x_{VA}) = 0.5\pi$. This is illustrated in Fig. 5.6 from where we have extracted the position $x_{VA} = 0.256L_c$. The results of the procedure applied to configurations with combustion are presented below.

[3]It can be verified that this minimum is an absolute minimum among the local minima of the pressure amplitudes obtained by varying f_0.

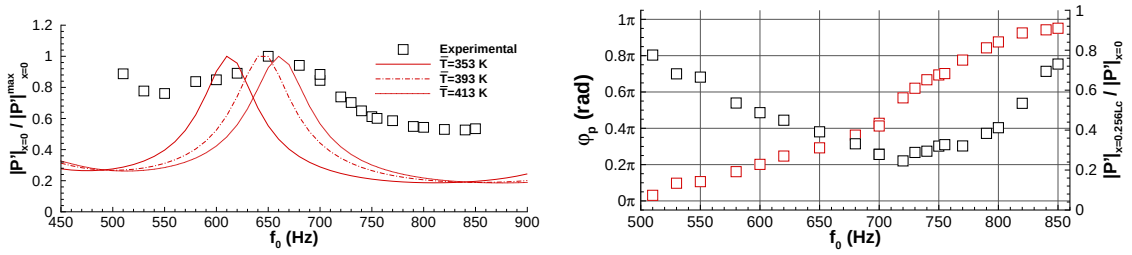

(a) (b)

Figure 5.7: (a) Normalized pressure $|P'|_{x_1,y_2,z_1}/|P'|^{max}_{x_1,y_2,z_1}$ (□), and simulations for various constant temperatures (red solid, dash dot and dotted lines). Experimental pressure peak at $f_r = f_0 = 650$ Hz; (b) normalized pressure at $x = x_2 = 0.256L_c$: $|P'|_{x_2,y_2,z_1}/|P'|_{x_1,y_1,z_1}$ (□) and phase lag $\varphi_p(f_0, x_2)$ (□). $L_c = 0.8$ m, without combustion and without convergent element.

5.2.2 Results with combustion and uniform temperature field hypothesis

The following results are given for a cavity length of $L_c = 0.8$ m, without convergent element and for operating conditions corresponding to P= 5 kW ($\dot{m}_{fuel} = 0.111$ g/s and $\dot{m}_{air} = 1.72$ g/s). Pressure is measured by implementing microphones at two specific points, $(x_1; y_2; z_1)$ and $(x_2; y_2; z_1)$. Fig. 5.7(a) shows the experimental curve $|P'|_{x_1,y_2,z_1}/|P'|^{max}_{x_1,y_2,z_1}$ versus f_0. The maximum is found experimentally at $f_0 = 650$ Hz. The ratio $|P'|_{x_2,y_1,z_1}/|P'|_{x_1,y_1,z_1}$ and $\varphi_p(f_0, x_2)$, are reported in Fig. 5.7(b) as functions of f_0. It is verified that $\varphi_p(f_0, x_2)$ varies from 0 to π and the profile of $|P'|_{x_2,y_1,z_1}/|P'|_{x_1,y_1,z_1}$ has a minimum[4]. To complete the method, an equivalent thermal system with a constant temperature $\bar{T}$ is simulated such that its pressure amplitude response to the forcing frequencies corresponds to the one obtained experimentally. For that purpose, the mean speed of sound which depends on $\bar{T}$, an unknown temperature, is increased until the frequency peak of the simulated profile coincides with the experimental peak. This is illustrated in Fig. 5.7(a) where the simulated profiles obtained for constant temperatures $\bar{T} = 353$ K, 393 K and 413 K are added to the experimental curve. The temperature leading to the good peak location, $\bar{T} = 393$ K, is congruent with measurements carried out at different points within the cavity (see Fig. 2.3). As the 2T1L mode is tuned while keeping unchanged the cavity geometry, $k = \sqrt{k_x^2 + k_y^2 + k_z^2}$ is also unchanged provided that the speed of sound is constant. Entering for $c_0(T)$ the value obtained from $\bar{T} = 393$ K in Eq. 5.31, gives $f_r = 686$ Hz, a value consistent with the experimental one.

For the same length $L_c = 0.8$ m and with the convergent element at the top of the cavity, the following results were obtained for flow rates conditions equal to $\dot{m}_{fuel} = 0.108$ g/s and $\dot{m}_{air} = 1.72$ g/s (P= 4.8 kW). The experimental curve $|P'|_{x_1,y_2,z_1}/|P'|^{max}_{x_1,y_2,z_1}$ versus f_0 presented a pressure maximum for $f_0 = 784$ Hz while $|P'|_{x_2,y_2,z_1}/|P'|^{max}_{x_1,y_2,z_1}$

[4]Here, $x_{min} = x_2 = 0.256L_c$ is the position of a local minimum associated to the forcing frequency 710 Hz, but is not the velocity antinode position x_{VA} of the searched 2T1L mode associated to 650 Hz. Here, the precise localization of x_{VA} is not looked for.

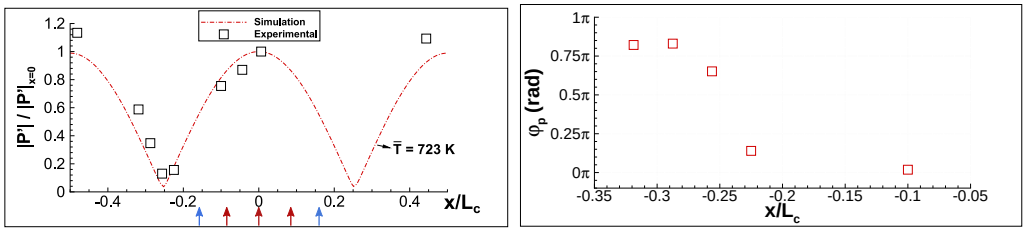

(a) (b)

Figure 5.8: Acoustic pressure field characteristics with flames: (a) Reduced amplitude measured (□) and simulated with a constant temperature $\bar{T} = 723$ K (dash dot line); vertical arrows indicate the position of flames (red) and non-reactive flows (blue). (b) phase lag $\varphi_p(f_r, x/L_c)$ corresponding to the points located in the near vicinity of the pressure minimum. $L_c = 0.8$ m, $f_r = 784$ Hz.

was minimum very close to that forcing frequency. The phase $\varphi_p(f_0, x_2)$ continuously increased from 0 to π (rad). These two results meet the conditions for identification of the 2T1L mode. As seen in section 2.1, the convergent element causes the temperature within the cavity to increase, leading therefore to a higher resonance frequency. To fully validate the acoustic mode identification, acoustic pressure fluctuations have been measured simultaneously by flush-mounted sensors placed at several points located on the front inner wall during combustion (see Fig. 5.8(a)). Pressure amplitudes show maximums at the expected positions, $x/L_c = 0$ and $x/L_c \pm 0.5$, and minimums in the vicinity of $x/L_c = \pm 0.25$. The phase $\varphi_p(f_r, x)$ measured in the vicinity of $x/L_c = -0.25$ (see Fig. 5.8(b)) varies from 0 to π with the presence of an inflection point, characterized by $\varphi(f_r, x = -0.25) \approx 0.5\pi$ (rad). Simulations performed using an equivalent thermal system with a constant temperature $\bar{T} = 723$ K agree with the experimental results. This temperature is congruent with temperature measurements made by thermocouples (see fig. 2.3).

5.2.3 Results with combustion and non-uniform temperature field hypothesis

The following results are given for a cavity length of $L_c = 0.8$ m, with the convergent element. The central flame is positioned at each of the three locations of interest (VAN, IAN, PAN). The operating conditions are equals to $\dot{m}_{fuel} = 0.108$ g/s and $\dot{m}_{air} = 1.72$ g/s, P= 4.8 kW, for the case at PAN. For the cases at VAN and IAN, the operating condition is equal to $\dot{m}_{fuel} = 0.097$ g/s and $\dot{m}_{air} = 1.72$ g/s (P= 4.3 kW). In hot conditions (with combustion), the temperature field is modified and not uniform and in consequence the speed of sound can not be considered as a constant anymore. We have studied experimentally and numerically how the 2T1L acoustic mode is influenced by the non-constant speed of sound condition. First, the temperature of the hot gases, at some points inside the cavity, has been measured by thermocouples flush mounted through the lateral walls (at several x positions for $y/e = 0.5$ and $z/h_c = 0.025$). These temperature measurements have been carried out when the injection system was positioned such that the central flame was positioned at each of the location of

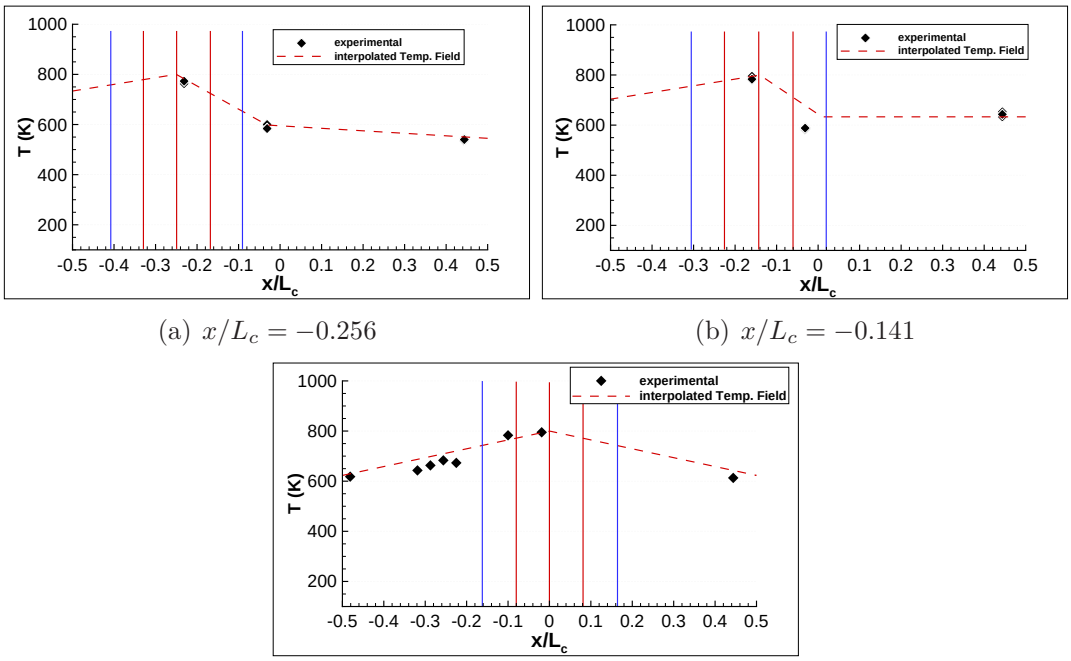

(a) $x/L_c = -0.256$ (b) $x/L_c = -0.141$

(c) $x/L_c = 0$

Figure 5.9: Temperature fields within the cavity, defined according to some experimental temperature measurements, depending on the position of the flames. Injector system at the basin of influence of VAN (a), IAN (b) and PAN (c). The vertical lines correspond to the position of the five swirling injectors: blue lines are non-reactive, red lines are reactive. $L_c = 0.8$ m.

interest. Taking these measurements as a reference, for each case we have defined a temperature field as a function of the position of the flames within the cavity. The temperature fields and the experimental temperature measurements are presented in Fig. 5.9 for each location, namely the basin of influence of VAN ($x/L_c = -0.256$), IAN ($x/L_c = -0.141$) and PAN ($x/L_c = 0$). In this figure, the vertical lines indicate the position of each swirling injector. The blue lines correspond to the stabilization non-reactive flows while the red lines represent the injectors with a flame. These temperature fields are used for simulations, considering the speed of sound as a function of the temperature $c_0(T)$.

Results of the simulation are presented in Fig. 5.10. Experimental measurements of the pressure amplitude performed at particular positions x and $y/e = 0.5$, $z/h_c = 0.025$, are also presented in the same figure for each case[5]. These experimental measurements indicate that the 2T1L mode is always well established. The pressure signals measured at $x/L_c = -0.48$ are out-of-phase relatively to the pressure signal measured at $x/L_c = 0$ for the three cases. Also at $x/L_c = -0.48$, the pressure amplitude is between 1 and 1.2 times the pressure amplitude at the center of the cavity as usually. An exception is the case at IAN where the pressure amplitude on the side wall can reach up to 1.6 times

[5]The same experimental data are used for Fig. 5.10(c) and Fig. 5.8(a), whereas the simulations correspond to the variable temperature field in Fig. 5.10(c) and to a constant temperature field in Fig. 5.8(a).

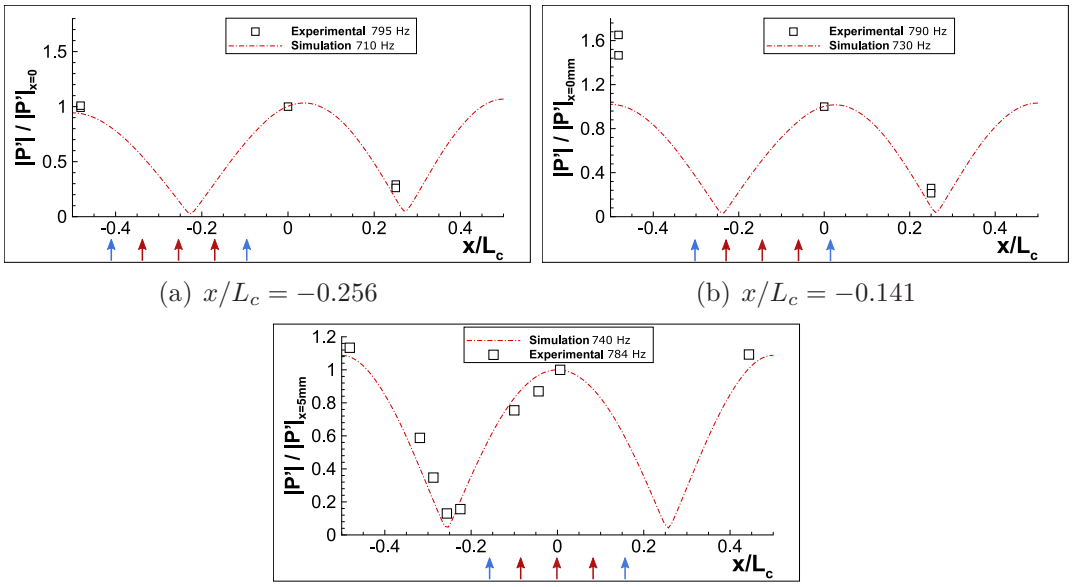

(a) $x/L_c = -0.256$ (b) $x/L_c = -0.141$

(c) $x/L_c = 0$

Figure 5.10: Experimental measurements of the pressure acoustic field within the cavity for three positions of the injection system, with the central flame at the basin of influence of VAN (a), IAN (b) and PAN (c) respectively. The arrows correspond to the position of the five swirling injectors: blue arrows are non-reactive air-flows, red arrows are the flames. $L_c = 0.8$ m. Simulations (dash dot line) are made using the temperature field defined in Fig. 5.9.

the amplitude measured at the center of the cavity, as the acoustic level imposed by the compression drivers is augmented. The signal of the acoustic pressure measured at $x/L_c = 0.256$, for each case, has a maximum amplitude about 0.25 times the amplitude measured at the center, so it can be considered as a minimum of pressure amplitude[6]. Also, it has been verified that the phase φ_p is close to 0.5π, therefore this position has the properties of the basin of a velocity antinode.

The absolute pressure amplitude profile obtained by simulations match fairly well with the experimental data. The resonance frequency obtained for each case is quite close to what is found experimentally. It is highlighted that in the case of PAN, the simulation curve is still perfectly symmetric with respect to the center of the cavity. However, in the case of VAN and IAN, the pressure amplitude profile is slightly deformed towards the region of lower temperatures[7], the maximum pressure amplitude is slightly deviated to the right ($x/L_c > 0$) and the two minimums of pressure amplitude corresponding to the VAN positions are slightly displaced towards the right, but this is almost negligible. These features, linked with the temperature field, can be appreciated in Fig. 5.11 that presents some of the simulated pressure acoustic profiles. Finally, it is possible to say that the central injector of the injection system is placed, for each case, at the desired basin of the acoustic field.

[6]This is not the minimum minimorum but, what we want to show is that it is placed at the basin of the pressure amplitude minima.

[7]This deformation, being very slight, seems to be accentuated in the case of VAN.

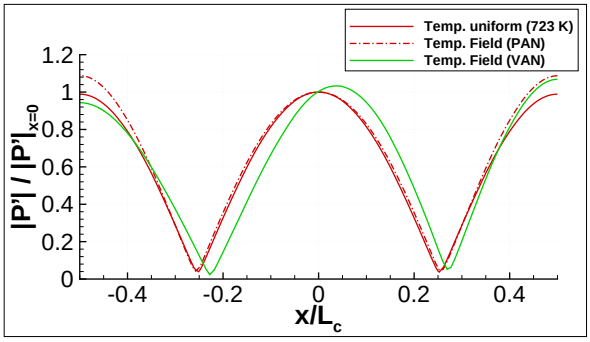

Figure 5.11: Simulated acoustic pressure profiles as a function of the considered temperature field. The profiles, taken at $y/e = 0, z/h_c = 0.025$, correspond to the cases with an uniform temperature field (solid red line), with a variable temperature field as the central injector is at PAN (dash dot red line) and at VAN (solid green line). $L_c = 0.8$ m.

5.3 Acoustic compactness of the system

The injector compactness with respect to the acoustic field is analyzed in terms of the ratio of the injector exit diameter D_{exit} to the cavity length[8] L_c, i.e. D_{exit}/L_c. In our case this ratio gives 1%, indicating that the injector is acoustically compact. This is appropriate as far as the injector is placed for instance at the basin of PAN where the acoustic disturbance is symmetric for the injector.

This criterion is no longer adequate for the neighboring injectors as the central injector is positioned at PAN, the side injectors are affected by a non-symmetric acoustic disturbance field. Therefore, the compactness should be analyzed in terms of the ratio between the injectors inter-axis distance (a_{inj}) and a half of the cavity length ($L_c/2$), i.e. $a_{inj}/0.5L_c$. The last ratio gives about 16% which can be considered as a limit value for the compactness with respect to the acoustic field. This means that as the central injector is positioned at one of the basin of influence of the acoustic field, the side injectors are also affected by the adjacent basins. An example can be found in the Fig. 6.29 of section 6.4.3, for a case with the system positioned such that the central injector is at the basin of the central PAN. It is noticeable that the flame front behavior of the central injector is not exactly the same than the motion of the left flame front. As the asymmetries of the temperature field can slightly deform the acoustic field, even if the central injector remains well positioned at the basin of interest, the influence of the adjacent basin on the side injector can be accentuated.

[8]Note that the reason of this choice is that L_c is the wavelength of the 2T resonant standing wave established in the x-direction of the cavity.

Chapter 6

Study at the pressure antinode (PAN)

The central flame is placed at the basin of influence of the pressure antinode (PAN) of the transverse field (see chapter 5). Experiments were carried out in the presence of neighboring swirling flames, such as those present in a full 360° combustor. In the following, the length L_c of the cavity, characterizing the 2T1L mode, is fixed at $800mm$. The space occupied by the two-phase flow of an injector, and by the associated flame is small compared to L_c ($D_{exit}/L_c = 1\%$) whatever the value of the resonant frequency. Thus, the two-phase flow and its flame can be considered as spatially compact relatively to the acoustic field.

In order to improve the understanding of the mechanisms driving the flame dynamics response, a detailed analysis has been performed mainly on the central flow and flame. First, the study of the gaseous air flow (n-heptane is not injected) perturbed by the acoustic forcing is presented (section 6.1). Tomography views and LDA velocity measurements were used to highlight the link between the main characteristics of the perturbed flow, namely the formation and development of coherent structures of the flow, and the pressure fluctuations, and how the formed structures are convected downstream into the flow.

Next, we present results of the investigation of the perturbed two-phase flow with combustion (sections 6.2 and 6.3). Here, tomography and LDA measurements give access to the two-phase behavior of the perturbed flow. In particular the liquid phase flow is characterized by the time-space evolution of the droplet number per surface area, the droplet distribution and the spray angle at the injector exit. These characteristics have been followed during several cycles of the acoustic forcing. A spatially averaged vertical velocity is calculated to quantify the global instantaneous modulation of the flow rate [36, 67].

When pressure fluctuation amplitudes are high enough, flames feature strong OH* (CH*) emission oscillations at the forcing frequency along the injection axis. The flame response to the acoustic perturbations is characterized by measuring OH* or CH* radicals emissions (section 6.4). Global radical flame emission signals were obtained

over time by means of a photomultiplier. In parallel radical flame emission is captured by means of either a high-speed camera able to follow the phenomenon evolution or by a slower camera from which phase-averaged data are deduced. In all the cases, the perturbed flame motion was followed or reconstructed. Moreover from these images, it was possible to extract local time or phase-averaged data. Information provided by these emissions was adequately correlated with measurements of various perturbed two-phase flow quantities, *e.g.* the gaseous flow structures or the droplet distribution. Eventually, a correlation between acoustic pressure fluctuations and flame emissions is found. It is characterized by a flame response saturation. This non-linear behavior has been already encountered in gas premixed flames, but it is highlighted for the first time in the case of spray-flames.

6.1 Air-flow behavior under acoustic forcing and without combustion

The study of the air flow without combustion provides data that help understanding its behavior during combustion. Some of its basic features without combustion will remain, even if the presence of the flame could modify specific air-flow characteristics (*e.g.* thermal expansion, stream line deviation, addition of the evaporation process).

In section 3.3, the air flow from the middle burner has been characterized without acoustic forcing. In the following subsections, the air flow is seeded with DEHS or olive oil particles. It is investigated in the presence of the acoustic forcing, corresponding to the resonant 2T1L mode, by means of tomography views and LDA velocity measurements performed at various vertical z-positions above the burner exit. As the acoustic compactness of the fluid system from any nozzle was established, the central injector located at PAN is considered to be submitted only to the influence of symmetric acoustic pressure fluctuations.

6.1.1 Air-flow structures characteristics

The air flow of the central injector (line B) is seeded with olive oil such that laser tomography images can be recorded in horizontal or axial vertical planes with a high-speed camera. This allows to follow the spatial and temporal evolution of the main structures of the air flow perturbed by the pressure fluctuations.

6.1.1.1 Flow Structure in the near vicinity of the burner exit

Horizontal views are captured in the vicinity of the exit burner at several heights (z) ranging from $0.187D_{exit}$ to $1.062D_{exit}$. All recordings are synchronized with the acoustic pressure signal measured by microphone M1 placed at the center of the cavity length, i.e. at PAN (see subsection 2.3.1). An illustration is given in Fig. 6.1 for a resonant acoustic forcing of frequency $f_r = 540$ Hz and pressure amplitude $|P'| \approx 2600$

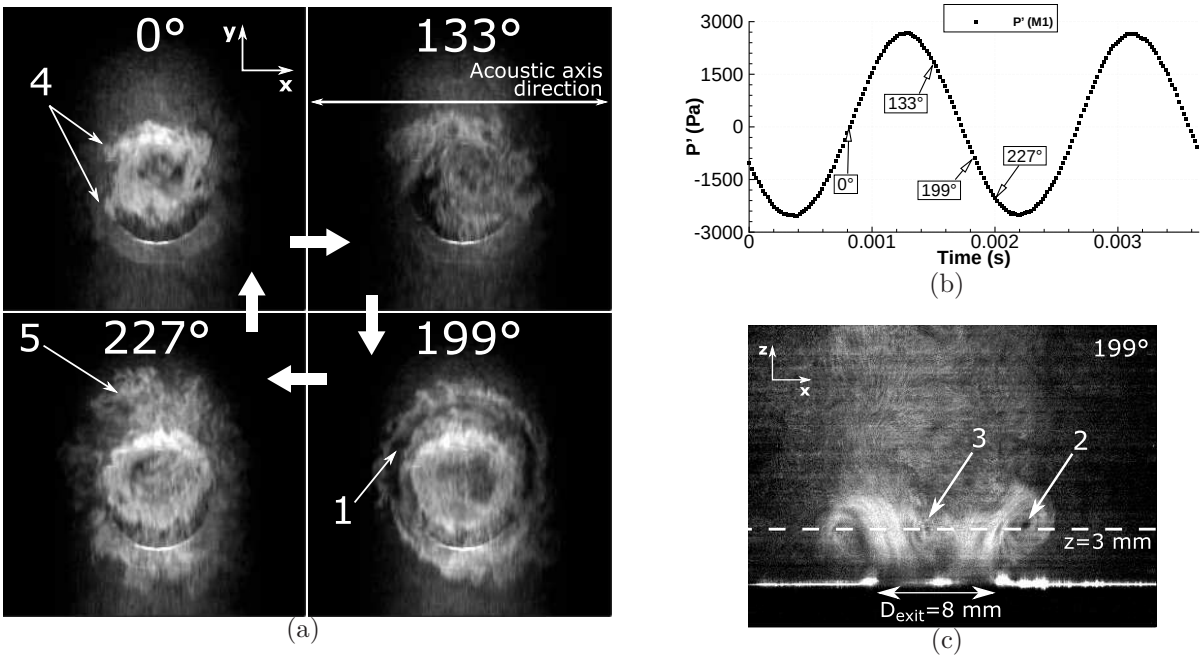

Figure 6.1: (a) Horizontal laser tomography images recorded at $z = 3$ mm ($z/D_{exit} = 0.375$) at four different times during a cycle of the acoustic forcing. (b) Synchronized pressure perturbation signal. (c) The moment of the shedding of a large torus vortex, captured by a vertical laser tomography image. Cut of the ring (1) formed by the large torus vortex, with its cross-section (2); small vortical structures (3); small streamwise vortices (4); large ejection of matter (5). $|P'| \approx 2600$ Pa, $f_r = 540Hz$, $\dot{m}_{air} = 1.72$ g/s ($U_b = 28.6$ ms^{-1}), without combustion.

Pa[1]. Instantaneous views are specified over time by their phases φ (expressed in degrees) which are labeled on the pressure signal reproduced in Fig. 6.1(b). Phase $\varphi = 0°$ is arbitrary chosen when the pressure signal is equal to 0 Pa and increasing. Four significant phases ($\varphi = 0°, 133°, 199°$ and $227°$) are chosen to present a cycle in the horizontal plane $z/D_{exit} = 0.375$, completed by a vertical view at $\varphi = 199°$. In the near vicinity of the burner exit, the jet deformation still remains axisymmetric on average, i.e. no specific direction is favored at the pressure antinode of the acoustic field. This feature was already highlighted by Baillot & Lespinasse [67], but for a laminar non-swirling jet. It was shown that it came from the action of a strong longitudinal mode induced at the pressure antinode by the transverse wave. During the forcing, several vortical structures are generated, a consequence of the adaptation of the bulk modulation of the flow to the fluctuating surrounding environment. Several structures have been identified: a large vortex ring (1 and 2), periodically ejected at the forcing frequency when the pressure fluctuations become negative enough ($\varphi \approx 199°$); small vortical structures (3) in the inner jet region initially occupied by the CRZ; streamwise vortices (4) ejected laterally, characterizing connected filaments initiated by 3D

[1]The laser sheet is introduced in the system from the top to the bottom of the image. To collect sufficient information on the camera sensor, it has been necessary to concentrate the light by avoiding a too wide sheet spreading in the **x**-direction. This induces a visual small elongation in the **y**-direction.

secondary streamwise instabilities in the outer layer of the jet. The latter instabilities are induced by the stretch of the jet, being particularly efficient by the rolling-up of the vortex ring. The formed filaments deform the jet braid (defined as the jet–air interface between two successive large vortices) and the large vortex, as explained by Demare & Baillot [113]. In addition, an agglomeration of matter fed by the filaments can form around the jet and grows (5); as it is pushed away from the jet periphery, its convective velocity is then reduced. All of the structures (1 to 5) are submitted to the swirling movement, which facilitates the destabilization of the above-mentioned averaged axisymmetry, as the jet is convected downstream. Especially, this favors the tilting of the large vortex, as also reported by Hansford *et al.* [40]. Thus in Fig. 6.1(a) (199°), only half of the annular ring is observed. This phenomenon also contributes to the vortex breaking downstream, as seen afterwards.

6.1.1.2 Downstream Flow Structure development

To complete these first observations, the air-flow behavior observed in an axial vertical plane is depicted for three acoustic pressure amplitudes: (a) 800 Pa, (b) 1400 Pa and (c) 2100 Pa at the resonant frequency $f_r = 560$ Hz. Three sequences of images are reported in Fig. 6.2 (a), (b) and (c) corresponding to the above-mentioned levels. The images serving as an illustration are extracted from series of vertical laser tomography views distributed at six instants during a cycle. An image is then marked by the number of a row (ranging from 1 to 6) and the letter of a column (a, b or c). The times are marked in Fig.6.2(d). The white horizontal line seen at the bottom of images comes from the light of the laser sheet scattered by the burner exit plate located in the bottom wall of the cavity ($z = 0$). The region of interest extends up to $z = 2.35D_{exit}$ and has an horizontal length of $3.75D_{exit}$.

General description

At the lowest amplitude (images (1-6) in Fig. 6.2(a)), if a large vortex is periodically shed, most features of the non-forcing behavior of the swirling flow still remain visible. When the vortex ring is passing, it is possible to recognize Kelvin-Helmholtz type vortices formed in the outer layer behind it. In the central zone, the double helix type vortex breakdown is periodically damaged, but not totally disrupted. Thus the double dark pattern, characteristic of the double helix, is well identified in image (2, a). The periodic perturbation does not allow the double helix to be well formed. Concurrently, some small vortices of Kelvin-Helmholtz type also form in the inner layer.

The inner Kelvin-Helmholtz vortices are better visualized at higher amplitude levels of the pressure perturbation (see Fig. 6.2(b) and (c)). In these cases the center recirculation zone (CRZ) induced by the vortex breakdown seems to be totally disrupted during the flow large vortex formation (images (1-2), b and c)). However, when the values of the pressure amplitude are still low but growing, the vortex breakdown re-appears and consequently so does the CRZ. The vortex breakdown is identified in the form of a single spiral type rather than a double helix type (images (3-4), b and c).

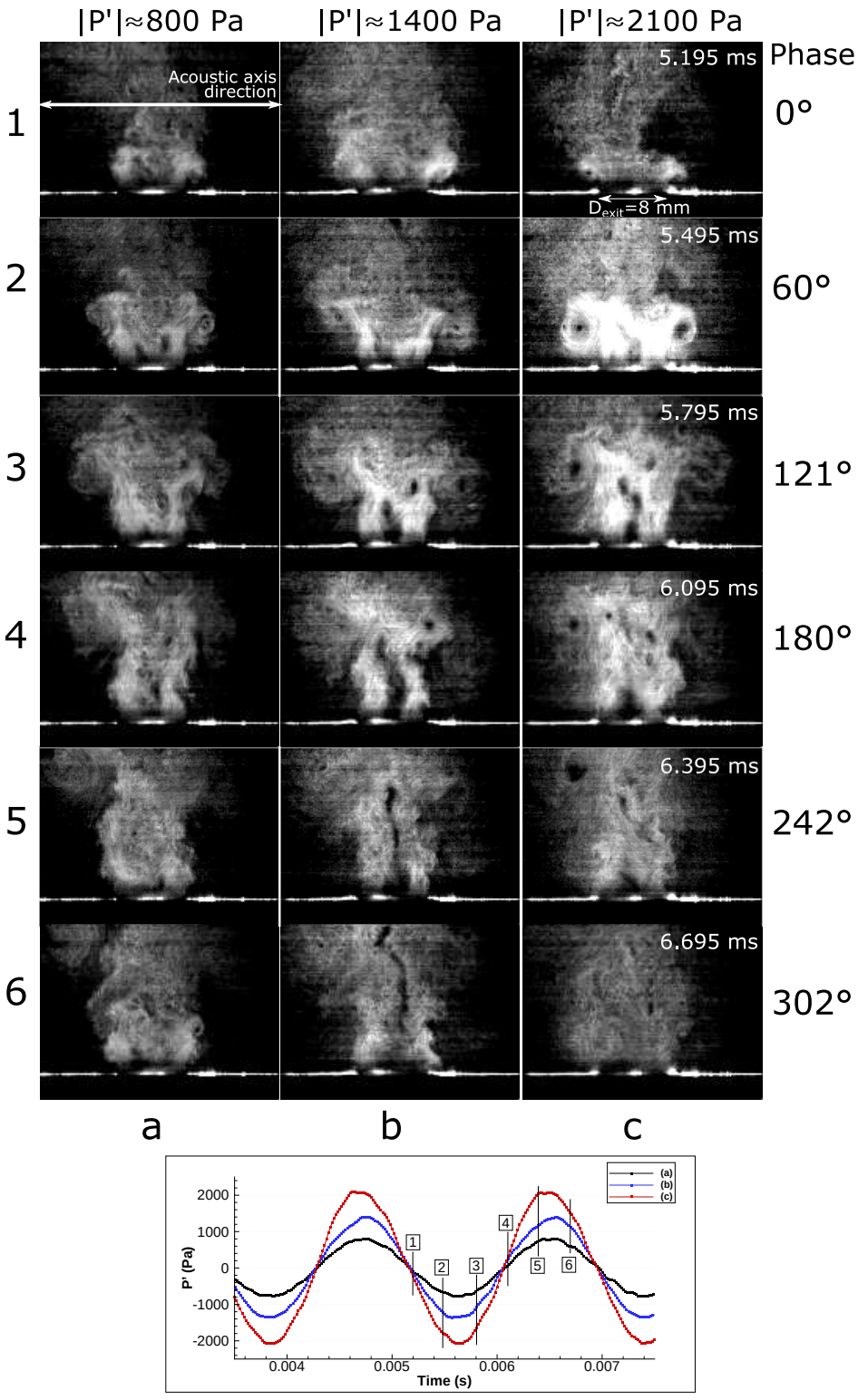

(d)

Figure 6.2: Vertical tomography views of the seeded swirling air flow during an acoustic cycle for three forcing amplitudes: (a) $|P'| \approx 800$ Pa, (b) $|P'| \approx 1400$ Pa, (c) $|P'| \approx 2100$ Pa. (d) Pressure signals of the three series corresponding to columns (a), (b) and (c). Labels 1 to 6: numbers of rows constituted of images extracted at the same phase for the 3 amplitudes. $f_r = 560Hz$, $\dot{m}_{air} = 1.724$ g/s, without combustion.

In the case of the three levels studied, the inner vortices interact downstream with the outer primary vortex. At the left side of the image (see for example image (3-5), c), an inner Kelvin-Helmholtz vortex is entrained and stretched by the outer large primary vortex, the two vortices finally merging with each other. At the right side of the image (image (3-5), c), an inner vortex that comes afterwards, impacts the outer primary vortex without any merging before it vanishes downstream. The impact leads to a faster diminishing of the strength on the right side of the primary vortex than on the left side. This scenario is noted systematically at each cycle of the acoustic forcing studied. We verified that this non-axisymmetric behavior and the outer primary vortex tilting, occur from $z = 0.375D_{exit}$ even in the presence of the axisymmetric pressure fluctuating field.

Large vortex dynamics

In an investigation of a non-reacting swirling flow by Hansford et al. [40], the authors explained the vortex tilting as a consequence of the inherent non-axisymmetric instability characteristics of the flow field. But they did not detail the mechanism by which it occurred. Indeed, the manner in which the primary vortex is tilted, impacted and which of its sides vanishes first, should be the result of a complex interaction between the characteristics of the non-forcing flow field, the swirl level and direction, the acoustic forcing frequency level, and maybe the direction of the acoustic forcing axis. Thus, in the case of spray flames, these parameters will play an important role on the flame front dynamics, and front wrinkle formation and propagation, as Acharya et al. proposed in a study on premixed swirling flames [114]. The side toward which the primary vortex is tilted and how it is impacted by the inner vortices depend on the present direction of swirl which is clockwise (seeing from the top). Therefore, in the vertical views, the flow turning motion is from the right to the left, whether the tomography plane is on the acoustic axis (as in the Fig. 6.2(a)) or not. If the swirl direction is changed while keeping the same order of magnitude of the forcing frequency, the same vortex behavior would be observed but mirrored along the injector axis.

Convection velocity of the vortex core

As mentioned by Demare and Baillot [115], by following the vertical and horizontal displacement of the core of the vortex, on high-speed vertical tomography images, one can roughly estimate its convection velocity, during its lifetime. An estimation has been made over several cycles for the three acoustic forcing levels, over 7 successive images corresponding to 0.35 ms. We find that the left side cross-section of the outer large vortex is correctly traceable until approximately $z/D_{exit} = 2.25$, where it virtually vanishes. The results give a vertical convection velocity ($U_{c,z}$) in a range of 12 to 15 m/s, and an almost negligible ($U_{c,x} \approx 0.5$ m/s) horizontal convection velocity, regardless the acoustic forcing level. Taking the bulk velocity (U_b), the convection velocity is found to follow the classical correlation given by Bernal and Roshko [116]:

$$U_{c,z} = U_b/(1 + (\rho_{air}/\rho_{jet})^{1/2}) \tag{6.1}$$

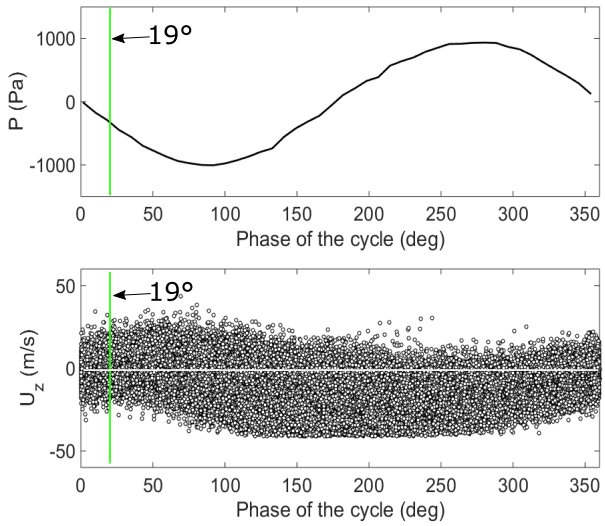

Figure 6.3: A cycle of the acoustic pressure fluctuation (top) and the phase angle of each velocity points measured by LDA defined relative to this cycle. LDA measurement made at $r/D_{exit} = 0$, $z/D_{exit} = 0.375$; $f_r = 568$ Hz.

with $\rho_{air}/\rho_{jet} = 1$ and $U_b = 28.6$ m/s Eq. 6.1 leads to $U_{c,z} = 14.3$, which lies within our estimated range from 12 to 15 m/s. Thus, the acoustic forcing level does not significantly change the dynamics of the primary vortex initiation. Instead, as seen in Fig. 6.2, increasing the acoustic pressure amplitude modifies the vortex topology[2].

Robustness of the CRZ stability

It was mentioned in section 3.3.2 that without forcing, the CRZ shows instantaneous positive vertical velocities at the nearest accessible location to the nozzle exit ($z/D_{exit} = 0.375$), even if the CRZ is defined by a negative vertical velocity on average. Here, the axial velocity measured at $z/D_{exit} = 0.375$ and $r/D_{exit} = 0$ with acoustic perturbations ($f_r = 568$ Hz and $|P'| = 1000$ Pa) is analyzed. We have recorded 4 seconds of the velocity signal, synchronized with the pressure signal. Such an analysis has been made in the presence of the acoustic perturbation, in the plane $z/D_{exit} = 0.375$. Velocity measurements are phased with the acoustic signal as done by Cala *et al.* [20], with the origin (0°) chosen arbitrarily to the time when the acoustic signal is null and diminishing (see Fig. 6.3). The recorded signal reveals a periodic modulation at frequency f_r of the statistical occurrence of positive velocities. The increase in the number of the positive values corresponds to the time-interval during which the pressure fluctuation is diminishing towards its minimum and the large vortex is formed.

In this figure we notice a cyclic variation of the velocity point cloud, governed by the forcing. At the phase angle of $\approx 19°$, measurements present the same number of positive and negative values. The ratio of the number of positive velocity to the total of measurement points is maximum around the phase angle of $\approx 44°$, i.e. 58.1%

[2]Its shape and size with time.

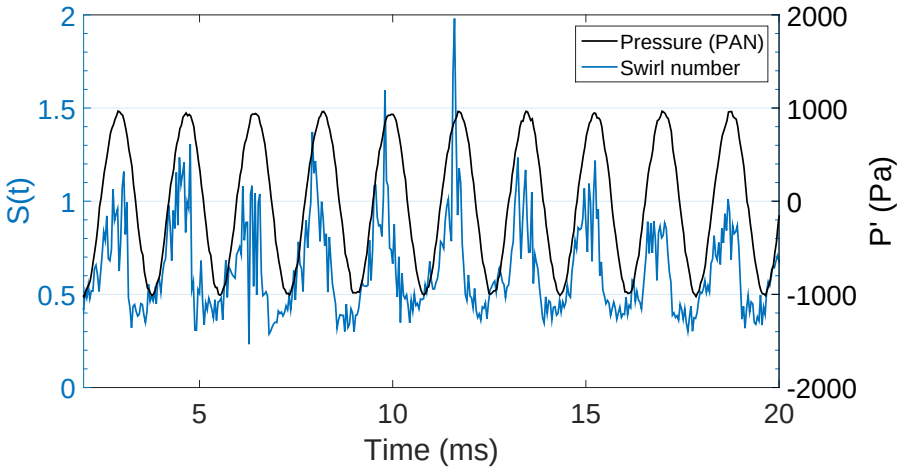

Figure 6.4: Periodic modulation of the flow swirl level at f_r. The Swirl number over time has been calculated using the LDA velocity signals measured at $z/D_{exit} = 0.375$, in the Eq. 3.7; $f_r = 568$ Hz.

and its mean value over one cycle is 17.8%. This is 4% higher than the case without forcing. These features show the competition between the natural structure of the flow and the forcing effects on it. Indeed, in the CRZ, during the time-interval when the pressure fluctuations are diminishing towards its lower values, the axial pressure gradient induced by the pressure gradient in the radial direction (this latter caused by the centrifugal force due to the azimuthal velocity component [3]), is not enough to reverse the air flow, which is strongly accelerated (see also Fig. 6.9(c)). This corresponds to the time-interval at which the large vortex is formed, seen in Fig. 6.2 (image (1-2), b-c). The periodic acceleration undergone by the air flow is dominated by the temporal fluctuation which is necessarily at the forcing frequency, while the convective component of the acceleration is $2f_r$. This is corroborated by the PSD of the velocity signals along a diametrical segment at $z/D_{exit} = 0.375$, where the PSD at f_r has always a higher peak (Fig. 6.5).

Despite the continuous presence of the centrifugal force due to the azimuthal component of the velocity field of the flow, at each cycle of the acoustic forcing, there is a time-interval of the cycle during which the swirl level significantly decreases as shown in Fig. 6.4. Thus the vortex breakdown does not occur and the CRZ is not formed. As the CRZ depends on the swirl level, its periodic disruption could explain the flame extinction shown by our team in [117]. The azimuthal velocity is weakly modulated with respect to the vertical velocity which is strongly modulated periodically (see Fig. 6.6). In consequence, the swirl number S is not only periodically diminished but also amplified. This modulation of S can lead to different types of vortex breakdown, since this phenomenon depends on the swirl level imparted to the flow, as is noted by Lucca-Negro and O'Doherty [13]. The mechanism is clearly seen within the tomography views of our air-flow under forcing, where two types of vortex breakdown seem to compete (the single spiral type and the double helix type).

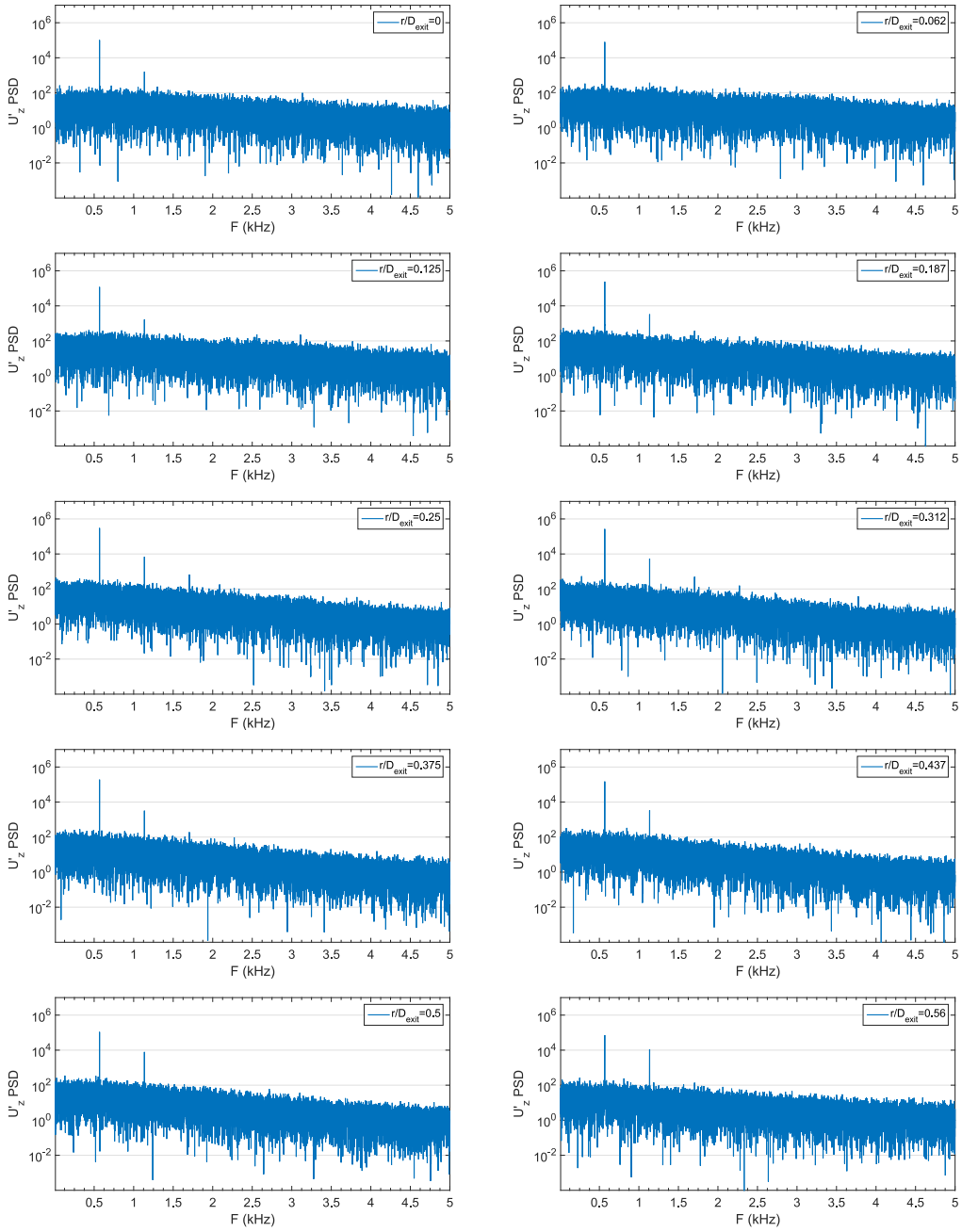

Figure 6.5: PSD of velocity signals measured by LDA at $z/D_{exit} = 0.375$ for several radial positions along a diametrical segment. $f_r = 568$ Hz.

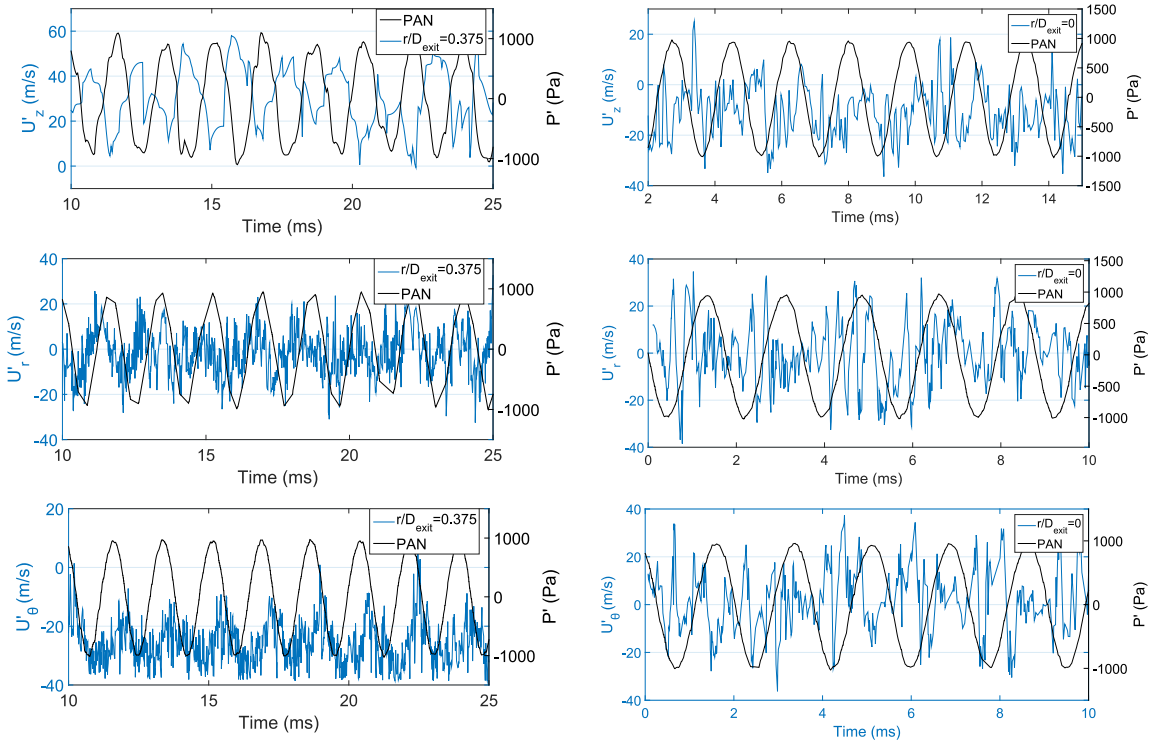

Figure 6.6: LDA velocity signals measured at $z/D_{exit} = 0.375$ synchronized with the acoustic pressure fluctuation at PAN. Left: velocity signals at $r/D_{exit} = 0.375$. Right: velocity signals at $r/D_{exit} = 0$. $f_r = 568$ Hz.

6.1.2 Kinematic behavior of the air flow

6.1.2.1 Air-flow-velocity measurements

The velocity profiles of the air flow, seeded with DEHS particles, have been obtained from LDA measurements made at $z/D_{exit} = 0.375$ and $z/D_{exit} = 0.75$ with an acoustic forcing. Fig. 6.7 shows the mean and RMS velocity profiles corresponding to the vertical (□), radial (○) and azimuthal (□) velocity components, measured for the 0-peak amplitude $|P'|$ of the pressure fluctuations fixed at 1000 Pa.

At $z/D_{exit} = 0.375$, the profile of the mean vertical velocity, U_z^{mean} exhibits a central recirculation zone (CRZ) within a region delimited by $r/D_{exit} \approx \pm 0.15$. The maximum value, of about 35 m/s, is found near of the burner lip at $r/D_{exit} = \pm 0.4$. The profile of the mean azimuthal velocity, U_θ^{mean} shows extreme values equal to 25 m/s at $r/D_{exit} = \pm 0.3$. The radial mean velocity, U_r^{mean} reaches its extreme of about 7 m/s (namely 20% of the mean vertical velocity maximum), which is not negligible, at $r/D_{exit} = \pm 0.5$. The RMS vertical velocity, U_z^{RMS} shows maximum values at $|r/D_{exit}| = \pm 0.25$. They reach a quite high value of about 20 m/s, (namely 57% of the mean vertical velocity maximum). The profiles of the azimuthal and radial RMS velocities, U_θ^{RMS} and U_r^{RMS}, reach their maximum values, of about 12 m/s, on the jet axis ($r/D_{exit} = 0$). They present two additional (little) bumps symmetrically positioned at $r/D_{exit} = \pm 0.55$.

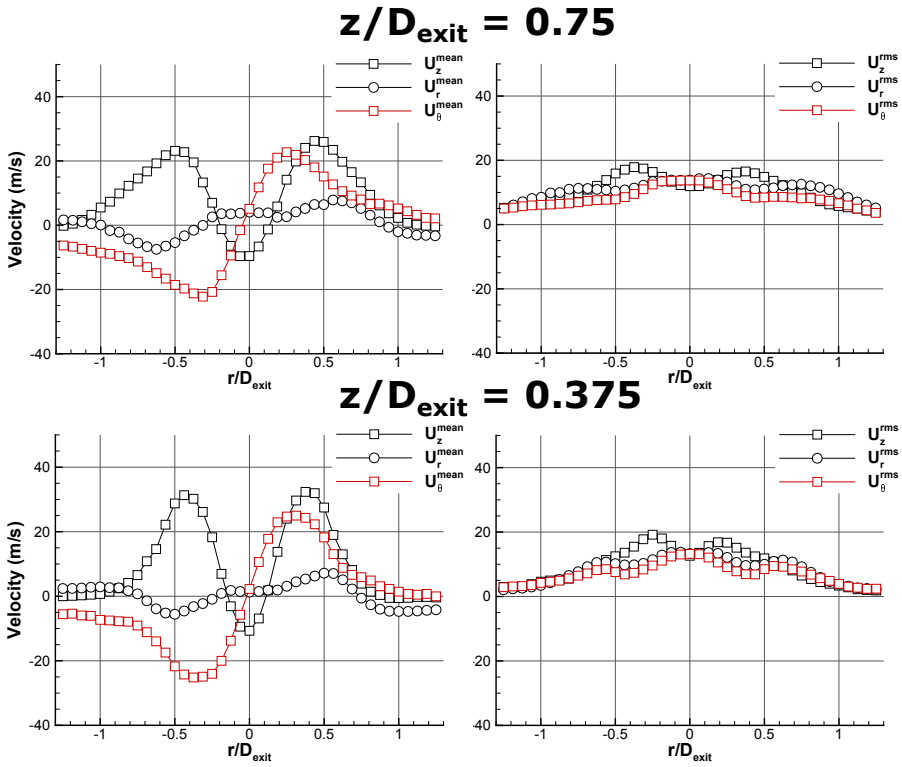

Figure 6.7: Mean (left) and RMS (right) velocities' profiles of the seeded swirling air jet made above the exit plane of the middle nozzle: U_z (vertical), U_r (radial) and U_θ (azimuthal) for $\dot{m}_{air} = 1.72$ g/s ($U_b = 28.6$ ms^{-1}) and $f_r = 568$ Hz.

These bumps are related to the passage of the large vortex, formed in the outer layer of the air flow ($r/D_{exit} = \pm 0.55$), as shown in the previous section. The positions of the mean and RMS extremes (including the bumps) positioned outside the z-axis move outward with increasing z (see results for $z/D_{exit} = 0.375$ and $z/D_{exit} = 0.75$). Moreover, the mean extreme values decrease with increasing z, which corresponds to a spreading of the jet on average while the RMS extreme values remain quite constant. It is interesting to note that although a complex structure of the flow, it persists an axisymmetric behavior on average with a slow diverging evolution.

Hereafter, these features are compared with those presented in section 3.3.1 for cold conditions without acoustic forcing at $z/D_{exit} = 0.375$ and $z/D_{exit} = 0.75$ (see Fig. 3.9). First, comparison concerns mean properties. With acoustics, profiles of all the velocity components radially spread with increasing z more than those observed without forcing. Simultaneously to the spreading, the maximums of the mean vertical and azimuthal velocities diminish while those of the radial velocity increase (for the present illustration, the maximums of the radial velocity are about doubled, reaching 10 m/s instead of 5 m/s.) The radial spreading and the modification of the maximum values are dependent on the periodic formation of the large vortex which rolls up outwardly and engulfs matter as it is convected downstream (see Fig. 6.1(c)). Secondly, the comparison with and without acoustic forcing indicates that the RMS vertical velocity largely increases with acoustics. According to this illustration, the RMS vertical velocity maximums increase from 15 m/s to 20 m/s, while the RMS radial velocity profiles are practically unchanged. This is consistent with the indirect longitudinal mode induced by a transverse acoustic field at PAN as shown in [67]. While the amplitudes of the azimuthal RMS velocity maximums are practically the same for both configurations, their radial positions differ. Indeed, under the forcing it is situated on the injector axis whatever z, whereas with no-forcing the maximum is laterally positioned at $r/D_{exit} = \pm 0.2$ beyond $z/D_{exit} = 0.375$. The RMS velocity maximum position modification is interpreted as an effect of acoustics on the vortex breakdown formation and on the induced CRZ, which are periodically disrupted as was explained in section 6.1.1.2. If the basic elements of the swirling flow are still persistent, new characteristics induced by the forcing can be noted particularly impacting the Mean and RMS vertical velocity components.

6.1.2.2 Global flow rate fluctuations

In the preceding subsections, we have visualized the jet structure by means of the tomography views. By using the velocity signals, which are measured by LDA at the burner exit and synchronized with the pressure fluctuations recorded in the cavity (at $x/L_c = -0.48$), information on the global flow rate modulated by the acoustic forcing has been calculated in the form of a spatially axial velocity averaged along the radial direction, across a diametrical segment of $1.25D_{exit}$, ranging from $r_1 = -0.625D_{exit}$ to $r_2 = 0.625D_{exit}$, at the height $z/D_{exit} = 0.375$. Its expression in a linear Cartesian approach is reported in Eq. 6.2 while another formulation in a cylindrical approach is written in Eq. 6.3:

$$< U > (t) = \frac{\int_{r_1}^{r_2} U_z(r,t)dr}{r_2 - r_1} \tag{6.2}$$

$$< U > (t) = \frac{2\int_{0}^{D_{exit}/2} U_z(r,t)rdr}{(D_{exit}/2)^2} \tag{6.3}$$

Velocity profiles for a given time t are reconstructed from LDA measurements synchronized with the acoustic forcing signal. As LDA velocity are measured randomly, the missing points are interpolated by shape-preserving piecewise cubic polynomials. Results are shown in Fig. 6.8. The spatially averaged axial velocity, reconstructed according to Eq. 6.2 (curve a) and Eq. 6.3 (curve c), is presented in the bottom of Fig. 6.8. The curve (b) in Fig. 6.8 corresponds to Eq. 6.2 where negative data corresponding to the CRZ are omitted.

The three curves evolve in phase over time. Curves (b) and (c) are quite similar in amplitude while curve (a) is shifted towards lower values. This results from the influence of the negative data when summing the velocities values along the radial direction. Indeed, the influence of the CRZ on the calculation of the curve (c) is lower than on the calculation of the curve (a) since velocities are weighted by the distance r where the measurement is performed. This is confirmed by the curve (b) for which negative data from the CRZ are omitted. The mean value of the curve

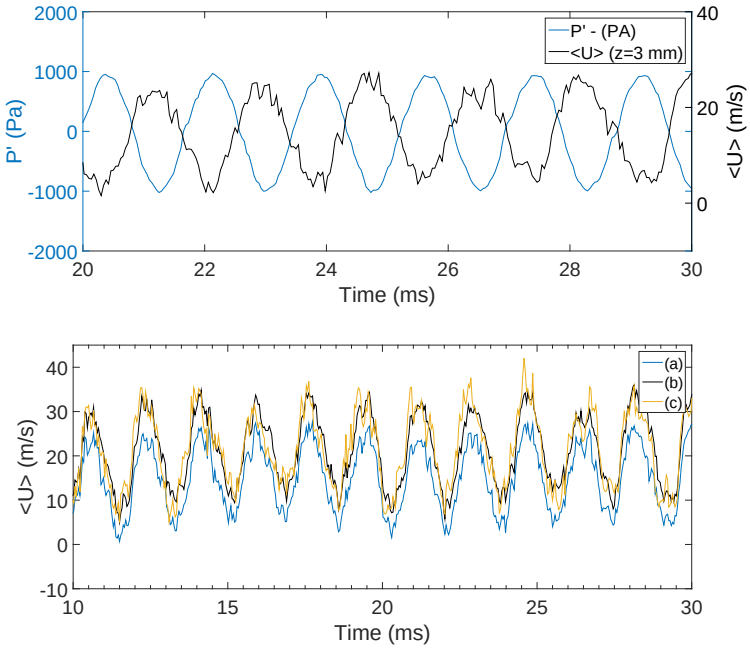

Figure 6.8: Top: pressure signal synchronized with the spatially averaged vertical velocity ($< U > (t)$). Bottom: comparison between the $< U > (t)$ velocity obtained taking into account all the points in the position range from $r_1 = -0.625D_{exit}$ to $r_2 = 0.625D_{exit}$ (line a), the velocity obtained without the velocity signals of the CRZ (line b), and the velocity obtained by Eq. 6.3 (line c). $f_r = 568$ Hz, without combustion.

(a) is $\bar{U}_{aver} = 14.5$ m/s which is consistent with the mean value of the axial velocity profile obtained by LDA (see Fig. 6.7), equal to 16.4 m/s, as was expected because the velocities of the CRZ are included. Otherwise, whatever the chosen calculations, $< U > (t)$ is well modulated at f_r. It is globally out-of-phase with the pressure signal. The coupling between the pressure fluctuations associated with the acoustic mode within the chamber and the modulation of the flow rate from the injector, is called "injector coupling" in the rocket engines literature (e.g. [58, 66]).

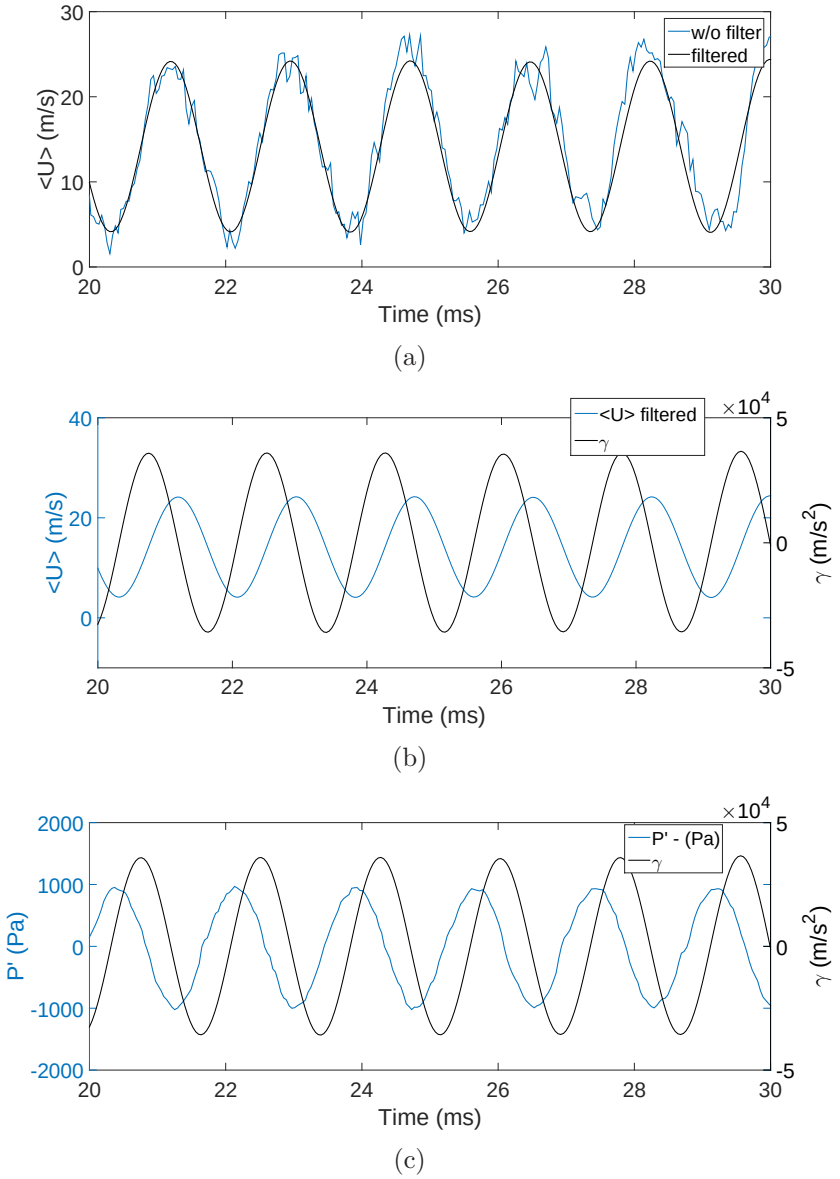

Figure 6.9: (a) Spatially averaged vertical velocity filtered around f_r and without filter. (b) Filtered, spatially-averaged vertical velocity and the acceleration (γ) obtained with this signal. (c) Pressure signal synchronized with γ. $f_r = 568$ Hz, without combustion.

From this spatially averaged velocity signal we can obtain a global acceleration signal ($\gamma(t)$) of the flow. We first apply a band pass filter to $< U > (t)$, between 518 and 618

Hz. The resulting filtered velocity is illustrated in Fig. 6.9(a). Then, we compute its temporal derivative (see Fig. 6.9(b)). The phase gap between the acceleration signal and the pressure signal is of about 70° (see Fig. 6.9(c)). The maximum acceleration is reached each time the pressure is near zero and gets negative. It is during this interval of the acoustic period that the large primary vortex is shed. As the pressure starts to grow, the flow is greatly decelerated. The flow is accelerated again when the pressure fluctuation is diminishing. This phenomenon, induced by the transverse acoustic field, is recognized as a "plugging" effect on the flow rate [67, 83, 118].

6.2 Air-flow behavior under acoustic forcing during combustion

The laser tomography technique and velocity measurements by LDA, are applied to the two-phase flow during combustion. Two kinds of two-phase flow are investigated : one with olive oil droplets seeded into the air flow, in the presence of the n-heptane droplets. The other one where only n-heptane droplets are traced. In the first case tomography images are post-treated in order to keep only the seeded air-flow pattern. The characterization of n-heptane droplet dynamics, during combustion and under acoustic forcing, will be presented in the next section.

Structures of the air flow during combustion

The evolution of the seeded air-flow pattern can be obtained after identifying and removing the fuel droplets from the high-speed horizontal tomography views recorded during combustion (for details about this procedure see section 4.2). From each image, all the pixels that form the seeded air pattern are taken into account in order to obtain a signal over time ($A_{eff}(t)$). Each point of $A_{eff}(t)$ gives a surface value (measured in pixels) linked with the amount of seeded air injected, excluding the n-heptane droplets (see Fig. 6.10(b)). A signal thus obtained is then reduced by the mean value of a signal obtained in the same way in the case without acoustic forcing. An illustration is shown in Fig. 6.10(a) from a series of 2000 images (recorded at the plane $z/D_{exit} = 0.375$) with combustion and an acoustic forcing with a pressure level of about $|P'| = 2000$ Pa. The labels (1 to 4) here correspond to the rows of Fig. 6.10(b) where the left and right column correspond to the planes $z/D_{exit} = 0.375$ and $z/D_{exit} = 1.062$ respectively.

The profile of the signal obtained is like a catenary curve. In Fig. 6.10(a), as the acoustic pressure is growing from a minimum, the values of this seeded air signal are the lowest. At $z/D_{exit} = 0.375$, a dark zone linked to the vortex breakdown can be recognized in the seeded air pattern in some cycles of the recorded series, like what was observed in 6.1.1. This is associated to the presence of the double helix pattern competing with the single spiral. This is important because it means that the swirling air-flow with combustion behaves similarly to the case without combustion.

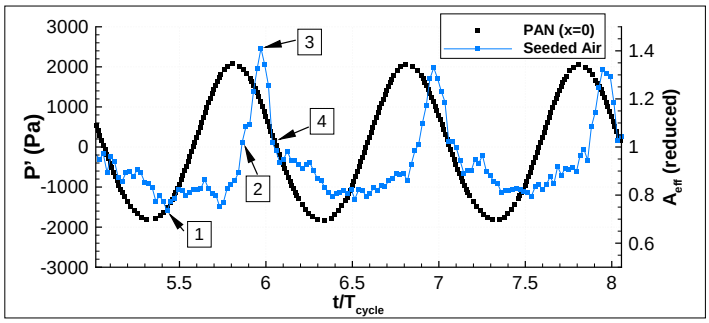

(a)

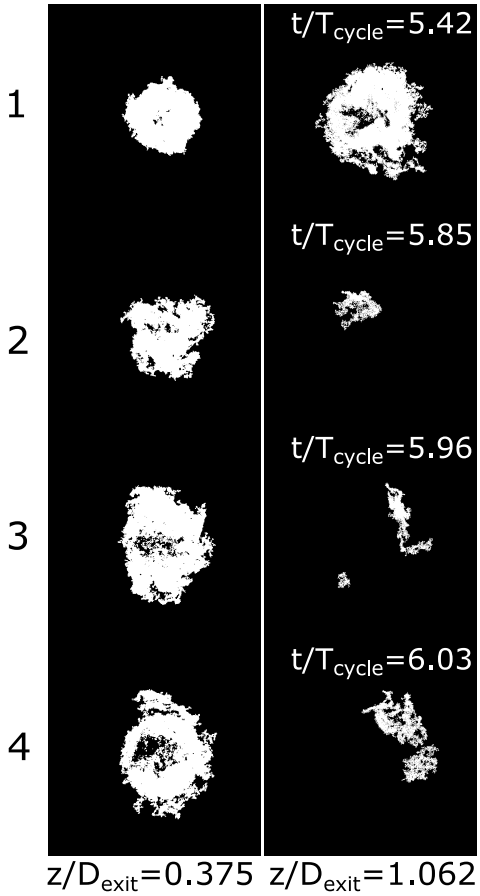

(b)

Figure 6.10: (a) $A_{eff}(t)$ signal from views recorded in the plane $z/D_{exit} = 0.375$ at the pressure antinode, reduced by the mean number of pixels forming the seeded air pattern without acoustic forcing, synchronized with the pressure perturbation signal. (b) Horizontal tomography views (recorded at 35 kfps) of the seeded air-flow pattern at four different times during a single cycle of acoustic forcing. $|P'| = 2000$ Pa, $f_r = 760$ Hz, $\dot{m}_{air} = 1.724$ g/s, $\dot{m}_{fuel} = 0.097$ g/s, $\phi_{LB} = 0.85$.

6.3 N-heptane droplets behavior during combustion and acoustic forcing

In this section, the fuel droplets are characterized during combustion, under acoustic forcing and without seeding the air flow. This characterization is made by means of the laser tomography technique, applied at various z-positions, and of LDA performed at $z = 3$ mm ($z/D_{exit} = 0.375$) above the injector exit.

6.3.1 Fuel droplet velocity measurements at the injector exit

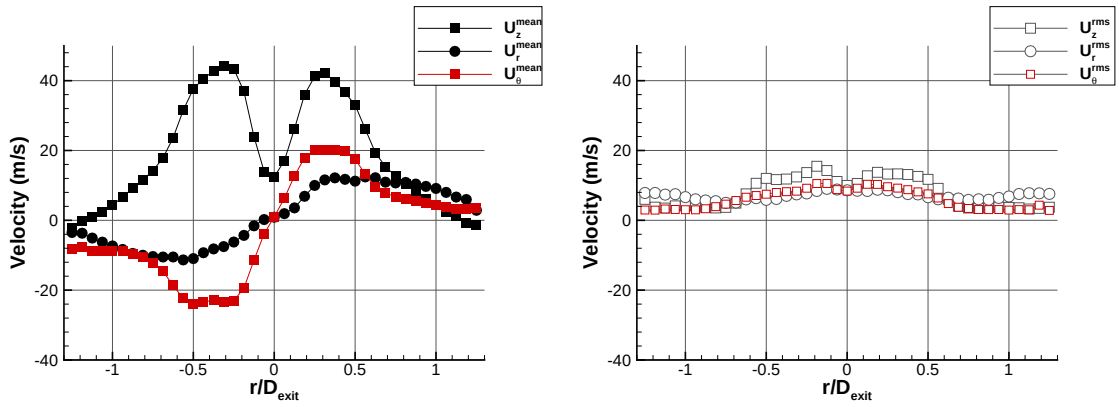

Figure 6.11: Mean (left) and RMS (right) velocity profiles measured by LDA at $z = 3$ mm from the injector exit during combustion, with acoustic forcing. $\dot{m}_{air} = 1.724$ g/s, $\dot{m}_{fuel} = 0.108$ g/s, $\phi_{LB} = 0.95$, $f_r = 765$ Hz, $|P'| \approx 2000$ Pa.

The profiles of the Mean and RMS velocities of the n-heptane droplets (Fig. 6.11), obtained by LDA, are characteristic of the swirling flow, similar to those seen previously (see Fig. 3.22 and 6.7). The vertical mean velocity maximums are positioned at $r/D_{exit} = \pm 0.3$. They reach values up to 44 m/s. In the inner region the fuel droplets do not correctly trace the CRZ region because of their size the Stokes number characterizing these droplets being about 0.9 (see Fig. 3.21(b)). The vertical mean value at $r/D_{exit} = 0$ is ≈ 16 m/s. This value is significantly higher than that of the case without acoustic forcing which is ≈ 8 m/s (see Fig. 3.22). The higher value can be explained by the periodic acceleration of the flow due to the forcing (the plugging effect) and also because the fluctuating position of the flame foot. This latter causes a faster evaporation of fuel droplets of lower size, which could better follow the CRZ dynamics, the remaining droplets having larger diameters and a more ballistic trajectory. The azimuthal mean velocity extremes are positioned between $r/D_{exit} = \pm 0.2$ and ± 0.4. Their values of about 20 m/s are virtually the same than the values without forcing. The radial mean velocity values grow from $r/D_{exit} = 0$ to $\approx \pm 0.4$, then remain almost constant until $\approx \pm 0.7$ and then decrease. The values decrease very slowly with r here compared to the radial mean velocity profile of the case without forcing.

The vertical RMS velocity profile presents two maximums positioned at $r/D_{exit} = \pm 0.2$.

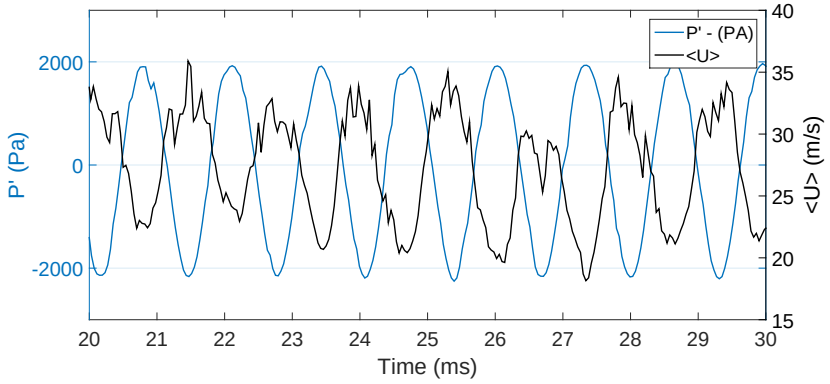

Figure 6.12: Pressure signal synchronized with the spatially averaged vertical velocity (U_{aver}), obtained from LDA measurements on the n-heptane droplets, at $z/D_{exit} = 0.375$. $\dot{m}_{air} = 1.724$ g/s, $\dot{m}_{fuel} = 0.108$ g/s, $\phi_{LB} = 0.95$, $f_r = 765$ Hz.

The maximums values ($\approx$ 16 m/s) are higher compared to the case without forcing ($\approx$ 12 m/s), but their position is the same. The azimuthal RMS velocity profile also presents two maximums positioned at $r/D_{exit} = \pm 0.2$. The position of these maximums is the same to what we have found without forcing. Their values ($\approx$ 12 m/s) are almost the same. Finally, the radial RMS velocity profile presents a maximum of $\approx$ 8 m/s at $r/D_{exit} = \pm 0.2$. This value is the same to that found in the case without acoustic. According to the mean and RMS velocity profiles presented, the vertical component is globally the most affected by the acoustic forcing.

6.3.1.1 Global modulation of the fuel droplets injection

In order to evaluate the modulation of the fuel droplet injection, we have calculated the spatially averaged vertical velocity ($< U >$), defined in Eq. 6.2, using the axial velocity signals of the fuel droplets in the radial direction, along a segment of $1.25D_{exit}$, passing through the center of the injector exit, from $r_1 = -0.625D_{exit}$ to $r_2 = 0.625D_{exit}$, at $z/D_{exit} = 0.375$. The same treatment has been applied to the velocity signals as that explained in section 6.1.2.2, and the pressure signal is used as as time reference. The result shows a periodic modulation of the fuel droplets injection at the frequency f_r. The signal $< U > (t)$ is out-of-phase with pressure (Fig. 6.12), as was in the case of the seeded air without combustion. In order to calculate the acceleration signal ($\gamma(t)$), the $< U >$ signal is filtered with a band pass filter, between 715 and 815 Hz. The acceleration ($\gamma(t)$) is in phase-quadrature with the pressure, so the droplets begin to be accelerated when pressure starts to decrease (Fig. 6.13(c)). It is worth noting that the modulation of fuel droplets injection has the same behavior with respect to the pressure fluctuation than the air-flow rate modulation seen in section 6.1.2.2.

The periodic modulation will create a periodic burst of the fuel droplets that feed the combustion process. As a consequence, the heat release rate (HRR) will be also modulated. Since the droplets start to be evaporated from the moment they enter into the chamber, the evaporation time (droplet lifetime) will intervene in the phase-lag

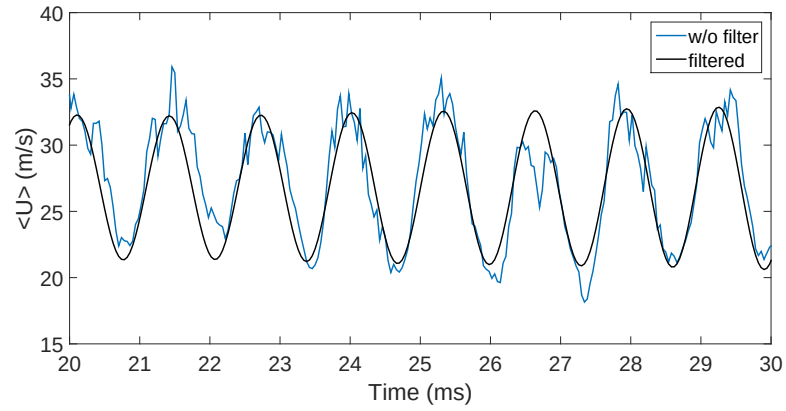

(a)

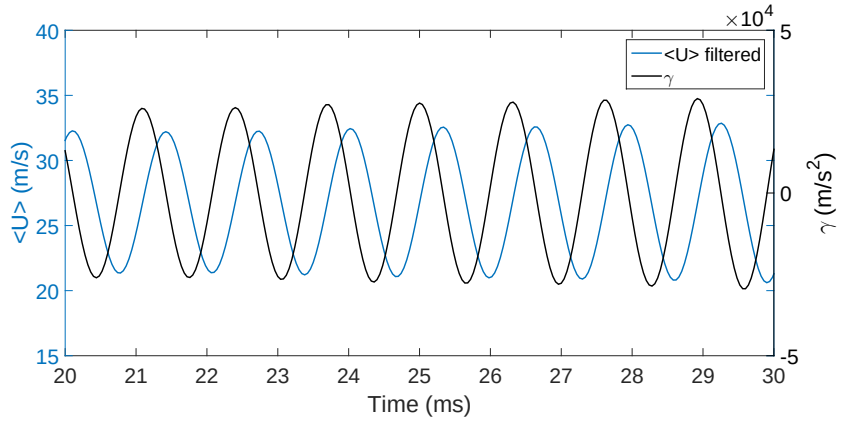

(b)

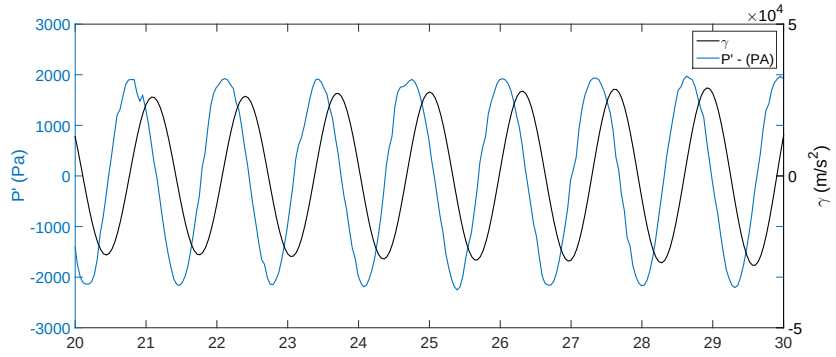

(c)

Figure 6.13: (a) Spatially-averaged, filtered (around f_r) and unfiltered vertical velocity. (b) Filtered spatially averaged vertical velocity and the acceleration (γ) obtained with this signal. (c) Pressure signal synchronized with γ. $\dot{m}_{air} = 1.724$ g/s, $\dot{m}_{fuel} = 0.108$ g/s, $\phi_{LB} = 0.95$, $f_r = 765$ Hz.

between the pressure signal and the HRR (φ). It has been shown in section 3.6.2 (see Fig. 3.26) that the spray is mostly formed by fuel droplets of small size (up to 10 μm). Considering this population of droplets within an environment of temperature $T_\infty = 713$ K, and using the evaporation model 2 of the section 3.6.2 we have estimated

a droplet lifetime of about ≈ 0.32 ms. This value could be overestimated for the case with acoustic forcing considering that the flame foot periodically goes towards the injector exit which can increments the environment temperature seen by the droplets. To the droplet lifetime it is also necessary to add the chemical time of the fuel [119]. The addition of these two times will give a characteristic combustion time. The combination of the droplet injection rate modulation and the characteristic combustion time will determine φ. Thus, there can exist a resulting time delay that could lead to a positive coupling ($cos(\varphi) > 0$) between the acoustic pressure perturbation and the HRR.

6.3.2 Temporal and spatial structuring of n-heptane droplets

6.3.2.1 Horizontal views exploration

Visualization of the injection modulation

Here, horizontal tomography views are only formed by the n-heptane droplets. The intersection of the fuel droplets with the laser sheet gives the effective droplet flow area. For each image of the series, pixels excited by the light scattered by the droplets are summed giving the effective area value (A_{eff}). Even though a pixel intensity cannot be assimilated to the signal of one droplet, the signal $A_{eff}(t)$ is linked to the number of

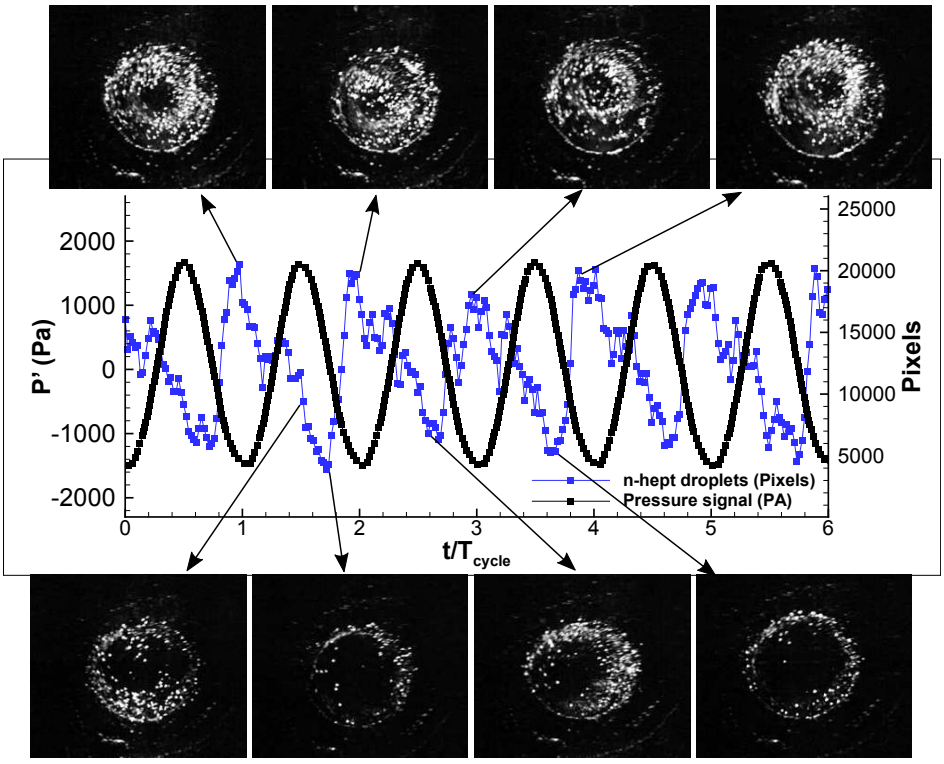

Figure 6.14: Droplets signal, obtained from tomography images at $z = 1.5$ mm ($z/D_{exit} = 0.187$), synchronized with the pressure fluctuation signal. $|P'| = 1600$ Pa, $f_r = 760$ Hz, $\dot{m}_{air} = 1.724$ g/s, $\dot{m}_{fuel} = 0.097$ g/s, $\phi_{LB} = 0.85$.

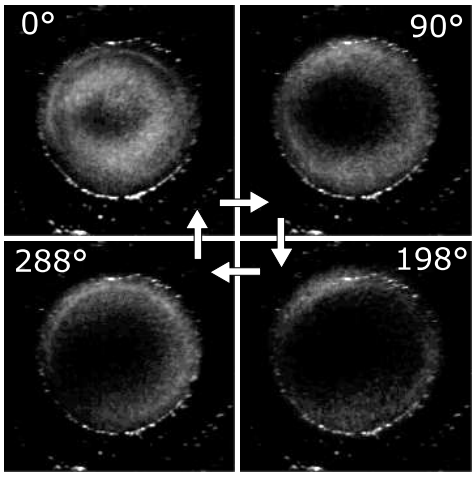

Figure 6.15: Reconstruction of a cycle of acoustic forcing perturbation by mean of phase averaged images of the droplets. Images at $z = 1.5$ mm ($z/D_{exit} = 0.187$), $|P'| \approx 1600$ Pa, $f_r = 760$ Hz, $\dot{m}_{air} = 1.724$ g/s, $\dot{m}_{fuel} = 0.097$ g/s, $\phi_{LB} = 0.85$.

droplets and it can give information on its modulation over time (see section 4.2.1). A series of 3000 images is recorded at 35000 fps with an exposure time of 10 μs. We must keep in mind that with the laser tomography applied to the droplets, the visualization of droplets with a diameter equal or higher than 20 μm is favored (see section 3.6.2). As an illustration, we plot in Fig. 6.14 the droplet signal obtained at $z/D_{exit} = 0.187$. The modulation of the droplet number is clearly noted. The images reveal that droplets almost occupy the total surface of the injector exit when the pressure reaches is lowest value. But while pressure is growing, the droplets are deviated radially outward and its number decrease. It is noted that the behavior of the signal $A_{eff}(t)$ with respect to the pressure signal is the same than that of the air-flow modulation in the case without combustion seen in section 6.1.2.2. The spatially averaged velocity $< U > (t)$ in the case of the air flow as well as $A_{eff}(t)$ both are out-of-phase with the acoustic pressure fluctuations. This means that during the time interval when the air flow is accelerated also the fuel droplets are accelerated.

The fuel droplets behavior is well reproduced over time, so it can be highlighted by means of the class-averaged images (Fig. 6.15). As the pressure is reaching its minimum value (0° on image), on average there is always a dark region in the center of the spray. This is the hollow cone characteristic of this kind of atomizer. When the droplets are accelerated the hollow cone diameter decreases, but when the pressure grows the hollow cone diameter increases until the droplets seem to vanish (see image at 198°). These images show that the droplet injection modulation is globally out-of-phase with the acoustic pressure perturbation and in-phase with the spatially averaged velocity ($< U > (t)$) obtained with the droplets vertical velocity signals (section 6.3.1.1).

Dynamics of the injection at several z-positions

The profile of the droplet signal is like a saw wave, that sharply rises and smoothly decreases. One can wonder why the signal profile is not like the catenary, as was seen

for the seeded air with combustion. A reason could be that the position of this signal is far away from the flame foot. Moving downstream the signal profile is still more like the saw wave, even though the decreasing time interval is shorter with increasing z (see Fig. 6.16). This is due to the fact that the fuel droplets visualized do not evaporate fast enough to cause the sudden decrease of $A_{eff}(t)$ periodically observed in the case of the seeded air with combustion. It was seen in section 3.6.2.1 that the visualized fuel droplets belong to a population with a diameter size greater than 20 μm, so they need to travel a longer distance to be totally evaporated. With the evaporation model 2, and considering the fuel droplets within an environment of temperature $T_\infty = 713$ K, the evaporation distance estimation gives about 40 mm . This distance can be lower if we consider that with acoustic forcing the flame foot periodically go towards the injector exit, which can impose upon the droplets a higher environment temperature than $T_\infty = 713$ K, but it will remain higher than 8.5 mm ($z/D_{exit} = 1.062$)(see Fig. 3.30(b)).

Transportation velocity and spatial structure of the spray

Another important issue is that the signals of droplets shown in Fig. 6.16 for different z-positions are not in-phase. There is a time delay between their maximums, corresponding to the time needed to information to be transported downstream. The velocity associated to this time delay is calculated by using the distance between two horizontal tomography planes, and the time delay between two maximums identified in each signal obtained in the considered planes. It is found a transportation velocity of about 30 ± 1 m/s. This is a convective velocity 5% higher than the air-flow bulk velocity ($U_b = 28.6$ m/s).

We remember that, in the case of the seeded air without combustion, the perturbation created by the acoustic forcing ($f_r = 550$ Hz) is transported with a convection velocity (≈ 15 m/s) where the large vortex passage is implicated, since this velocity

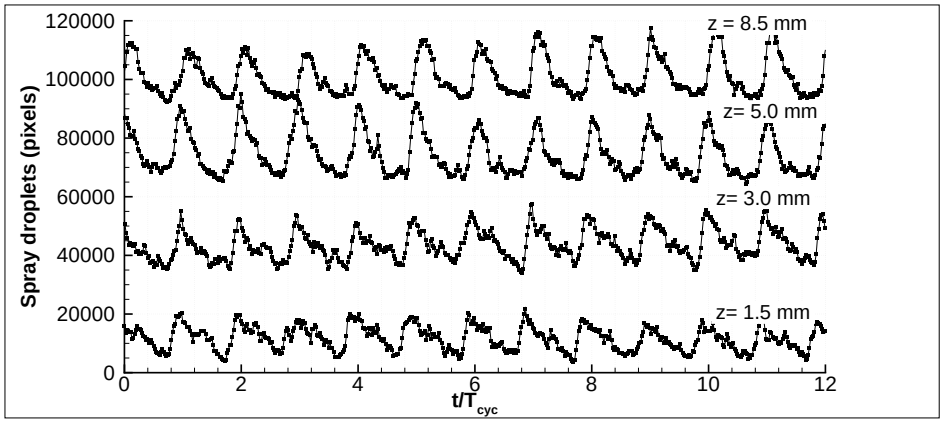

Figure 6.16: Droplets signal, obtained from tomography images at various z positions from 1.5 to 8.5 mm ($z/D_{exit} = 0.187$ to $z/D_{exit} = 1.062$), showing a phase lag between signals. $|P'| \approx 1600$ Pa, $f_r = 760$ Hz, $\dot{m}_{air} = 1.724$ g/s, $\dot{m}_{fuel} = 0.097$ g/s, $\phi_{LB} = 0.85$. Droplets signals are shifted of 30 kpixels.

corresponds also to $U_{c,z}$, the vortex convection velocity. We are going to see next that with combustion, when the air flow is seeded, it is still possible to roughly follow the vortex convection and to estimate a convection velocity. We anticipate that it has been found a velocity $U_{c,z} \approx 18$ m/s. This is a velocity value not so far from that of the case without combustion. Thus, it is expected that the large vortex passage will be implicated in the perturbation transportation in the air flow with combustion. While the perturbation in the air-flow is transported at a velocity directly linked to the vortex passage, this is not the case for the droplets visualized here at different z-positions. This could be explained by classifying the fuel droplets into three groups according to the droplet size: droplets with a size small enough such that they are rapidly evaporated; those becoming small enough to be rolled up by the large vortex; finally those with a sufficiently large size such that they are only deviated from their trajectory and follow a rather ballistic trajectory. The droplets visualized in the tomography views rather belong to the third group. Thus, the perturbed air-flow affects differently the droplets depending on their size.

It was seen that, due to the modulation mechanism during the acoustic forcing, there are periodic bursts of droplets that will modify the spray spatial structure and its evaporation process with respect to the case without forcing. We intend to globally quantify this modification by calculating a distribution of the droplets number density. The calculation is made as described in section 4.2. In Fig. 6.17(a) and 6.17(b), we present an illustration of the density signal at various z-positions, and the corresponding sliding-averaged values, calculated with a moving window of 5 cycles width and by applying an overlapping of 50%.

Without acoustic forcing we note that at the injector exit and up to $z = 5$ mm ($z/D_{exit} = 0.625$), the averaged droplet number densities have virtually the same values, varying slightly around 0.3 (Fig. 6.17(c)). At the position $z = 8.5$ mm ($z/D_{exit} = 1.0625$), the averaged density value drops down to 0.2. This may be ascribed to the expansion of the radial droplet positions and an increase of the droplet dispersion, rather than the evaporation of the visualized droplets.

With acoustic forcing, we highlight a modification of the averaged droplet number density distribution along the z-positions (Fig. 6.17(d)). The averaged density regularly decreases downstream. From $z = 1.5$ mm ($z/D_{exit} = 0.1875$) to $z = 8.5$ mm ($z/D_{exit} = 1.0625$), the values at every z-position are lower than those obtained without acoustic forcing. This indicates a regular increase of the droplets dispersion fluctuations, called δ_r and defined in section 4.2.3 as the deviation from the mid radius of the droplet spatial distribution (r_d^{mid}). The regular increase of δ_r is verified in Fig. 6.19 (see the left column). This increase can be explained by the passage of the primary vortex that deviates fuel droplets from their initial trajectories.

In Fig. 6.18, we plot over time the mid radius of the droplet spatial distribution (r_d^{mid}) defined in section 4.2.3 and in Fig. 6.19, along with the droplet position dispersion (δ_r), the evolution of the number of pixels linked with the number of droplets. By using the horizontal high speed tomography views, the evolution over time of these quantities has been computed within a rectangular region defined in each image of a series. The region extends on the acoustic axis direction, on the left and right sides of

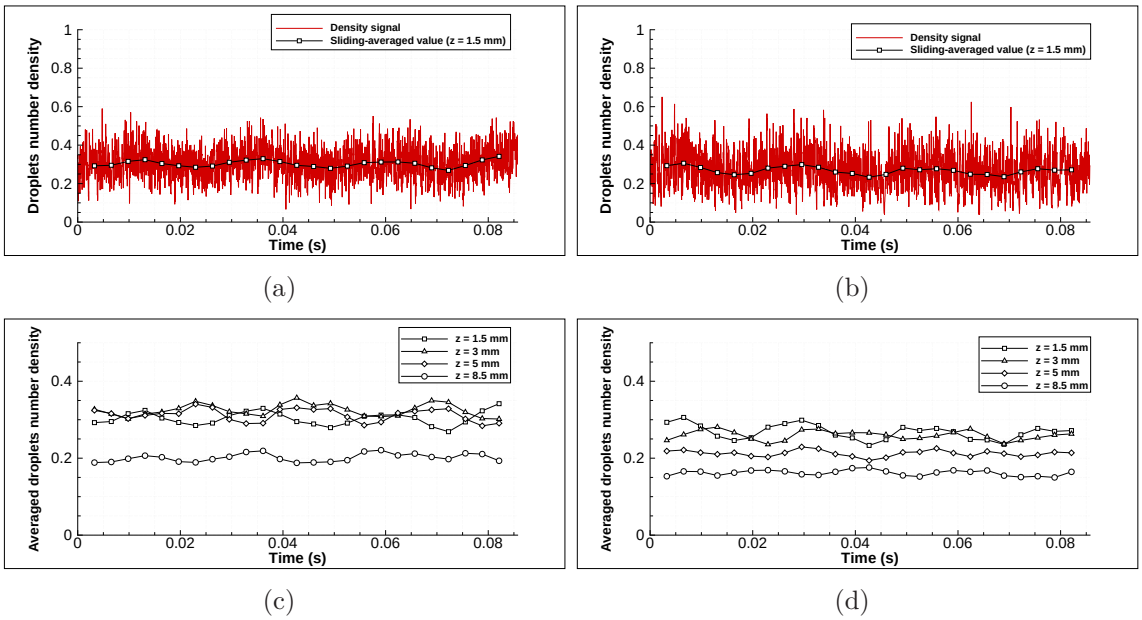

Figure 6.17: Signals of the droplets density and its sliding-averaged value, calculated from the horizontal tomography images at $z = 1.5$ mm ($z/D_{exit} = 0.1875$), without (a) and with (b) acoustic forcing. The sliding-averaged values calculated at various z positions from 1.5 to 8.5 mm, without (c) and with (d) acoustic forcing. $|P'| \approx 1600$ Pa, $f_r = 760$ Hz, $\dot{m}_{air} = 1.724$ g/s, $\dot{m}_{fuel} = 0.097$ g/s, $\phi_{LB} = 0.85$.

the injector axis (see section 4.2). The zero values in the plots of Fig. 6.18 belong to points where no droplet was detected in the region where calculation was made. These points are also zero in the plots linked with the number of pixels, and they are not accounted for in the dispersion calculation. It is noted that r_d^{mid} and the number of pixels fluctuate periodically at f_r, the acoustic forcing frequency. With z-positions, the amplitude of the fluctuation of r_d^{mid} grows with z-positions (Fig. 6.18). Moreover, by comparing the left and right sides at a given z-position, this quantity evolves globally in phase and shows the same fluctuations. It is seen that the fluctuations of the number of pixels does not change significantly along the considered z-positions (see Fig. 6.19 right column (a) to (d)). The difference in the number of pixels between the left and right side can be attributed to the asymmetries of the droplets injection inherent to the atomizer.

6.3.2.2 Vertical views exploration

In order to complete the analysis of the two-phase flow behavior, we have recorded a series of vertical tomography views of the n-heptane droplets, either with the air-flow seeding with olive oil particles or not. Because the intensity of the light scattered by the fuel droplets is higher than the intensity of the light scattered by the seeding particles, it is now more difficult to trace the seeded air structures than it was made previously without combustion. The camera parameters have been chosen (the exposure time is equal to 40 μs, and the camera speed is 20 kfps) here in order to get a satisfactory

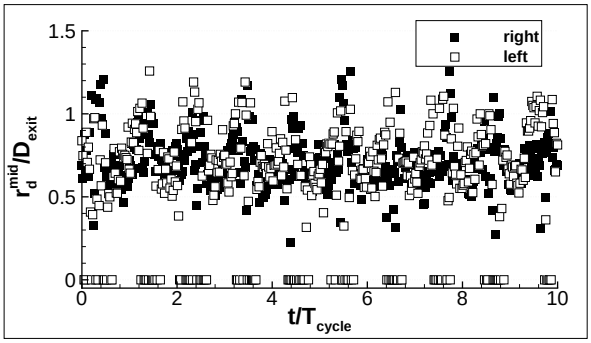

(d) $z/D_{exit} = 1.062$

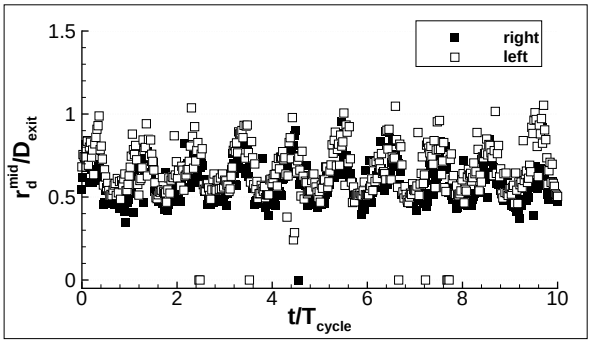

(c) $z/D_{exit} = 0.625$

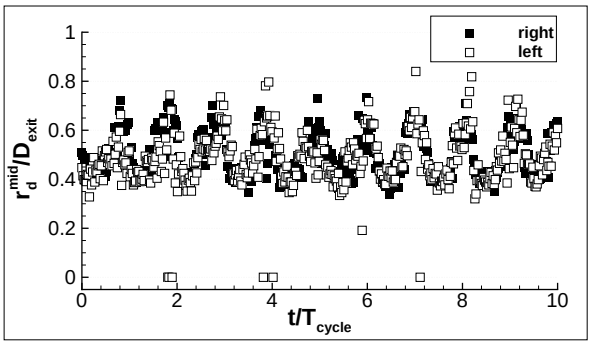

(b) $z/D_{exit} = 0.375$

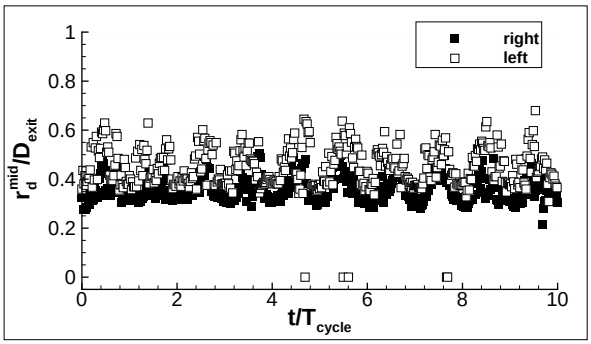

(a) $z/D_{exit} = 0.187$

Figure 6.18: Evolution of the mid radius of the droplet spatial distribution (r_d^{mid}) calculated from horizontal tomography views (for droplets size > 20 μm). Pressure-perturbation amplitude measured by M1: $|P'| \approx 1600$. Central injector at the PAN basin of influence. $f_r = 760$ Hz, $\dot{m}_{air} = 1.724$ g/s, $\dot{m}_{fuel} = 0.097$ g/s , $\phi_{LB} = 0.85$.

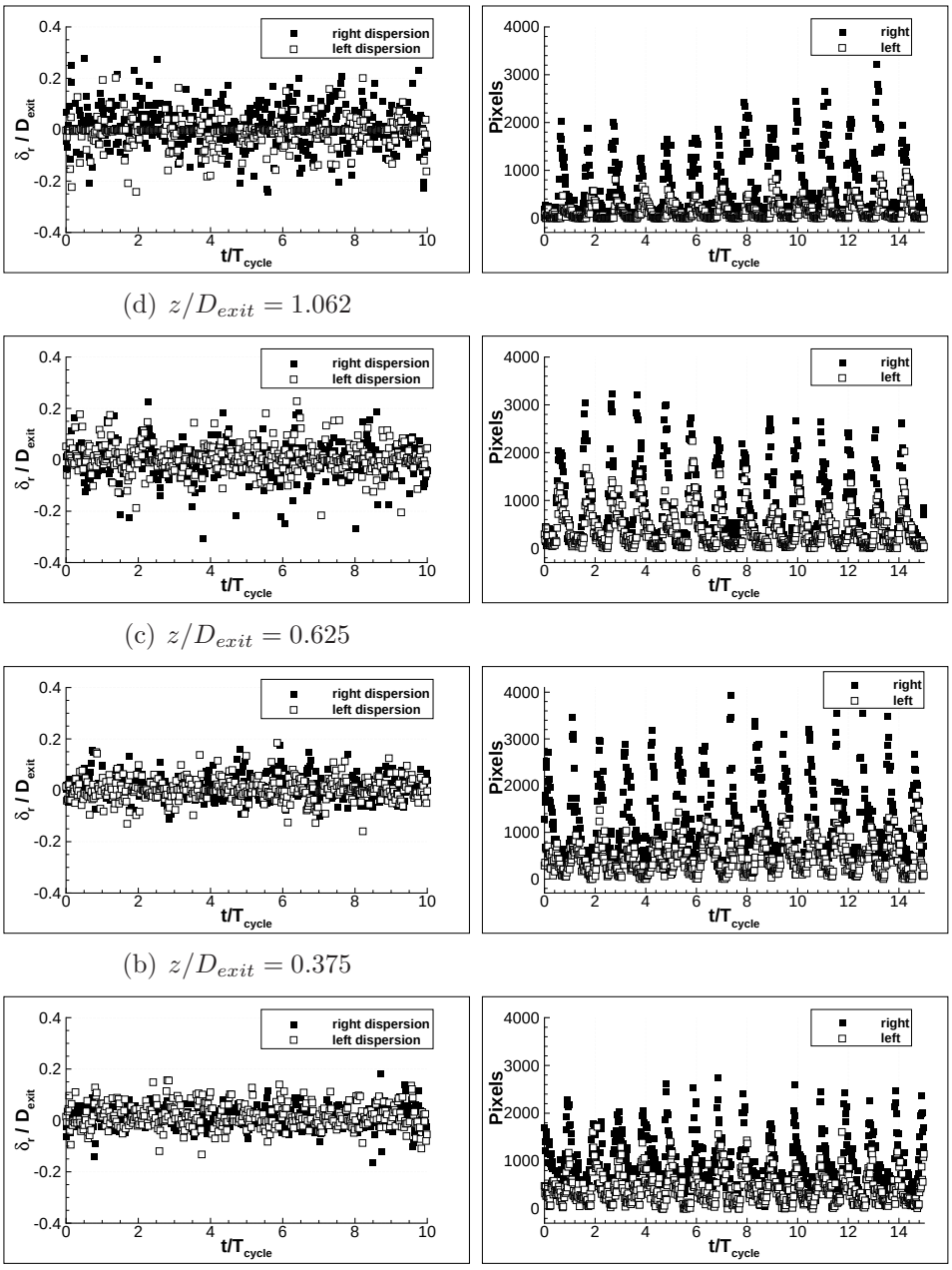

(d) $z/D_{exit} = 1.062$

(c) $z/D_{exit} = 0.625$

(b) $z/D_{exit} = 0.375$

(a) $z/D_{exit} = 0.187$

Figure 6.19: Evolution of the fuel droplets dispersion, δ_r (left column) and the number of pixels (right column) linked with the number of droplets, calculated from horizontal tomography views (for droplets size > 20 μm). Pressure-perturbation amplitude measured by M1: $|P'| \approx 1600$. Central injector at the PAN basin of influence. $f_r = 760$ Hz, $\dot{m}_{air} = 1.724$ g/s, $\dot{m}_{fuel} = 0.097$ g/s , $\phi_{LB} = 0.85$.

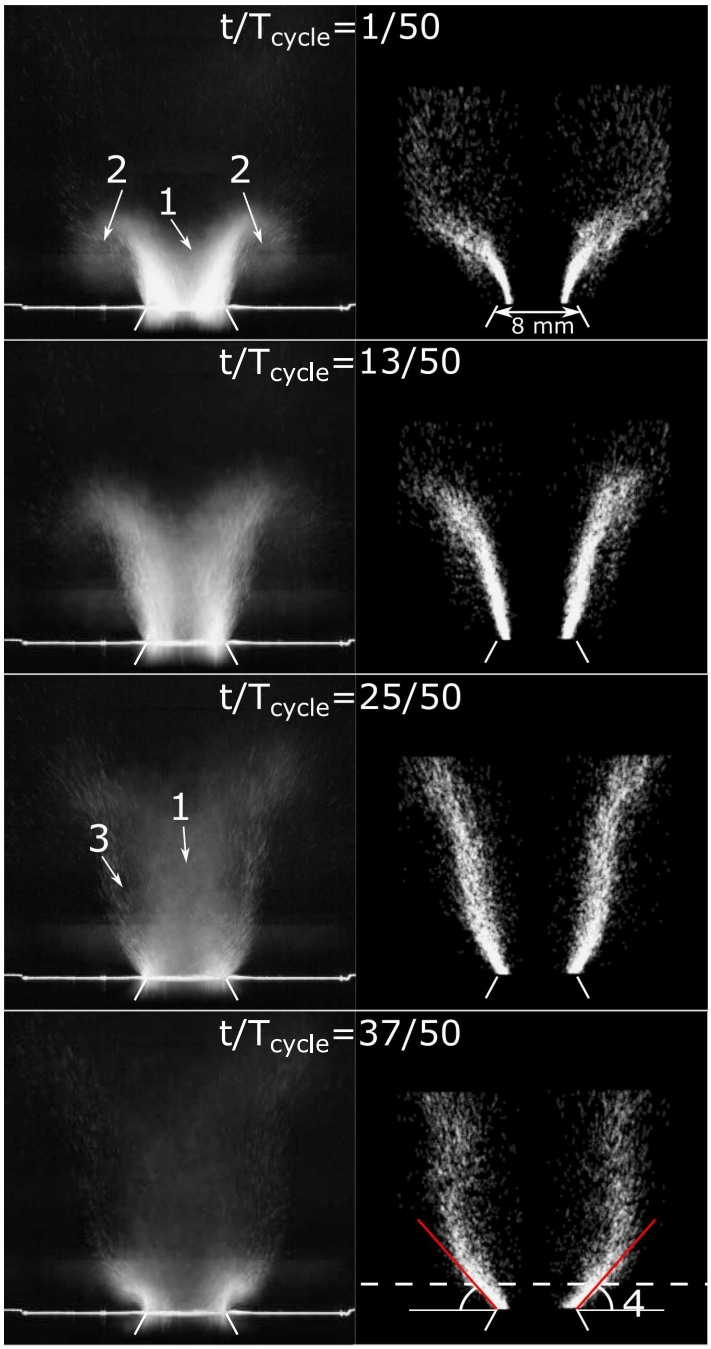

Figure 6.20: Class-averaged images at four times of the acoustic forcing cycle, obtained from vertical tomography views of the seed-air flow and n-heptane droplets during combustion: n-heptane droplets and seeded air-flow (left), droplets mid positions (right). (1) seeded air; (2) vortex ring; (3) the biggest droplets do not follow the seeded air; (4) injection angle of the droplets, calculated at $z/D_{exit} = 0.4$. $|P'| \approx 2200$, $f_r = 785$ Hz, $\dot{m}_{air} = 1.724$ g/s, $\dot{m}_{fuel} = 0.097$ g/s , $\phi_{LB} = 0.85$

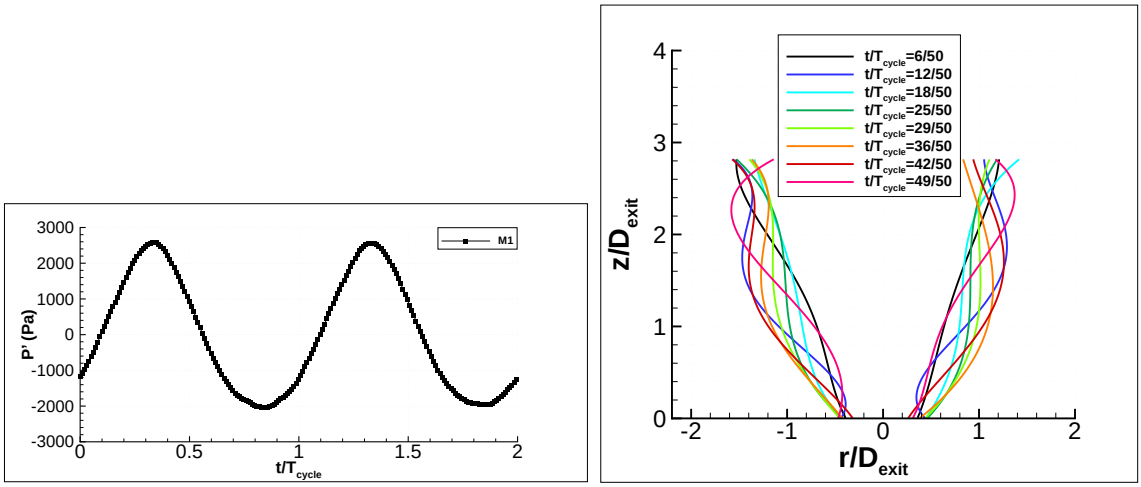

(a) (b)

Figure 6.21: (a) Pressure perturbation signal corresponding to the central PAN. (b) Droplets mid-position lines at several times of a cycle of the acoustic forcing. The central injector is positioned at PAN. f_r = 785 Hz, $\dot{m}_{air}$ = 1.724 g/s, $\dot{m}_{fuel}$ = 0.097 g/s , $\phi_{LB} = 0.85$.

visualization of both, the seeded air and n-heptane droplets. By recording a series of 2000 tomography images of the n-heptane droplets and seeded air, it is possible to reconstruct a full cycle of the acoustic forcing, calculating 50 class-averaged images as shown in Fig. 6.20. The procedure to obtain a class-averaged image is explained in section 4.1. With this procedure the visualization of the averaged image post-treatment motion of the seeded air (Fig. 6.20 left) is quite improved. In particular, the primary vortex formation can be highlighted (see the label 2 in Fig. 6.20 left). As the vortex is formed and starts to be convected downstream, fuel droplets and seeded air both evolve almost superimposed upstream the position of the large vortex (see images at $t/T_{cycle} = 1/50$ and $t/T_{cycle} = 13/50$). In the region occupied by the large vortex, the droplets are deviated from their trajectories. In the image at $t/T_{cycle} = 25/50$, it is noted that the cloud of fuel droplets (indicated by the label 3) is no longer superimposed with that of the seeded air (indicated by the label 1) which path is quite straightened compared to that of the droplets.

Mid values of the droplet's radial positions are extracted from both sides of the injector axis, by detecting the first and the last droplet in each row of the region of interest, forming the skeleton of the spray (see section 4.3) in every images of a series. A full cycle is reconstructed at the acoustic forcing frequency using 50 class-averaged images (Fig. 6.20 right) in order to enhance the visualization of the droplets motion during the acoustic forcing. Finally, a polynomial fit of these mid positions is computed for the left and right sides respectively. They are reported in Fig. 6.21(b). These fits give a simplified representation of the droplets positions along one cycle of acoustic excitation. In Fig. 6.21(a) is reproduced the pressure signal simultaneously measured with the series of images, which serves as a time base function for the cycle reconstruction.

The mid lines show that it is at the very exit of the injector that the pressure perturba-

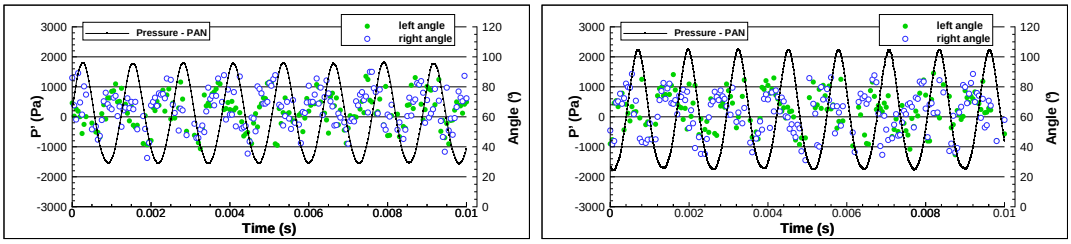

(a) (b)

Figure 6.22: Evolution of the angle of injection formed by the n-heptane droplets at the left and right side of the injector, in vertical tomography views of the n-heptane droplets, at the injector exit: (a) Pressure amplitude $|P'| \approx 1800$ Pa, and (b) $|P'| \approx 2200$. $f_r = 785$ Hz, $\dot{m}_{air} = 1.724$ g/s, $\dot{m}_{fuel} = 0.097$ g/s, $\phi_{LB} = 0.85$.

tion impacts the injection, and then this information is propagated downstream. The lower ends of the lines corresponding to times $t/T_{cycle} = 6/50$ and $t/T_{cycle} = 12/50$, are moving radially outwards when the pressure grows. Just after that, as the pressure starts to decrease, the lower ends of the lines start to be straightened. The lower end of the line corresponding to time $t/T_{cycle} = 49/50$, is straightened when the pressure value is low. As the acoustic perturbation at PAN is axisymmetric, there is an induced longitudinal perturbation propagating in an axisymmetric way [38]. Nevertheless, we note that there is a slight phase shift between the line wrinkles on the left and on the right side (take for example the lines $t/T_{cycle} = 12/50$ or $t/T_{cycle} = 49/50$). This is caused by the asymmetry introduced by the swirling flow that tilts the vortex ring (see section 6.1.1), which affects the droplet emission path, causing the mentioned phase shift of line wrinkles.

Moreover, by using the instantaneous views of the spray skeleton, we have estimated an injection angle of the droplets, at the injector exit, on the left and right sides of its axis. This extraction was made for two levels of the pressure amplitude. Fig. 6.22 shows the results for $|P'| \approx 1800$ Pa (case (a)) and $|P'| \approx 2200$ Pa (case (b)). The injection angle values characterizing the left and right sides evolve well in phase as expected, since the acoustic perturbation is symmetrical. Moreover, the modulation of the injection angle is out-of-phase with the acoustic pressure oscillations. While the injection angle without acoustic forcing is $66° \pm 2°$, here we observe that the maximum values of the injection angle reach 90° in both cases whereas the minimum values seem to be different. Indeed, in case (a), the value decreases down to 40°, and seldom goes below this limit. In case (b) the injection angle always decreases below 40° and can go as low as 30°.

6.4 Flame behavior at PAN

In this section is analyzed the coupling between combustion intensity which is linked to heat release rate (HRR) fluctuations (described by OH* or CH* emissions) and pressure fluctuations within the chamber at the flame location. An effective coupling is obtained if the Rayleigh criterion is satisfied, this is when the phase gap between pressure and HRR harmonic oscillations is $-\pi/2 \leq \varphi \leq \pi/2$. If this condition is met thermoacoustic instabilities could be driven. It has been shown that global HRR evaluated from OH* and CH* chemiluminescence agrees very well in the case of laminar and turbulence premixed flames [120]. In spray flames, OH* can be safely used while CH* emissions can be also used to describe the HRR behavior over time providing that we do not have sooty flames [74].

For the study presented the flame issued from the central injector is positioned at the center of the cavity bottom plate, which corresponds to the pressure antinode (PAN) location of the transverse mode. For the acoustic pressure amplitude reached here the flame never blows out. The maximum of $|P'|_{x,y,z}$ measured by microphone M1 at $x/L_c = 0$, $y/e = 0.5$, $z/h_c = 0.025$, is approximately 2200 Pa with resonant frequencies (f_r) in the range 760-780 Hz, for the results presented in this part. The results essentially focus on the dynamics of the central flame.

6.4.1 Analysis of the flame emission signals

Figure 6.23(a) shows the signal $I'_{OH^*}(t)$ and the acoustic pressure $P'(t)$ simultaneously recorded by PM and by the microphone M1 respectively (see Fig. 2.5). It is noted that the mean quantity $\bar{I}'_{OH^*}$, calculated over a period of the recorded signal under acoustic forcing, is systematically lower than $\bar{I}'^{o}_{OH^*}$ obtained without forcing (for the present illustration, $\bar{I}'_{OH^*}$ =1.81(u.a.) while $\bar{I}'^{o}_{OH^*} = 2.14$(u.a.)). This characteristic was already noted for a single premixed flame placed in an ambient temperature environment and perturbed by a transverse standing wave [67], but also for premixed flames self-excited by transverse modes of an annular chamber [94]. This phenomenon truly appears as an objective feature caused by acoustics. One may think that dilution of fresh gases by hot gases, is enhanced by acoustics, which decreases OH^* emission intensity. As expected, the PSD of $I'_{OH^*}(t)$ shows a well pronounced frequency peak at the forcing frequency, which coincides with that of the PSD of $P'(t)$ (see Fig. 6.23(c)).

In order to describe the flame dynamics, first is studied the behavior of the mean OH^* emission over time by using a sliding averaged value ($< I_{OH^*} > (t)$) over the entire forcing duration ($\sim$ 3880 cycles). In the example presented here, $< I_{OH^*} >$ is evaluated from 38 successive cycles with an overlap of 50%. While $\bar{I}'_{OH^*}$ is 1.81 (a.u.), $< I_{OH^*} > (t)$ evolves from 1.45 (a.u.) to 2 (a.u.) (see Fig. 6.23(a)). Second, the evolution of the frequency response of the flame is analyzed by performing a Short Time Fourier Transform (STFT) of $I'_{OH^*}(t)$. This calculation allows to add a temporal component to the classical PSD calculations, by dividing the entire flame emission signal in signals of short duration. Here, each short signal corresponds to 50 cycles of forcing with an overlap of 50%. It is thus possible to analyze the response of the

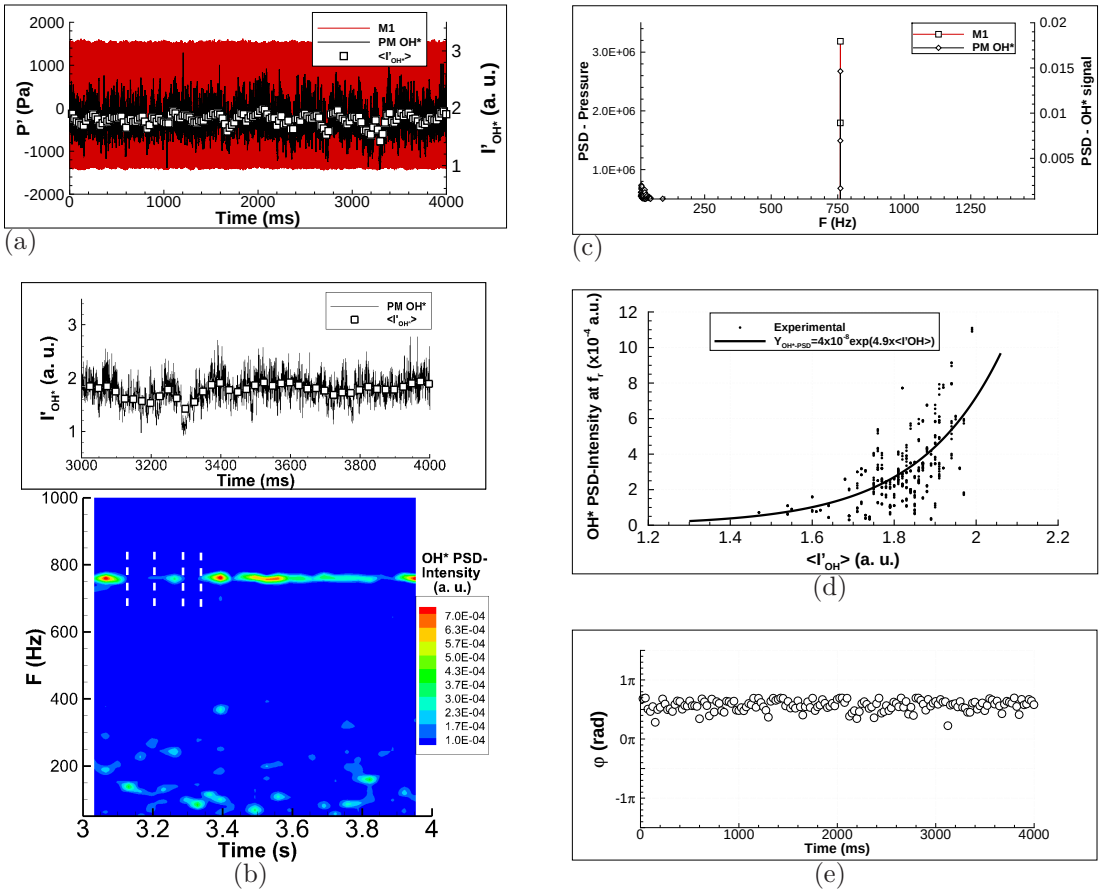

Figure 6.23: (a) Acoustic pressure signal $P'(t)$ from microphone M1 at $x/L_c = 0$, $y/e = 0.5$, $z/h_c = 0.025$ and OH^* emission intensity signal $I'_{OH^*}(t)$ recorded by a PM. (b) $I'_{OH^*}(t)$, its sliding-averaged value $< I_{OH^*} > (t)$ and STFT vs. time. (c) PSDs of $P'(t)$ and $I'_{OH^*}(t)$. (d)sliding OH^* PSD-intensity at 760 ± 1 Hz vs. $< I_{OH^*} > (t)$ during entire forcing. (e) Phase lag between $P'(t)$ recorded by M1 and $I'_{OH^*}(t)$ during entire forcing. $|P'| \approx 1600$ Pa, $f_r = 760$ Hz, $\dot{m}_{air} = 1.724$ g/s, $\dot{m}_{fuel} = 0.108$ g/s, $\phi_{LB} = 0.95$.

flame over time. Fig. 6.23(b) illustrates a result that shows the flame response well-established at f_r. But, some variations in the main peak intensity of the PSDs obtained from the STFT are noted. In particular some dips occur, which are associated with low values of $< I_{OH^*} > (t)$ (see for example time intervals delimited by the vertical dashed lines in the Fig. 6.23(b)) while conversely, peaks of $< I_{OH^*} > (t)$ are associated with strong PSD-intensity values.

In order to verify such a link between intensity peaks and $< I_{OH^*} > (t)$, a systematic characterization of the overall signal was made. To that end, OH* PSD-Intensities extracted at f_r from the STFT calculation, are compared against $< I_{OH^*} > (t)$. Data reported in Fig. 6.23(d) show that the weak spectral efficiency (low OH^* PSD Intensity in the bandwidth 760 ± 1 of the forcing) is linked to low averaged intensity $< I_{OH^*} > (t)$. In particular most of dips are associated to values of $< I_{OH^*} > (t)$ lower than 1.8 (a.u.). A global trend is extracted from the data, highlighting that OH* PSD-Intensity

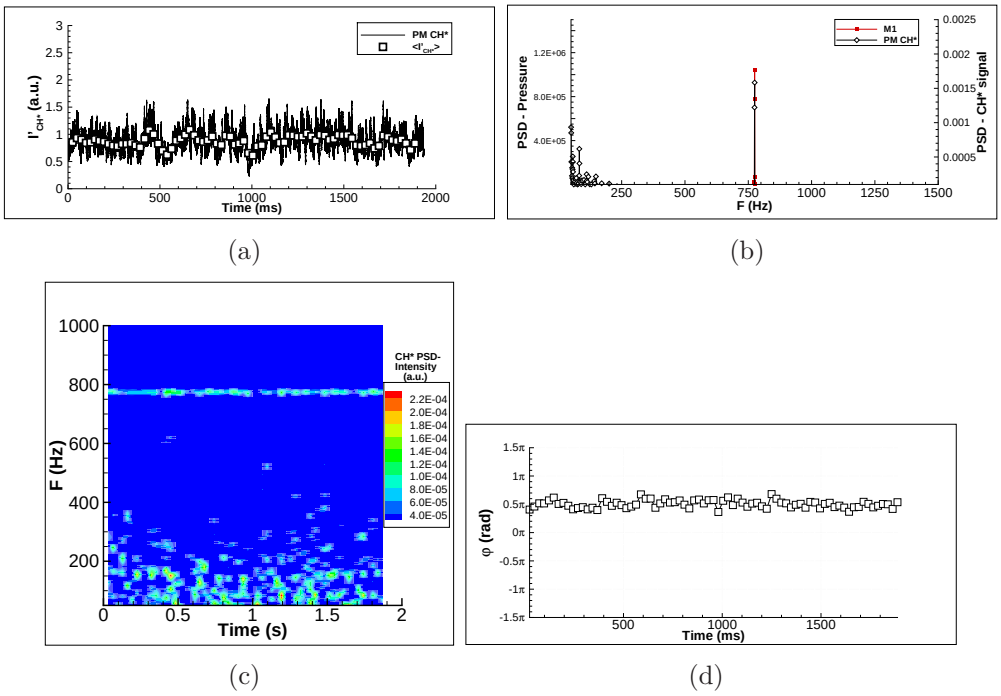

Figure 6.24: (a) $I'_{CH^*}(t)$ signal and its sliding-averaged value $< I_{CH^*} > (t)$. (b) PSDs of $P'(t)$ and $I'_{CH^*}(t)$. (c) STFT vs. time. (d) Phase lag between $P'(t)$ recorded by M1 and $I'_{CH^*}(t)$ during 1395 cycles of the acoustic forcing. $|P'| \approx 1600$ Pa, $f_r = 775$ Hz, $\dot{m}_{air} = 1.724$ g/s, $\dot{m}_{fuel} = 0.097$ g/s, $\phi = 0.85$.

increases as $< I_{OH^*} > (t)$ increases[3]

$$Y_{OH^*-PSD} = 4 \cdot 10^{-8} e^{(4.9 < I_{OH^*} >)} \tag{6.4}$$

The flames have dimensions small enough to be considered as compact, relatively to acoustics, at least to the main order. Taking this into consideration, data were processed to obtain the relative phase (φ) at the forcing frequency between the acoustic pressure ($P'(t)$) measured at PAN and $I'_{OH^*}(t)$. This quantity is essential, since it gives access to the global Rayleigh criterion which indicates if instabilities could be amplified. An evaluation was made from each 38 successive cycles (50 ms), with an overlap of 50%, of the entire signals. Fig. 6.23(e) shows the evolution of φ over ~ 3040 cycles (4000 ms). The extracted mean value and deviation lead to an averaged phase lag φ in radians equal to $(0.57 \pm 0.09)\ \pi$.

The same analysis has been conducted for flame CH* emissions signals ($I'_{CH^*}(t)$) recorded by PM. It is noted that its mean signal value is lower than its mean value without acoustic forcing, as it was observed for OH* emissions. The temporal evolution of this signal shows same characteristics as OH* emissions: the variations of the sliding averaged value ($< I_{CH^*} > (t)$) are also linked to the dips noted in the STFT calcu-

[3]Data has been fitted by means of an exponential curve presented in Eq. 6.4. This fitting is not based on the least-squares method, but the fitting curve was defined in order to well represents the cloud of intensity points.

lation; the CH* emission response is well established at f_r. The results are presented in Fig. 6.24. The φ evolution leads to an averaged value equal to that obtained with OH*, but with a relatively smaller dispersion of $\pm 0.05\ \pi$ (see Fig. 6.24(d)).

For these illustrations at $f_r = 760$ Hz, based on the measurements of both radicals and according to Rayleigh criterion, the coupling between flame OH*/CH* emissions and pressure fluctuations is at the limit to be positive and to amplify an instability. The description of the HRR behavior made either by OH* or CH* chemiluminescence leads to the same conclusion.

6.4.2 Relationship between combustion intensity and pressure fluctuations

As verified in the latter section, it is possible to describe HRR fluctuations by the spray flame CH* chemiluminescence emissions. The transfer function between the flame response and acoustic pressure fluctuations is obtained from the CH* emission recorded by PM and the acoustic pressure measured by M1 (see Fig. 2.14(b)).

Several measurements have been carried out as a function of the acoustic forcing level. The measurements begin with the cavity free of acoustic forcing and subsequently the acoustic forcing is applied with levels upto $P_{rms} = 1500$ Pa, where P_{rms} is the Root Mean Square (RMS) value of the pressure perturbation amplitude. The I_{CH*}^{mean} quantity is the mean value calculated over each signal recorded during 1.3 s (1000 cycles at $f_r = 780$ Hz). The I_{CH*}^{rms} quantity is the RMS amplitude calculated for f_r using the Matlab's pwelch signal processing tool (see explanation in [121]).

As highlighted in section 6.4.1, the mean value of the flame CH* emission decreases with forcing with respect to the case without forcing. This is shown in Fig. 6.25(a) for I_{CH*}^{mean} vs. P_{rms}. We can distinguish three distinct parts in the curve. Initially the curve stays nearly constant with P_{rms} upto a value of about 200 Pa. Beyond this point the curve exhibits a strong decay upto $P_{rms} = 600$ Pa after which only a mild decay is noted.

On the other hand, data plotted in Fig. 6.25(b) show that I_{CH*}^{rms} values grow linearly with P_{rms} until they saturate. Then, when the P_{rms} value is close to 600 Pa, the values of I_{CH*}^{rms} begin to decrease, even if the amplitude of the pressure fluctuations continues to grow. Within this part of the plot, from $P_{rms} = 600$ Pa upto the end, one can note a growth in the spread of the data. This feature is not present in the I_{CH*}^{mean} behavior.

Fig. 6.25(c) plots the normalized quantity $I_{CH^*}^{rms}/I_{CH^*}^{mean}$ versus pressure fluctuations P_{rms}. The results show a linear increase with respect to P_{rms} until $P_{rms} = 600$ Pa. Subsequently, the normalized RMS amplitude saturates showing scattered values within a range delimited by $0.05 \leq I_{CH*}^{rms}/I_{CH*}^{mean} < 0.15$. This scattering is due to the behavior of I_{CH*}^{rms} values, already noted in Fig. 6.25(b). Thus, it is found that $P_{rms} = 600$ Pa corresponds to a value at which the flame response saturates. This value is then called P_{sat} and is used in order to normalize pressure fluctuations.

The nonlinear saturation of the heat release rate is a phenomenon commonly encoun-

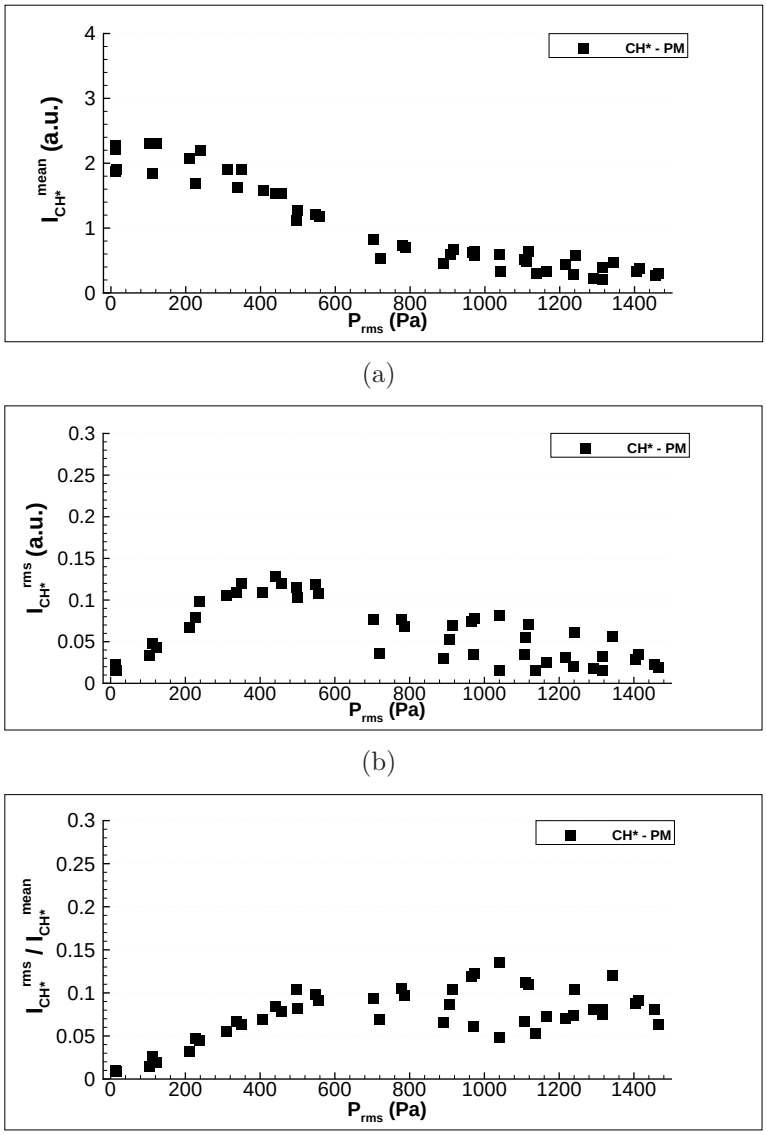

Figure 6.25: Evolution of I_{CH*}^{mean} (a) and I_{CH*}^{rms} (b) as a function of P_{rms}, the RMS value of the acoustic pressure fluctuation measured within the chamber by M1. (c) Relationship between P_{rms} and $I_{CH*}^{rms}/I_{CH*}^{mean}$, the normalized amplitude of the RMS value of the CH* emission fluctuations. f_r between 760 and 780 Hz, $\dot{m}_{air} = 1.724$ g/s, $\dot{m}_{fuel} = 0.097$ g/s , $\phi_{LB} = 0.85$.

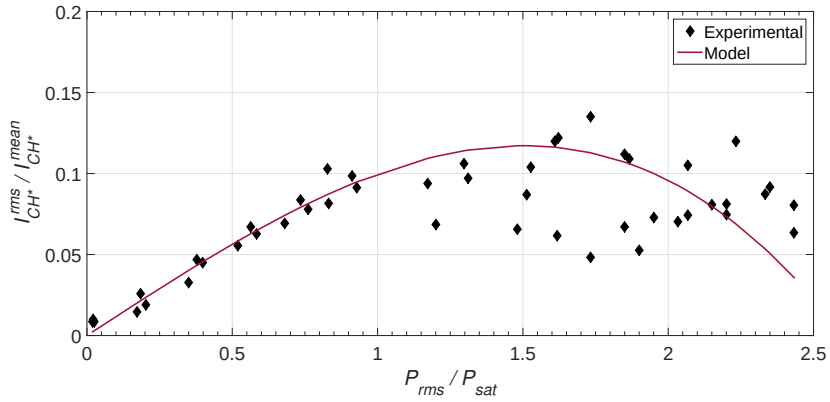

Figure 6.26: Saturation of $\dot{Q}'/\bar{\dot{Q}}$ (represented by CH*-emissions) as function of P_{rms}/P_{sat}. (♦) Experimental data; (–) $\dot{Q}'/\bar{\dot{Q}} = \beta \cdot (P_{rms}/P_{sat}) - k \cdot (P_{rms}/P_{sat})^3$; $\beta = 11.7 \cdot 10^{-2}$, $k = 1.728 \cdot 10^{-2}$.

tered and well documented in the literature in the case of premixed flames subjected to velocity and pressure perturbations (e.g. [69, 72, 120, 122–127]). Noiray et al. in [63] propose to model this nonlinearity by a third order term that we write as:

$$\frac{\dot{Q}'}{\bar{\dot{Q}}} = F(P_{rms}) = \beta \frac{P_{rms}}{P_{sat}} - k \left(\frac{P_{rms}}{P_{sat}} \right)^3 \tag{6.5}$$

where $\dot{Q}'/\bar{\dot{Q}}$ is the fluctuating heat release rate normalized by its time-averaged value, β is the source term and k represents the nonlinear coupling between the heat release rate and the acoustic field. We show in Fig. 6.26 that the experimental measurements are adequately approximated by this model. The model matches very well during the flame response growth, and gives the good trend in the zone of data scattering. The reason for this scattering has not yet been clarified. These results suggest that the saturation of the flame response, in the case of spray flames, can be well approached by a third order term model, as has been done in [63] for a turbulent premixed flame. The possible mechanism that can explain the saturation in the response of the flame will be discussed in section 7.4.

6.4.3 Flame front motion

Following the flame front motion with a high-speed camera brings to light important features. Images are captured at 6120 fps with a Phantom V10 camera, exposure time of 160 μs and a recording duration of 163.4 ms. Thus, the duration of the series is long enough to give pertinent information. The PSD of the OH* emission signal, obtained from 1000 images recorded at 6120 fps, is consistent with the signal recorded by the PM. In Fig. 6.27(a), the peaks of f_r on the PSD of both signals obtained from PM and from images are clearly noted. A complete cycle showing the flame perturbation has been reconstructed by using 24 class-averaged images (the class-averaging method is defined in section 4.1).

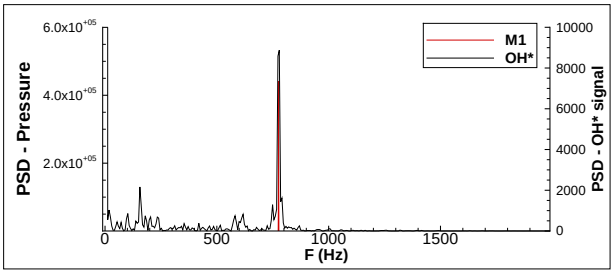

(a)

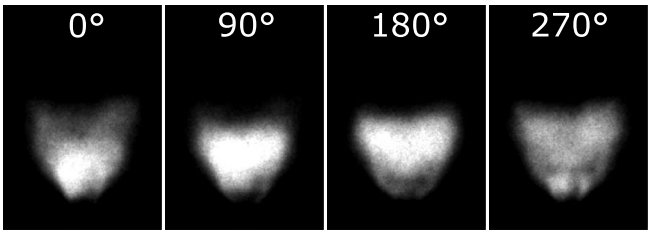

(b)

Figure 6.27: (a) PSDs of pressure fluctuations registered by M121 and of $OH*$ intensity fluctuations from images recorded by a high-speed camera. (b) Phase-averaged images of middle flame OH^* emissions during a full cycle of the acoustic forcing. $|P'| \approx 1600$ Pa, $f_r = 776$ Hz, $\dot{m}_{air} = 1.724$ g/s, $\dot{m}_{fuel} = 0.108$ g/s , $\phi_{LB} = 0.95$.

An axial modulation of the front is clearly visible, while the averaged position of the flame bottom extremity in these images seems to be almost constant over the cycle

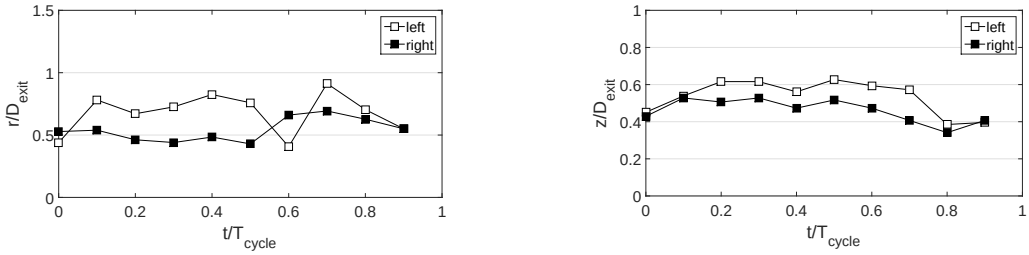

(a)

(b)

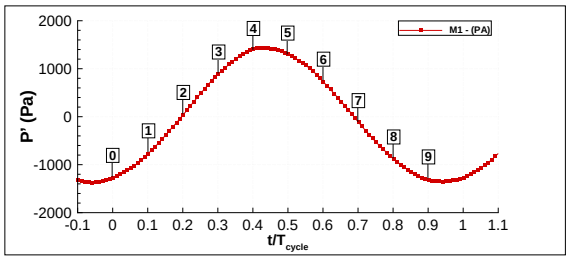

(c)

Figure 6.28: (a) Evolution of the axial position (r/D_{exit}) of the left and right branches of the flame foot. (b) Evolution of the vertical position (z/D_{exit}) of the left and right branches of the flame foot. (c) Pressure signal synchronized with the phase-averaged positions evolution. $f_r = 775$ Hz, $\dot{m}_{air} = 1.724$ g/s, $\dot{m}_{fuel} = 0.097$ g/s, $\phi_{LB} = 0.85$.

(Fig. 6.27(b)). Using ten phase-averaged images of the flame front CH* emissions, averaged over 100 images, obtained at the positions of the pressure perturbation cycle (labeled from 1 to 10) shown in Fig. 6.28(c), we can roughly follow the position of the left and right sides of the flame foot. Defining a threshold value of the intensity level in these images, over a level considered as noise, it is possible to identify the flame foot sides. It is difficult to say if the radial position evolution during a perturbation cycle is really correlated with the acoustic forcing (Fig. 6.28(a)). However, the axial position of the flame foot seems to slightly evolve with the acoustic perturbation. In Fig. 6.28(b), when the pressure amplitude grows, the flame foot sides move away from the injector exit until $z/D_{exit} = 0.6$, since the reactive flow rate entering into the chamber decreases. As the pressure amplitude decreases, the flame foot sides go upstream to the injector until a value slightly lower than $z/D_{exit} = 0.4$, This is due to the increase of the reactive flow rate that enters into the chamber. It was shown in section 3.5.2.2 that, without acoustic forcing and with the flame foot stabilized on average close to $z/D_{exit} = 1$, the temperature within the reactive flow near to injector axis at $z/D_{exit} = 0.625$, is equal to ≈ 64°C. With forcing, the flame foot position fluctuates lower than $z/D_{exit} = 0.625$ (between $z/D_{exit} = 0.6$ and $z/D_{exit} = 0.4$). This may periodically modulate the temperatures in the region close to the nozzle exit.

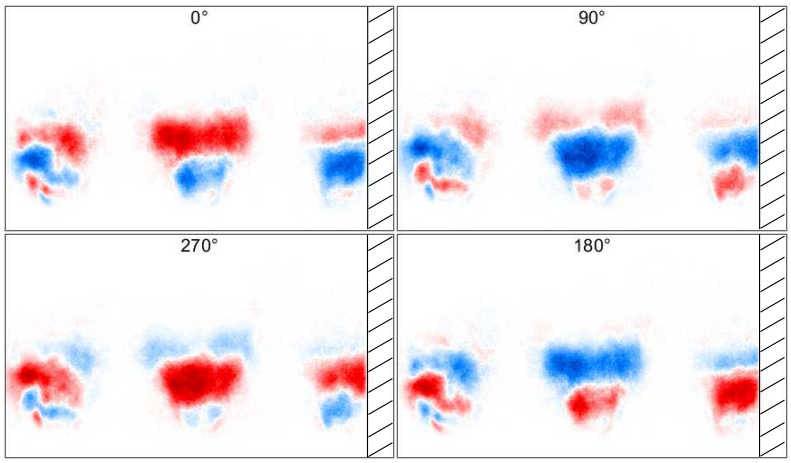

Figure 6.29: DMD of the OH^* emission intensity (false color) at the acoustic forcing frequency. $f_r = 776$ Hz, $\dot{m}_{air} = 1.724$ g/s, $\dot{m}_{fuel} = 0.108$ g/s , $\phi_{LB} = 0.95$.

Dynamic Mode Decomposition (DMD) [128] was performed by using 101 images from the series of high-speed images of the three flame fronts during the forcing. In Fig. 6.29 the decomposition confirms the axial periodic modulation of the OH*-intensity of the middle flame while flame on the left side shows a less pure axial behavior. On the left flame the influence of the pressure gradient and of the non-negligible acoustic velocity fluctuations starts to be well noticeable. This behavioral response is studied in section 7.3.1.

In addition, in order to assess the pertinence of the flame "global emission" assumption, the OH* emission intensity has been computed over time for the middle flame images of the series at high-speed acquisition, in four horizontal bands of 10 mm height, starting at $z = 0$ mm (Fig. 6.30(a)). The resulting intensities are divided by the size of the

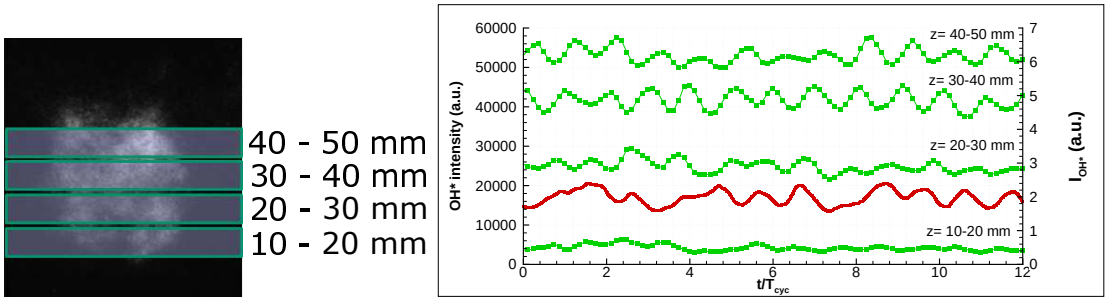

(a) (b)

Figure 6.30: (a) Zones delimiting each band (image by a high-speed camera) and (b) OH^* emission signals of each bands shifted of 15k, 30k and 45k a.u beginning with the 20-30 mm band. In red the PM signal $I'_{OH^*}(t)$. $f_r = 765$ Hz, $\dot{m}_{air} = 1.724$ g/s, $\dot{m}_{fuel} = 0.108$ g/s , $\phi_{LB} = 0.95$.

band (in pixels) in which they are computed. The signal s_0 coming from the zone of the flame foot position (0-10 mm) is very weak, remaining almost constant relatively to the other signals. The intensity density signals s_i coming from each band, starting from region 10-20 mm, are presented against time in Fig. 6.30(b) along with the PM signal. For the sake of clarity, except signal s_1 corresponding to the zone 10-20 mm, the three next signals are successively incremented by 15k (a.u.) from signal s_2 to s_4.

The lower zone (10-20 mm) has a weaker mean intensity than the others, which have almost the same intensity level. The signals of the different zones do not oscillate in-phase. A phase-lag (τ), expressed in time units, can be estimated between consecutive maximums of signals of different zones. It has been verified that this phase-lag is almost the same between two consecutive zones. The PM signal $I'_{OH^*}(t)$ (in red) corresponding to the global emission of the flame is included in Fig. 6.30(b). Its phase is closer to the phase of the signal from the zone 20-30 mm than the phase of the others signals. By using τ and the distance between the center of two zones (Δz) it is possible to calculate:

$$U_w = \frac{\Delta z}{\tau} \tag{6.6}$$

which is the speed of the propagation of the scalar information, in this case the intensity of the flame emission. The value obtained is $U_w = 27.5$ m/s which is nearly equal to $\approx U_b$, the bulk velocity at the injector exit. This propagation is also illustrated in Fig. 6.31 by means of iso-intensity lines extracted from the class-averaged images of OH* emissions. These iso-lines reveal an axisymmetric region delimited by the higher iso-intensity line propagating downstream. To estimate its propagation speed, one may take the center of the region delimited by the higher iso-intensity line, and measure its displacement Δz between two images with time delay τ. By applying Eq. 6.6, is obtained a speed value approximately equal to $U_b = 28.6$ m/s. These results confirm the convective nature of the perturbation propagation. The propagation velocity of this perturbation is the bulk velocity (U_b).

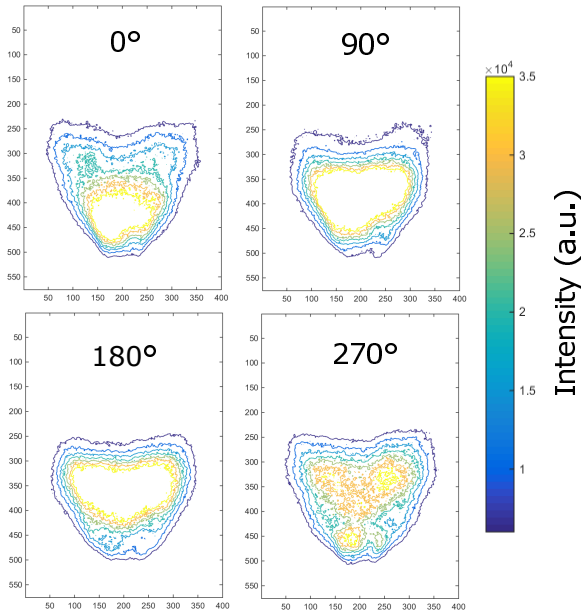

Figure 6.31: OH^* emission iso-intensity lines extracted from images. $|P'| \approx 1600$ Pa, $f_r = 776$ Hz, $\dot{m}_{air} = 1.724$ g/s, $\dot{m}_{fuel} = 0.108$ g/s , $\phi_{LB} = 0.95$.

6.5 Elements for the Flame Describing Functions

In this section we show flame transfer functions from measurements of flame chemiluminescence emissions and velocity and pressure fluctuations both in the air plenum and within the combustion chamber, and their link in the case of our downstream transverse acoustic forcing. The Flame Describing Function (FDF) defines a flame transfer function which depends upon both the input frequency and perturbation amplitude. The FDF based on the velocity perturbation (u'), and on the acoustic pressure fluctuations (p') are respectively defined by:

$$\mathcal{F}_u(\omega_r, \frac{u'}{\bar{u}}) = \frac{\dot{Q}'}{\bar{\dot{Q}}} / \frac{u'}{\bar{u}} \tag{6.7}$$

$$\mathcal{F}_p(\omega_r, \frac{p'}{\bar{p}}) = \frac{\dot{Q}'}{\bar{\dot{Q}}} / \frac{p'}{\bar{p}} \tag{6.8}$$

FDFs have been measured by Prieur [1] in a range of forcing frequencies from 100 Hz to 900 Hz for a spray flame stabilized in a round tube serving as a combustion chamber, called SICCA-SPRAY. There the burner (nozzle, swirler, air distributor, atomizer) was identical, but the air plenum differed from the present one. The spray flame, positioned within the cylindrical combustion chamber, was subjected to an upstream longitudinal acoustic forcing. p' was measured in the cylindrical chamber at the burner exit and the velocity perturbation, u', upstream in the air plenum. In the case of the FDF model defined by Eq. 6.7, author corrected the phase diagram of this FDF in order to account for the role of the injector on the stability. Making this, it is as if he used an equivalent

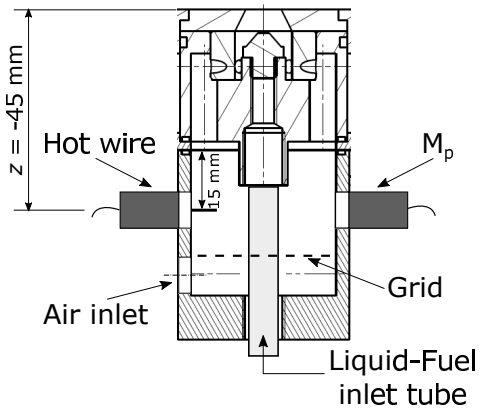

Figure 6.32: Sketch of the setup of the hot wire and a microphone (M_p) inside the plenum.

velocity signal situated at the burner exit, thus introducing the acoustic response of the system (see [129]). So he added a measured injector admittance (δ) that shifted their FDF phase diagram. Prieur found that δ was quite constant with the frequency, having a value close to $-\pi/2$. Thus, he has calculated potentially unstable bands from where it is possible to obtain the frequency boundaries of potential unstable modes. The final calculation of the effective FDF shows the stable and unstable regions of the response of the system (Fig. 6.33).

Prieur found that the frequency of the self-sustained instability mode of their annular chamber was well predicted. However, the gain was relatively low at this frequency. It was expected that the mutual flame interactions, an aspect not considered in the calculation, might modify the FDF gain plot.

Using the model defined by Eq. 6.8 same author has determined the FDF presented in Fig. 6.34. He recovered a phase diagram of the FDF constant over most of the frequency range considered. The phase value was nearly equal to $\pi/2$. The gain of this FDF has a different shape with respect to the gain of Fig. 6.33. It decreased with frequency and no peak could be detected. This FDF did not predict the self-sustained instability of the annular chamber. As a consequence, authors concluded that p', measured in the chamber, is an incorrect input parameter for the FDF in the case of a longitudinal forcing. This is true here in particular because they imposed an upstream longitudinal forcing, but due to pressure drop caused by acoustic losses, the p' measured in the cylindrical chamber corresponds rather to the combustion noise induced by the flame. Gaudron et al. [129] shows that is with a downstream forcing where the FDF determined by using the pressure signal in the chamber near of the burner exit can be directly linked with the FDF based on pressure or velocity fluctuations measured upstream of the burner exit since acoustic pressure drop can be neglected. The link between these two latter FDF is made simply through the acoustic impedance at the velocity measurement position (see also [78]).

In our work, we have calculated the two FDF as a function of the amplitude of pressure perturbations $|P'|$ from measurements performed at the angular resonant frequency (ω_r) and we have used the ratio $I'_{CH^*}/\bar{I}'_{CH^*}$ in order to represent $\dot{Q}'/\bar{\dot{Q}}$. In

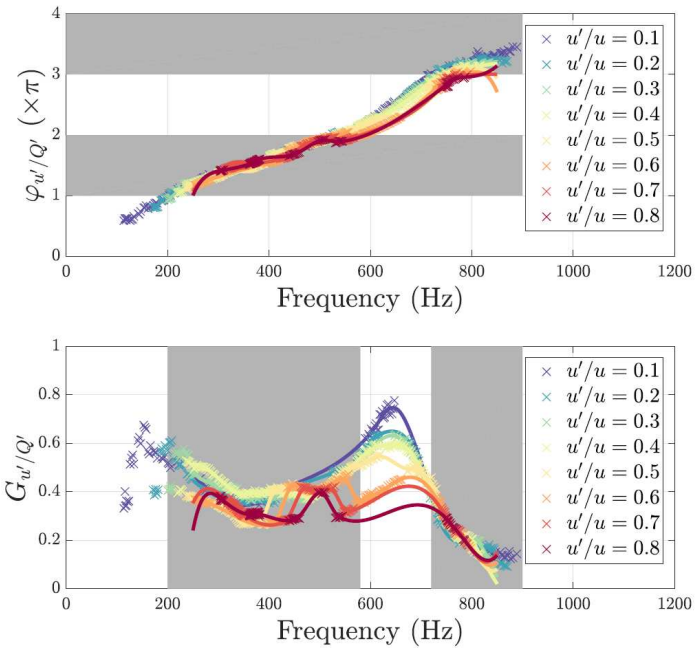

Figure 6.33: Top: Phase of the FDF corrected with the burner admittance coupled with the instability band in grey. Bottom: Gain and deduced position of the instability bands. Reproduced from [1].

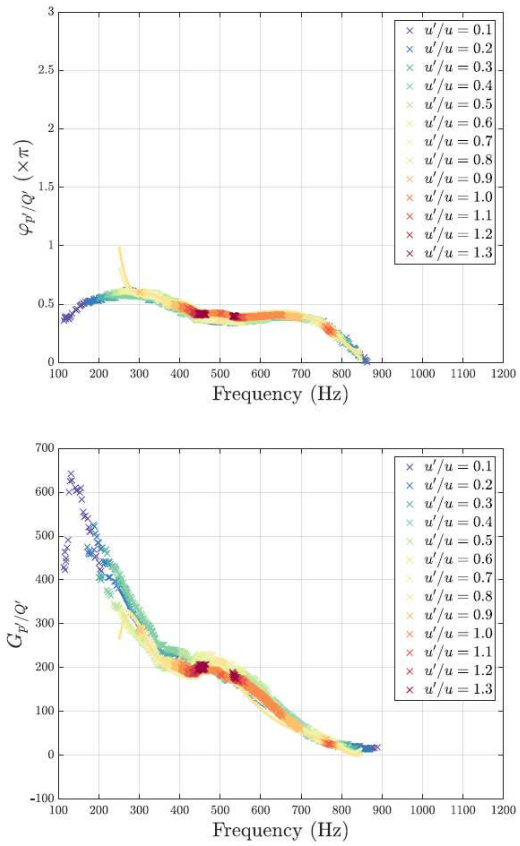

Figure 6.34: Phase (top) and Gain (bottom) of the FDF based on the acoustic pressure fluctuation within the cylindrical chamber. Reproduced from [1].

the case of the FDF defined in Eq. 6.7, the velocity fluctuations (u') are measured by a hot-wire installed at 45 mm upstream from the nozzle exit in the air plenum (see Fig. 6.32). For the FDF defined in Eq. 6.8, the pressure fluctuations are measured within the combustion chamber at the exit of the central injector by microphone M1 at $(x/L_c, y/e, z/h_c) = (0; 0.5; 0.025)$ and is posed $p' = |P'|$ to conserve the nomenclature in the FDF definition. A FDF also based on pressure fluctuations has been determined, this time by using measurements performed by the microphone M_p inside the air plenum, at 45 mm from the nozzle exit (Fig. 6.32). In the case of FDF based on pressure fluctuations, we have replaced $\bar{p}$ by $\sqrt{2}P_{sat}$ as the forcing pressure signal is sinusoidal. P_{sat} is the value found in section 6.4.2.

The amplitude of the pressure fluctuations within the cavity has been progressively varied within the range $[100 - 2100]$ Pa. By applying Eq. 6.8 with M1 measurements, we find that the gain, $G_{I'_{CH*}/p'}$, increases with the amplitude of the pressure fluctuations upto a value $G_{I'_{CH*}/p'} \approx 0.2$ for a pressure amplitude of about 750 Pa (Fig. 6.35(a)). From this $|P'|$ value, $G_{I'_{CH*}/p'}$ decreases (Fig. 6.35(a) top). The same behavior is noted for the gain based on pressure fluctuations measured in the plenum by M_p. In this case the maximum value reached is $G_{I'_{CH*}/p'} \approx 0.26$. In Fig. 6.35(a)(bottom), the phase plot shows that $\varphi_{I'_{CH*}/p'}$ is slightly lower than $-\pi/2$ and zero for the phase obtained with measurements of $M1$ and M_p respectively. From these results is noted that the phase is not dependent on the perturbation amplitude. HRR fluctuates nearly in phase with the pressure signal obtained in the plenum while there is a phase lag slightly higher than $\pi/2$ with pressure fluctuations within the chamber. The gain is dependent on the perturbation amplitude upto about 1350 Pa from where it is slightly dependent.

By applying Eq. 6.7 with the measurements of the hot wire in the plenum, we find that the gain $G_{I'_{CH*}/u'}$, grows from 16 to 22 where the perturbation amplitude is 750 Pa, then the gain decreases. From approximately $|P'| = 1350$ Pa, $G_{I'_{CH*}/u'}$ remains virtually constant (Fig. 6.35(b) top). The profile of this gain plot is similar to that based on pressure fluctuations. The phase plot shows that $\varphi_{I'_{CH*}/u'}$ evolves from -0.15π to a value of about -0.7π with pressure amplitudes upto $\approx$ 750 Pa. From this value the phase remains between -0.5π and -0.8π (Fig. 6.35(b) bottom). It is possible to easily pass from the $\mathcal{F}_p$ of Fig. 6.35(a) to $\mathcal{F}_u$ of Fig. 6.35(b) by performing:

$$\mathcal{F}_u = Z\frac{\bar{u}}{P_{sat}}\mathcal{F}_p \tag{6.9}$$

where Z is the acoustic impedance at the hot wire position obtained as the transfer function determined between signals measured by M_p and the hot wire. Fig. 6.36 plots $Z\bar{u}/P_{sat}$.

As deduced from the FDF determined before, I'_{CH*} is nearly in phase with the pressure in the plenum while with pressure fluctuations in the chamber the phase gap is of about 0.6π. The phase gap between pressure signals from $M1$ and M_p is of about 0.6π and remains constant. The phase gap between the pressure signal from $M1$ and the velocity signal (u') measured by the hot wire depends on the pressure perturbation amplitude. For low values of the perturbation amplitude the phase gap is upto 0.45π while for higher it is lower than 0.2π. The signals plotted in Fig. 6.37(b) corresponds

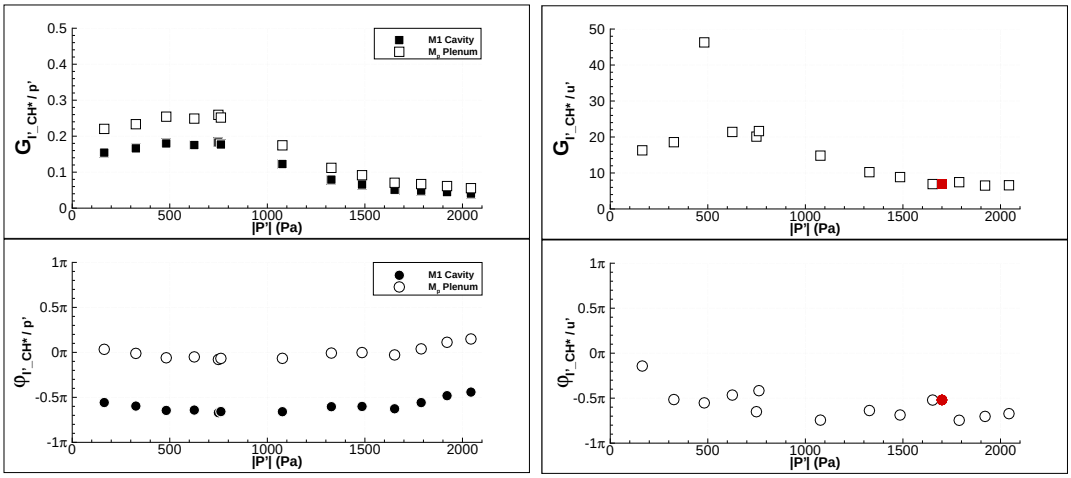

(a) (b)

Figure 6.35: (a) FDF, based on the acoustic pressure fluctuations p' measured at the central injector exit by microphone $M1$ (filled symbols) and measured by microphone M_p (blank symbols), in the case of the transverse forcing within the cavity. (b) FDF, based on the velocity perturbation u' measured by a hot-wire installed upstream in the air plenum. In each sub-figure, the gain G (top) and phase φ (bottom) are plotted as functions of the pressure perturbation amplitude measured by M1. Red symbols were obtained using Eq. 6.12. $f_r = 780Hz$, $\dot{m}_{air} = 1.724$ g/s, $\dot{m}_{fuel} = 0.097$ g/s , $\phi_{LB} = 0.85$.

to $|P'| \approx 1700$. For these latter signals the phase gap obtained at $f_r = 780$ Hz is lower than 0.1π.

Let determine a transfer function between I'_{CH*} and velocity fluctuations within the combustion chamber at the nozzle exit. In order to do this, one can use the LDA velocity measurements on n-heptane droplets carried out at $z/D = 0.375$ from the nozzle exit during combustion. As we have seen in section 3.6.1, the local S_t indicates that the air velocity can be well traced by n-heptane droplets. This S_t, is calculated using $\tau_{air} = D_{exit}/U_b$. One may be led to believe that S_t needs to be calculated with $\tau_{ac} = 1/f_r$, rather than τ_{air}, however for the forcing frequencies used here, the results indicate that the S_t values are even lower. We have chosen the U'_z velocity signal measured at $r/D = \pm 0.5$, because at this point, the PSD spectrum of the velocity signal shows a high response to the acoustic forcing at f_r. A transfer function can be calculated between this signal and the pressure fluctuations p' within the chamber. It is defined as:

$$\frac{U'_z}{\bar{U}_z} / \frac{p'}{P_{sat}} = G_{U'_z/p'} e^{i\varphi_{U'_z/p'}} \tag{6.10}$$

With these transfer functions defined by equations 6.7, 6.8 and 6.10, we are in a position to obtain a relationship between the velocity U'_z and u' as well as, the relationship between I'_{CH*} and U'_z. The first one allows us to obtain a phase corresponding to the admittance (δ) of our injector plus a convective component δ_{conv} since U'_z is measured 3 mm ($z/D = 0.375$) from the nozzle exit.

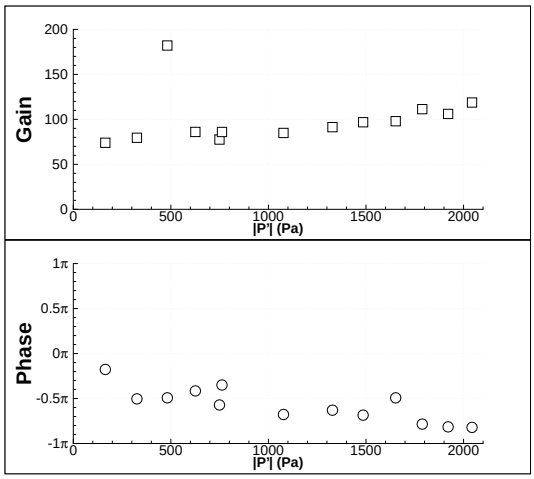

Figure 6.36: $Z(\bar{u}/P_{sat})$ transfer function between pressure (M_p) and velocity (hot wire) fluctuations both in the air plenum. Gain (top) and phase (bottom).

In order to illustrate this, an analytic application is made at $\omega_r = 2\pi f_r$ ($f_r = 780$ Hz), for a pressure perturbation amplitude of ≈ 1700 Pa. We recall that $\dot{m}_{air} = 1.72$ g/s and the velocity fluctuation ratio, within the air plenum, resulting from our transverse forcing is then $u'/\bar{u} = 0.0113$. The ratio of the velocity fluctuation, measured by LDA at $r/D = 0.5$ and $z/D = 0.375$, inside the chamber, is $U'_z/\bar{U}_z = 0.355$.

The gain of the transfer function defined by Eq. 6.10 is $G_{U'_z/p'} = 0.15$ while the phase $\varphi_{U'_z/p'} = -0.77\pi$. The signals are plotted in Fig. 6.37(c). A transfer function may be found between u' measured by the hot wire and p' measured by $M1$ in the chamber, from equations 6.8 and 6.7 where $\dot{Q}'/\bar{\dot{Q}}$ is thus removed. By using this latter transfer function one can then calculate the gain and the phase between the velocities $U'_z/\bar{U}_z$ and $u'/\bar{u}$. The result obtained shows a gain $G_{U'_z/u'} = 20.05$, and a phase $\varphi_{U'_z/u'} = -0.664\pi$. We considered an acoustic propagation of the velocity perturbation in the 15 mm distance between the measurement location of u' and the air distributor inlet. LES calculations of the SICCA-SPRAY burner presented in [1] have demonstrated that velocity perturbation (u') is transported at the speed of sound upto a distance of about 80 mm from the air distributor inlet. The result of the phase is thus:

$$\delta + \delta_{conv} = -0.664\pi \tag{6.11}$$

The convective component δ_{conv} can be obtained by using the time delay of the perturbation transportation found in section 6.3.2. With a velocity of $U_w = 30$ m/s, the time delay from the nozzle exit ($z = 0$) until the measurement location of U'_z is of about 0.1 ms. This corresponds to a $\delta_{conv} = -0.159\pi$ which can be put into Eq. 6.11 to obtain $\delta = -0.505\pi$. The admittance allows to pass from the transfer function between I'_{CH*} and u' to one between I'_{CH*} and a velocity located at $z = 0$ ($U'_{z=0}$), and inversely.

Another way is combining equations 6.8 and 6.10 to obtain the transfer function between I'_{CH*} and U'_z. We found a gain value $G_{I'_{CH*}/U'_z} = 0.346$, and a phase value $\varphi_{I'_{CH*}/U'_z} = 0.144\pi$. Then, as U'_z is located at $z = 3$ mm, we consider δ_{conv} to obtain the phase of $U'_{z=0}$ assuming that this signal differs from U'_z only in the phase. Thus

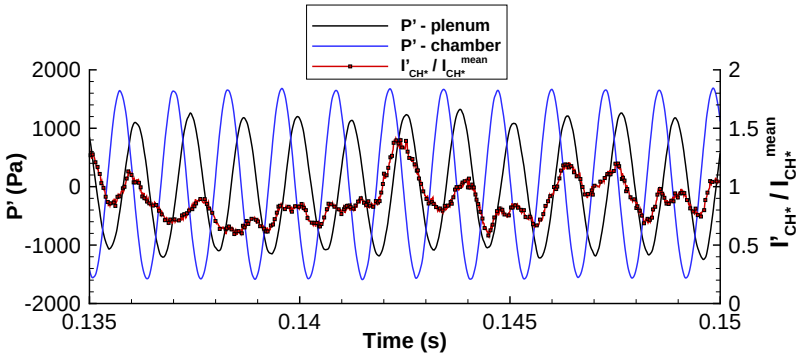

(a)

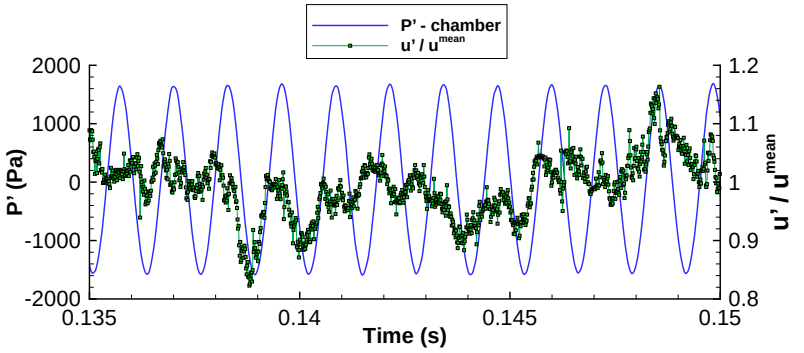

(b)

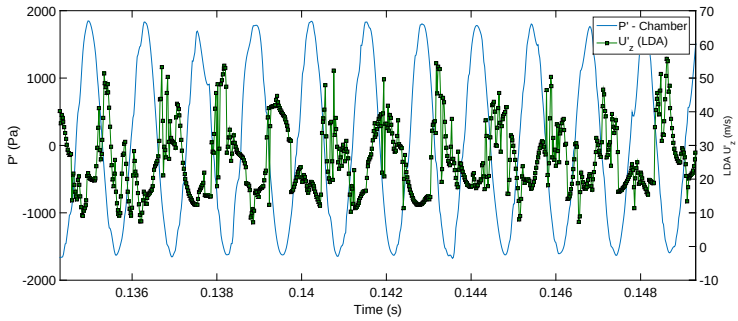

(c)

Figure 6.37: (a) Signals of $I'_{CH^*}/\bar{I}'_{CH^*}$ and pressure fluctuations. (b) Pressure fluctuation signal within the chamber and $u'/\bar{u}$ signal within the plenum. (c) Pressure fluctuation signal within the chamber and the velocity signal U'_z measured by LDA at the injector exit ($z/D = 0.375$, $r/D = \pm 0.4$). $f_r = 780Hz$, $\dot{m}_{air} = 1.724$ g/s, $\dot{m}_{fuel} = 0.097$ g/s , $\phi_{LB} = 0.85$. Signals are not filtered.

we obtain $\varphi_{I'_{CH*}/U'_{z=0}} = -0.015\pi$. Let find the transfer function between I'_{CH*} and u' from the latter result and the injector admittance found previously by applying the following formulation:

$$G_{(I'_{CH*}/u')} e^{i\varphi_{(I'_{CH*}/u')}} = \left(G_{U'_z/u'} \cdot G_{(I'_{CH*}/U'_{z=0})}\right) e^{i\left(\varphi_{(I'_{CH*}/U'_{z=0})}+\delta\right)} \tag{6.12}$$

For a pressure amplitude $|P'| = 1700$ Pa Eq. 6.12 gives $G_{I'_{CH*}/u'} = 6.9$ and $\varphi_{I'_{CH*}/u'} = -0.52\pi$. These results are indicated with red symbols in Fig. 6.35(b).

In the literature is accepted that the system is potentially unstable when the phase of the FDF based on the velocity perturbation is bounded between π and 2π [mod. 2π] [35, 71].From the phase value $\varphi_{I'_{CH*}/U'_{z=0}} = -0.015\pi$ and adding 2π it is noted that the system is inside and at the border of an instability band delimited by π and 2π. From values of $\varphi_{I'_{CH*}/p'}$ the system is also at the border but outside of an instability band delimited by -0.5π and 0.5π.

At this frequency, the FDF phase and gain based on pressure fluctuations measurements show a low dependency on the perturbation amplitude, evolving in a relatively narrow band. Compared with FDF based on pressure fluctuations, the FDF based on velocity measurements inside the plenum presents a relatively higher dependence on the perturbation amplitude.

Some sources of uncertainty in the FDF calculation should be mentioned:

- The estimation of δ, used in [1] to correct the FDF phase diagram, may vary with the value of the air-flow rate ($\dot{m}_{air}$). This was not considered in the calculation of the FDF reproduced from [1].
- Another issue is that δ may be dependent on the condition of measurement, in particular if it is made in cold condition or during combustion where the temperature of the injector close to the chamber might be higher, therefore the speed of sound will be higher and consequently the velocity of the perturbation propagation will be modified.
- The experimental configuration also plays a role. Calculations using measurements from a single confined injector may be quite different from those using measurements in presence of neighboring flames. This is not only because of the possible mutual front interactions, but also because adjacent flames may increase the temperature field, causing gas expansion, impacting the fuel droplets evaporation and by consequence the flame response.
- As velocity measurements at the nozzle exit ($z = 0$) is experimentally difficult to perform, measurements often have to be at a higher location. For this reason it has to be taken into account the convective transport of the perturbation from $z = 0$ to the measurement location. This convective component may be dependent on the operation condition and the way it is measured is source of uncertainty.

The choice of the position of measurement for the velocity perturbation is still open to discussion. The theory states that FDFs based on velocity perturbations should

be calculated using a velocity signal measured as close as possible to the flame. This condition must to be fulfilled provided that the chosen signal has the least complex and easiest to quantify characteristics [95]. Works of Gaudron et al. [129] conclude that the best results will be obtained with measurements at $z = 0^-$ on the upstream side. We have chosen to measure the velocity fluctuations by LDA as close as the setup allows from the nozzle exit, and at a point where the signal is highly sensitive to the acoustic perturbation. Here, the normalization of U'_z by U_b, the bulk velocity, is not used for the FDF calculation. This is proposed in the literature for FDF calculations, when the velocity fluctuation considered is measured at the exit of the burner. The reason for our choice is that the U_b velocity is linked to the mass flow rate injected into the burner, but it does not represent a characteristic velocity of the swirling flow.

6.6 Conclusion

A global picture of the effects of the acoustic perturbation at the basin of PAN, on each element that forms the energetic system is shown in Fig. 6.38. This figure presents, by means of class-averaged images of the two-phase flow and phase-averaged images of the spray flame, a reconstruction of their behavior at f_r illustrated at four times of one cycle of the acoustic forcing. Fig. 6.38 joins images of different experiments with f_r between 760-790 Hz. The operating point corresponding to the spray is $\dot{m}_{fuel} = 0.097$ g/s and $\dot{m}_{air} = 1.72$ g/s. The spray flame corresponds to an operating point equal to $\dot{m}_{fuel} = 0.108$ g/s and $\dot{m}_{air} = 1.72$ g/s, giving an equivalent ratio equal to $\phi_{LB} = 0.95$ and a power P equal to 4.8 kW. Even if these results were not obtained simultaneously, the set of images presented in this figure are synchronized on the basis of the acoustic forcing signal over time.

In Fig. 6.38: the row-a corresponds to the class-averaged images, obtained from high-speed tomography views of the fuel droplets, recorded at the injector exit ($z/D_{exit} = 0.187$); the row-b corresponds to the class-averaged images, obtained from high-speed tomography views of the spray when the air flow was seeded with olive oil, during combustion; the images of the radial mid position of fuel droplets, obtained from tomography views of the spray without seeding the air flow, are presented in the row-c; the Abel transform of CH* emissions of the flame front is presented in the row-c for four times of one cycle of the acoustic forcing.

Main characteristics of the perturbed flow field in cold condition are found again during combustion and allow understanding its behavior. Under the impact of the axisymmetric disturbance field of PAN the flow field behavior is virtually but not perfectly axisymmetric due to the presence of the swirl. A large vortex is periodically formed at the same moment at the injector exit but does not evolve in the same manner on each side of the injector axis. A slight phase delay appears between the vortex ring observed in tomographic views of the flow seeded with olive oil. Regardless the perturbation amplitude studied here this large vortex is convected almost at the same velocity. The fuel droplets spatial evolution depends on their size. It is possible to classify three groups: droplets with a size small enough such that they are rapidly evaporated; those becoming small enough to be rolled up by the large vortex; finally those with a suf-

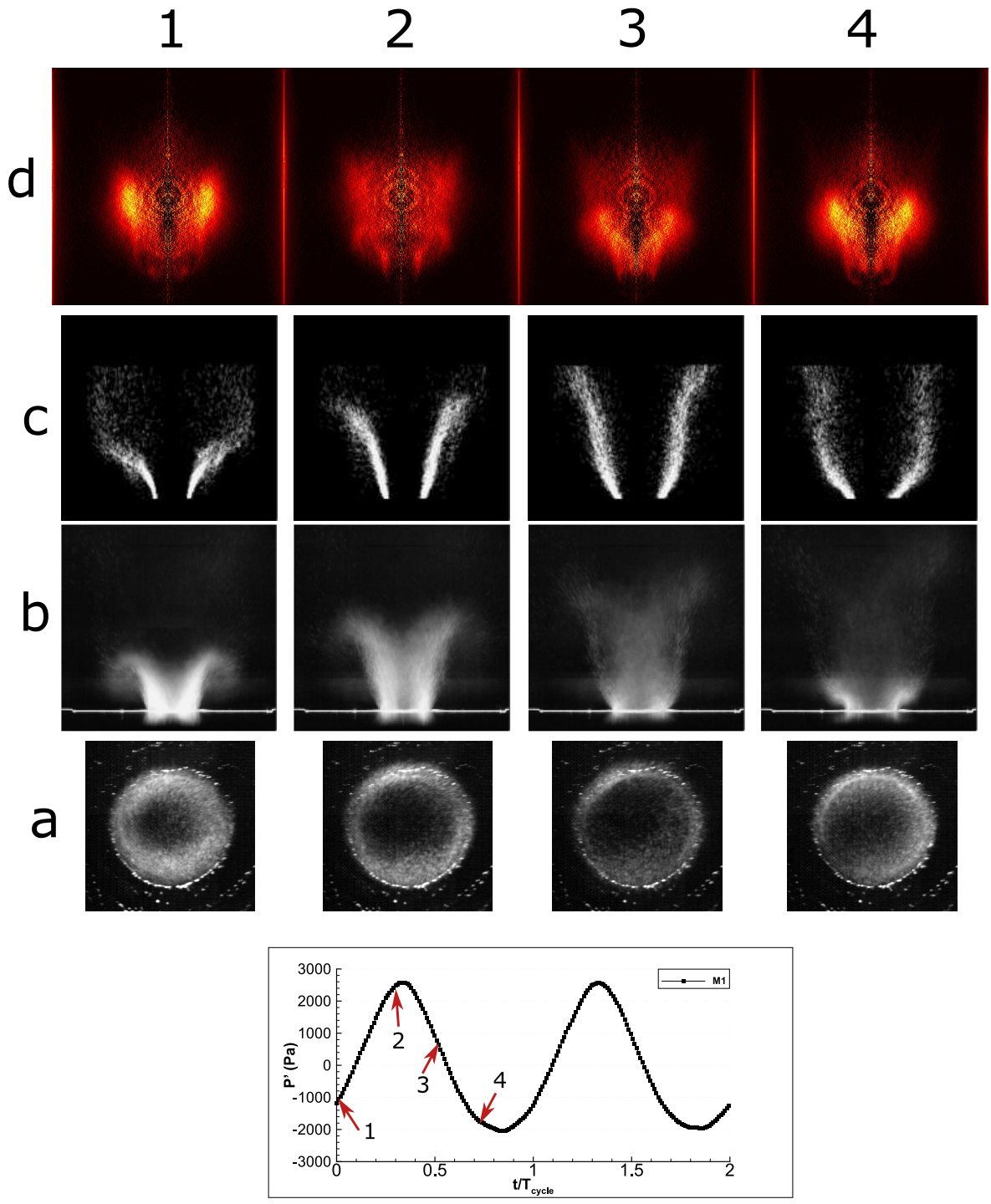

Figure 6.38: Reconstruction of the behavior of the two-phase flow and the spray flame of the central injector, during one cycle of the acoustic forcing: horizontal class-averaged images of the droplet (row-a), vertical class-averaged images of the spray with the air flow seeded (row-b), vertical views of the mid radial position of the droplets (row-c), images of the Abel transform of the CH* emissions of the flame. A half of the flame was deconvoluted and symmetrically duplicated to generate the entire flame (row-d).

ficiently large size such that they are only deviated from their trajectory and follow a rather ballistic trajectory. The droplets visualized in the tomography views belong rather to the third group.

The flow rate periodically modulated, accelerated and decelerated, and so the measured Swirl number periodically varying (between 0.3 and 1.5 for $|P'| = 1000$ Pa) generates at least two type of vortex breakdown (single spiral or double helix type) and even the periodic disruption of the CRZ induced by the vortex breakdown. As the CRZ is the main mechanism by which the flame is stabilized, its behavior directly impacts the flame response. The phase and class-averaged images of the flame front have revealed an axial pulsating motion at the forcing frequency. By the chemiluminescence signal recorded for perturbation amplitudes in the range of 100 to 2100 Pa a saturation phenomenon has been highlighted. Velocity and pressure fluctuations measured within the air plenum and within the chamber allowed to determine flame transfer functions at f_r in the case of a downstream transverse forcing. In particular we have shown that FDF based on velocity fluctuations in the chamber can be linked with FDF determined from velocity fluctuations measured in the air plenum by the consideration of the measured injector admittance and neglecting acoustic pressure drop, something not possible in upstream forcing [129]. A convective term has been also considered as soon as the velocity measurement within the chamber is not made in the nozzle exit section ($z = 0$).

Chapter 7

Generalization of the approach and the saturation phenomenon

In this chapter the investigation made at the pressure antinode is extended to the intensity (IAN) and velocity antinodes (VAN). Each section, with the exception of the last one, is divided in two parts related to IAN and VAN respectively. The last section of this chapter addresses the saturation phenomenon, which was highlighted at PAN, putting together results from PAN, IAN and VAN basins of influence.

Study at the intensity antinode (IAN)

As mentioned in chapter 5, the basin of influence of **the intensity antinode** (IAN) is the region where the acoustic flux reaches its maximums values. It is associated to strong acoustic pressure and velocities gradients even though these are not at their maximums. When injected in this region the flow is therefore spatially disturbed over time by a local distribution of the acoustic field not axisymmetric with respect to the injector geometry. Here, the basin is defined in the spatial domain at $2/16 \leq |x/L_c| \leq 3/16$. The central injector is positioned within the IAN region, at $x/L_c = -2.24/16$ ($L_c = 0.8$ m). At this position, in addition to the non-axisymmetric impacts of the acoustic field, the flow is submitted to the influence of the acoustic velocity characterized by a lateral displacement presenting a non negligible spatial gradient. In the first section of this chapter we analyze the structure of the seeded air flow by means of tomography views. Subsequently, we use quantities based on droplet visualization (median radial position of the spray, droplets dispersion, median vertical streaklines) in order to describe the droplet spatial and temporal evolution during combustion. In the last section of this chapter, quantification of the flame light emissions and the characterization of its shape depict the perturbed flame behavior in the IAN basin.

Study at the velocity antinode (VAN)

The basin of influence of **the velocity antinode** (VAN) is the region where the transverse acoustic velocity reaches it maximum values. Firstly, the perturbed air-flow positioned at VAN, shows characteristics similar to those without acoustic (see

section 3.3.2) predominating near to the injector exit. Downstream, the entire air-flow oscillates laterally at the forcing frequency, exhibiting a movement that can be *a priori* assimilated to a rocking motion. Secondly, analysis is made with combustion. The spray behavior during the acoustic forcing shows that the fuel droplets mostly follow the air-flow motion. The study of the flame front behavior under acoustic forcing, reveals the formation on average of wrinkles, alternatively generated on the left and right sides of the flame front. The combustion intensity, characterized by the OH* or CH* chimiluminescence, features an intensity pulsation that moves diagonally from the right to the left coinciding with the clockwise swirl turning direction imparted to the spray flow. These features reveal a more complex motion of the flame front than a simply lateral oscillation. Our observations suggest that the obtained flame motion is due to the wrinkles formed on its front that would follow a helical spiral path as result of the flow swirl motion along with its vertical velocity.

7.1 Theoretical acoustic velocity field within the chamber

At the positions of IAN and VAN, the effects of the acoustic velocity field cannot be neglected anymore, as was in the case at PAN. So, it is necessary to start defining the acoustic velocity field.

Theoretically, pressure fluctuations may be expressed as a sine wave function of time:

$$P_{ac}(x,y,z,t) = P_{ac}(x,y,z)cos(2\pi f_r t) \tag{7.1}$$

Considering that the acoustic pressure is constant along the y-direction and also in a region of interest along z, in which the flame is situated[1], the acoustic pressure can be written as:

$$P_{ac}(x,t) = P_{max}cos(k_x x)cos(2\pi f_r t) \tag{7.2}$$

with $|P_{max}|$ the pressure fluctuation amplitude. The associated acoustic velocity field may be then obtained by Eq. 7.3:

$$\boldsymbol{V_{ac}}(x,t) = -\frac{1}{\rho}\int \boldsymbol{grad}\,[P_{ac}(x,t)]\,dt = V_{max}sin(k_x x)sin(2\pi f_r t)\boldsymbol{e_x} \tag{7.3}$$

with $V_{max} = (P_{max}k_x)/(\rho 2\pi f_r)$. An example of the theoretical acoustic field is presented in Fig. 7.1. As it is possible to see from this latter figure and the precedent formulations, acoustic velocity and pressure fluctuations are spatially and temporally in phase quadrature between each other.

[1]Measurements in chapter 5 show that pressure amplitude is almost constant up to $z/h_c = 0.3$, which is a distance larger than the flame height ($z/h_c \approx 0.24$).

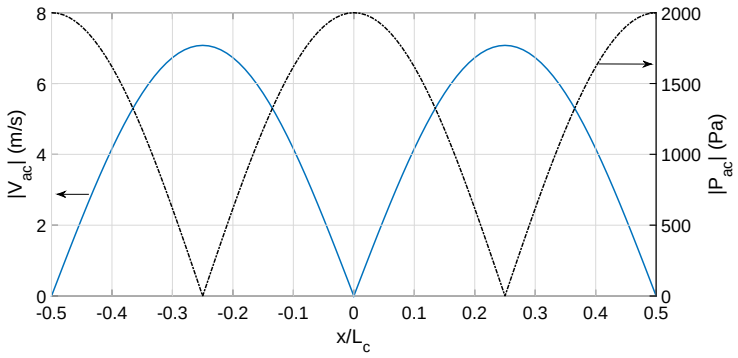

Figure 7.1: Theoretical acoustic field vs. x/L_c for $f_r = 785$ Hz, $L_c = 0.8$ m. The solid line is the velocity amplitude $|V_{ac}|$ and the dashed dot line is the pressure amplitude $|P_{ac}|$, both calculated from Eq. 7.3 and Eq. 7.2 respectively.

7.2 Two-phase flow behavior under acoustic forcing

In the first part of this section, the air-flow seeded with olive oil particles is studied without combustion, as it is subjected to the acoustic perturbations of the intensity antinode basin of influence first, and second perturbations of the velocity antinode (VAN). Vertical and horizontal tomography views are analyzed in particular in order to highlight the structure of the air-flow during the acoustic forcing. The second part of this section is devoted to the characterization of the n-heptane droplet behavior with combustion, also by means of tomographic views. There, measurements are performed in two cases, i.e. with and without seeding the air-flow. The aim of this investigation is to highlight the effects of the acoustic field on the flow with respect of those seen with the system located at PAN, since outside PAN the acoustic velocity field influence is not negligible anymore.

7.2.1 Air-flow structure characteristics without combustion

7.2.1.1 Intensity Antinode

Three levels of the acoustic pressure amplitude have been successively applied to the central injector placed in the IAN basin. The pressure amplitude is measured at the M1 position ($x/L_c = 0$), each pressure signal is simultaneously recorded with the capture of vertical tomography images by a high speed camera. The three signals are post-phased in order to facilitate analysis and comparison between them and the associated images. Fig. 7.2 shows the pressure signals and vertical images corresponding to the three levels of forcing: (a) $|P'| \approx 800$ Pa, (b) $|P'| \approx 1400$ Pa, (c) $|P'| \approx 2100$ Pa at the resonant frequency $f_r = 550$ Hz. The theoretical pressure amplitude at the central injector position ($x/L_c = -0.14$), is of about 52% of the amplitude measured by M1.

Three sequences of images are reported in Fig. 7.2(b) (a), (b) and (c) corresponding to the above-mentioned levels. The images serving as an illustration are extracted from

series of vertical laser tomography views distributed at six instants during a cycle. An image is then marked by the number of a row (ranging from 1 to 6) and the letter of a column (a, b or c). The times are marked in Fig. 7.2(a). The white horizontal line seen at the bottom of images comes from the light of the laser sheet scattered by the burner exit plate located in the bottom wall of the cavity ($z = 0$). The region of interest extends up to $z = 2.35D_{exit}$ and has an horizontal length of $3.75D_{exit}$.

It is highlighted that at the lower amplitudes (columns a and b) the air-flow conserves some features of its natural behavior, like the formation of Kelvin-Helmholtz type vortices at the outer layer, or the double pattern at the inner region, characteristic of the double helix type vortex breakdown (row-1 of the column-a circled in red). Nevertheless, in image of row-2 column-b, the overall flow is slightly tilted to the righ side. At the highest amplitude studied here, features of its natural behavior are not clearly identified. In image of the Fig. 7.2(b) row 2 column-c, is also noted that the overall flow is slightly tilted to the right side. This is interpreted as an effect of the lateral acoustic velocity perturbation which is at its maximum and in the positive x-direction when pressure is zero. Moreover, at the row-3, the instant where the pressure amplitude is diminishing from its maximum, for the three levels of forcing we note the formation of a vortex ring on the left outer layer at the injector exit (label 5 in the image). This structure belongs to a large primary vortex, similar to that observed when the central injector is placed at PAN. But contrary to PAN, the vortex is formed only at one side of the injector axis, namely the nearest side to the velocity antinode. Nevertheless, next to its formation the vortex ring is rapidly distorted and destroyed (see images in row-4). At this instant of the acoustic perturbation, the pressure amplitude is zero and the transverse acoustic velocity is maximum but in the negative x-direction. Thus, the air-flow in the row 4 seems to be laterally buffeted and in consequence deviated to the left. This can induce some matter ejections. The vortex is formed as a consequence of the flow acceleration, changing the swirl level of the flow (as we have explained in section 6.1.1), and causing a transient disruption of the CRZ induced by the vortex breakdown. Then, when the pressure amplitude is at its lowest value, the transverse acoustic velocity is close to zero and the flow is only very slightly tilted. At this moment of the acoustic perturbation, in row-6 column-a, the double helix type vortex breakdown seems to be recovered. In the case of higher levels (columns (b) and (c)), is possible to note the formation of Kelvin-Helmholtz type vortices at the inner layer, followed by the restoring of a vortex breakdown which occurs rather as single spiral type. This was already seen in the case of the axisymmetric perturbation of the flow at the basin of influence of the pressure antinode.

The competition between the double helix and single spiral types of vortex breakdown, as was observed in the study at PAN, is also present at IAN. By looking at the horizontal tomography views of the Fig. 7.3(b) rows 1 and 2, recorded at $z/D_{exit} = 0.375$, we see a single dark pattern that becomes a double pattern. Then, the pattern vanishes which is interpreted as the vortex breakdown disruption due to the flow acceleration, as was explained in section section 6.1.1.

In the IAN basin, the periodical tilting of practically the overall air injected caused by the acoustic disturbance field is well noted. Moreover, the large vortex structure is not well formed neither convected, there is a little amount of seeded air rolled up, and

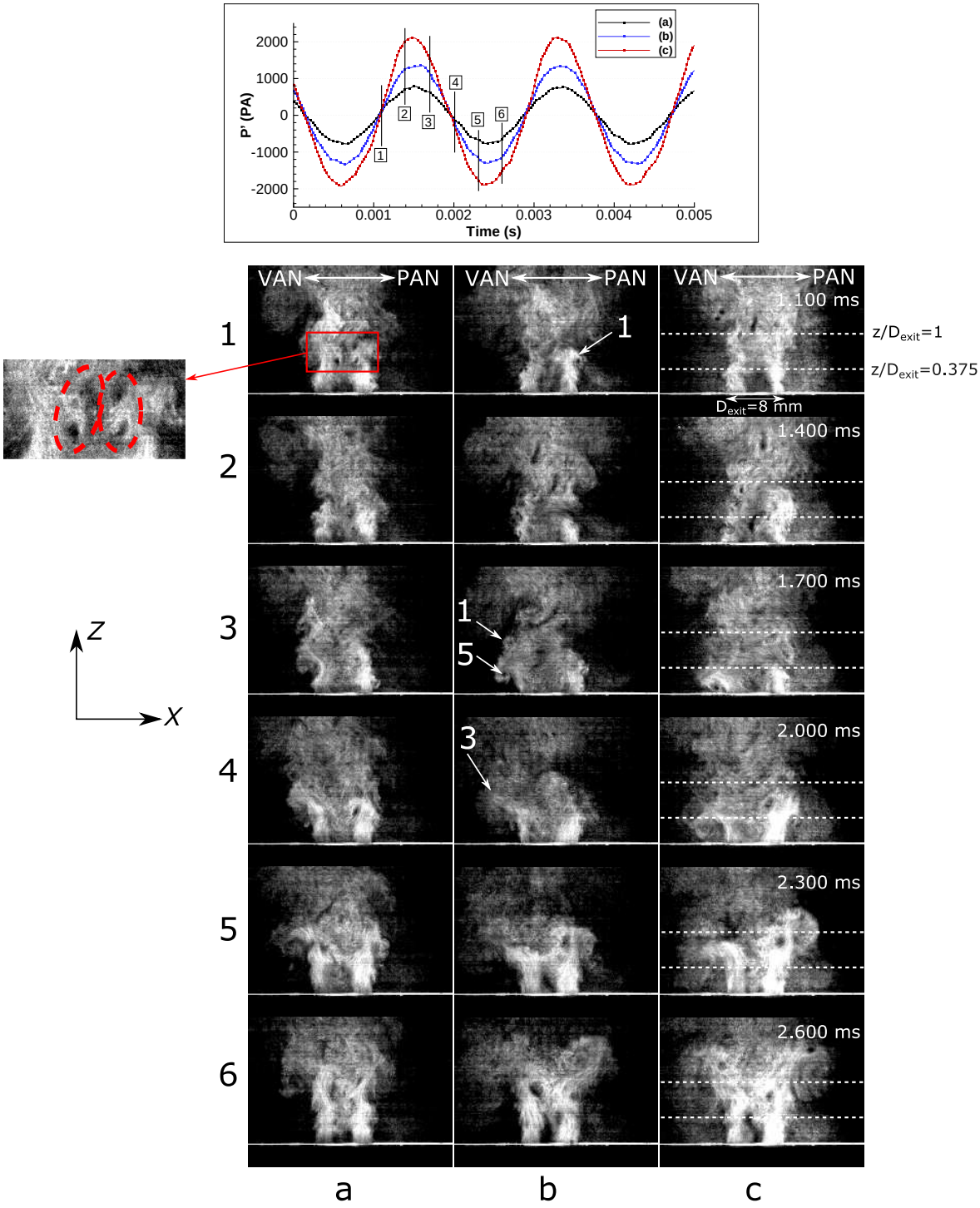

Figure 7.2: (Top) Signals of the three different levels of acoustic pressure amplitude measured at the M1 location. Central injector at the IAN basin. Labels 1 to 6 correspond to the image row number of the bottom figure. (Bottom) Vertical tomography views of the seeded air-flow, for 6 different times, during a cycle of the acoustic forcing. (a) $|P'| \approx 800$ Pa, (b) $|P'| \approx 1400$ Pa, (c) $|P'| \approx 2100$ Pa. (1) Kelvin-Helmholtz type vortices; (3) matter ejected; (5) Cross-section of the ring of the primary vortex. $f_r = 550$ Hz, $\dot{m}_{air} = 1.724$ g/s, without combustion.

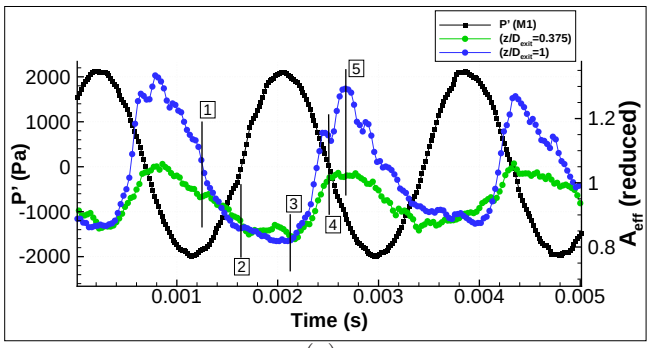

(a)

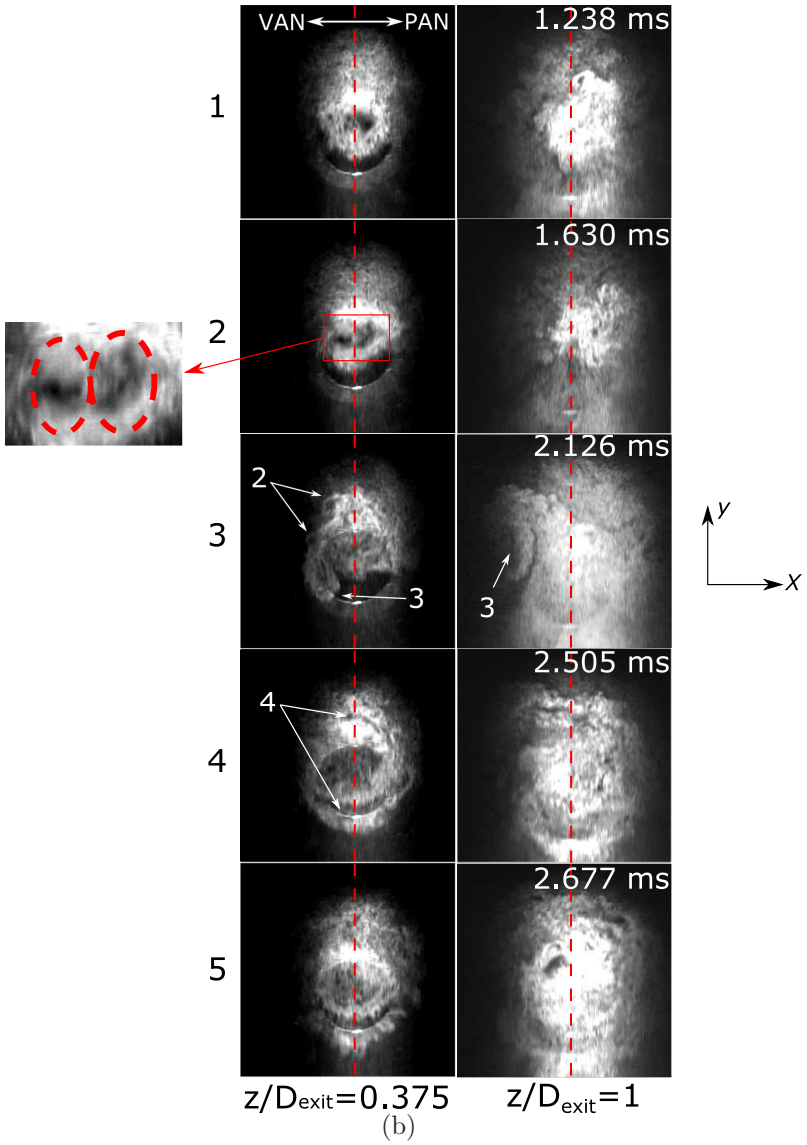

(b)

Figure 7.3: (Top) A_{eff} signals from horizontal tomography views reduced by its mean value, and pressure perturbation signal at the position of M1. Central injector at the IAN basin. Labels 1 to 5: image row number of the bottom figure. (Bottom) Horizontal tomography views of the seeded air-flow, for 5 different times, during a cycle of the acoustic forcing, and for two z-positions. (2) Small azimuthal vortices; (3) ejection of matter; (4) cut of the ring of a primary vortex. $|P'| \approx 2100$ Pa, $f_r = 550$ Hz, $\dot{m}_{air} = 1.724$ g/s, without combustion.

the perturbation is not well transported by this structure to downstream regions. The signals of A_{eff} (see section 4.2.1) reduced by its mean values are plotted in Fig. 7.3(a). They were obtained from horizontal tomography views of the seeded air-flow, at two z-positions separated of $0.625D_{exit}$. Despite the distance between these two planes we see that the signals evolve in-phase.

As we can see in vertical tomography views, the large vortex periodically formed is very distorted at $z/D_{exit} = 0.375$ and almost vanished by this z-position. In image of Fig. 7.3(b) row-4 left column, the vortex ring is barely visible on the top and bottom of the image while on the sides it is not recognized. The images recorded at $z/D_{exit} = 1$ are presented in the right column of Fig. 7.3(b). At this position, as the flow expands radially, the visualized seeded air-flow pattern is extended toward the zones where the intensity of the laser sheet (used for the tomography technique) decays (left and right edges of the images). In order to still visualize the seeded air-flow in these zones, the brightness of the images of the right column has been enhanced. Whatever the instants the air-flow pattern does not show an identifiable coherent structure. What is noted is that flow pattern is deviated alternatively to the sides. The right image of the row-1 shows the flow pattern deviated to the right and at the row 3 the pattern shows an ejection of matter probably connected with the ejections visualized at $z/D_{exit} = 0.375$. This tomography views highlight that the air-flow is rather buffeted to the left, and tilted to the right side. As the transverse acoustic velocity has the same amplitude when it is positive or negative, one can wonder why this difference is noted. This is because, when the pressure amplitude is zero and growing, the flow rate was previously accelerated, and now is being decelerated at the injector exit. But the air already injected still owns an important impulsion. The impulsion can be estimated as $\rho < U >$ with $< U >$, the spatially averaged vertical velocity. When the flow is accelerated it can reach velocities of same order of magnitude than the air flow bulk velocity ($U_b = 28.6$ m/s). Consequently, it is difficult to deviate it since the impulsion imparted by the acoustic velocity is ρV_{max} with the acoustic velocity amplitude V_{max} of about 4 m/s. In the other hand, during the time interval when the pressure is zero and decreasing, the flow rate is being accelerated at the injector exit but the air previously injected is flowing downstream with a low velocity. As a consequence, the flow impulsion is lower and the same acoustic impulsion is now more important compared to it. Hence, the transverse acoustic velocity perturbation is able to greatly deviate (buffet) the air-flow during this time interval.

As a conclusion of this part, we observe that the air flow positioned at IAN shows behavioral effects observed at PAN, but rapidly modified by the addition of a lateral buffet and tilted motion caused by the transverse velocity perturbation. We highlight that the vortex breakdown is periodically disrupted, even at the lowest level investigated here, due to the periodic fluctuation of the swirl level imparted to the flow. This leads to modifications of the center recirculation zone, and as a consequence, should impact the flame stabilization. It is expected that features highlighted in cold condition will help to understand the flow behavior during combustion, even though the flow structure is also modified by combustion The presence of the flame will modify what happens downstream due to the presence of hot gases products of the combustion process.

7.2.1.2 Velocity Antinode

Three levels of the acoustic pressure amplitude have been successively applied to the central injector placed in the VAN basin. The pressure amplitude is measured at the M1 position ($x/L_c = 0$), each pressure signal is simultaneously recorded with the capture of vertical tomography images by a high speed camera. The three signals are post-phased in order to facilitate analysis and comparison between them and the associated images. Fig. 7.4 shows the pressure signals and the vertical images corresponding to the three levels of forcing: (a) $|P'| \approx 800$ Pa, (b) $|P'| \approx 1400$ Pa, (c) $|P'| \approx 2100$ Pa at the resonant frequency $f_r = 550$ Hz. The pressure amplitude measured at the central injector position ($x/L_c = -0.256$), is not directly measured for this setup due to the presence of the quartz windows. However, the local acoustic pressure is interpolated from a measurement performed by the microphone M2 at $x/L_c = 0.25$, $y/e = 0.5$ and $z/h_c = 0.025$, the position of the other velocity antinode. The amplitude of the minimum of acoustic pressure found in cold conditions at this position can be up to 15% of the amplitude measured by M1, and so it is considered as residual.

Three sequences of images are reported in Fig. 7.4(b) (a), (b) and (c) corresponding to the above-mentioned levels. The images serving as an illustration are extracted from series of vertical laser tomography views distributed at six instants during a cycle. An image is then marked by the number of a row (ranging from 1 to 6) and the letter of a column (a, b or c). The times are marked in Fig. 7.4(a). The white horizontal line seen at the bottom of images comes from the light of the laser sheet scattered by the burner exit plate located in the bottom wall of the cavity ($z = 0$). The region of interest extends up to $z = 2.35D_{exit}$ and has an horizontal length of $3.75D_{exit}$.

For the three levels of acoustic forcing, it is noted that the air flow is periodically and laterally blown to the left and right side at the forcing frequency, with increasing amplitudes of the lateral displacement as the level of acoustic forcing is augmented. This is clearly noted downstream, but near to the injector exit the air-flow is rather tilted, that is why the overall movement can be assimilated to the rocking motion. Images in row-1 show that the air-flow exits straight from the injector. These images correspond to a moment where the amplitude of the acoustic pressure is minimum and so the transverse acoustic velocity is null. Downstream, the air flow deviated on the left side corresponds to the lateral displacement of the previous acoustic forcing cycle. As the amplitude of the pressure increases from its minimum value, the amplitude of the acoustic velocity grows and the air-flow close to the injector exit is tilted to the right side (see images in rows 2 and 3). When the amplitude of the pressure is maximum, the air flow close to the injector recovers its straight position (images in row-4). The air injected previously is now deviated on the right side of the images. The formation of Kelvin-Helmholtz type vortices at the outer layer can be identified at the lowest level of the perturbation (row-4, column-a). Images in row 5 show the air flow being first tilted when exits the injector to be then laterally displaced on the left side at the downstream zone (see images in row-6), whereas at the zone close to the injector exit the air flow recovers the straight position again. By analyzing the images of each column during the forcing cycle, it is noted that there is a delay of about $\pi/2$, between the tilted of the air-flow close to the injector exit, and the lateral deviation

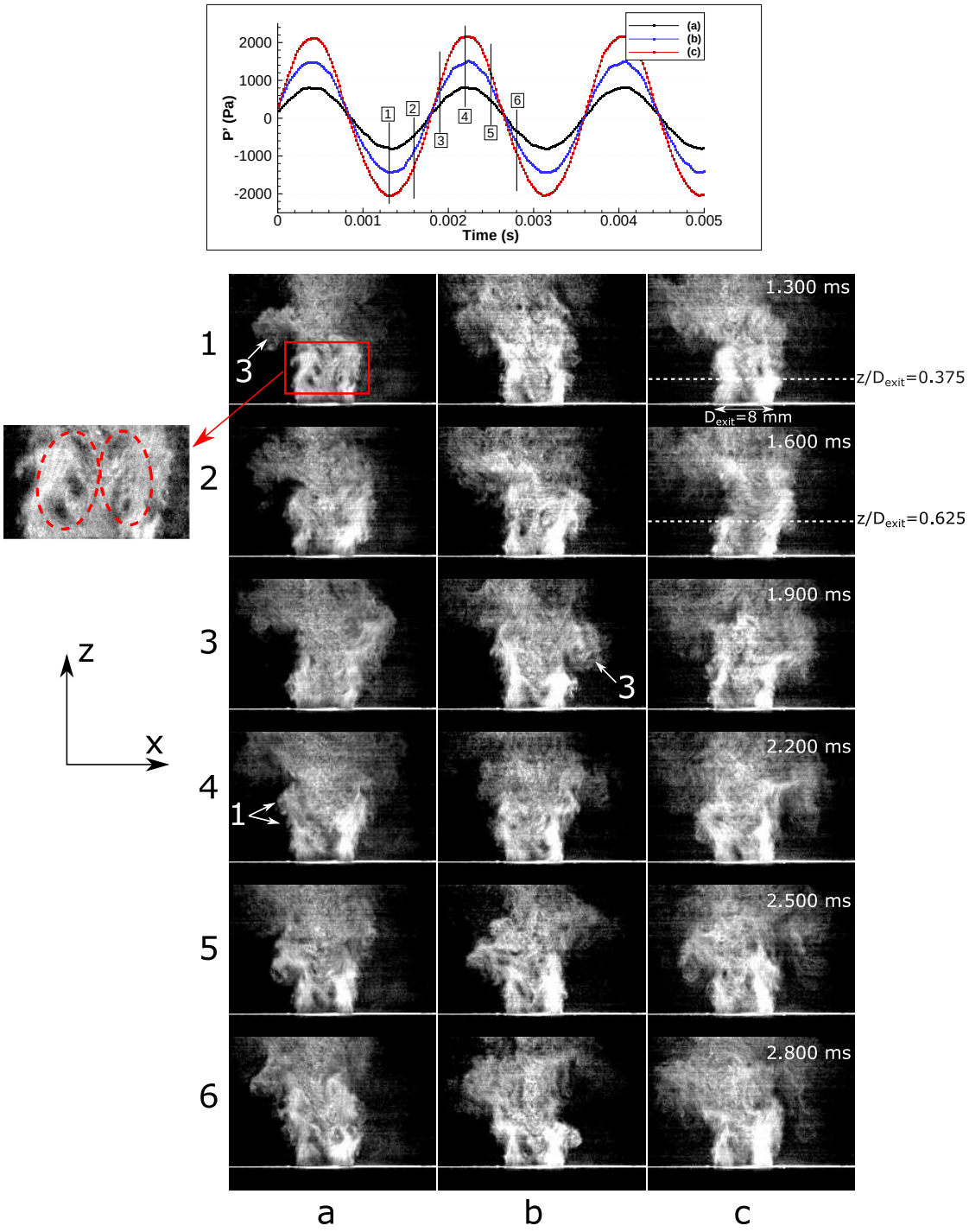

Figure 7.4: (Top) Signals of three levels of the acoustic pressure measured at the center of the cavity by M1. Central injector at the basins of VAN. Labels 1 to 6: image row number of the bottom figure. (Bottom) Vertical tomography views of the seeded air-flow, for 6 different times, during a cycle of the acoustic forcing. (a) $|P'| \approx 800$ Pa, (b) $|P'| \approx 1400$ Pa, (c) $|P'| \approx 2100$ Pa. (1) Kelvin-Helmholtz type vortices; (3) matter ejected. $f_r = 550$ Hz, $\dot{m}_{air} = 1.724$ g/s, without combustion.

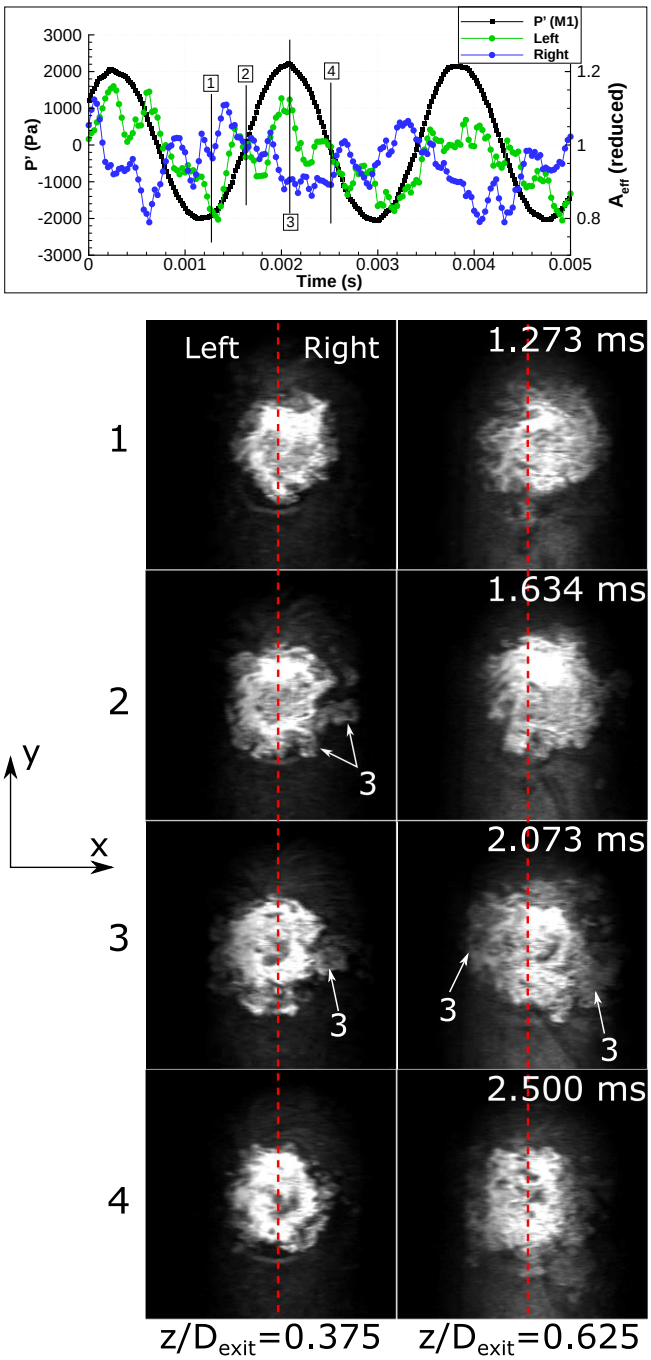

Figure 7.5: (Top) A_{eff} signals from the left and right sides of the horizontal tomography images ($z/D_{exit} = 0.375$), reduced by its mean value, synchronized with the pressure signal at the position of M1. Central injector at the basin of VAN. Labels 1 to 4: image row number of the bottom figure. (Bottom) Horizontal tomography views of the seeded air-flow, for 4 different times, during a cycle of the acoustic forcing and for two z-positions. (3) Ejection of matter. $|P'| \approx 2100$ Pa, $f_r = 560$ Hz, $\dot{m}_{air} = 1.724$ g/s, without combustion.

downstream.

For the three levels of the forcing, in several of the images, at the inner layer the pattern characteristic of the double helix vortex breakdown is recognizable (see for instance row-1 column-a). The vortex breakdown does not seem to be disrupted during the acoustic forcing, but greatly deformed as the amplitude of the transverse acoustic velocity increases (note for instance the double pattern in row-1 or row-4 both of column c). No effect is noted on the air-flow behavior that could be attributed to the residual acoustic pressure fluctuation at the basin of VAN.

By using a series of horizontal tomography views, the left and right half of each view were considered in order to obtain two signals over time, each one corresponding to one side. Values of the signals ($A_{eff}(t)$) are the total light intensity resulting from the contribution of all pixels within the left half and the right half of an image. Each signal is then reduced by its mean value. As illustration, the two reduced signals of $A_{eff}(t)$, obtained from horizontal views at $z/D_{exit} = 0.375$, are plotted in Fig. 7.5 synchronized with the pressure fluctuation recorded at the central PAN. They evolve out-of-phase, as expected, evidencing the lateral and periodic displacement of the flow. Four high-speed horizontal tomography views are plotted in Fig. 7.5 (bottom). These views correspond to series taken at $z/D_{exit} = 0.375$ and $z/D_{exit} = 0.625$ respectively. Some dark patterns are noted within the visualized seeded air. These patterns correspond to slice of the vortex breakdown but, as the air-flow is tilted and laterally displaced the slices do not clearly form the pattern associated with the double helix vortex breakdown.

7.2.2 Spatial and temporal behavior of n-heptane droplets during combustion

7.2.2.1 Intensity Antinode

Properties by means of horizontal views exploration

In Fig. 7.6 is plotted over time, for several z-positions, the radial mid position values of the droplets r_d^{mid}. The droplet position dispersion (δ_r) and the evolution of the number of pixels linked with the number of droplets are plotted in Fig. 7.7. By using the horizontal high speed tomography views, the evolution over time of these quantities has been computed within a rectangular region defined in each images of a series. The region extends on the acoustic axis direction, on the left and right sides of the injector axis (see section 4.2). The zero values in the plot of Fig. 7.6 belong to points where no droplet was detected in the region where calculation was made. These points are also zero in the plots linked with the number of droplets, and they are not accounted for in the dispersion calculation. The three quantities fluctuate at the acoustic forcing frequency (f_r). Due to the cone injection, the radial mid position of the droplets r_d^{mid} increases with z while the amplitude of its fluctuations also increases. By comparing the left and right sides at a given z-position, this quantity evolves in-phase with a similar amplitude of fluctuations. The same behavior with z is detected for fluctuations of the droplet position dispersion on the left and right sides (Fig. 7.6).

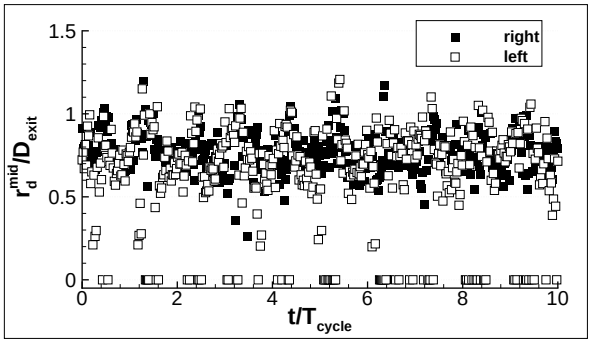

(d) $z/D_{exit} = 1.062$

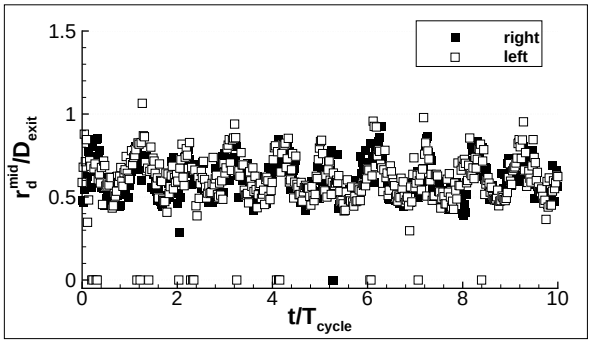

(c) $z/D_{exit} = 0.625$

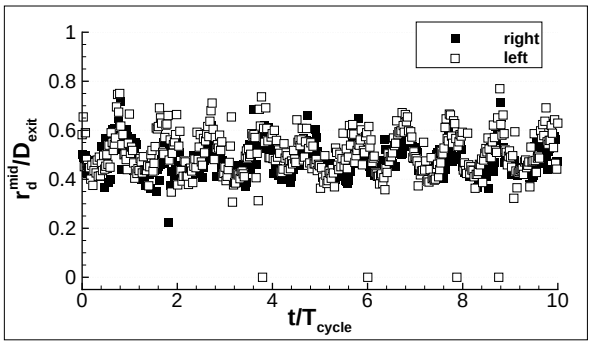

(b) $z/D_{exit} = 0.375$

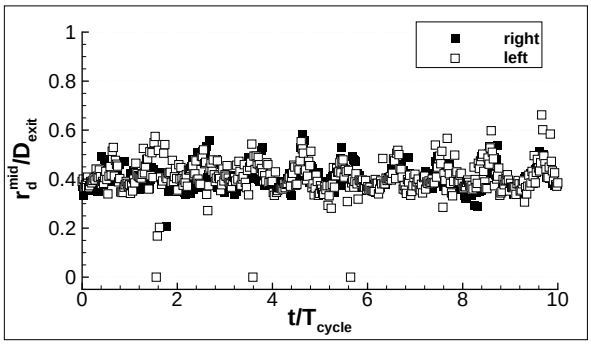

(a) $z/D_{exit} = 0.187$

Figure 7.6: Evolution of the radial mid position of the droplets (r_d^{mid}) calculated from horizontal tomography views (for droplets size > 20 μm). Pressure-perturbation amplitude measured by M1: $|P'| \approx 1300$ Pa. Central injector at the IAN basin. $f_r = 790$ Hz, $\dot{m}_{air} = 1.724$ g/s, $\dot{m}_{fuel} = 0.097$ g/s , $\phi_{LB} = 0.85$.

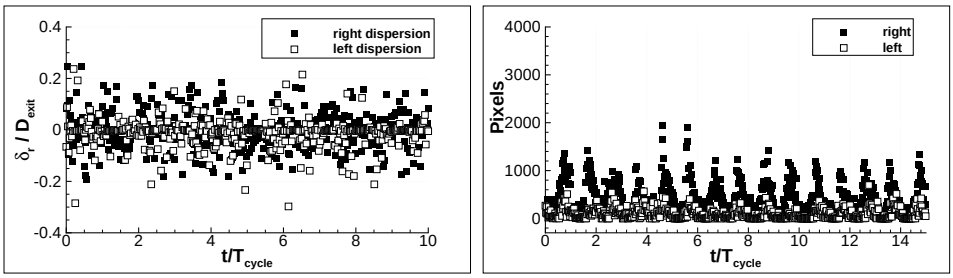

(d) $z/D_{exit} = 1.062$

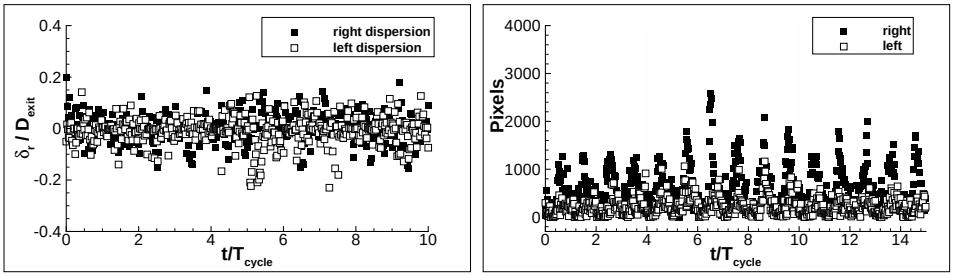

(c) $z/D_{exit} = 0.625$

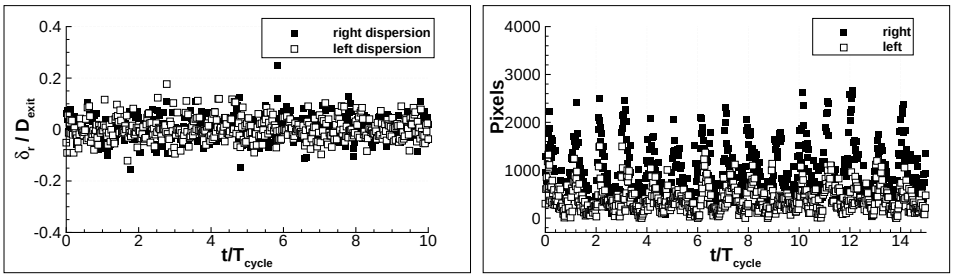

(b) $z/D_{exit} = 0.375$

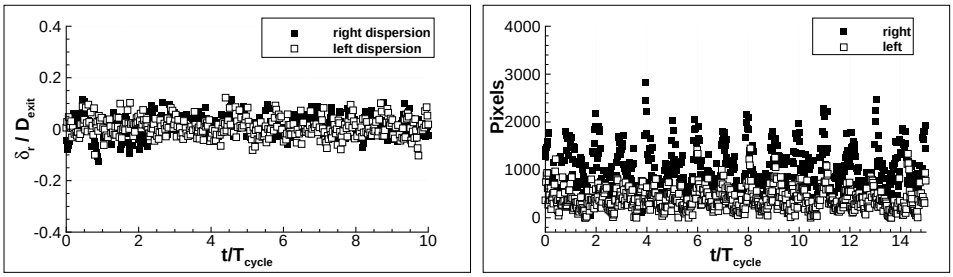

(a) $z/D_{exit} = 0.187$

Figure 7.7: Evolution of the fuel droplets dispersion δ_r (left column) and the number of pixels (right column) linked with the number of droplets, calculated from horizontal tomography views (for droplets size > 20 μm). Pressure-perturbation amplitude measured by M1: $|P'| \approx 1300$ Pa. Central injector at the IAN basin. $f_r = 790$ Hz, $\dot{m}_{air} = 1.724$ g/s, $\dot{m}_{fuel} = 0.097$ g/s , $\phi_{LB} = 0.85$.

The dispersion δ_r is defined in section 4.2.3 as the deviation from the mid radius of the droplet spatial distribution (r_d^{mid}). The left column of Fig. 7.7 shows that δ_r increases with z-positions. Whatever the z position, δ_r presents a mean value of about zero over time. As it is calculated using the radial mid position value of the droplets as reference, this fact indicates that droplets are quite equally distributed around r_d^{mid}. The number of pixels between the left and right sides of the injector axis is different. This was also observed with the injector at PAN, so this asymmetry is attributed to defects in the liquid injection. Globally, the droplets behavior seems to be governed mostly by the pressure amplitude fluctuations, since no significantly shift is noted in the fluctuations of these quantities between the left and right sides, that can be ascribed to transverse velocity fluctuations. As we have seen in the case without combustion (see section 7.2.1), effects of the transverse acoustic velocity may be more important for higher levels of the acoustic pressure amplitude applied within the cavity.

Properties by means of vertical views exploration

By using a series of 2000 high speed tomography images of the n-heptane droplets and the seeded-air, we have performed a reconstruction of a full cycle of the acoustic forcing, with 50 class-averaged images, calculated by the procedure explained in section 4.1. We have set the camera with an exposure time of 40 μs and a recording speed of 20 kfps, in order to obtain a satisfactory visualization of both n-heptane droplets and seeded-air. Fig. 7.8(left) shows the averaged images at four instants of the acoustic forcing cycle. The pressure fluctuation amplitude measured by microphone M1 at the center of the cavity is of about 2000 Pa. In these figures it is possible to distinguish between the droplets (high intensity of the light scattered) and the seeded-air (low light intensity). The seeded-air near the injector exit seems to envelope the droplets, but downstream the seeding particles evaporate faster due to their smaller diameters compared to the range of diameters of visualized fuel droplets ($> 20\mu$m). There is a vortex formation only on the left side of the injector exit (label 2 in the image), which is rapidly deformed when it is convected, due to the effects of the transverse acoustic velocity. On the side towards the PAN position the vortex ring is not recognized. This is similar to what was observed in the case without combustion previously presented, where only a not well formed half of the vortex ring (towards the VAN position) was recognized from horizontal tomography views. Due to this vortex shedding the droplets are more or less deviated according to their diameter sizes. The droplets of lower diameter size could be greatly deviated by the vortex when it is formed. The magnified views of Fig. 7.8 shows that emission lines of visualized droplets are greatly affected by the vortex. The exposure time is long enough to note that some fuel droplets describe a trajectory close to the horizontal direction. Hence, the amount of n-heptane droplets that arrives to the flame front is spatially not uniformly distributed.

From the high speed vertical tomography views of the spray without seeding the air-flow, we calculate again the radial mid position value of droplets distribution, on the left and right side of the injector axis. This is carried out row by row, by detecting the first and the last droplet in the row, within the region of interest defined on each side of the injector axis. By performing this, we get a series of vertical views of the skeleton of the spray (see section 4.3). In order to enhance the visualization of the

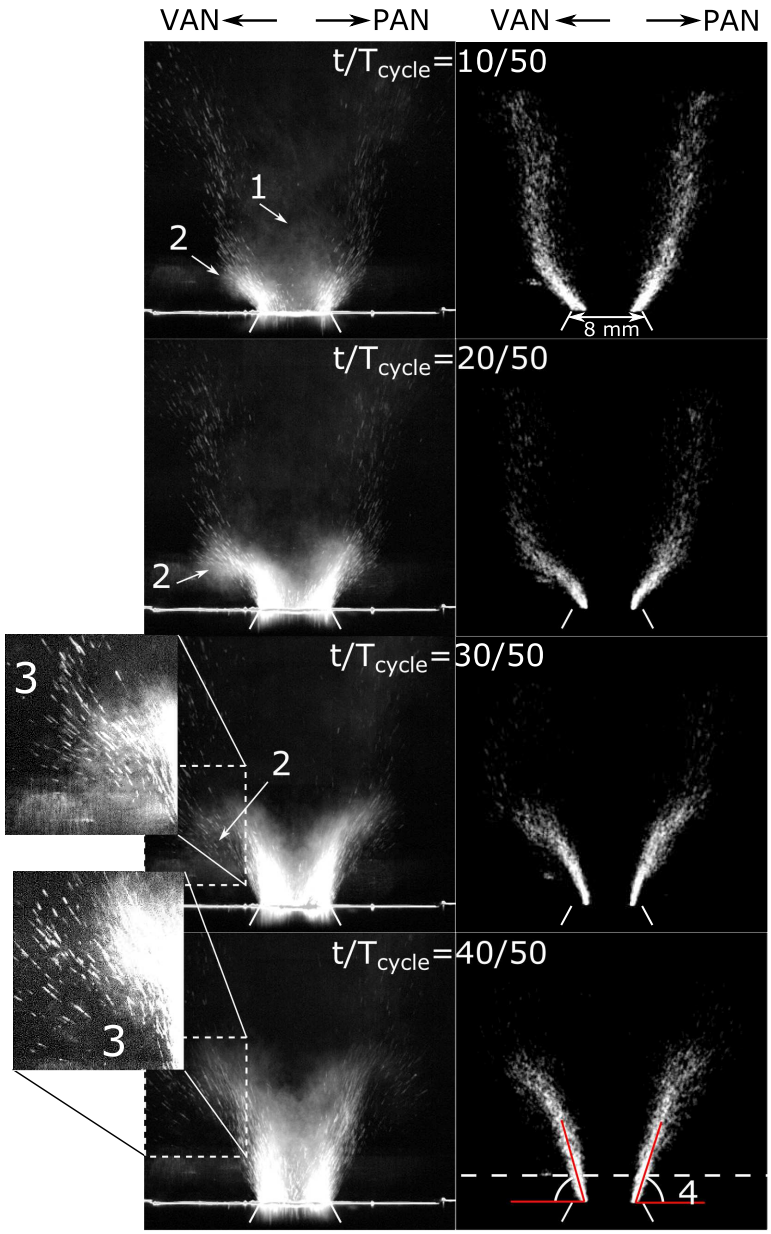

Figure 7.8: Class-averaged images at four instants of the acoustic forcing cycle, obtained from vertical tomography views of the seed-air flow and n-heptane droplets during combustion: n-heptane droplets and seeded air-flow (left), droplets mid positions (right). (1) seeded air; (2) vortex formation; (3) droplets deviated by the vortex; (4) injection angle of the droplets, calculated at $z/D_{exit} = 0.4$. $|P'| \approx 2000$ Pa measured by M1, $f_r = 795$ Hz, $\dot{m}_{air} = 1.724$ g/s, $\dot{m}_{fuel} = 0.097$ g/s, $\phi_{LB} = 0.85$.

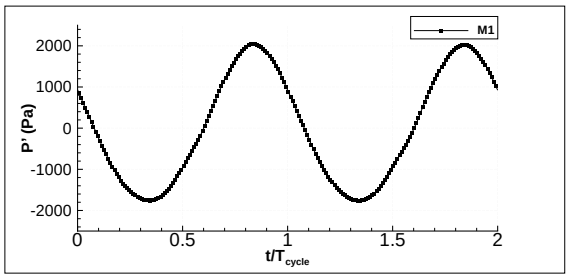

(a)

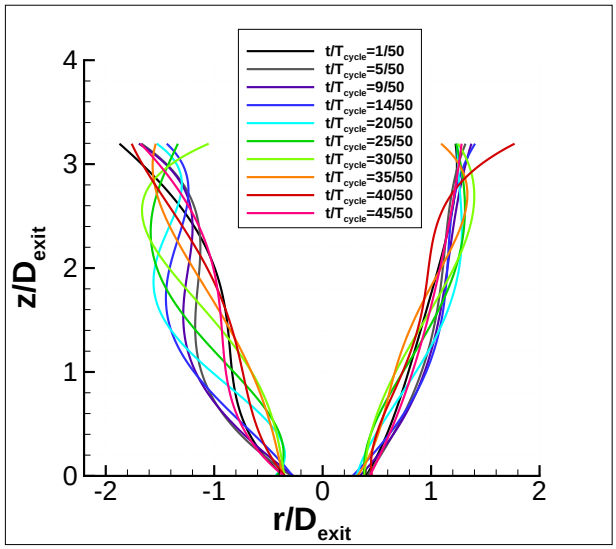

(b)

Figure 7.9: (a) Pressure perturbation signal measured at the central PAN (M1 position). (b) Droplets position lines at several instants of a cycle of the acoustic forcing. The central injector is positioned at the basin of IAN. $f_r = 795$ Hz, $\dot{m}_{air} = 1.724$ g/s, $\dot{m}_{fuel} = 0.097$ g/s , $\phi_{LB} = 0.85$.

droplets motion during the acoustic forcing, by using the skeleton images of the spray, a full cycle is reconstructed at the acoustic forcing frequency. The reconstruction is made with 50 class-averaged images (as those in Fig. 7.8 right), each of them leading to a region of radial mid positions along z. Finally, a polynomial fitting is performed on the data points of the regions associated to the left and right sides respectively. Results are plotted in Fig. 7.9. For this level of the acoustic perturbation it is well noted that the amplitude of the fluctuation of r_d^{mid} of the left side is higher than that of the right side. Fig. 7.9(b) indicates that this dissymmetry of the visualized droplets is rather the consequence of the vortex formation on the left side of the injector exit than the effect of the transverse acoustic velocity. The fitted lines of the left side at IAN are similar to the fitted lines found when the injector is positioned at PAN. By using the series of vertical views of the skeleton of the spray, we estimate the evolution over time of the injection angle defined with respect to the horizontal axis and the mid position of a droplet at $z/D_{exit} = 0.4$, on the left and right sides of the injector axis (see Fig. 7.8). The injection angles evolve globally in-phase at the forcing frequency, reaching maximum angle values close to 90°. However, the left injection angle signal

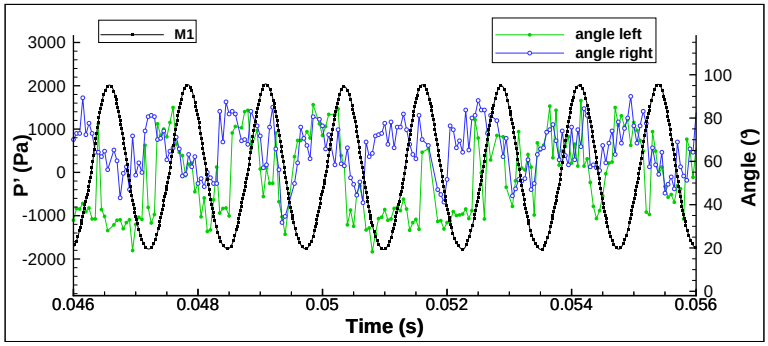

Figure 7.10: Evolution of the angle of injection formed by the n-heptane droplets at the left and right side of the injector, in vertical tomography views of the n-heptane droplets, at the injector exit. $f_r = 795$ Hz, $\dot{m}_{air} = 1.724$ g/s, $\dot{m}_{fuel} = 0.097$ g/s , $\phi_{LB} = 0.85$

at each cycle reaches lower values than the right signal. This is again an effect of the vortex formation at the injector exit. These results are plotted in Fig. 7.10, where the injection angle signals are synchronized with the pressure fluctuation signal measured by M1 at $x/L_c = 0$.

The dissymmetry found on the spray flow, is characterized by a discrepancy in the vortex formation between the left and right sides of the injector axis. The side where the vortex formation is clearly visualized is the nearest to the velocity antinode. This feature is something similar to that found in [83] for a configuration with a laminar premixed jet V-flame. In particular the nearest side to PAN was the most perturbed while on the side nearest to VAN the vortex ring formation is better recognized. Authors explain the symmetry rupture as the result of a cross contribution of the pressure and pressure x-gradient. This implies that an important pressure gradient is necessary, but also a pressure amplitude high enough to produce the most visible dissymmetry. Thus, the cross-contribution of the acoustic pressure and its x-gradient, may explain the dissimetry of the flow response encountered here. We remember that the theoretical acoustic pressure field along the x-direction can be approximated by:

$$P_{ac} = P_{max} cos(k_x x) \tag{7.4}$$

where the temporal term is omitted. The x-gradient of this acoustic pressure field is:

$$\frac{\partial P_{ac}}{\partial x} = -P_{max} k_x sin(k_x x) \tag{7.5}$$

where $k_x = 2\pi/L_c$. The product of the acoustic pressure by its x-gradient is in fact the x-gradient of the acoustic energy density (e_{ac}), multiplied by ρc^2. This is written in Eq. 7.6, where the temporal term is omitted.

$$\rho c^2 \frac{\partial e_{ac}}{\partial x} = -P_{max}^2 k_x cos(k_x x) sin(k_x x) \tag{7.6}$$

We see in Fig. 7.11 that at the location $x/L_c = 0.14$, even if the absolute value of the

acoustic pressure x-gradient is not maximum, the absolute value of Eq. 7.6 is close to its maximum.

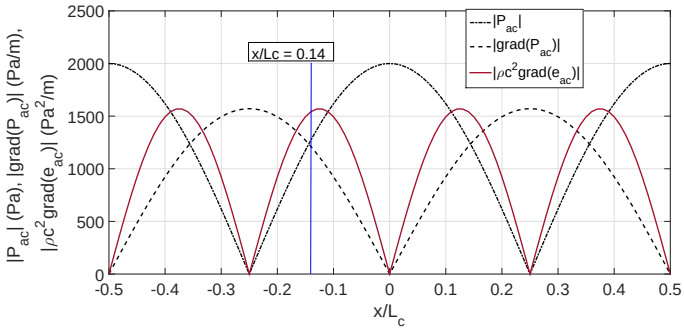

Figure 7.11: Absolute values of the theoretical acoustic pressure (dash dotted line), acoustic pressure x-gradient (dashed line) and the x-gradient of the acoustic energy density (red solid line), versus x/L_c. For this plot $|\boldsymbol{grad}(P_{ac})|$ and $|\rho c^2 \boldsymbol{grad}(e_{ac})|$ are divided by 10 and $1 \cdot 10^4$, respectively.

7.2.2.2 Velocity Antinode

The same procedure applied for the spray flow analysis made for IAN is now applied to analyze the series of vertical tomography views of the n-heptane droplets for the case at VAN. The diagnostics applied also keep the same parameters used before. Class-averaged images are again computed (see procedure in section 4.3) from 2000 high speed tomography views of the air-flow seeded with olive oil particles and also of only n-heptane droplets. In Fig. 7.12(left) It is observed that at the downstream regions where the lateral periodic displacement is more noticeable, the n-heptane droplets are not displaced as much as the seeded air is. In order to enhance the visualization of the droplets motion during the acoustic forcing, by using the skeleton images of the spray, a full cycle is reconstructed at the acoustic forcing frequency. The reconstruction is made with 50 class-averaged images (as those in Fig. 7.12 right), each of them leading to a region of radial mid positions along z. Finally, lines fit data of the regions associated to the left and right sides respectively. Results are plotted in Fig. 7.13.

The fitted lines clearly highlight that the spray is also impacted by the transverse acoustic velocity which induces a periodic lateral displacement of the droplets. The fluctuation amplitude of the horizontal position of the droplets increases as we move downstream. This implies a perturbation of the droplet position that propagates downstream as wave on the fitted lines. They are alternatively formed on the left and right sides of the injector axis as is revealed by the fitted lines. Each of the fitted lines corresponds to a time of the position wave propagation. The estimation of an injection angle defined with respect to the horizontal axis and the mid position of a droplet at $z/D_{exit} = 0.4$, on the left and right side of the injection axis, was made by using the skeleton views of the spray. Thus, we obtain the evolution over time of the injection angles. Here the fluctuation of the injection angle during the acoustic forcing is smaller

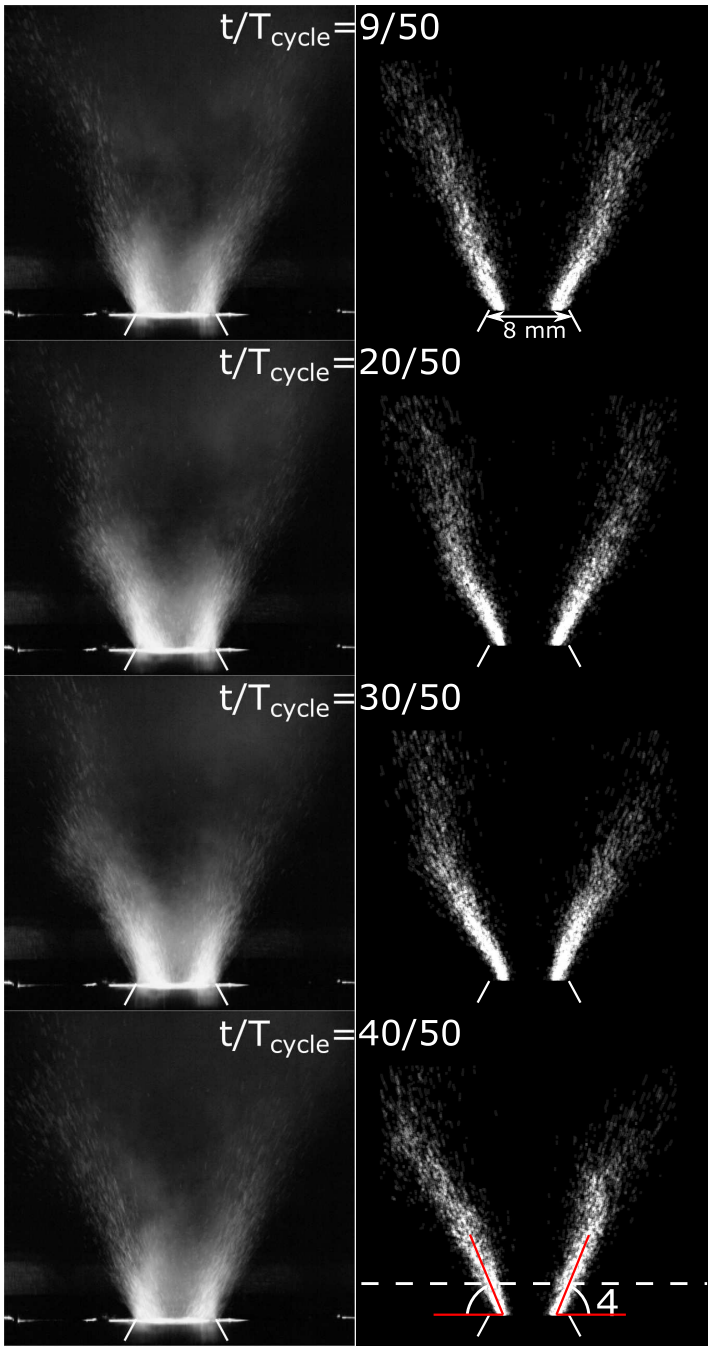

Figure 7.12: Class-averaged images at four times of the acoustic forcing cycle, obtained from vertical tomography views of the seed-air flow and n-heptane droplets during combustion: n-heptane droplets and seeded air-flow (left), droplets median positions (right). (1) seeded air; (4) injection angle of the droplets, calculated at $z/D_{exit} = 0.4$. The central injector is positioned at the basin of VAN. $|P'| \approx 2000$ Pa measured by M1, $f_r = 830$ Hz, $\dot{m}_{air} = 1.724$ g/s, $\dot{m}_{fuel} = 0.097$ g/s , $\phi_{LB} = 0.85$.

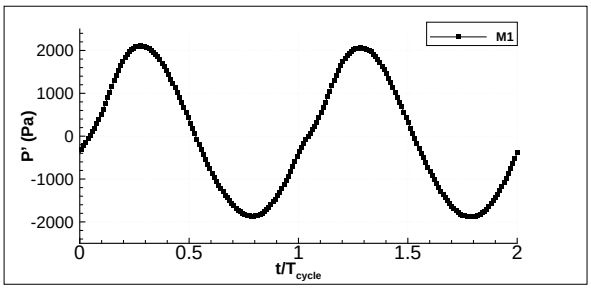

(a)

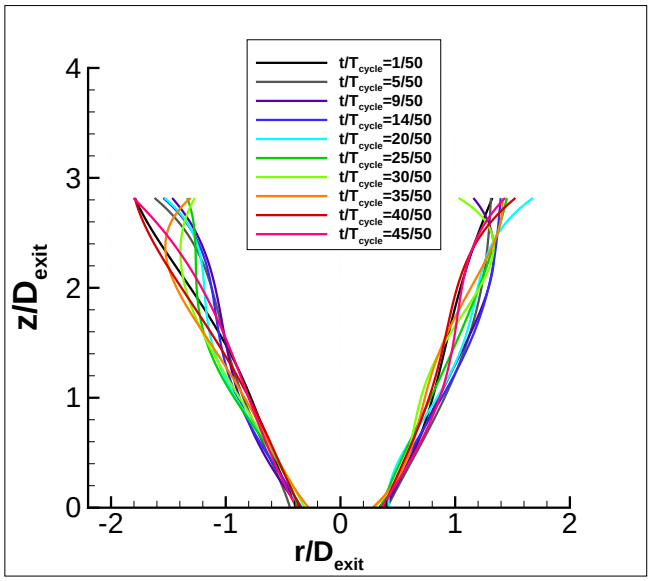

(b)

Figure 7.13: (a) Pressure perturbation signal measured at the central PAN (M1 position). (b) Droplets position lines at several times of a cycle of the acoustic forcing. The central injector is positioned at the basin of VAN. $f_r = 830$ Hz, $\dot{m}_{air} = 1.724$ g/s, $\dot{m}_{fuel} = 0.097$ g/s , $\phi_{LB} = 0.85$.

compared with the cases at PAN and IAN. The values are found essentially between 50° and 85°. The injection angle is not strongly modulated at the forcing frequency. A phase difference between the evolution of the injection angle on the left and right side is not really noticeable because the oscillations of the radial position of the droplets at the injector exit are small with respect to the downstream region.

7.3 Flame behavior

7.3.1 Intensity Antinode

The swirling spray flame issued from the central injector is positioned at the basin of influence of IAN ($x/L_c = -0.14$). Simulations considering a variable temperature field related to the position of the flames, support the excitation of the 2T1L acoustic mode,

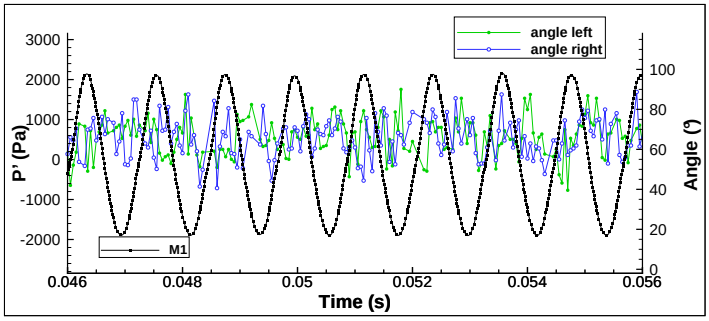

Figure 7.14: Evolution of the angle of injection formed by the n-heptane droplets at the left and right side of the injector, in vertical tomography views of the n-heptane droplets, at the injector exit. f_r = 830 Hz, $\dot{m}_{air}$ = 1.724 g/s, $\dot{m}_{fuel}$ = 0.097 g/s , $\phi_{LB} = 0.85$

which is corroborated by experimental measurements within the cavity. Fig. 7.15(a) shows a simulated profile of the acoustic field obtained at $y/e = 0$ and $z/h_c = 0.025$. In this figure is also plotted the normalized absolute amplitude of the acoustic pressure measured at x/L_c equal to 0 (M1), 0.256 (M2) and -0.481 (M3), for $y/e = 0.5$ and $z/h_c = 0.025$. The simulated acoustic field is constant along y whatever the position x, z. It is also constant along z up to $z/h_c = 0.3$ ($z/D_{exit} = 7.5$). The signals of the acoustic pressure measured at these points are reported in Fig. 7.15(b). We note that the signals of M1 and M3 are, as expected, out-of-phase. Minimums of the pressure amplitude are found where the basins of VAN are expected, with a signal phase (φ_p) close to 0.5π (see section 5.2), taking the phase of the signal measured by M1 as a reference. These features satisfy the cavity resonance at the 2T1L acoustic mode.

By using images of the CH* chemiluminescence recorded by the ICCD camera PIMAX 4, and by calculating phase-averaged images, a full cycle of the response of the flame front was reconstructed during the acoustic forcing. It is highlighted a pulsation of the front flame intensity in the injection direction. Four phase-averaged images synchronized with the pressure signal measured by microphone M1 are used to illustrate

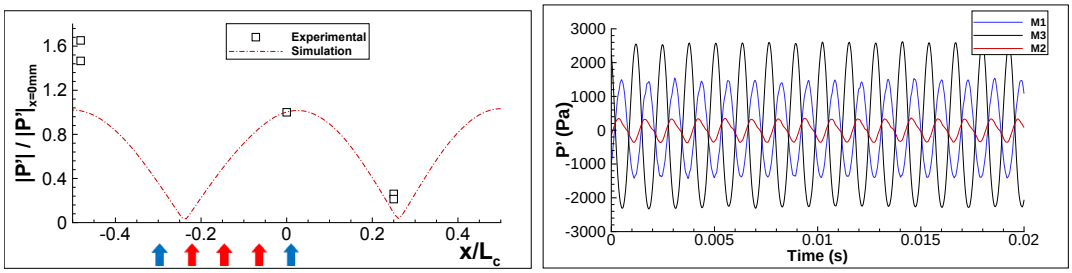

(a) (b)

Figure 7.15: Dynamic of the pressure acoustic field within the combustion chamber. (a) Pressure field by simulation, considering a variable temperature field (see section 5.2.3); open square symbols are the experimental measurements. (b) Pressure signals inside the cavity measured at the position of M1, M2 and M3. Arrows indicate the position of the injectors. f_r = 775 Hz, $\dot{m}_{air}$ = 1.724 g/s, $\dot{m}_{fuel}$ = 0.097 g/s , $\phi_{LB} = 0.85$

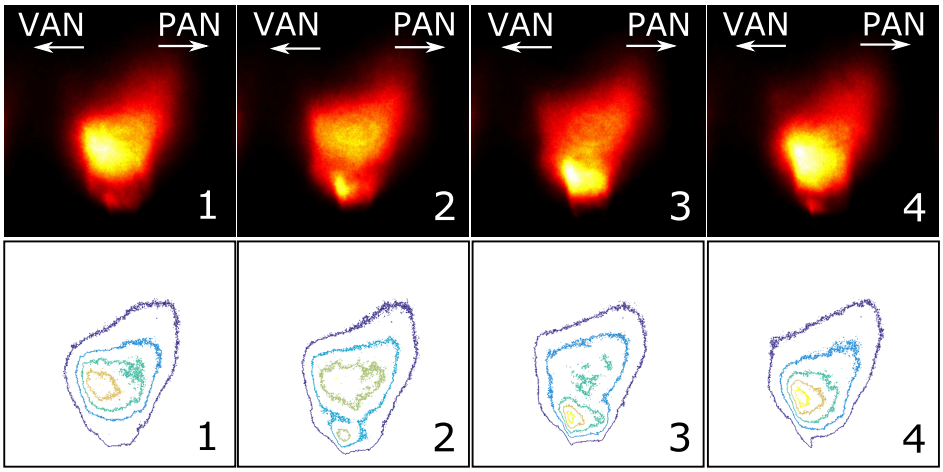

(a)

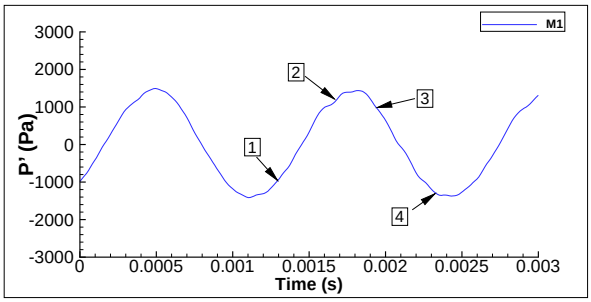

(b)

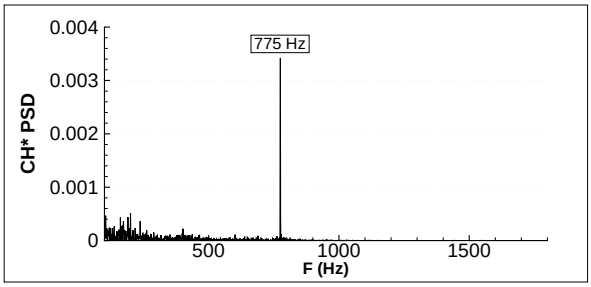

(c)

Figure 7.16: (a) Four flame front phase-averaged images (CH*, false color) along with its intensity iso-contours (dark blue and yellow lines represent the low and high intensities respectively), from a reconstruction of a full cycle of the acoustic forcing. (b) Position in time of the four images with respect to the pressure signal measured by microphone M1. (c) PSD of CH* emissions recorded by PM. The central flame is positioned at the basin of IAN. $|P'| \approx 1400$ Pa, $f_r = 775$ Hz, $\dot{m}_{air} = 1.724$ g/s, $\dot{m}_{fuel} = 0.097$ g/s , $\phi_{LB} = 0.85$.

the intensity pulsation (see Fig. 7.16(a) top and Fig. 7.16(b)). This axial pulsation is non-symmetric, contrary to what was noted for the flame response at PAN. A periodic intensity wave that propagates on the left side of the injector axis is highlighted. This side is the nearest to the velocity antinode, where a vortex formation has been observed on spray tomography images. The propagation of the intensity pulsation wave is ac-

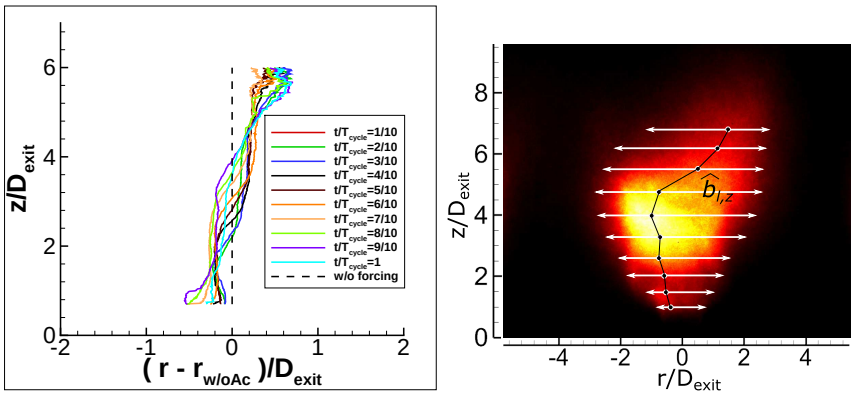

(a) (b)

Figure 7.17: (a) Median lines of the flame front, calculated from its phase-averaged CH* emissions images, and (b) a phase-averaged CH* emission image of the flame front, during the acoustic forcing along with some of the points $\hat{b}_{l,z}$ to obtain a median line. $f_r = 775$ Hz, $\dot{m}_{air} = 1.724$ g/s, $\dot{m}_{fuel} = 0.097$ g/s , $\phi_{LB} = 0.85$.

companied by a visible wrinkle of the flame front on the same side. The iso-intensity contours of the CH* emission phase-averaged images, clearly show the intensity pulsation wave evolution and the wrinkle formation, both on the left side (Fig. 7.16(a) bottom). The frequency of this intensity pulsation is corroborated by the PSD of the CH* emission signal recorded by the photomultiplier (Fig. 7.16(c)).

The flame front can be also described by means of the calculation of front median lines. These lines are obtained from each of the phase-averaged images of the CH* chemiluminescence. A median line is constituted of points ($\hat{b}_{l,z}$) which are barycentres of horizontal segments delimited by the outer contour of the front. The contour has been previously defined by fixing an intensity threshold value of about 20% of the maximum intensity value (see Fig. 7.17(b)).

The points are chosen to be representative of the CH* light intensity integrated on the line of sight of the camera. They are defined as CH* intensity barycentres, obtained from the following relationship:

$$\hat{b}_{l,z} = \frac{\sum_j I^j_{CH^*} r_{l,j}}{\sum_j I^j_{CH^*}} \tag{7.7}$$

In Eq. 7.7, the sum are computed horizontally line by line along the segment delimited by the flame front contour. The position of each point of a segments is $r_{l,j}$, while the CH* emission intensity of each of these points is $I^j_{CH^*}$. Thus, these lines give information about the flame front shape and spatial CH* emission intensity distribution over time during a cycle of the acoustic forcing. In Fig. 7.17(a), the median line obtained from a flame front phase-averaged image without acoustic forcing (dashed line) is used as a reference position from which the others median lines are plotted. Fig. 7.17(a) indicates the dissymmetry of the flame with respect to the case without acoustic forcing. The deviation on the left side of the flame lowest zone is coherent with the aerodynamic dissymmetry imposed to the two-phase flow. However, this aerodynamic

dissymmetry effect cannot explains the flame top region mean displacement over time on the right side of the reference position. There is another effect that is added to the aerodynamic dissymmetry. This possible effect is presented hereafter.

7.3.1.1 Effect of the radiation force

In [95], authors observed a deviation in the case of a front of a laminar premixed V-shape flame subjected to a transverse acoustic field. Sevilla et al. [130] investigated this phenomenon in the case of a droplet combustion. They observed the deviation of the liquid fuel droplet, the flame front and the burned gases, when the burner is located at different positions within a standing transverse acoustic field, from the basin of VAN up to near the basin of PAN. Previously, Baillot et al. [131] and Baillot et al. [132], highlighted the deviation of a liquid jet as this is subjected to a high frequency (1 kHz) transverse acoustic field. Recently, the behavior of the injection of three liquid jet subjected to a high frequency transverse acoustic perturbation has been investigated by Ficuciello [97], both experimentally and theoretically. The authors show that the liquid jet and droplets are deviated and this deviation can lead to strong interactions between the jets. Moreover, they have developed an analytic model to explain the mechanism behind the spray behaviors observed, depending on the position of the injectors within the standing acoustic field.

The observed deviation, either in the case of the flame front, or the droplets, or hot gases product of the combustion, is a stationary phenomenon consequence of a harmonic acoustic field. As the effects of the linear acoustic are null on average, this phenomenon is generated by a non-linear effect of the acoustic [95]. This is manifested as a radiation pressure (P_{rad}) acting on a system that can be solid or fluid. The resulting force, known as the radiation force ($\tilde{F}^*$), is obtained from the integration of the radiation pressure efforts acting on the studied system placed within a standing acoustic field. This force is able to create the observed deviation. The characteristics of this deviation phenomenon rely on the nature of the studied system, this one having a density ρ_1 and presenting an interface with the environment (of density equal to ρ_0). The density of the system and that of the environment, allow to introduce a parameter (η), defined as the ratio of the medium density over the object density (ρ_0/ρ_1). In [95, 97], it is found a threshold value for this parameter that depends on the shape of the object that represents the studied system. Considering a spherical object they found $\eta = 2.5$, while for a cylindrical object they obtain $\eta = 3$. Let consider a cylindrical system located for instance at the IAN basin within the standing acoustic field. The radiation force $\tilde{F}^*(\eta)$ evolves from positive values to negatives, being null at the threshold value of η (see Fig. 7.18(a)). Thus, with the system (solid or fluid) considered as a cylindrical object, placed within the standing field it is obtained that:

- as the parameter $\eta < 3$, the radiation force deviates the system from the pressure antinode (PAN) to the nearest velocity antinode (VAN).
- as the parameter $\eta > 3$, the radiation force deviates the system from the velocity antinode (VAN) to the nearest pressure antinode (PAN).

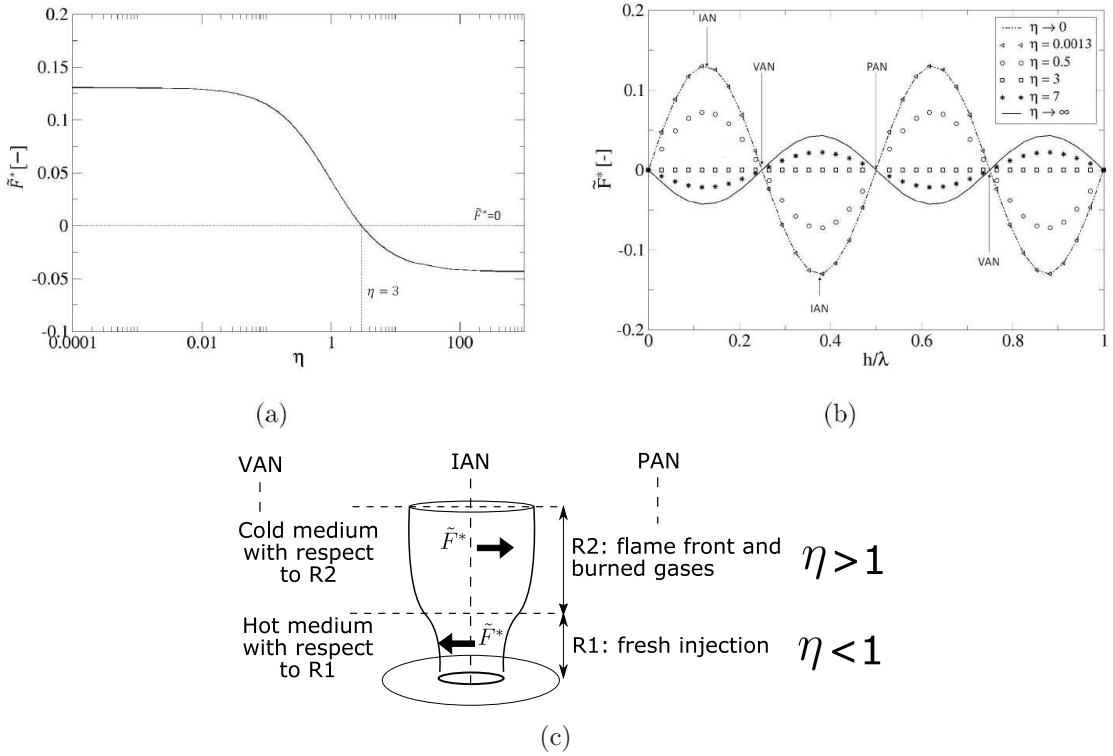

Figure 7.18: (a) Dimensionless radiation force per unit length $\tilde{F}^*$ at IAN acting on a cylindrical object placed in a standing wave field as a function of η. (b) Dimensionless radiation force per unit length $\tilde{F}^*$ around a cylindrical object placed in a standing wave field as a function of h/λ (or x/L_c). For $\eta < 3$, $\tilde{F}^*$ is directed toward the nearest VAN, whereas for $\eta > 3$ it is directed toward the nearest PAN (reproduced from [97]. (c) Spray and flame sketched as a cylindrical object composed by two regions: fresh injection and flame front with burned gases.

As illustration, the magnitude and the direction of the radiation force, as a function of the system position within the standing acoustic field, is shown in Fig. 7.18(b).

When the studied system and the environment have the same density ($\eta = 1$), whether if the system is spherical or cylindrical, the radiation force is never zero. However, in [95] is shown experimental results for a system and environment with $\eta = 1$ where any deviation is observed. Same authors mentioned that Gor'Kov in [133] have introduced a corrective coefficient $C(\eta)$ in order to account for fluid compressibility effects. This coefficient shift the plot of the radiation force versus η leading to a zero force for $\eta = 1$ in accord with experimental observations in [95].

In the case of our system, the stationary deviation highlighted by means of the flame front median lines, is coherent with these radiation force phenomenological features. Our system is considered as a cylindrical object with two regions, the first one situated at the injector exit, where a fresh flow is injected within a hot medium, such that the ratio of densities may be $\eta < 1$, since the injected flow have a temperature of about 330 K while the environment is a approximately 700 K (see section 3.5.2). Thus, the system may be deviated to the left, towards the nearest VAN, contributing with the

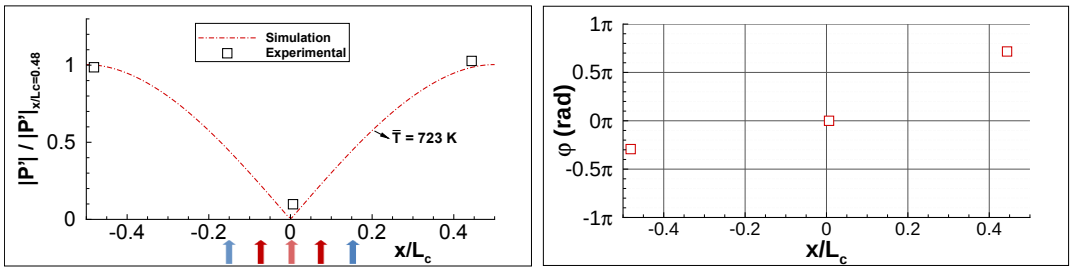

(a) (b)

Figure 7.19: Dynamic of the pressure acoustic field within the combustion chamber when compression drivers are out-of-phase. (a) Pressure field by simulation considering a constant temperature field ($\bar{T} = 723$ K); (b) phase (φ) of the pressure signals defined relative to the signal measured at the center of the cavity. Open square symbols are the experimental measurements. Arrows indicate the position of the injectors. $f_r = 520$ Hz, $\dot{m}_{air} = 1.724$ g/s, $\dot{m}_{fuel} = 0.108$ g/s , $\phi_{LB} = 0.95$

aerodynamic dissymmetry observed. The second region can be considered as composed by the flame front and burned gases, both within an environment with a lower temperature. In this case the ratio of densities will be $\eta > 1$, causing the radiation force deviates the system towards the nearest PAN as highlighted by the front median lines of Fig. 7.17(a). Fig. 7.18(c) schematizes these observations.

7.3.2 Velocity Antinode

The response of the swirling spray flame to the acoustic perturbation generated in the basin of influence of the velocity antinode (VAN) is investigated in the case of two configurations. The first one consists in locating the central injector at the center of the cavity and set the compression drivers to work out-of phase. This creates a velocity antinode at the center of the cavity. The second configuration, as all the cases investigated up to now, which uses the actuators in phase, generates two VAN at $x/L_c \approx \pm 0.25$. In that case the central injector is located in the basin of the VAN situated at $x/L_c \approx -0.25$.

7.3.2.1 Compression drivers out-of-phase

When the compression drivers work out-of-phase a transverse standing acoustic field 1T1L is excited. The wavelength (λ) of the 1T acoustic mode is equal to two times the cavity length ($2L_c$). At the center of the cavity a velocity antinode is generated while a pressure antinode is generated at $x/L_c = \pm 0.5$. The acoustic pressure fluctuations of the sides are out-of-phase between each other. Simulations of this case have been performed by adjusting the *normal acceleration* boundary condition to be out of phase (see section 5.1.1). It has been considered an uniform temperature field equal to $\bar{T} = 723$ K. This field is congruent with temperature measurements within the cavity (see section 5.2.2).

Pressure measurements verify the results of simulations of this case. These measurements have been performed within the cavity during combustion. Microphones have been installed at $y/e = 0.5$ and $z/h_c = 0.025$ for three positions x/L_c, namely $x/L_c = 0$, $x/L_c = -0.48$ and $x/L_c = 0.44$. The measured resonant frequency of this mode is $f_r = 520$ Hz. The simulation agree with the measured f_r giving the same value. Amplitudes of the simulation are normalized by the maximum value of the pressure field while the measurements are normalized by the amplitude measured at $x/L_c = -0.48$. The normalized experimental and simulated pressure amplitudes are reported in Fig. 7.19(a). The normalized pressure amplitudes ($|P'|/|P'|_{x/L_c=-0.48}$) found experimentally at the positions indicated previously, match with the calculated values at the same positions. Experimentally, it is found that the signals, corresponding to the acoustic pressure on the sides of the cavity ($x/L_c = -0.48$ and $x/L_c = 0.44$) are out-of-phase, as shown in Fig. 7.19(b) by a relative phase of $\varphi = \pi$. The phase plot shows, taking as reference the signal measured at center of the cavity, that the signal on the right has a phase gap of $\varphi = 0.7\pi$, while the signal on the left have $\varphi = -0.3\pi$. This imbalance means that, in reality, the exact position of the VAN is slightly on the right of the center of the cavity. Nevertheless, the central flame is at the basin of influence of the VAN created at the center of the cavity.

The signals of the acoustic pressure measured by the microphones M1 ($x/L_c = 0$) and M2 ($x/L_c = -0.256$) are presented in Fig. 7.20(a). The pressure amplitude measured by M1 is of about 100 Pa that represents 9% of the maximum measured at $x/L_c = -0.48$. Thus, this amplitude can be considered as residual and its effects on the flow and flame as negligible. The OH* chemiluminescence emissions signal, recorded by means of the photomultiplier, is also plotted in Fig. 7.20(a). The Power Spectral Density (PSD) of these signals are displayed in Fig. 7.20(b). The PSD of the pressure as well as the OH* signal present a peak at 520 Hz, the forcing frequency.

By using a series of 1000 high-speed images of the OH* emissions (camera speed 6000 fps), 48 class-averaged images have been obtained in order to reconstruct the flame front response during a cycle of the acoustic forcing. As illustration, Fig. 7.21 shows four class-averaged images of the flame front during a full cycle of acoustic perturbation. The result of the reconstruction also reveals a pulsation of intensity of emission OH* that begins in the lower right part of the front and evolves diagonally towards the upper left part of the front. The diagonal evolution in the direction of the swirl imparted to

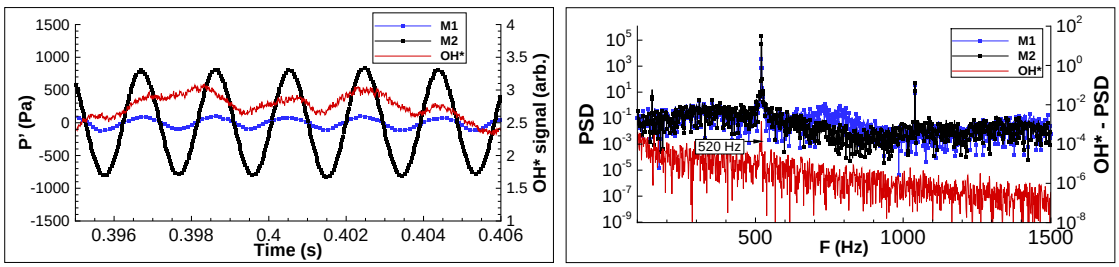

(a) (b)

Figure 7.20: Signals and PSD of the acoustic pressure and OH* emission recorded by the PM. $f_r = 520$ Hz, $\dot{m}_{air} = 1.724$ g/s, $\dot{m}_{fuel} = 0.108$ g/s , $\phi_{LB} = 0.95$.

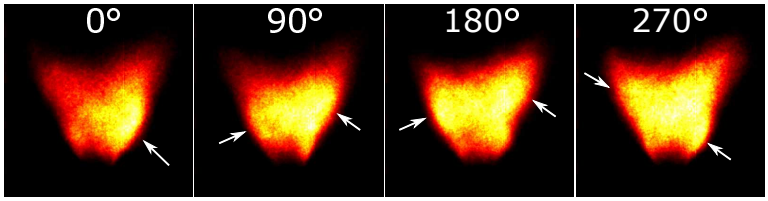

Figure 7.21: Flame front averaged images during a full cycle of the acoustic forcing with compression drivers out-of-phase. Flames are positioned at the basin of VAN. $f_r = 520$ Hz, $\dot{m}_{air} = 1.724$ g/s, $\dot{m}_{fuel} = 0.108$ g/s , $\phi_{LB} = 0.95$.

the reactive flow is clearly captured by the Dynamic Mode decomposition presented in Fig. 7.22. Please note that this representation is not the real motion of the flame. It is a reconstruction made by filtering the series of flame images at the frequency of the highest mode (here 520 Hz) found by the DMD method. Instead, the reconstruction made by using the phase or class-averaged images captures the averaged motion since no mode decomposition is applied to the images in this case.

By using the class-averaged images, it is noted that wrinkles form alternatively on the left and right side of the flame bottom (see the white arrows in Fig. 7.21). In order to investigate the dynamics of these wrinkles, four exploration windows have been defined in the series of high speed images of the flame front OH* chemiluminescence (Fig. 7.23). The windows are placed in order to detect light intensity variations linked with the wrinkle passage on the edge of the flame front image. Windows in the low zone of the flame front are labeled as (1) while those positioned higher are labeled as (2). Windows labeled with (1) have the same z-coordinates as well as those labeled with (2). The signals obtained in each of the windows are plotted in Fig. 7.24. Signals reveal that the wrinkles form periodically with a frequency equal to f_r. An illustration is given in Fig. 7.25 where the PSD of the signal from an exploration window is plotted. The phase gap between the left and right sides has been calculated for the two z-positions.

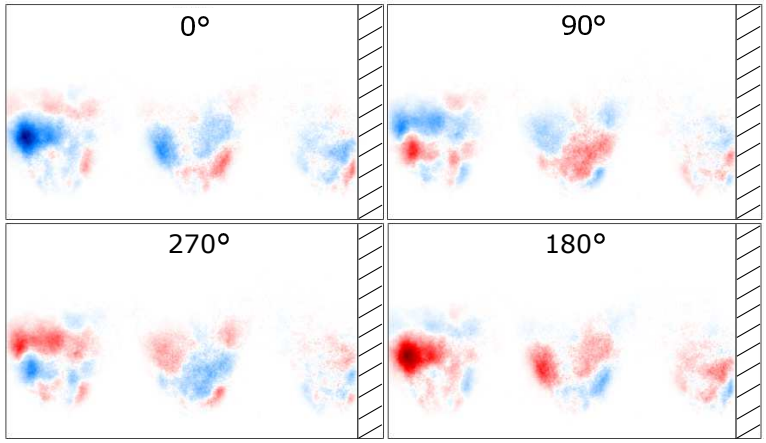

Figure 7.22: DMD of the OH^* emission intensity (false color) when the flames are positioned at the basin of VAN, during a cycle of the acoustic forcing with the compression drivers out-of-phase. $f_r = 520$ Hz, $\dot{m}_{air} = 1.724$ g/s, $\dot{m}_{fuel} = 0.108$ g/s , $\phi_{LB} = 0.95$.

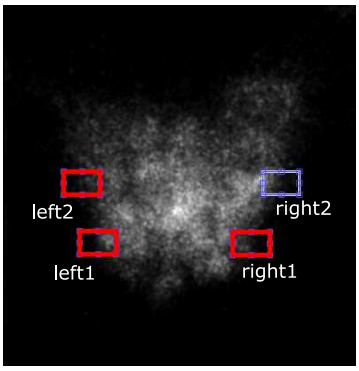

Figure 7.23: Exploration windows positions defined in high speed images of the flame front OH* chemiluminescence.

A phase gap of π is found between the left and right side windows labeled with (1), while the phase gap between the windows labeled with (2) is 1.23π. Analyzing the signals of windows on the same side, a phase gap of 0.328π is obtained for the left side and 0.55π for the right side, both from the signals filtered at $f_r = 520$ Hz. It has been calculated the wrinkled velocity for each side based on these latter phase gaps and the vertical distance between the two respective windows. For the left side it has been found a velocity equal to ≈ 35 m/s while for the right side the velocity is equal to ≈ 21 m/s. These velocities do not correspond to the wrinkle transportation speed but they are trace velocities as it is explained hereafter.

The number of wrinkles formed, their amplitude and the phase gap between them, depend mainly on the parameter σ_w, defined as the ratio of the characteristic azimuthal frequency (angular rate of swirl) and the frequency of acoustic forcing. This is proposed in [114], where the authors develop a model that predicts the flame front dynamics of a swirling premixed flame under the effects of a non-axisymmetric harmonic excitation, as a function of the parameter σ_w. The predicted motion is not a simply lateral oscillation of the front, but a more complex behavior characterized by a helical spiral motion of the wrinkles formed (see an illustration in Fig. 7.26). The axial cut of the flame shown in Fig. 7.26(b) indicates that the phase gap between the wrinkle on the left and that on the right side is constant with z. Authors emphasize that the velocity obtained with the phase gap between wrinkles on the same side seen in vertical axial cuts, is an apparent convection speed that can not be always interpreted as physical convection velocities. This is because, as the wrinkle is created, it is also affected by the swirl transport component of the velocity field, resulting in an apparent phase between consecutive wrinkles. Moreover, as in our case the phase-gap is obtained from flame images integrated along the horizontal direction and projected in a vertical plane, this can explain the slight variation between the phase gap obtained from windows labeled with (1) and that obtained from windows labeled with (2).

As it was done in the previous chapter, the flame front evolution can also be described by means of the calculation of median lines of the front. These lines are obtained from each of the class-averaged images of the OH* chemiluminescence. A median line is constituted of points $(\hat{b}_{l,z})$ which are barycentres of horizontal segments delimited by the outer contour of the front. The contour has been previously defined by fixing an in-

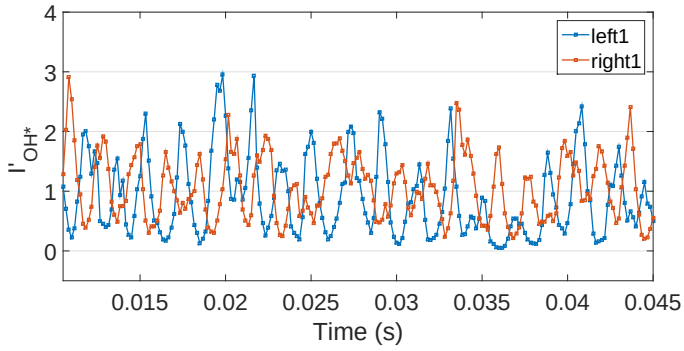

(a)

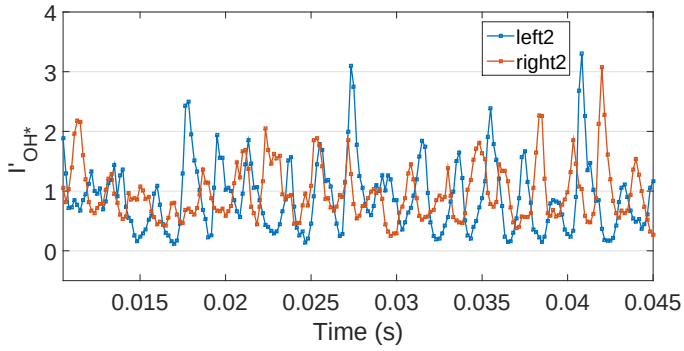

(b)

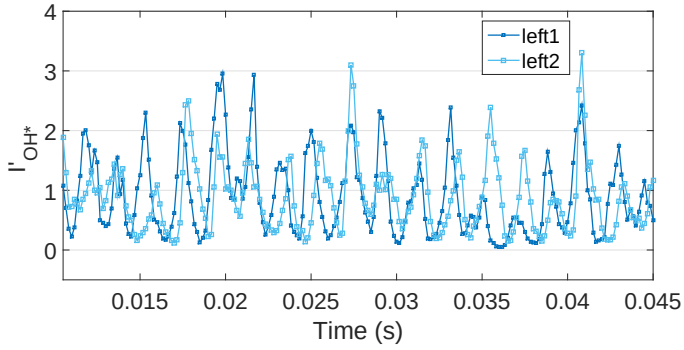

(c)

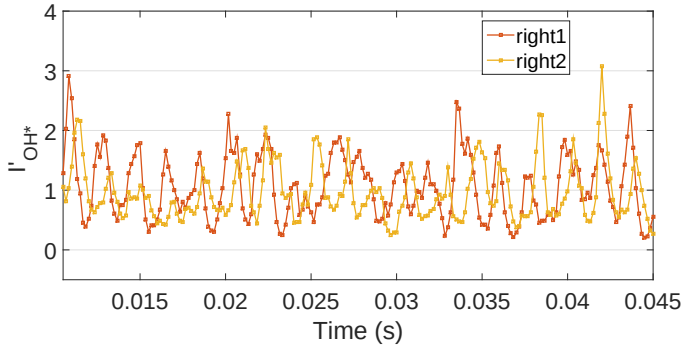

(d)

Figure 7.24: Signals obtained in each of the four exploration windows from high speed images of the flame front OH* emissions. Plots (a) and (b): signals of the left and right sides at two z-positions. Plots (c) and (d): signals of the same side at two z-positions.

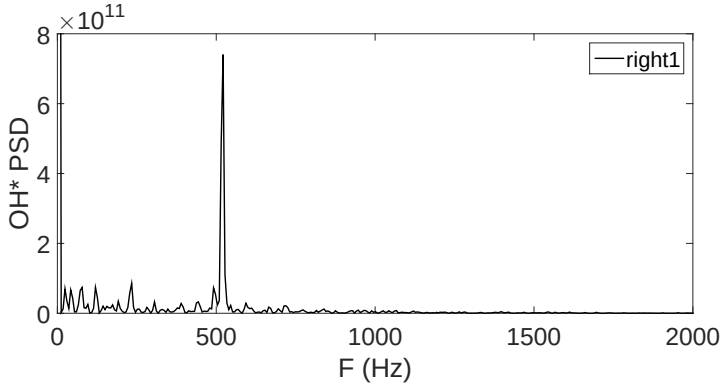

Figure 7.25: PSD of the signal obtained in the exploration windows "right1" showing a peak at $f_r = 520$ Hz.

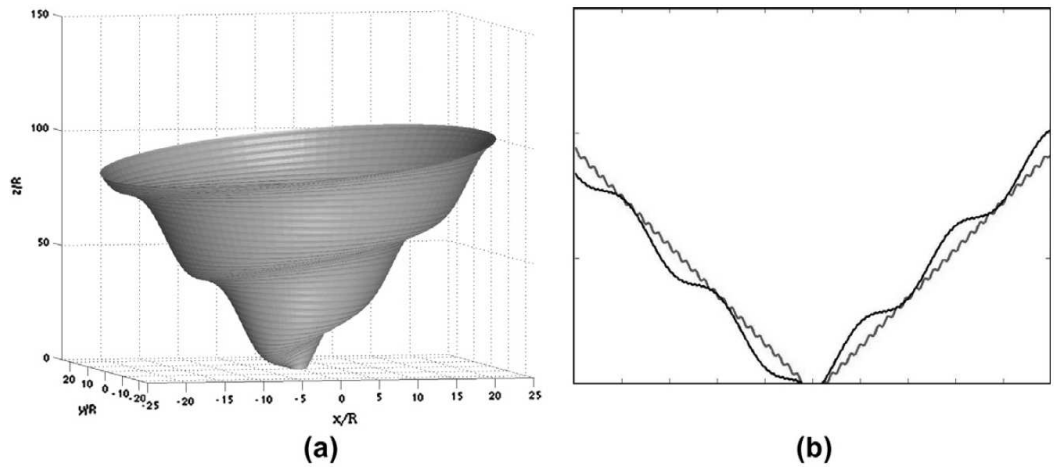

Figure 7.26: Theoretical prediction of the front motion of a swirling premixed flame for a given σ: (a) flame surface, (b) axial vertical cut of the flame front showing its sides. Reproduced from [114].

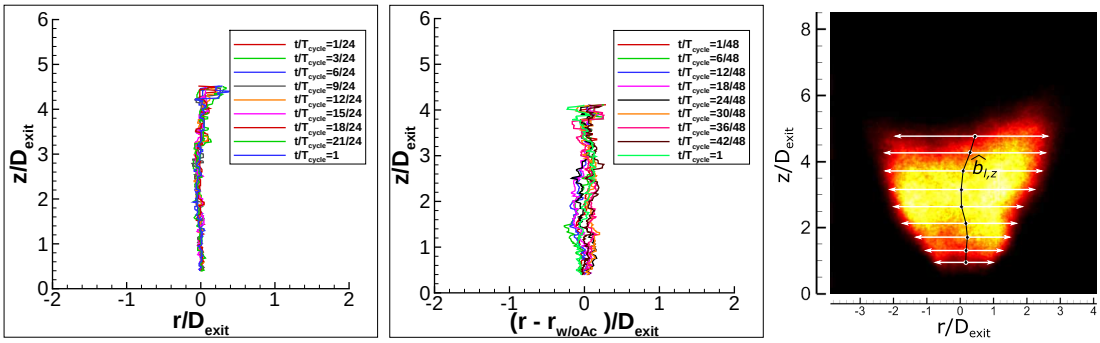

(a) (b) (c)

Figure 7.27: Median lines of the flame front, (a) without acoustic forcing and (b) with acoustic forcing, calculated from its phase-averaged OH* emissions images (c). $f_r = 520$ Hz, $\dot{m}_{air} = 1.724$ g/s, $\dot{m}_{fuel} = 0.108$ g/s , $\phi_{LB} = 0.95$.

tensity threshold value of about 15% of the maximum intensity value (see Fig. 7.27(c)). The points are chosen to be representative of the OH* light intensity integrated on the line of sight of the camera. They are defined as OH* intensity barycentres, obtained from the relationship 7.7 introduced in section 7.3.1.

The median lines of the flame front have been calculated first from a series of OH* class-averaged images without acoustic forcing. The class-averaged images have been obtained over a time equal to an acoustic period ($T_{cycle} = 1/f_r$) even in the case without acoustic forcing. Thus, these lines characterize the flame front, on average, during a time interval equal to T_{cycle}. As we can see in Fig. 7.27(a) for the case without forcing, the median lines are overlapped over time revealing a symmetric shape of the flame front. It is observed a slight deviation of the upper end of the median lines, to the right. This is because the right side of the flame front is a little longer than the left side. For the case with acoustic forcing, the lines position are plotted with respect to a line without forcing. During a cycle of the acoustic forcing, the median lines of the flame front highlight a small lateral oscillation of the flame foot. It has been verified, by means of an animated stack made with each of the lines, that they traces a helical path that seems to turn over time like a left-handed screw. This observation is coherent with a helical spiral[2] motion of the flame front motion.

[2]By spiral we denote here the circular motion, around an axis, that trace a curve in the space with an increasing diameter of its successive loops.

7.3.2.2 Compression drivers in-phase

The compression drivers were working in-phase to generate the 2T1L transverse acoustic mode at the resonant frequency (f_r). The injector system is moved such that the central injector is placed at $x/L_c = -0.256$, the basin of influence of one of the VAN. The simulated pressure acoustic field presented in Fig. 7.28(a), is obtained by considering the non-uniform temperature field introduced in section 5.2.3. It corresponds to the 2T1L acoustic mode of the cavity for $f_r = 710$ Hz. Experimentally, the resonant frequency is determined by following the procedure explained in section 5.2. For the present illustration a maximum response of the cavity was obtained at $f_r = 775$ Hz. The nature of the mode was verified by making pressure measurements simultaneously. They were performed at $y/e = 0.5$, $z/h_c = 0.025$, by microphones M1 ($x/L_c = 0$), M2 ($x/L_c = 0.25$) and M3 ($x/L_c = -0.48$). The found normalized pressure amplitudes ($|P'|/|P'|_{x/L_c=0}$) match well with the simulation results as seen in Fig. 7.28(a). The values measured at the M2 position correspond to pressure amplitudes in a basin of pressure minima. Its amplitude, of about 200 Pa, represents about 10% of the pressure amplitude measured at $x/L_c = 0$. The acoustic pressure signals recorded by M1 and M3 are out-of-phase and the signal recorded by M2 has a phase gap with respect to

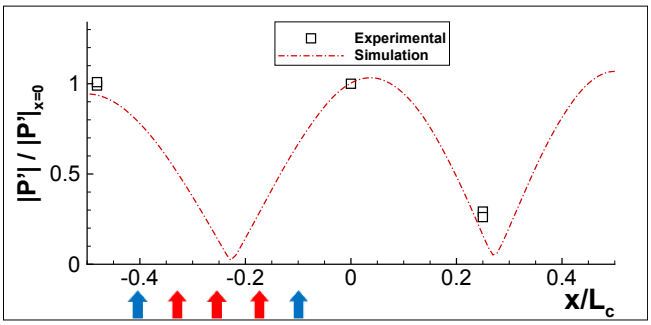

(a)

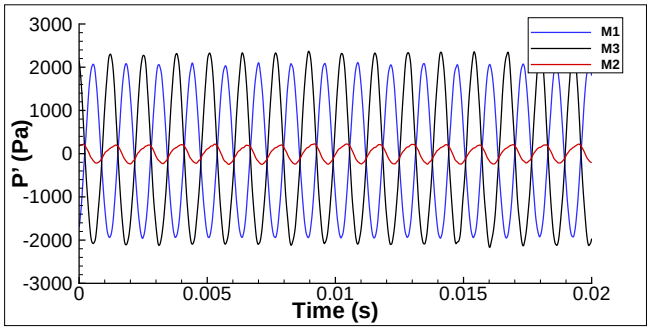

(b)

Figure 7.28: Dynamic of the pressure acoustic field within the combustion chamber when compression drivers are in-phase. (a) Pressure field by simulation, considering a variable temperature field (see section 5.2.3); open square symbols are the experimental points of measure. (b) Pressure signals inside the cavity measured at the position of M1, M2 and M3. Arrows indicate the position of the injectors. $f_r = 775$ Hz, $\dot{m}_{air} = 1.724$ g/s, $\dot{m}_{fuel} = 0.097$ g/s , $\phi_{LB} = 0.85$

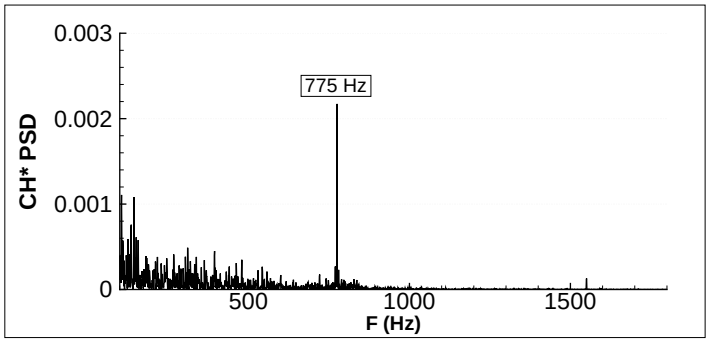

(a)

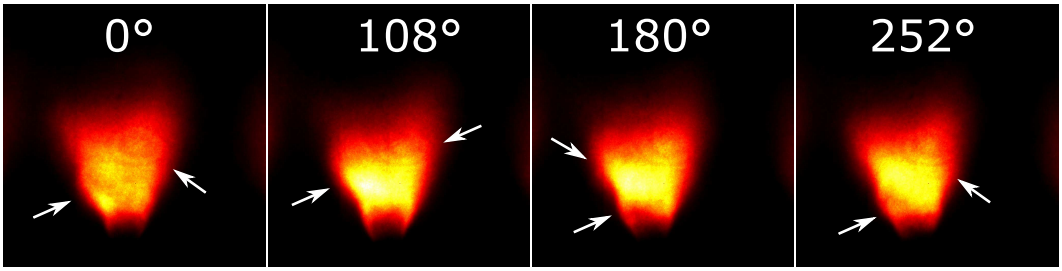

(b)

Figure 7.29: (a) PSD of CH* emissions recorded by PM. The central flame is positioned at the basin of VAN of the 2T1L acoustic mode. (b) Flame front phase-averaged images (CH*) during a full cycle of the acoustic forcing with compression drivers in-phase. $|P'| \approx 2000$ Pa, $f_r = 775$ Hz, $\dot{m}_{air} = 1.724$ g/s, $\dot{m}_{fuel} = 0.097$ g/s , $\phi_{LB} = 0.85$.

the two others signals close to 0.5π (Fig. 7.28(b). These features indicate that the field can be interpreted as the 2T1L acoustic mode at $f_r = 775$ Hz.

First, the flame front dynamics was followed by a photomultiplier equipped with a CH* interferential filter. The PSD of the recorded signal reported in Fig. 7.29(a) shows a peak at the forcing frequency $f_r = 775$ Hz. Secondly, the flame front motion was reconstructed during a cycle of the acoustic forcing by using ten phase-averaged images, each one obtained from 100 phased images recorded by a ICCD camera equipped also with a CH* interferential filter. The reconstruction reveals the generation of flame front wrinkles alternatively formed on the left and right side of the front. The wrinkle formed on the left protrudes more than the wrinkle formed on the right which is barely visible. Four exploration windows are placed on the phase-averaged images as shown in Fig. 7.30. The signals obtained from the exploration windows allow to roughly estimate that the formation delay between the left and right wrinkle, is of about π (see Fig. 7.31), while in the case of the acoustic actuators working out-of-phase this delay was around 0.5π. This difference may be explained by the parameter σ_w presented in the precedent subsection, which value is not the same between both cases since the experimental swirl number ($S = 0.68$) does not change, but the resonant frequencies are different ($f_r = 520$ Hz for actuators out-of-phase). The reconstruction also reveals a lateral CH* emission intensity pulsation with an almost diagonal pattern in the swirl direction. This pattern is more noticeable in the phase-averaged images at 180° and 252° of the cycle presented in Fig. 7.29(b).

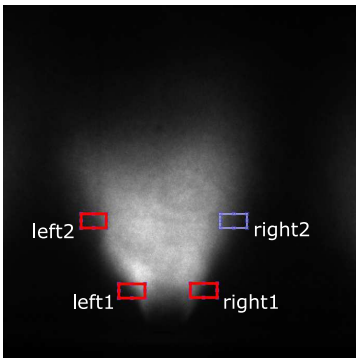

Figure 7.30: Exploration windows positions defined in phase-averaged images of the flame front CH* chemiluminescence.

From each of the ten phase-averaged images is subtracted a reference images, being this a mean image of the front obtained without acoustics. The intensities thus obtained represent positions not occupied by the reference front or where the phase-averaged front has a higher intensity. Then, from each resultant image iso-intensity contours have been extracted (Fig. 7.32). In the image at 0° the contours on the left and right sides are almost the same in size and intensity. There is a time interval where no intensity is observed on the right (image at 180° and 288°). On the left side the iso-contours is always present evolving in size and intensity. These iso-contours indicate that upper zones of the flame laterally oscillate more than regions close to the injector exit, with respect to its mean position without acoustic. These results exhibit the intensity growing on the left side of the front, moving to the right side, passing by the center of the image, to finally restart the cycle.

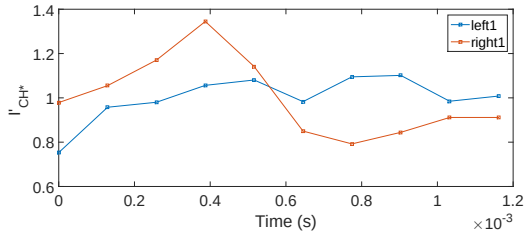

(a)

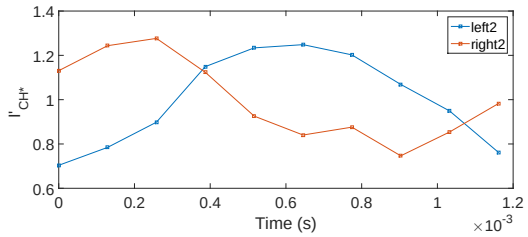

(b)

Figure 7.31: Signals obtained in each of the four exploration windows from phase-averaged images of the flame front CH* emissions. Signals of the left and right sides bottom (a) and top (b) exploration windows.

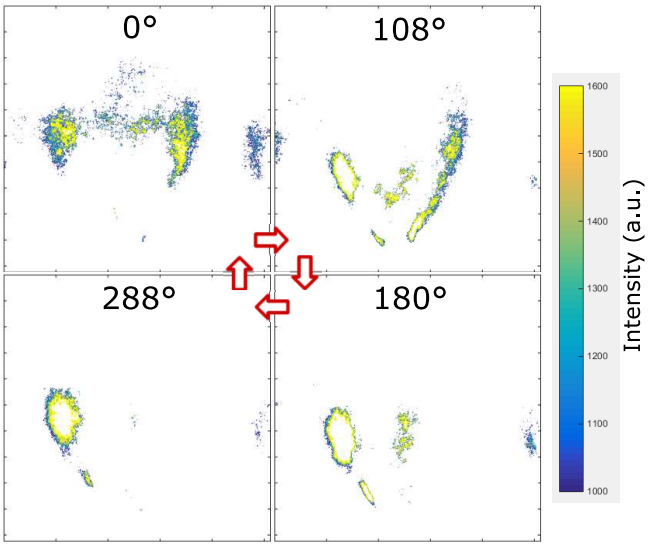

Figure 7.32: Iso-contour images calculated from flame front phase-averaged images (CH*) during a full cycle of the acoustic forcing, with compression drivers in-phase. The central flame is positioned at the basin of VAN of the 2T1L acoustic mode. $f_r = 775$ Hz, $\dot{m}_{air} = 1.724$ g/s, $\dot{m}_{fuel} = 0.097$ g/s , $\phi_{LB} = 0.85$.

The median lines of the front, calculated as it was explained in the precedent subsection, trace and helical path in the space (Fig. 7.33(a)). This can be verified by means of an animated stack made with each of the lines, from which the lines seems to turn over time like a left-handed screw. This is congruent with what was observed previously in the case of OH* emissions.

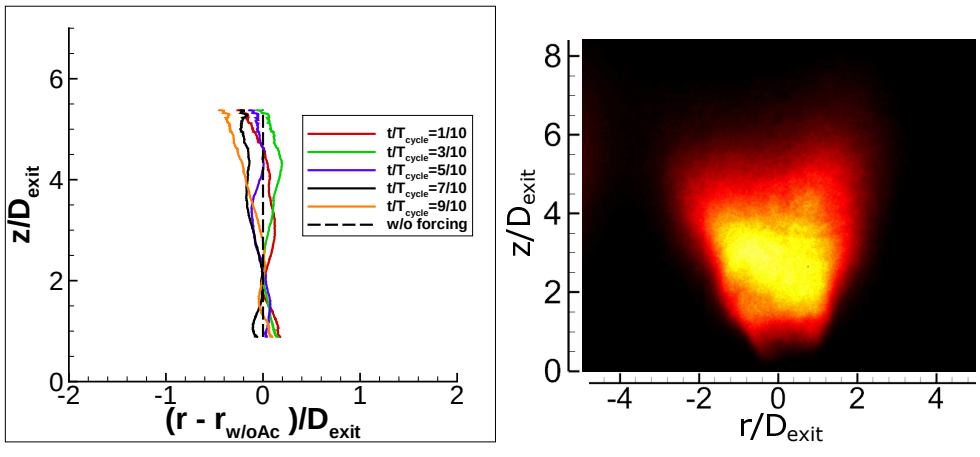

(a) (b)

Figure 7.33: (a) Median lines of the flame front, calculated from its phase-averaged CH* emissions images, and (b) a phase-averaged CH* emission image of the flame front, both during the acoustic forcing. Compression drivers are in-phase. $f_r = 775$ Hz, $\dot{m}_{air} = 1.724$ g/s, $\dot{m}_{fuel} = 0.097$ g/s , $\phi_{LB} = 0.85$.

7.4 The saturation phenomenon

Three campaign of measurements have been performed, with the central flame positioned at PAN, VAN and IAN basin of influence. Results are obtained for imposed acoustic pressure perturbations with varying amplitude at a given resonant frequency f_r. Acoustic pressure fluctuations are recorded by means of the microphone M1 placed at the pressure antinode of the center of the cavity. This position is considered as a local position, and measurements there as the local pressure fluctuations, when the central flame is positioned at PAN. Otherwise this position is the reference position of pressure measurements. The RMS perturbation amplitude measured at the reference position ranges from 100 to 1600 Pa. For cases with the central flame at the basin of IAN and VAN, measurements at the reference position for RMS pressure perturbation amplitudes lower than 400 Pa were not performed. When the central flame is positioned at the IAN basin, the local acoustic pressure fluctuations at $x/L_c = -0.14$, is interpolated from the simulated acoustic field. The amplitude of the pressure fluctuation at IAN is 52%±12% of the amplitude at the central location PAN. The incertitude of this value is related to temperature uncertainty since this pressure amplitude is interpolated from simulation results with a variable temperature field. When the central flame is positioned at the VAN basin, the local acoustic pressure fluctuations is that

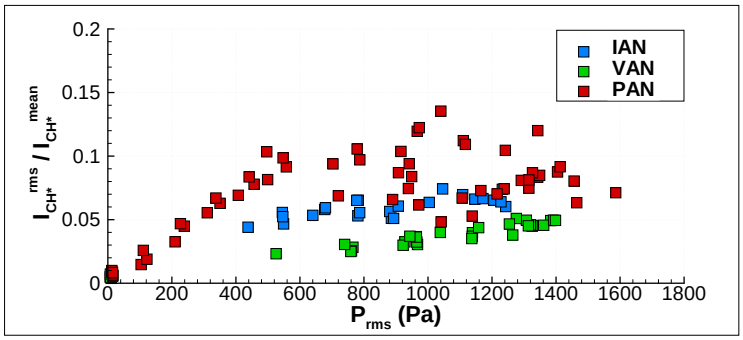

(a)

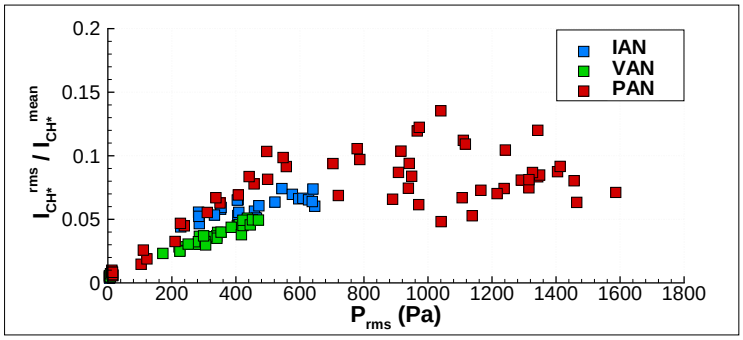

(b)

Figure 7.34: Relationship between P_{rms} and $I_{CH*}^{rms}/I_{CH*}^{mean}$, the normalized amplitude of the RMS value of the CH* emission fluctuations. (a) P_{rms} is measured at the center of the cavity. (b) P_{rms} is a local pressure according to the position (PAN, IAN or VAN). f_r between 760 and 800 Hz, $\dot{m}_{air} = 1.724$ g/s, $\dot{m}_{fuel} = 0.097$ g/s , $\phi_{LB} = 0.85$.

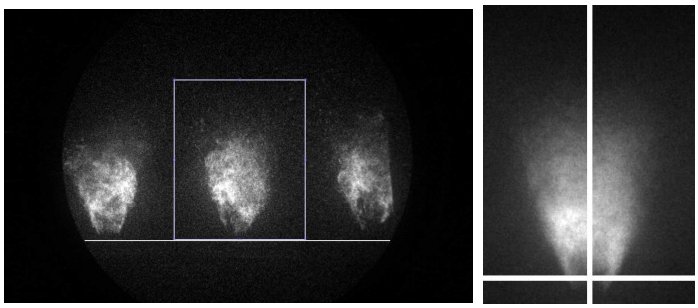

(a) (b)

Figure 7.35: (a) Region of interest in high speed images of the flame front for OH* signal extraction. (b) Intensity profile positions in class-averaged images: verticals are on the injector axis, horizontals are at $z = 7.5$ mm ($z/D_{exit} = 0.93$). $\dot{m}_{air} = 1.724$ g/s, $\dot{m}_{fuel} = 0.097$ g/s , $\phi_{LB} = 0.85$.

recorded by means of the microphone M2 placed at $x/L_c = -0.256$, the basin of influence of the velocity antinode. The combustion intensity is described by the flame front CH* chimiluminescence emission. The mean value of the CH* emission (I^{mean}_{CH*}), is calculated from a signal recorded during 1000 cycles of the acoustic forcing. The RMS amplitude of the CH* emission signal (I^{rms}_{CH*}) is calculated for f_r using the Matlab's pwelch signal processing tool as is explained in [121].

Fig. 7.34(a) shows the experimental correlation found between I^{rms}_{CH*}, normalized by I^{mean}_{CH*}, and the amplitude of the RMS pressure fluctuations measured at the reference position. Data in the case of PAN reveal a linear behavior with the amplitude of pressure fluctuations up to $P_{rms} \approx 600$ Pa. From this value the flame response saturates showing scattered values. As seen in section 6.4.2 the data scattering is due to the behavior of I^{rms}_{CH*} with the pressure perturbations. Data in the case of the central flame at IAN show a low amplitude dependence with respect to the pressure perturbations measured at the reference position. $I^{rms}_{CH*}/I^{mean}_{CH*}$ points show a very slightly increase with pressure amplitudes and can be considered as almost constant. Data acquired when the central flame is at the basin of VAN show a linear dependence with the pressure perturbation with a low slope compared with data at PAN. Reporting the data of IAN and VAN to the local pressure perturbation amplitude it is obtained a rather different behavior of the flame CH* emission response (Fig. 7.34(b)). In the case of IAN data reveal now a quite linear behavior with P_{rms}. A slope, slightly lower than that for data at PAN, is noted in the evolution of $I^{rms}_{CH*}/I^{mean}_{CH*}$. The slight dispersion of the data may be explained by the fact that the local pressure amplitude is interpolated from simulation results with a variable temperature field. The $I^{rms}_{CH*}/I^{mean}_{CH*}$ values increase as P_{rms} is augmented and for a value close to $P_{rms} = 600$ Pa, the flame response also saturates, as seen for the case at PAN. The flame CH* emission response at VAN shows a linear behavior with P_{rms}, with a slope similar to that found at IAN. In this case no saturation $I^{rms}_{CH*}/I^{mean}_{CH*}$ is reached.

In order to explore the underlying mechanism for saturation, two series of high speed line-of-sight images of the flame OH* emission are analyzed. The setup is composed of a Phantom V2512 high speed camera, an image intensifier LAMBERT HICATT

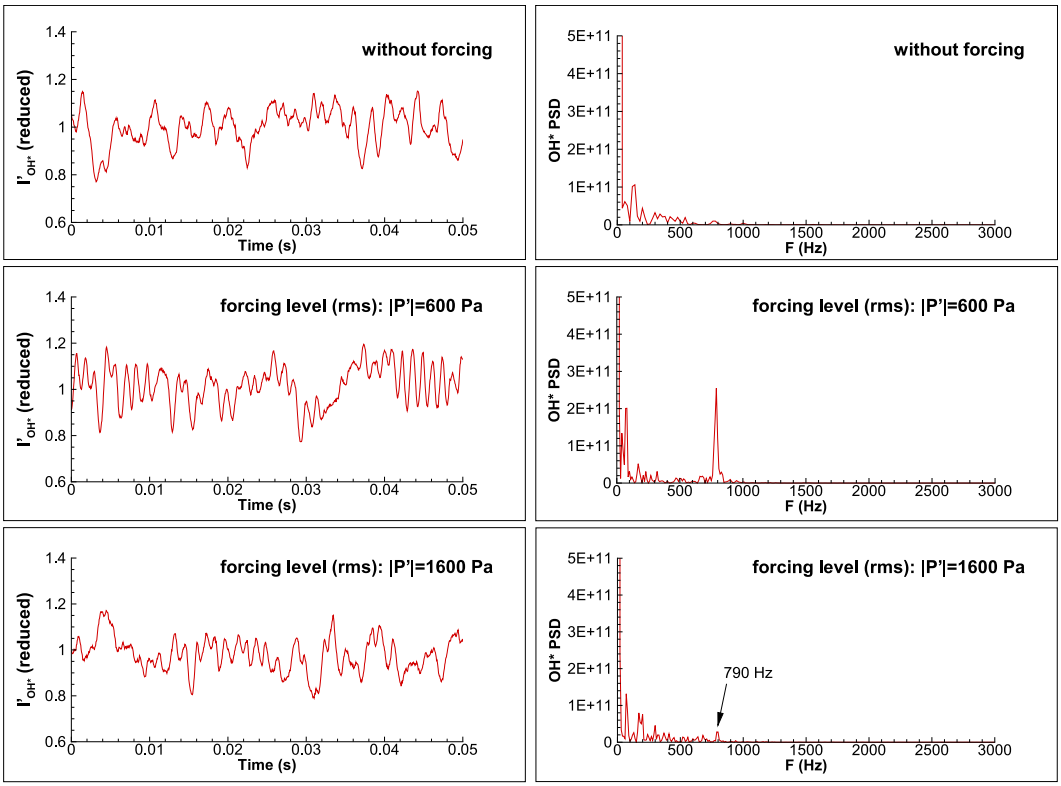

Figure 7.36: OH* emissions signals, reduced by their mean values, and their PSD obtained from high speed images of the central flame located at PAN. f_r = 790 Hz, $\dot{m}_{air}$ = 1.724 g/s, $\dot{m}_{fuel}$ = 0.097 g/s , ϕ_{LB} = 0.85.

25 equipped with a UV-100 mm lens and an interference filter centered at λ = 325 nm. The images have been recorded at 20 kfps, exposure time of 40 μs and a spatial resolution of 0.19 mm/pixel. These images correspond to the case with the central flame positioned at the basin of PAN. Each series corresponds to a pressure perturbation amplitude P_{rms}, of about 600 and 1600 Pa, in the transition between the linear and the saturation regime and in the saturation regime of the flame response respectively. Thus, results from the case at PAN are presented for the remainder of this section. Investigation is focused in a region of interest (65 × 70 mm) including only the central flame as shown in Fig. 7.35(a). Signals over time are extracted from the two series of high speed images, computing the overall intensity of pixels within the ROI. In addition, a signal from a series of images without forcing is also computed. Signals and their respective PSD are presented in Fig. 7.36. The signal without forcing shows oscillations which are consequence of the turbulent combustion, but as shown by its PSD spectrum, there is no really strong organized oscillations at a given frequency. The signal of the case at P_{rms} = 600 Pa, in the transition regime, shows a strong oscillation at the driving forcing frequency as it is verified by the strong peak at f_r in its PSD spectrum. Increasing the perturbation amplitude to P_{rms} = 1600 Pa, in the saturation regime, it is noted that the signal oscillation amplitude diminishes. Its PSD spectrum confirms this observation showing that the flame response at the driving resonant frequency importantly decreases.

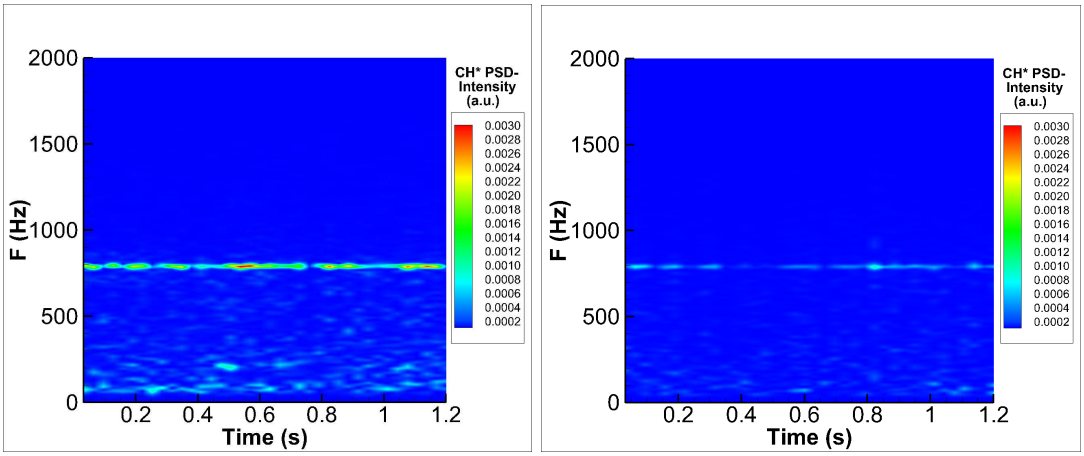

(a) (b)

Figure 7.37: Short time Fourier transform of CH* emission signals from the central flame located at PAN, recorded by PM. (a) $|P'|_{rms} = 600$ Pa and (b) $|P'|_{rms} = 1600$ Pa. $f_r = 790$ Hz, $\dot{m}_{air} = 1.724$ g/s, $\dot{m}_{fuel} = 0.097$ g/s , $\phi_{LB} = 0.85$.

In order to get a more complete insight on the flame dynamics over time, STFT calculations of CH* emission signals, recorded by a PM in the two cases analyzed here, have been performed. The results presented in Fig. 7.37 show that both responses are established at the driving frequency f_r. But, the intensity of the response over time at high perturbation amplitude (Fig. 7.37(b)) is much lower than the case in the transition regime (Fig. 7.37(a)). From the STFT diagram of Fig. 7.37(a), the response at f_r appears, with some intermittences of very short duration, but the response is strongly established over time. In contrast, the response at f_r in the STFT diagram of Fig. 7.37(b) presents intermittences of longer duration and so the response is weakly established over time. Note from the STFT diagrams that in the case at the transition regime (Fig. 7.37(a)) there is more energy transferred to low frequencies, with some peaks that appear punctually but not established over time, compared to the case in the saturation regime where there is almost no response at low frequencies (Fig. 7.37(b)).

A reconstruction of a forcing cycle is carried out by means of 40 class-averaged images from high speed views of the OH* flame front for each case. Four class-averaged images of each reconstructed forcing cycle are presented in two columns and four rows (Fig. 7.38 bottom). Left and right column correspond to cases in the transition regime and saturation regime respectively. Class-averaged images of each case are synchronized with its respective pressure perturbation signals (Fig. 7.38 top) and then post-synchronized between them. The time (t/T_{cycle}) indicated on flame images are with respect to the pressure perturbation signal, being $t/T_{cycle} = 0$ the instant where the pressure is zero and increasing. From images in the transition regime, the flame shows a fairly well defined shape evolution with a stabilization points well noticeable. The flame in the saturation regime presents a quite different structure. Its shape evolution during the cycle of forcing is not well discernible and so it is difficult to recognize stabilization points.

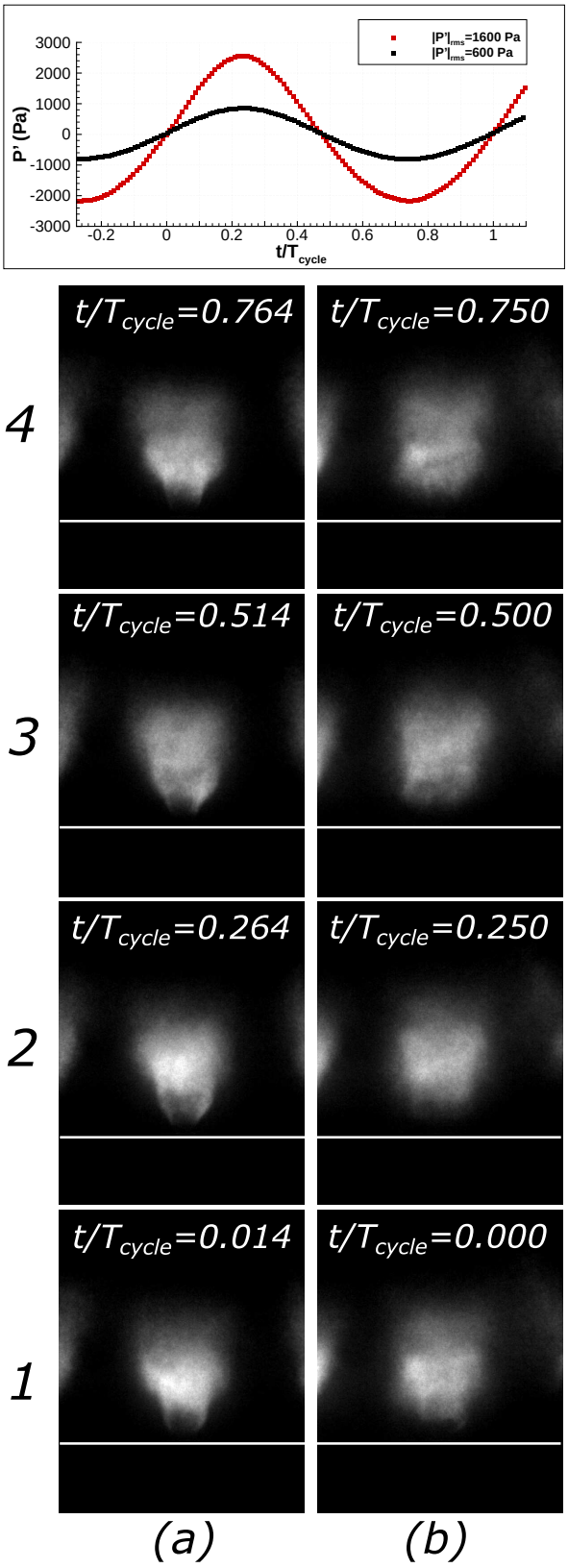

Figure 7.38: Top: Post-synchronized pressure signals measured at PAN, corresponding to the bottom images. Bottom: Flame front OH* emission class-averaged images of a reconstruction of a full acoustic forcing cycle for two levels of perturbation: (a) $|P'|_{rms} = 600$ Pa and (b) $|P'|_{rms} = 1600$ Pa. $f_r = 790$ Hz, $\dot{m}_{air} = 1.724$ g/s, $\dot{m}_{fuel} = 0.097$ g/s , $\phi_{LB} = 0.85$. System at PAN.

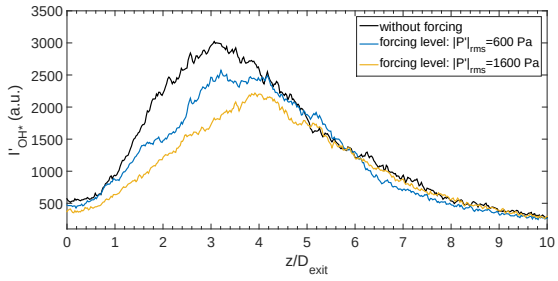

(a)

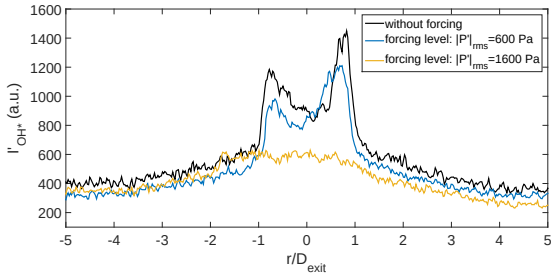

(b)

Figure 7.39: Class-averaged profiles of the flame front OH* emissions along the: (a) vertical line and (b) horizontal line defined in Fig. 7.35(b). Profiles are extracted from a image without forcing and from images of row 2 of Fig. 7.38(b). $f_r = 790$ Hz, $\dot{m}_{air} = 1.724$ g/s, $\dot{m}_{fuel} = 0.097$ g/s , $\phi_{LB} = 0.85$.

Vertical profiles, obtained on the injector axis (see Fig. 7.35(b)), of the two cases are compared with a profile of a case without forcing (Fig. 7.39(a)). The profiles with acoustic forcing correspond to images in row-2 of Fig. 7.38 (bottom). These profiles, at almost the same time of the forcing cycle, reveal a different front structure between the two cases. By choosing $I'_{OH} = 800$ (a.u.) as a threshold to for the presence of the flame, it is noted that the flame in the case at $P_{rms} = 600$ Pa stabilizes closer to the nozzle exit than the case at $P_{rms} = 1600$ Pa. The maximum intensity is higher and appears at a lower z-position for $P_{rms} = 600$ Pa than for $P_{rms} = 1600$ Pa. Both maximums are lower than the maximum intensity of the case without forcing. Analyzing the vertical profiles of the four images in the column (a) of Fig. 7.38 (bottom), it is noted that the maximum value of intensity evolves spatially and in magnitude, indicating the passage of an intensity wave (see Fig. 7.40(a)). The vertical profile of the row-1 column (a) is very similar to the profile without forcing (maximum value and position) suggesting that, during a time interval, the flame recovers the structure of a flame without forcing. The vertical profiles of the four images in the column (b) of Fig. 7.38 (bottom), show a lower evolution of the OH* intensity with a maximum of about 75% of the maximum value without forcing (see Fig. 7.40(b)). The flame in this case never recovers a structure similar to that without forcing.

Horizontal profiles are obtained at $z/D_{exit} = 0.93$ from an image without forcing (see Fig. 7.35(b)) and from images in row-2 (Fig. 7.39(b)). At this position and for this instant of the forcing cycle, the flame stabilization of the case at $P_{rms} = 600$ Pa is similar to that without forcing. In contrast, the profile corresponding to the case at

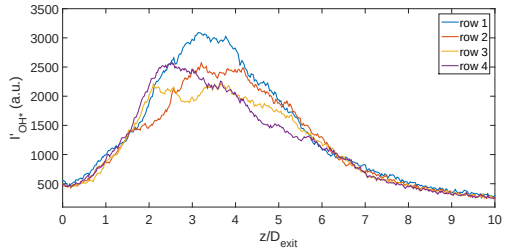

(a) 1: $|P'|_{rms} = 600$ Pa

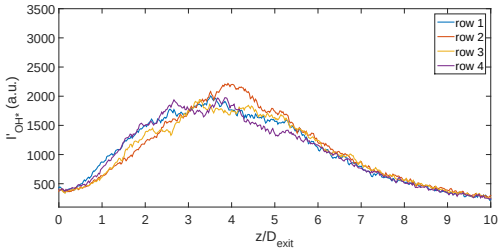

(b) 1: $|P'|_{rms} = 1600$ Pa

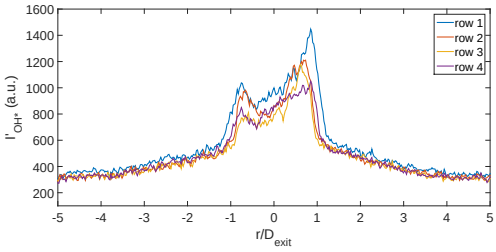

(a) 2: $|P'|_{rms} = 600$ Pa

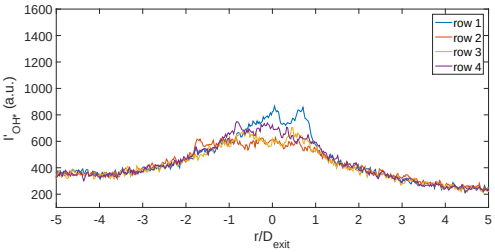

(b) 2: $|P'|_{rms} = 1600$ Pa

Figure 7.40: Vertical (top) and horizontal (bottom) profiles of the flame front OH* emission at four moments of a reconstructed acoustic forcing cycle. Profiles are from class-averaged images of the four rows of Fig. 7.38(b). Profiles positions indicated in Fig. 7.35(b). $f_r = 790$ Hz, $\dot{m}_{air} = 1.724$ g/s, $\dot{m}_{fuel} = 0.097$ g/s , $\phi_{LB} = 0.85$.

$P_{rms} = 1600$ Pa shows intensity values lower than $I'_{OH} = 800$ (a.u.) along the entire profile. This denotes that flame stabilization in this case is located higher downstream. Analyzing the horizontal profiles of the four images in the column (a) of Fig. 7.38 (bottom), it is noted the evolution of the maximum intensity indicating a fluctuation of the flame stabilization position (see Fig. 7.40(a)). Considering the threshold value $I'_{OH} = 800$ (a.u.) it is possible to conclude that by this position the flame is always present. The profiles of the images in column (b) of Fig. 7.38 (bottom) also show a fluctuation of maximum values denoting the fluctuation of the flame stabilization position (see Fig. 7.40(b)). However, based on the intensity threshold value, there is only a time interval (corresponding to the image in row-1) when the stabilization position hardly goes down to the position $z/D_{exit} = 0.93$.

The observed flame behaviors suggest that the change between the flame shape/structure in the linear and transition regime of response and the shape/structure in the saturation regime can explain the saturation of the response. Moreover, in the saturation regime, the higher position of the flame stabilization could be the reason of the weak combustion intensity and this in turn may be the prelude of the flame blowout. Thus, the flame response evolution at a given resonant frequency is associated to a change in its shape/structure as the imposed perturbation amplitude is incremented, passing from a wrinkled flame response to a more chaotic behavior. The wrinkled response observed here is characterized by symmetrical oscillations of the front about the injection axis, whereas the chaotic response is characterized by a disordered response and asymmetric oscillation of the flame sides at the stabilization region. Bourehla and Baillot in [60] already proposed this change, among others possibilities, in the

flame shape/structure to imposed velocity oscillations for a laminar conical premixed flame over a wide range of frequencies and perturbation amplitudes. In the case of a single premixed swirling flame longitudinally forced, the change of the stabilization position from near of a centerbody to a position downstream is found as one of the key mechanism behind the saturation process [134].

Chapter 8

Conclusions and perspectives

Within the domain of thermoacoustic instabilities, this work is placed among the experimental test benches in open-loop forcing. In particular, the focus of this study is the dynamics of a system composed by a two-phase swirling flow and its flame, undergoing the effects of a downstream transverse acoustic perturbation. A new setup has been designed to stabilize three flames produced by swirling two-phase flows linearly arranged in a combustion chamber. This combustion chamber mimics a sector of the MICCA-Spray annular chamber of the EM2C laboratory [1]. An ingenious aerodynamic injection arrangement, devised during this work, ensures the combustion stabilization without strong wall strong confinement. This is an important achievement since until now investigation of neighboring flames and their interaction in an open-loop forcing setup mimicking a sector of an annular chamber was not possible [82]. The cavity, with an adjustable length L_c, has been conceived to obtain the resonance of the 2T1L mode for any forcing frequencies f_0 generated in the range $0.5 - 1.4$ kHz by means of two compression drivers mounted on two opposite walls of the chamber.

The approach of this study has been to investigate first the swirling air flow, then the spray and finally the flame response, this last one to a wide range of imposed acoustic pressure perturbations.

Identification of the 2T1L acoustic mode

The experimental response of the cavity with f_0 is well reproduced by simulations, both considering a mean constant temperature coherent with temperature measurements and a 1D variable temperature field defined from measurements within the combustion chamber. Along with simulations, theoretical calculations allow interpreting the acoustic behavior of the chamber. For a given length L_c, as the forcing frequency f_0 is approaching the resonance frequency f_r, the pressure amplitude in the center of the cavity grows and the minimum of the pressure amplitudes moves its position toward $x/L_c = 0.25$. Simultaneously, the phase $\varphi(f_0, x)$ measured at a fixed point in the vicinity of $x/L_c = 0.25$, passes from 0 to π when the forcing frequency varies from $f_0 < f_r$ to $f_0 > f_r$. At $f_0 = f_r$, the pressure amplitude measured at the center of the cavity defines the pressure antinode (PAN) of the 2T1L acoustic mode and its

velocity antinode (VAN) is positioned at x_{VA} where acoustic pressure fluctuations are and absolute pressure minimum satisfying that $\varphi(f_r, x_{VA}) = 0.5\pi$.

Based on the aforementioned characteristics, a method has been proposed to determine whether the the 2T1L mode is well excited with or without combustion. The defined criterion is based on pressure measurements made at two points in the forcing frequency domain, namely at the center of the cavity and another one in the vicinity of $x/L_c = 0.25$. The maximum of pressure amplitude at the center of the cavity is searched by varying f_0. To confirm that the identified frequency corresponds to a 2T1L mode, $\varphi(f_0, x)$ have to pass from 0 to π at any point x near to $x/L_c = 0.25$. The method was validated first in cold conditions and then during combustion.

Once the desired acoustic mode is established, the system composed by the spray flow and flame was positioned at three acoustic basin of interest in the 2T1L acoustic resonant mode of the chamber, namely the pressure antinode (PAN), the intensity antinode (IAN) and the velocity antinode (VAN).

Two-phase flow behavior

The investigation of the swirling air flow in inert conditions has allowed to describe its natural characteristics. The determination of the level of swirl imparted to the flow by means of the swirl number calculation has shown the coherence of the swirl level with the fluid dynamical structures observed. The swirling flow issued of the injector used for this work, in the operating conditions investigated here, presents a well recognized Central Recirculation Zone (CRZ), induced by a double helix type vortex breakdown. A Precessing Vortex Core (PVC) has been identified with a frequency between 2.25 and 2.5 kHz. This frequency may depend on the flow rate. Kelvin-Helmholtz vortices have been recognized in the outer layer of the flow. The characteristics of the air-flow free of acoustic forcing are still presents at low levels of perturbations, persist at medium levels and are greatly affected at high levels. It has been quantified the modulation of the flow rate at the injector exit when it is located at PAN. It is characterized by an important periodic acceleration and deceleration of the flow driven by the acoustic forcing. All the velocity components of the swirling flow are modulated by the forcing. In particular the modulation of the vertical and azimuthal velocity components induces an strong modulation of the level of swirl imparted to the flow. This modulation explain the evolution of the flow pattern visualized at PAN. The pattern evolution indicates that as the swirl number S is periodically modulated, at least two type of vortex breakdown arises during a cycle of forcing including a time interval where the CRZ is momentarily disrupted. In reactive conditions, fuel droplets sizing performed in the spray flow has shown that the spray is formed mostly by droplets of lower size ($1-10\ \mu$m). Nevertheless, fuel droplets with higher size are formed. By correlating fuel droplets data rate contours with vertical tomography images, it its deduced that the visualization of the spray are mainly representative of large droplets as the intensity of the light scattered by a droplet is proportional to the square of its diameter. In the presence of the acoustic forcing, the spray adapts to the perturbation depending on its size population:

- droplets with a size small enough such that they are rapidly evaporated;

- those becoming small enough to be captured by fluid structures of the perturbed flow;
- finally those with a sufficiently large size such that they are only deviated from their trajectory and follow a rather ballistic trajectory. The droplets visualized in the tomography views belong rather to the third group.

At PAN, the visualized spray is symmetrically perturbed close to the injector exit and downstream the swirl component of the flow tends to break this symmetry.

As the system is moved to other locations of interest in the acoustic field, other effects arise as is in the case with the system at the intensity antinode (IAN). Here, the important level of acoustic velocity and pressure gradient explain the dissymmetry observed in the response of the air-flow in cold conditions as well as in the response of the spray. At VAN the overall flow is laterally disturbed showing a rocking motion, term borrowed from molecular vibrations with a similar motion. As at VAN, pressure fluctuations represent less than 10% of the amplitude in PAN, its effects are considered negligible. Very weak response to perturbations are noted close to the injector exit but the amplitude of the periodic lateral oscillation is accentuated downstream. These effects are observed both in the inert air-flow and the spray during combustion. Similar effects as those highlighted in this work were shown on a laminar premixed V-shape flame in the work by Lespinasse [95] Here, despite the high U_{bulk} velocity of the flow and its high level of swirl it manages to adapt to its environment disturbance condition being the observed structures the results of that adaptation.

Spray flame dynamics

Without acoustic forcing it has been verified that the three flame fronts, characterized by CH* or OH* chemiluminescence emissions, have similar properties (e.g. heights and open angles) and consequently they can well model neighboring flames of an annular chamber sector. The range of equivalence ratio used in this work does not introduce major changes in the shape of the reference flame.

Under the transverse acoustic forcing, the flame dynamics were shown to respond at the forcing frequency. The investigation was focused mainly in the central flame dynamics. The front response is characterized by a pulsation of the combustion intensity which is at its turn dependent of the behavior of the perturbed spray flow, both being driven at the resonant frequency of the mode. Thus, under an axisymmetric disturbance where the spray flow is symmetrically affected the pulsation motion of the front is also axisymmetric. This is accompanied by front wrinkles symmetrically and periodically formed. This pulsation shifted on a side of front with respect to the injection axis when the flame was submitted to high acoustic pressure and velocity gradient of the IAN basin. This is in accord with the dissymmetry observed on the flow within the acoustic field at this location. Added to this dissymmetry, a non-linear effect has been highlighted on the front. It is manifested as a stationary deviation of the front as it is clearly highlighted by the barycentric lines of the front obtained during the acoustic perturbation cycle. When the flame front is submitted to a high transverse acoustic velocity fluctuations the combustion intensity pulsation has rather a diagonal pattern

in the direction of the swirl as seen in the reconstruction of perturbation cycle. This is accompanied by front wrinkles propagated on each side of the front viewed from line-of-sight phase-averaged and class-averaged images. They are formed with a delay between each side of the front and it has been verified that this delay is not the same between two cases whit different f_r. It is suggested that the shape and motion of the front is governed by a combined effect of the flow swirling level and the frequency of the perturbation, similar to what it was theoretically predicted in the case of a premixed swirling flame by Acharya *et al.* [114]. The wrinkled formation along with the barycentric lines of the front suggest a more complex motion than a simply lateral oscillation. Indeed, the front might have a motion governed by the wrinkles which traces in the space a helical spiral path.

The correlation between the CH* emissions and pressure perturbations reveals a linear regime of the flame response in the three acoustic basin studied. In this regime, the slope of the response slightly decreases as the flame passes from the PAN location to IAN and VAN respectively. The different slope in the flame response is the consequence of the particular characteristics of the combustion intensity at each location in the acoustic field. The linear regime is followed by a saturation regime observed at PAN and IAN and not reached at VAN. In this regime, at the pressure antinode, it was noted a change in the shape/structure of the flame characterized by a shift of its stabilization position to another position downstream. Thus, at the end of the linear regime it is observed that the front shape remains well defined while it is symmetrically perturbed. The OH* signal of this flame shows a clear response at f_r. In contrast, in the saturation regime the flame shape become rather chaotic with a weak combustion intensity as shown by the spectrum of its OH* signal where the peak of the response at f_r comes down even with higher amplitude of the pressure perturbation. Bellows *et al.* [134] showed, in the case of a swirling premixed flame, that a key mechanism governing the saturation is the liftoff of the flame. At the IAN basin, the saturation regime of the flame response starts at a value close to that at PAN, but it is not necessarily the same since the possible mechanism of saturation is superposed with the others effects highlighted at this position, thus maybe anticipating the saturation regime. In the same way, at VAN and for higher levels of perturbation it is not evident if a saturation regime will be arise since the disturbance field here is completely different to that at PAN.

Perspectives

TACC-Spray configuration modularity allows in particular change the distance between injectors. The investigation of the flame dynamics in the case of a lower distance between injectors, started with the internship master degree work of A. Omri, is of fundamental interest. The distance between injectors is reduced in order to favor the flame and flow interactions. These interactions take place between neighboring injectors and the response of multiple injectors is not known. In particular, there is no indication when the response of these injectors can be considered decoupled from each other. A reduced injector distance might modify the environment encountered by the injected flow. Possible recirculations of hot gases confined by the flame fronts in contact can contributes to increase the environment temperature at the injector exit.

This might impact the fuel droplets evaporation process. Forcing such a configuration, flame responses different to those reported in this manuscript could be found.

As mentioned in other works (e.g. [1,82]), differences between stability/instability predictions in a single flame combustor and the instabilities encountered in annular chambers may come from the need to consider the effects of neighboring flames. Thus, based on the flame transfer functions elements given in this work for a given operating condition, FDF determination can be extended to a wider range of frequencies. Results could be compared with the behavior of the MICCA-Spray chamber of EM2C laboratory and can be useful as a data base for other systems with similar configurations.

It has been seen that the behavior of the fuel droplets submitted to acoustic perturbations plays an important role in the observed flame dynamics. This behavior could be different depending on the physical properties of the fuel. Moreover, the evaporation process of the fuel droplets also depend on the fuel properties. Since combustor instability depends on the characteristics of the fuel spray, for example a fuel with a lower evaporation rate can be used in order to investigate its impact on the flame dynamics [135].

The transition point and the subsequent saturation regime of the flame response highlighted in this work might be linked with the power of the flame. A saturation phenomenon was not identified in the work of Prieur [1] where the spray flame own the same equivalence ratio but higher power than a single spray flame in TACC-Spray. It will be interesting to vary the power of flames in TACC-Spray while keeping constant the equivalence ratio in order to see the sensitivity of the flame response to this parameter, in particular the transition point from the linear regime to the saturation.

Appendix

Appendix A

Helmholtz resonator

A.1 The Helmholtz resonator without mean flow

The Helmholtz resonator is a non-uniform pipe in the shape of a bottle (Fig. A.1). When the bottle is small compared to the acoustic wave length, the body of the bottle acts as an acoustic spring while the neck is an acoustic mass [105]. The volume of the bottle body is $V = L_b S_b$. If the cross-sectional area S_b of the bottle is large compared to the cross-sectional area S_n of the neck, the acoustic velocities in the body can be neglected compared to those in the neck. Thus the first assumption is that the pressure p'_{in} and the potential φ_{in} in the bottle are uniform. As the bottle is small compared to the wave length, this is $kl \ll 1$, compressibility is neglected and Bernoulli applied in the form:

$$\rho_0 \frac{\partial \varphi_{in}}{\partial t} + \frac{1}{2}\rho_0 u_{in}^2 + p'_{in} = \rho_0 \frac{\partial \varphi_{ex}}{\partial t} + \frac{1}{2}\rho_0 u_{ex}^2 + p'_{ex} \tag{A.1}$$

Assuming that $u_{in} = 0$ and also $u_{ex} = 0$ because there is not a mean flow, we rewrite the last equation as:

$$\rho_0 \frac{\partial}{\partial t}(\varphi_{in} - \varphi_{ex}) = p'_{ex} - p'_{in} \tag{A.2}$$

The potential difference over the neck is $\varphi_{ex} - \varphi_{in} = l u'_n$, in which the velocity u'_n is considered to be uniform (frictionless incompressible flow in a pipe with uniform cross section). We consider here that distance (l) is the the neck length with the end correction already added. For details about length correction lector can reference to [105]. Now we can write:

$$\rho_0 l \frac{du'_n}{dt} = p'_{in} - p'_{ex} \tag{A.3}$$

The change of mass must be equal to the flux through the bottle neck. In linearized form we find:

$$V \frac{d\rho'_{in}}{dt} = -\rho_0 u'_n S_n. \tag{A.4}$$

Assuming an adiabatic compression of the fluid in the bottle, ρ'_{in} can be removed using the constitutive equation $p'_{in} = c_0^2 \rho'_{in}$. With the latter relationship and the Eqn. A.4

into the Eqn. A.3 this yields:

$$\frac{d^2u'_n}{dt^2} + \frac{S_n c_0^2}{Vl} u'_n = -\frac{1}{\rho_0 l}\frac{dp'_{ex}}{dt}. \tag{A.5}$$

The natural resonance frequency of the Helmholtz resonator system is given by:

$$\omega_0^2 = \frac{S_n c_0^2}{Vl}. \tag{A.6}$$

For a harmonic excitation $p'_{ex} = \widehat{p}_{ex} e^{i\omega t}$ we find:

$$\frac{c_0 \rho_0 \widehat{u}_n}{\widehat{p}_{ex}} = -\frac{i\omega\omega_1/\omega_0^2}{1-(\omega/\omega_0)^2} \tag{A.7}$$

with $\omega_1 = c_0/l$. We note that u'_n and p'_{ex} are in phase quadrature. When the angular frequency of the external excitation is $\omega = \omega_0$ the pressure fluctuation inside the bottle (p'_{in}) will be amplified.

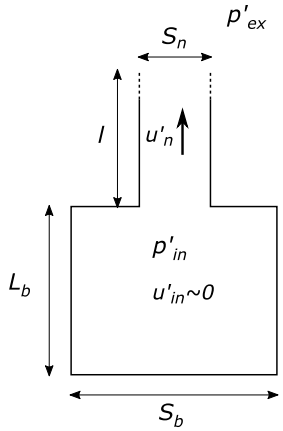

Figure A.1: Helmholtz resonator without a mean flow.

A.2 The Helmholtz resonator with a mean flow

The same bottle is considered, but in addition a continuous volume flow $Q_0 = u_0 S_n$, is injected (Fig. A.2). For this situation the Bernoulli equation is written as:

$$\rho_0 l \frac{du'_n}{dt} + \frac{1}{2}\rho_0 (u_0 + u'_n)^2 + p'_{ex} = p_0 + p'_{in} \tag{A.8}$$

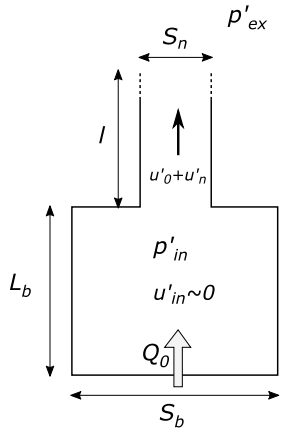

Figure A.2: Helmholtz resonator with a mean flow.

The left hand of this expression corresponds to a point at the exit section of the neck, while the right hand corresponds to a point within the bottle body. Because S_b is large compared to S_n, the velocity within the body (u'_{in}) is negligible, but the mean flow creates a static pressure within the bottle body, that is linked with the mean velocity in the neck (u_0) as follow:

$$p_0 = \frac{1}{2}\rho_0 u_0^2 \tag{A.9}$$

Furthermore, in the bottle neck we have the velocities $u_0 + u'_n$, and at the neck exit $u_0 + u'_{ex}$, in consequence $u'_n = u'_{ex}$. The Eqn. A.8 is then rewritten, neglecting second order terms to obtain:

$$\rho_0 l \frac{du'_n}{dt} + \rho_0 u_0 u'_n = p'_{in} - p'_{ex} \tag{A.10}$$

Using the linearized mas conservation law:

$$V \frac{d\rho'_{in}}{dt} = -(\rho_0 u'_n + \rho'_{ex} u_0) S_n \tag{A.11}$$

and the constitutive equation $p'_{in} = c_0^2 \rho'_{in}$ ($p'_{ex} = c_0^2 \rho'_{ex}$), to remove ρ'_{in} (ρ'_{ex}) and p'_{in} from Eqn. A.10, we obtain:

$$\frac{d^2 u'_n}{dt^2} + \frac{u_0}{l}\frac{du'_n}{dt} + \omega_0^2 u'_n = -\frac{\omega_0^2 M_0}{\rho_0 c_0} p'_{ex} - \frac{1}{\rho_0 l}\frac{dp'_{ex}}{dt}. \tag{A.12}$$

In this expression $M_0 = u_0/c_0$, and ω_0 is that defined in Eqn. A.6. The system response depend on the damping factor induced by the mean flow ($c_d = u_0/l$). In order

to highlight this we rewrite the Eqn. A.12 as follow:

$$\frac{d^2u'_n}{dt^2} + 2\varepsilon\omega_0\frac{du'_n}{dt} + \omega_0^2 u'_n = -\frac{\omega_0^2 M_0}{\rho_0 c_0}p'_{ex} - \frac{1}{\rho_0 l}\frac{dp'_{ex}}{dt} \tag{A.13}$$

where we have introduced the damping rate:

$$\varepsilon = \frac{c_d}{2\omega_0} \tag{A.14}$$

For a harmonic excitation $p'_{ex} = \widehat{p}_{ex}e^{i\omega t}$, we get:

$$\frac{c_0\rho_0\widehat{u}_n}{\widehat{p}_{ex}} = \frac{-(M_0 + i\omega\omega_1/\omega_0^2)}{1-(\omega/\omega_0)^2 + i2\varepsilon\omega/\omega_0} \tag{A.15}$$

where $\omega_1 = c_0/l$. The last expression can be reformulated in terms of $s = \omega/\omega_0$:

$$\frac{c_0\rho_0\widehat{u}_n}{\widehat{p}_{ex}} = \frac{-(M_0 + i\omega\omega_1/\omega_0^2)\left[(1-s^2) - i(2\varepsilon s)\right]}{(1-s^2)^2 + (2\varepsilon s)^2} \tag{A.16}$$

We write the magnitude and the phase of the last expression, then we search the condition to obtain a resonance of this system. The square of the magnitude and the phase of the expression in the Eqn. A.16 are:

$$\left|\frac{c_0\rho_0\widehat{u}_n}{\widehat{p}_{ex}}\right|^2 = \frac{M_0^2 + (\omega\omega_1/\omega_0^2)^2}{(1-s^2)^2 + (2\varepsilon s)^2} \tag{A.17}$$

$$arg\left(\frac{c_0\rho_0\widehat{u}_n}{\widehat{p}_{ex}}\right) = -\arctan\left(\frac{2\varepsilon s}{1-s^2}\right) \tag{A.18}$$

The condition for the resonance is found by satisfying:

$$\frac{d}{ds}\left[(1-s^2)^2 + (2\varepsilon s)^2\right] = 0 \tag{A.19}$$

and the second derivative of the extremum is positive. The last derivative shows that a resonance will exist if $s = \sqrt{1-2\varepsilon^2}$, with a damping ratio $\varepsilon < 1/\sqrt{2}$. The angular frequency of resonance is therefore:

$$\omega_r = \omega_0\sqrt{1-2\varepsilon^2} \tag{A.20}$$

and the amplitude at the resonance is:

$$\left|\frac{c_0\rho_0\widehat{u}_n}{\widehat{p}_{ex}}\right|^2 = \frac{M_0^2 + (\omega\omega_1/\omega_0^2)^2}{4\varepsilon^2(1-\varepsilon^2)} \tag{A.21}$$

For small values of the damping rate we have that $\omega_r \approx \omega_0$. The phase expressed in Eqn. A.18 is then $\approx -\pi/2$. Finally, we note that making $\varepsilon = 0$, this yields to the solution of the Helmholtz resonator without mean flow presented in the precedent section.

Appendix B

Compression Driver membrane velocity

The modeling of the oscillation movement of a compression driver made by Donnini and Quaranta in [136] leads to express its delivered acoustic power, for the range of frequencies of this work, as follows:

$$P_{ac} = R_{ac} v^2 = \frac{\rho S_{mem} a^2 \omega^2}{c} v^2 \tag{B.1}$$

where R_{ac} is the acoustic resistance which can be written in terms of the air density ρ, the area of the membrane S_{mem} and its radius a, $\omega = 2\pi f$ with f the frequency of the acoustic wave, c the speed of the acoustic wave and v the velocity of the membrane. It is noted that if the behavior of v with the frequency is in $1/f$ then the acoustic power will be constant.

Measurements have been carried out on the membrane of a compression driver that equips TACC-Spray. For the task it has been used a POLYTEC 3000 series laser vibrometer adjusted with a sensitivity equal to 1000 (mm/s)/Volt. The incertitude of these measurements is of about 1%. In the setup, the laser beam was aligned normal to the membrane surface impacting on it through a small hole made to its cover. Fig. B.1 reports the results for two conditions: (1) when the amplitude of the signal (V_{HAMEG}) of the HAMEG signal generator was kept constant giving a variable input tension (V_{CD}) in compression driver terminals; (2) when the amplitude of the signal (V_{HAMEG}) of the HAMEG signal generator was varied in order to kept constant the input tension on the compression driver terminals. The condition (1) corresponds to the scenario applied to study the acoustic response of the cavity with frequency. This condition gives a result closer to a behavior in $1/f$ than the condition (2).

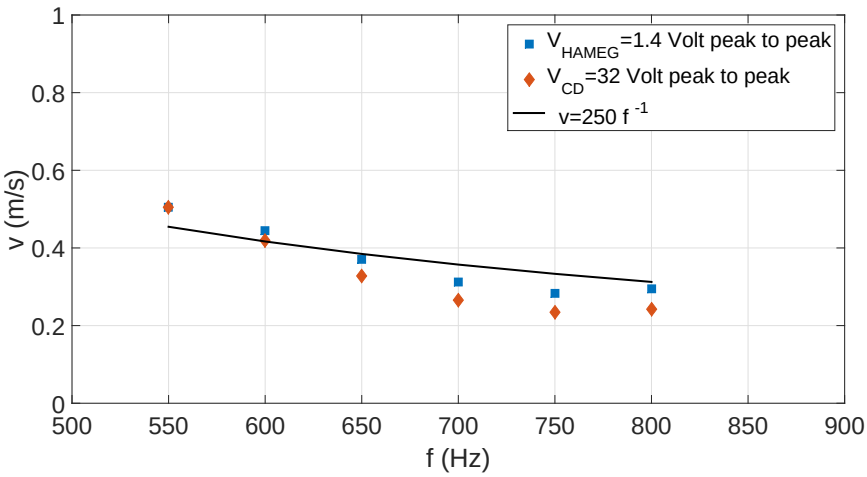

Figure B.1: Experimental measurements of the vibration velocity of the compression driver membrane.

Appendix C

Connection diagrams

C.1 Measurement instruments and a high speed camera

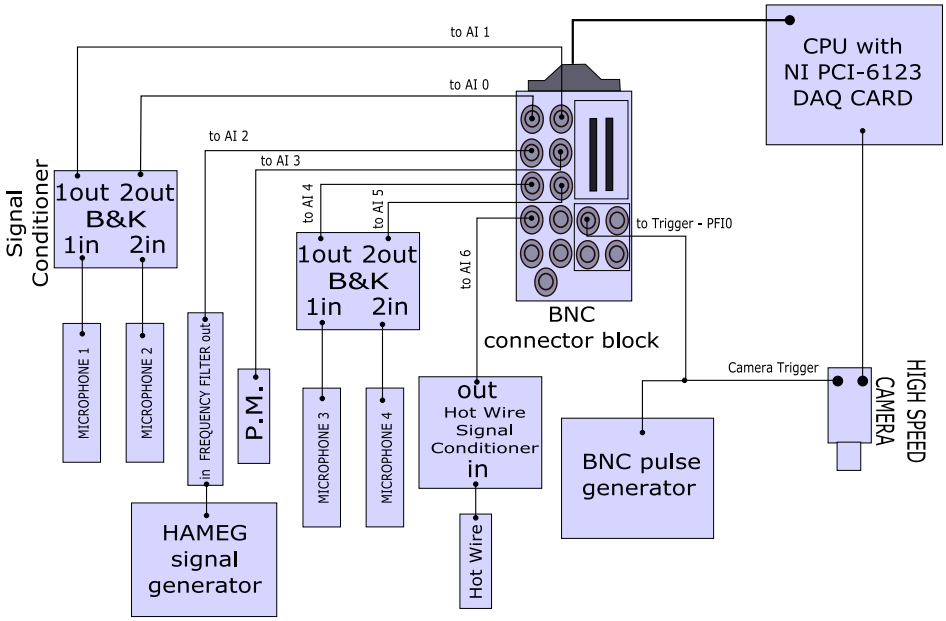

Figure C.1: Connection diagram of the measurement instruments and a high speed camera. The BNC pulse generator triggers the signals acquisition by means of the PFI0 connector of the BNC connector block, and the image acquisitions by means of the high speed camera. The Frequency Filter out signal is the signal that goes to the compression drivers.

C.2 Measurement instruments and the PIMAX4 ICCD camera

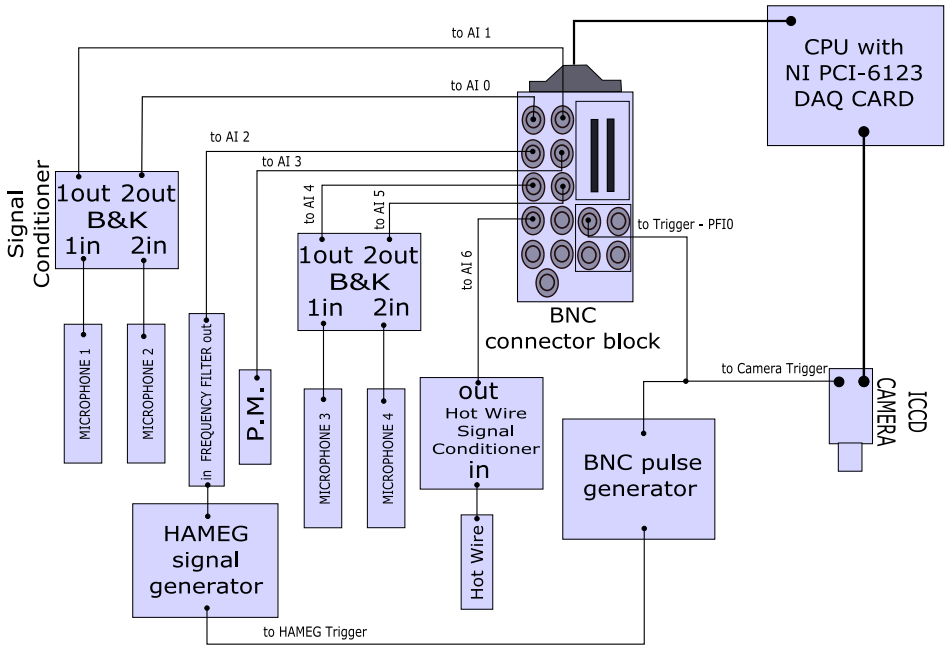

Figure C.2: Connection diagram of the measurement instruments and the PIMAX4 ICCD camera. The BNC pulse generator gives the signal frequency to the HAMEG signal generator and so impose its internal clock to the acoustic forcing. Thus it triggers and synchronizes a forcing cycle with the signals acquisition including images. The Frequency Filter out signal is the signal that goes to the compression drivers.

References

[1] Kevin Prieur. *Dynamique de la combustion dans un foyer annulaire multi-injecteurs diphasique*. PhD thesis, Université Paris-Saclay, 2017. (Cited on pages xvi, 18, 21, 149, 151, 154, 156, 205 & 209).

[2] High Level Group on Aviation Research. Flightpath 2050 europe's vision for aviation. Technical report, European Commission and the Advisory Council for Aeronautics Research in Europe, 2011. (Cited on page 1).

[3] Ying Huang and Vigor Yang. Dynamics and stability of lean-premixed swirl-stabilized combustion. *Prog. Energy and Combust. Sci.*, 35:293–364, 2009. (Cited on pages 1, 3, 8 & 118).

[4] Michel Cazalens, Sébastien Roux, Claude Sensiau, and Thierry Poinsot. Combustion instability problems analysis for high-pressure jet engine cores. *J. Prop. and Power*, 24:770–778, 2008. (Cited on page 1).

[5] A. K. Gupta, D. G. Lilley, and N. Syred. *Swirl Flows*. Abacus Press, 1984. (Cited on pages 3 & 5).

[6] Hanzhuang Liang and T. Maxworthy. Experimental investigation of a swirling jet in stationary and rotating surroundings. *Experiments in Fluids*, 45:283–293, 2008. (Cited on pages 3 & 56).

[7] J.-Z. Wu, H.-Y. Ma, and M.-D. Zhou. *Vorticity and Vortex Dynamics*. Springer, 2006. (Cited on pages 3 & 4).

[8] Jean Délery. *Handbook of Compressible Aerodynamics*. John Wiley & Sons, August 2010. (Cited on page 3).

[9] Mohamad Shaiful Ashrul Ishak and Mohammad Nazri Mohd Jaafar. The effect of swirl number on discharge coefficient for various orifice sizes in a burner system. *Journal Mekanikal*, 17:99–108, 2004. (Cited on page 4).

[10] Paul Billant, Jean-Marc Chomaz, and Patrick Huerre. Experimental study of vortex breakdown in swirling jets. *J. Fluid Mech.*, 376:183–219, 1998. (Cited on pages 4 & 5).

[11] C. Hirsch, D. Fanaca, P. Reddy, W. Polifke, and T. Sattelmayer. Influence of the swirler design on the flame transfer function of premixed flames. *Proceedings of the ASME Turbo Expo*, (GT2005-68195):151–160, 2005. (Cited on page 4).

[12] R. E. Spall, T. B. Gatski, and C. E. Grosch. A criterion for vortex breakdown. *Physics of Fluids*, 30(11):3434–3440, 1987. (Cited on page 4).

[13] O. Lucca-Negro and T. O'Doherty. Vortex breakdown: a review. *Progress in energy and combustion science*, 27:431–481, 2001. (Cited on pages 4, 5, 56 & 118).

[14] J.J. Choi, Z. Rusak, and A. K. Kapila. Numerical simulation of premixed chemical reactions with swirl. *Combustion Theory and Modelling*, 11(6):863–887, 2007. (Cited on page 4).

[15] N. Syred and J. M. Beer. Combustion in swirling flows: A review. *Combustion and Flame*, 23:143–201, 1974. (Cited on page 5).

[16] Nicholas Syred. A review of oscillation mechanisms and the role of the precessing vortex core (pvc) in swirl combustion systems. *Progress in Energy and Combustion Science*, 32:93–161, 2006. (Cited on pages 5 & 58).

[17] P.M. Anacleto, E.C. Fernandes, M.V. Heitor, and S.I. Shtork. Characterization of a strong swirling flow with precessing vortex core based on measurements of velocity and local pressure fluctuations. *10th International Symposium on Applications of Laser Techniques to Fluid Mechanics*, 2002. (Cited on page 5).

[18] M. R. Ruith, P. Chen, E. Meiburg, and T. Maxworthy. Three-dimensional vortex breakdown in swirling jets and wakes: direct numerical simulation. *Journal of Fluid Mechanics*, 486:331–778, 2003. (Cited on pages 5 & 56).

[19] S. Roux, G. Lartigue, T. Poinsot, U. Meier, and C. Bérat. Studies of mean and unsteady flow in a swirled combustor using experiments, acoustic analysis, and large eddy simulations. *Combustion and Flame*, 141:40–54, 2005. (Cited on page 5).

[20] C. E. Cala, E. C. Fernandes, M. V. Heitor, and S. I. Shtork. Coherent structures in unsteady swirling jet flow. *Experiments in Fluids*, 2006. (Cited on pages 5 & 117).

[21] K. Oberleithner, M. Sieber, C. N. Nayeri, C. O. Paschereit, C. Petz, H. C. Hege, B. R. Noack, and I. Wygnanski. Three-dimensional coherent structures in a swirling jet undergoing vortex breakdown: stability analysis and empirical mode construction. *Journal of Fluid Mechanics*, 679:383–414, 2011. (Cited on pages 5 & 56).

[22] Sergey V. Alekseenko, Sergey S. Abdurakipov, Mikhail Y. Hrebtov, Mikhail P. Tokarev, Vladimir M. Dulin, and Dmitriy M. Markovich. Coherent structures in the near-field of swirling turbulent jets: A tomographic piv study. *International Journal of Heat and Fluid Flow*, 70:363–379, 2018. (Cited on page 5).

[23] Shanwu Wang, Shih-Yang Hsieh, and Vigor Yang. Unsteady flow evolution in swirl injector with radial entry. i. stationary conditions. *Physics of Fluids*, 2005. (Cited on page 5).

[24] Yi-Huan Kao, Jacob B. Haseman, Samir B. Tambe, and San-Mou Jeng. Aerodynamics comparisons between two typical gas turbine combustion swirlers. *Proceeding of the ASME Turbo Expo*, 2014. (Cited on page 5).

[25] L. Selle, G. Lartigue, T. Poinsot, R. Koch, K.-U Schildmacher, W. Krebs, B. Prade, P. Kaufmann, and D. Veynante. Compressible large eddy simulation of turbulent combustion in complex geometry on unstructured meshes. *Combustion and Flame*, 137:489–505, 2004. (Cited on page 5).

[26] L. Selle, L. Benoit, T. Poinsot, F. Nicoud, and W. Krebs. Joint use of compressible large-eddy simulation and helmholtz solvers for the analysis of rotating modes in an industrial swirled burner. *Combustion and Flame*, 145:194–205, 2006. (Cited on page 5).

[27] Gabriel Staffelbach. *Simulation aux grandes echelles et analyse acoustique de turbines a gaz industrielles multi-bruleurs*. PhD thesis, INPT, 2006. (Cited on pages 5, 17 & 22).

[28] G. Staffelbach, L.Y.M. Gicquel, G. Boudier, and T. Poinsot. Large eddy simulation of self excited azimuthal modes in annular combustors. *Proc. Combust. Inst.*, 2009. (Cited on pages 5, 16, 17, 20 & 21).

[29] Abdulla Ghani. *Simulation aux grandes echelles des instabilités de combustion transverses des flammes parfaitement prémélangées et swirlées diphasiques*. PhD thesis, Institut National Polytechnique de Toulouse (INP Toulouse), 2015. (Cited on pages 6, 8 & 18).

[30] Jonas P. Moeck, Jean-François Bourgouin, Daniel Durox, Thierry Schuller, and Sébastian Candel. Nonlinear interaction between a precessing vortex core and acoustic oscillations in a turburlent swirling flame. *Comb. Flame.*, 159:2650–2668, 2012. (Cited on page 6).

[31] S. Candel, D. Durox, T. Schuller, J. F. Bourgouin, and J. Moeck. Dynamics of swirling flames. *Annual Review of Fluid Mechanics*, 46:147–173, 2014. (Cited on page 6).

[32] Shanwu Wang, Shih-Yang Hsieh, and Vigor Yang. Unsteady flow evolution in swirl injectors with radial entry. ii. external excitations. *Physics of Fluids*, 2005. (Cited on pages 6 & 56).

[33] P. Palies, D. Durox, T. Schuller, and S. Candel. The combined dynamics of swirler and turbulent premixed swirling flames. *Combustion and Flame*, 157(9):1698–171, 2010. (Cited on page 6).

[34] R. Santhosh and Saptarshi Basu. Acoustic response of vortex breakdown modes in a coaxial isothermal unconfined swirling jet. *Physics of Fluids*, 27(033601):1–22, 2015. (Cited on page 6).

[35] Daniel Durox, Jonas P. Moeck, Jean-François Bourgouin, Pascal Morenton, Marc Viallon, Thierry Schuller, and Sébastian Candel. Flame dynamics of variable swirl number system and instability control. *Combustion and Flame*, 160:1729–1742, 2013. (Cited on pages 6, 54 & 156).

[36] J. O'Connor and T. Lieuwen. Disturbance field characteristics of a transversely excited burner. *Combust. Sci. Technol.*, 183(5):427–443, 2011. (Cited on pages 6, 20, 49 & 111).

[37] J. O'Connor, T. Lieuwen, and M. Kolb. Visualization of shear layer dynamics in a transversely excited, annular premixing nozzle. *49th AIAA Aerospace Sciences Meeting, January 2011, Orlando, Florida*, (AIAA 2011-237):1–15, 2011. (Cited on page 6).

[38] J. O'Connor and T. Lieuwen. Further characterization of the disturbance field in a transversely excited swirl-stabilized flame. *Journal of Engineering for Gas Turbines and Power*, 134:1–9, 2012. (Cited on pages 6, 17, 20 & 139).

[39] Jacqueline O'Connor and Tim Lieuwen. Recirculation zone dynamics of a transversely excited swirl flow and flame. *Physics of Fluids*, 24(075107):1–30, 2012. (Cited on pages 6, 21 & 58).

[40] S. Hansford, J. O'Connor, K. Manoharan, and S. Hemchandra. Impact of flow non-axisymmetry on swirling flow dynamics and receptivity to acoustics. *Proc. ASME Turbo Expo*, GT2015(43377):1–16, 2015. (Cited on pages 6, 114 & 116).

[41] Y. Liao, A. T. Sakman, S.M. Jeng, and M. A. Jog. A comprehensive model to predict simplex atomizer performance. *ASME J. Eng. Gas Turbines Power*, (98-GT-441):1–11, 1998. (Cited on page 7).

[42] L. Martinez. *Simulation aux Grandes Échelles de l'Injection de carburant liquide dans les moteurs à combustion interne*. PhD thesis, Université de Toulouse. Ecole doctorale MEGeP, Institut Français du Pétrole, 2009. (Cited on page 7).

[43] M. Sanjosé, J. M. Senoner, F. Jaegle, B. Cuenot, S. Moreau, and T. Poinsot. Fuel injection model for euler-euler and euler-lagrange large-eddy simulations of an evaporating spray inside an aeronautical combustor. *International Journal of Multiphase Flow*, 37:514–529, 2011. (Cited on page 7).

[44] Grégory Hannebique. *Etude de la structure des flammes diphasiques dans les bruleurs aéronautiques*. PhD thesis, INP de Toulouse, 2013. (Cited on pages 7, 8 & 9).

[45] Arthur H. Lefebvre. *Atomization and Spray. Combustion: An International Series*. Hemisphere Publishing Corporation, 1989. (Cited on page 7).

[46] K. Rajamanickam and S. Basu. Insights into the dynamics of spray-swirl interactions. *Journal of Fluid Mechanics*, 810:82–126, 2017. (Cited on page 8).

[47] Théa Lancien. *Etude numérique de l'allumage diphasique de foyers annulaires multi-brûleurs*. PhD thesis, Université Paris-Saclay, 2018. (Cited on page 8).

[48] M. de la Cruz García, E. Mastorakos, and A. P. Dowling. Investigations on the self-excited oscillations in a kerosene spray flame. *Combust. Flame*, 156:374–384, 2009. (Cited on pages 9 & 21).

[49] Sergei S. Sazhin. Advanced models of fuel droplet heating and evaporation. *Progress in Energy and Combustion Science*, 32:162–214, 2006. (Cited on pages 9 & 74).

[50] Stephen R. Turns. *An Introduction to Combustion*. McGraw-Hill, second edition edition, 2000. (Cited on pages 9 & 11).

[51] Gilles Boisdron. *Etude de l'atomisation d'un jet liquide assisté par air soumis à une onde acoustique stationnaire transverse haute fréquence*. PhD thesis, Faculté des Sciences et Techniques de l'Université de Rouen, 2006. (Cited on page 13).

[52] Paul Clavin, Pierre Pelc&eacute, and Longting He. One-dimensional vibratory instability of planar flames propagating in tubes. *Journal of Fluid Mechanics*, 216:299–322, 1990. (Cited on page 13).

[53] N. Fogla. *Interplay Between Background Turbulence and Darrieus-Landau Instabilities in Premixed Flames via a model equation.* PhD thesis, Graduate College of the University of Illinois, 2010. (Cited on page 13).

[54] F.E.C. Culick. *Unsteady Motions in Combustion Chambers for Propulsion Systems*. RTO/NATO, 2006. (Cited on pages 13, 16 & 18).

[55] A. M. Morgans and I. Duran. Entropy noise: A review of theory, progress and challenges. *International Journal of Spray and Combustion Dynamics*, 8(4):285–298, 2016. (Cited on page 14).

[56] T. Schuller. *Mécanismes de Couplage dans les Interactions Acoustique-Combustion*. PhD thesis, Ecole Centrale Paris, 2003. (Cited on pages 15 & 16).

[57] L. Crocco and S.I. Cheng. Theory of combustion istability in liquid propellant rocket motors. *Butterworths scientific publications*, Agradograph 8:1–200, 1956. (Cited on page 15).

[58] J. O'Connor, V. Acharya, and T. Lieuwen. Transverse combustion instabilities: Acoustic, fluid mechanic, and flame processes. *Prog. Energy and Combust. Sci.*, 49:1–39, 2015. (Cited on pages 16, 17, 22 & 124).

[59] J-F. Bourgouin, D. Durox, J. P. Moeck, T. Schuller, and S. Candel. Self-sustained instabilities in an annular combustor coupled by azimuthal and longitudinal acoustic modes. *ASME Turbo Expo 2013, San Antonio, Texas, USA*, 1B(GT2013-95010):13, 2013. (Cited on pages 16, 20 & 21).

[60] A. Bourehla and F. Baillot. Appearance and stability of a laminar conical premixed flame subjected to an acoustic perturbation. *Combustion and Flame*, 1998. (Cited on pages 16 & 203).

[61] N. A. Worth and J. R. Dawson. Self-excited circumferential instabilities in a model annular gas turbine combustor: Global flame dynamics. *Proc. Combust. Inst.*, 34:3127–3134, 2013. (Cited on pages 16, 20 & 21).

[62] J. R. Dawson and N. A. Worth. Flame dynamics and unsteady heat release rate of self-excited azimuthal modes in an annular combustor. *Combust. Flame*, 161:2565–2578, 2014. (Cited on pages 16, 20 & 49).

[63] N. Noiray, M. Bothien, and B. Schuermans. Investigation of azimuthal staging concepts in annular gas turbines. *Combustion Theory and Modelling*, 15(5):585–606, 2011. (Cited on pages 16 & 145).

[64] Koushik Balasubramanian and R. I. Sujith. Thermoacoustic instability in a rijke tube: Non-normality and nonlinearity. *Physics of Fluids*, 20, 2008. (Cited on pages 16 & 19).

[65] Jean-François Bourgouin. *Dynamique de flamme dans les foyers annulaires comportant des injecteurs multiples*. PhD thesis, Ecole Centrale Paris, 2014. (Cited on pages 16, 17, 19 & 21).

[66] V. Yang and W. Anderson. *Liquid rocket engine combustion instability*, volume 169 of *Progress in Astronautics and Aeronautics*. AIAA Publications: Washington, DC, 1995. (Cited on pages 16 & 124).

[67] Françoise Baillot and Florian Lespinasse. Response of a laminar premixed v-flame to a high-frequency transverse acoustic field. *Combustion and Flame*, 161(5):1247–1267, 2014. (Cited on pages 17, 20, 21, 101, 111, 113, 122, 125 & 140).

[68] J. Blimbaum, M. Zanchetta, T. Akin, V. Acharya, J. O'Connor, D. R. Noble, and T. Lieuwen. Transverse to longitudinal acoustic coupling processes in annular combustion chambers. *Int. j. spray combust. dyn.*, 4:275–298, 2012. (Cited on page 17).

[69] A. P. Dowling. Nonlinear self-excited oscillations of a ducted flame. *Journal of Fluid Mechanics*, 346:271–290, 1997. (Cited on pages 17 & 145).

[70] M. Bauerheim, G. Staffelbach, N. A. Worth, J. R. Dawson, L. Y. M. Gicquel, and T. Poinsot. Sensitivity of les-based harmonic flame response model for turbulent swirled flame and impact on the stability of azimuthal modes. *Proccedings of the Combustion Institute*, 35(3):3355–3363, February 2015. (Cited on page 17).

[71] T. Schuller, D. Durox, and S. Candel. A unified model for the prediction of laminar flame transfer functions: comparisons between conical and v-flame dynamics. *Combust. Flame*, 134:21–34, 2003. (Cited on pages 17 & 156).

[72] N. Noiray, D. Durox, T. Shuller, and S. Candel. A unified framework for nonlinear combustion instability analysis based on the flame describing function. *Journal of Fluid Mechanics*, 615:139–167, October 2008. (Cited on pages 17, 19 & 145).

[73] P. Palies, D. Durox, T. Schuller, and S. Candel. Nonlinear combustion instability analysis based on the flame describing function applied to turbulent premixed swirling flames. *Combustion and Flame*, 158(10):1980 – 1991, 2011. (Cited on page 17).

[74] C. Mirat, D. Durox, and T. Schuller. Analysis of the spray and transfert function of swirling spray flame from a multi-jet steam assisted liquid fuel injector. *Proc. ASME Turbo Expo 2014, Düsseldorf, Germany*, 2014. (Cited on pages 18, 42 & 140).

[75] B. T. Zinn and E. A. Powell. Application of the galerkin method in the solution of combustion instability problems. *Proceedings of the Nineteenth International Astronautical Congres on Propulsion, Re-Entry Physics*, 3:59–73, 1970. (Cited on page 18).

[76] A. P. Dowling. A kinematic model of a ducted flame. *J. Fluid Mech.*, 394:51–72, 1999. (Cited on page 19).

[77] F. Boudy, D. Durox, T. Schuller, and S. Candel. Analysis of limit cycles sustained by two modes in the flame describing function framework. *C. R. Mécanique*, 341:181–190, 2013. (Cited on page 19).

[78] Renoud Gaudron. *Acoustic Response of Premixed Flames Submitted to Harmonic Sound Waves*. PhD thesis, Université Paris-Saclay, 2018. (Cited on pages 20 & 150).

[79] Pierre Wolf, Gabriel Staffelbach, Laurent Y.M. Gicquel, Jens-Dominik Müller, and Thierry Poinsot. Acoustic and large eddy simulation studies of azimuthal modes in annular combustion chambers. *Combust. Flame*, 159(Issue 11):3398–3413, 2012. (Cited on pages 20 & 21).

[80] G. Campa and S. M. Camporeale. Prediction of the thermoacoustic combustion instabilities in practical annular combustors. *ASME J. Eng. Gas Turbines Power*, 136:091504–1,9, 2014. (Cited on page 20).

[81] M. Bauerheim, F. Nicoud, and T. Poinsot. Progress in analytical methods to predict and control azimuthal combustion instability modes in annular chambers. *Phys. Fluids*, 28:021303–1, 27, 2016. (Cited on page 20).

[82] T. Poinsot. Prediction and control of combustion instabilities in real engines. *Proc. Combust. Inst.*, 36:1–28, 2017. (Cited on pages 20, 21, 205 & 209).

[83] Florian Lespinasse, Françoise Baillot, and Toufik Boushaki. Responses of v-flames placed in an hf transverse acoustic field from a velocity to pressure antinode. *C. R. Mécanique*, 341:110–120, 2013. (Cited on pages 20, 21, 101, 125 & 177).

[84] A. Saurabh, J. P. Moeck, and C. O. Paschereit. Swirl flame response to simultaneous axial and transverse velocity fluctuations. *ASME J. Eng. Gas Turbines Power*, 139:061502–1, 7, 2017. (Cited on page 20).

[85] J. O'Connor, N. A. Worth, and J. R. Dawson. Flame and flow dynamics of a self-excited, standing wave circumferential instability in a model annular gas turbine combustor. *ASME Turbo Expo 2013, San Antonio, Texas, USA*, 1B(GT2013-95897):1–15, 2013. (Cited on page 20).

[86] Daniel Durox, Kevin Prieur, Thierry Schuller, and Sébastian Candel. Different flame patterns linked with swirling injector interactions in an annular combustor. *Proceeding of the ASME Turbo Expo 2015*, 2015. (Cited on page 20).

[87] N. A. Worth and J. R. Dawson. Effect of equivalence ratio on the modal dynamics of azimuthal combustion instabilities. *Proc. Combust. Inst.*, 36:3743–3751, 2017. (Cited on pages 20 & 49).

[88] N. A. Worth, J. R. Dawson, J. AM Sidey, and E. Mastorakos. Azimuthally forced flame in an annular combustor. *Proc. Combust. Inst.*, 36:3783–3790, 2017. (Cited on page 20).

[89] T. Yi and D. A. Santavicca. Combustion instability and flame structure of turbulent swirl-stabilized liquid-fueled combustion. *J. Prop. and Power*, 28(5):1000–1014, 2012. (Cited on page 21).

[90] S. Tachibana, K. Saito, T. Yamamoto, M. Makida, T. Kitano, and R. Kurose. Experimental and numerical investigation of thermo-acoustic instability in a liquid-fuel aero-engine combustor at elevated pressure: Validity of large-eddy simulation of spray combustion. *Combustion and Flame*, 162:2621–2637, 2015. (Cited on page 21).

[91] F. Kappei, J. Y. Lee, C. E. Johnson, E. Lubarsky, Y. Neumeier, and B. T. Zinn. Investigation of oscillatory combustion processes in actively concontrol liquid fuel combustor. *in AIAA 36th Joint Propulsion Conference & Exhibit*, (AIAA 2000-3348):11, 2000. (Cited on page 21).

[92] P. Gajan, A. Strzelecki, B. Platet, R. Lecourt, and F. Giuliani. Investigation of spray behavior downstream of an aeroengine injector with acoustic excitation. *J. Prop. and Power*, 23:390–397, 2007. (Cited on page 21).

[93] T. Yi and D. A. Santavicca. Forced flame response of turbulent liquid-fueled lean-direct-injection combustion to fuel modulations. *J. Prop. and Power*, 25(6):1259–1271, 2009. (Cited on page 21).

[94] K. Prieur, D. Durox, T. Schuller, and S. Candel. Strong azimuthal combustion instabilities in a spray annular chamber with intermittent partial blow-off. *Proc. ASME Turbo Expo 2017, Charlotte, USA*, (Paper GT2017-63643):1–14, June 26-30 2017. (Cited on pages 21, 49, 61, 78 & 140).

[95] Florian Lespinasse. *Réponse de la dynamique d'une flamme prémélangée à des modes acoustique transverses*. PhD thesis, Normandie University, 2014. (Cited on pages 21, 36, 101, 157, 184, 185 & 207).

[96] J. F. Bourgouin, D. Durox, J. P. Moeck, T. Schuller, and S. Candel. A new pattern of instability observed in an annular combustor: The slanted mode. *Proc. Combust. Inst.*, 35:3237–3244, 2015. (Cited on page 21).

[97] Antonio Ficuciello. *Analysis of high frequency/high amplitude acoustic field effects on coaxial injection: application to liquid rocket engines*. PhD thesis, Normandie University, 2017. (Cited on pages 22, 38, 40, 184 & 185).

[98] N. Fdida. *Développement d'un système de granulométrie par imagerie. Application aux sprays larges et hétérogènes*. PhD thesis, University of Rouen, France, 2008. (Cited on page 38).

[99] Longfei Chen, Zhixin Liu, Penghao Sun, and Weiye Huo. Formulation of a fuel spray smd model at atmospheric pressure uing design of experiments (doe). *Fuel*, 153:355–360, 2015. (Cited on page 38).

[100] Longfei Chen, Guangze Li, Xiao Ma, Jongmook Lim, and Yudaya Sivathanu. A method for measuring planar sauter mean diameter of multi-component fuel spray based on the combined statistical extinction tomography and particle imaging velocimetry. *Fuel*, 214:154–164, 2018. (Cited on page 38).

[101] J. B. Blaisot and J. Yon. Droplet size and morphology characterization for dense sprays by image processing: application to the diesel spray. *Experiments in Fluids*, 39(6):977–994, 2005. (Cited on page 38).

[102] S. Barbosa, A. Boutier, F. Grisch, M. Lefebvre, F. Lemoine, A. Mohamed, J-M. Most, and F. Onofri. *Métrologie laser pour la mécanique des fluides*. Hermes Science, 2012. (Cited on page 39).

[103] K. Prieur, D. Durox, J. Beaunier, T. Schuller, and S. Candel. Ignition dynamics in an annular combustor for liquid spray and premixed gaseous injection. *Proc. Combust. Inst.*, 36:3717–3724, 2017. (Cited on page 49).

[104] Aditiya Saurabh and Christian Oliver Paschereit. Dynamics of premixed swirl flames under the influence of transverse acoustic fluctuations. *Combust. Flame*, 182:298–312, 2017. (Cited on page 49).

[105] S.W. Rienstra and A. Hirschberg. *An Introduction to Acoustics*. Eindhoven University of Technology, 2015. (Cited on pages 52 & 213).

[106] Turgut Sarpkaya. On stationary and travelling vortex breakdowns. *Journal of Fluid Mechanics*, 45:545–559, 1971. (Cited on page 56).

[107] J. R. Dawson, V. M. Rodriguez-Martinez, N. Syred, and T. O'Doherty. The effect of combustion instabiliy on the structure of recirculation zone in confined swirling flames. *Combustion Science and Technology*, 177(12):2349–2371, 2005. (Cited on page 58).

[108] J.C. Lasheras and E.J. Hopfinger. Liquid jet instability and atomization in a coaxial gaz stream. *Ann. Rev. Fluid Mech.*, 32:275–308, 2000. (Cited on page 60).

[109] William A. Sirignano. Advances in droplet array combustion theory and modeling. *Progress in Energy and Combustion Science*, 42:54–86, 2014. (Cited on page 74).

[110] P. Soille. *Morphological Image Analysis*. Springer-Verlag, 2004. (Cited on page 88).

[111] Wayne Rasband National Institutes of Health, USA. *Fiji is just Image J documentation*, 1.51 s edition. (Cited on page 88).

[112] S. Kotake. On combustion noise related to chemical reactions. *Journal of Sound and Vibration*, 42(3):399 – 410, 1975. (Cited on page 100).

[113] David Demare and Françoise Baillot. The role of secondary instabilities in the stabilization of a nonpremixed lifted jet flame. *Physics of Fluids*, 13:2662–2670, 2001. (Cited on page 114).

[114] V. Acharya, Shreekrishna, Dong-Hyuk Shin, and T. Lieuwen. Swirl effects on harmonically excited, premixed flame kinematics. *Combustion and Flame*, 159:1139–1150, 2012. (Cited on pages 116, 189, 191 & 208).

[115] D. Demare and F. Baillot. Acoustic enhancement of combustion in lifted non-premixed jet flames. *Combustion and Flame*, 139:312–328, 2004. (Cited on page 116).

[116] L. P. Bernal and A. Roshko. Streamwise vortex structure in plane mixing layers. *Journal of Fluid Mechanics*, 170:499–525, 1986. (Cited on page 116).

[117] M. Cáceres, F. Baillot, E. Domingues, J-B. Blaisot, G. Godard, and C. Gobin. New experimental setup for thermoacoustic instabilities investigation in two-phase flow swirled combustion. *Proc. 8th European Combustion Meeting 2017, Dubrovnik, Croatia*, (Paper ECM2017.0269):1–6, 2017. (Cited on page 118).

[118] M. Cáceres, F. Baillot, F. Lespinasse, and E. Domingues. Comparative study between transverse and longitudinal acoustic modes on a premixed v-shape flame. *Proc. 7th European Combustion Meeting 2015, Budapest, Hungary*, (P3-52):1–6, 2015. (Cited on page 125).

[119] Christophe Clanet, Geoffrey Searby, and Paul Clavin. Primary acoustic instability of flames propagating in tubes: cases of spray and premixed gas combustion. *J. Fluid Mech.*, 385:157–197, 1999. (Cited on page 130).

[120] R. Balachandran, B.O. Ayoola, C.F. Kaminski, A.P. Dowling, and E. Mastorakos. Experimental investigation of the nonlinear response of turbulent premixed flames to imposed inlet velocity oscillations. *Combust. Flame*, 143(1-2):37 – 55, 2005. (Cited on pages 140 & 145).

[121] Hanspeter Schmid. How to use the fft and matlab's pwelch function for signal and noise simulations and measurements. *FHNW/IME*, pages 2–13, August 2012. (Cited on pages 143 & 198).

[122] T. Poinsot, D. Veynante, F. Bourienne, S. Candel, E. Esposito, and J. Surget. Initiation and suppression of combustion instabilities by active control. *Proccedings of the Combustion Institute*, 22(1):1363–1370, 1989. (Cited on page 145).

[123] Tim Lieuwen and Yedidia Neumeier. Nonlinear pressrue-heat release transfer function measurements in a premixed combustor. *Proceedings of the Combustion Institute*, 29:99–105, 2002. (Cited on page 145).

[124] Lipika Kabiraj, Aditya Saurabh, Pankaj Wahi, and R. I. Sujith. Route to chaos for combustion instability in ducted laminar premixed flames. *Chaos*, 22:023129–1 – 023129–12, 2012. (Cited on page 145).

[125] Sebastian Schimek, Jonas P. Moeck, and Christian Oliver Paschereit. An experimental investigation of the nonlinear response of an atmospheric swirl-stabilized premixed flame. *Journal of Engineering for Gas Turbines and Power*, 133(101502):1–7, 2011. (Cited on page 145).

[126] S. Schimek, B. Cosić, J. P. Moeck, S. Terhaar, and C. O. Paschereit. Amplitude-dependent flow field and flame response to axial and tangential velocity fluctuations. *Journal of Engineering for Gas Turbines and Power*, 137(081501), 2015. (Cited on page 145).

[127] B. Ćosić, S. Terhaar, J.P. Moeck, and C. O. Paschereit. Response of a swirl-stabilized flame to simultaneous perturbations in equivalence ratio and velocity at high oscillation amplitudes. *Combustion and Flame*, 162:1046–1062, 2015. (Cited on page 145).

[128] Peter J. Schmid. Dynamic mode decomposition of numerical and experimental data. *J. Fluid Mech.*, 656:5–28, 2010. (Cited on page 147).

[129] R. Gaudron, M. Gatti, C. Mirat, and T. Schuller. Flame describing functions of a confined premixed swirled combustor with upstream and downstream forcing. *Proceeding of the ASME Turbo Expo*, (GT2018-76381):1–13, 2018. (Cited on pages 150, 157 & 159).

[130] Cristhian I. Sevilla-Esparza, Jeffrey L. Wegener, Sophonias Teshome, Juan I. Rodriguez, Owen I. Smith, and Ann R. Karagozian. Droplet combustion in the presence of acoustic excitation. *Combustion and Flame*, 161:1604–1619, 2014. (Cited on page 184).

[131] F. Baillot, J.-B. Blaisot, G. Boisdron, and C. Dumouchel. On the behavior of an air-assisted jet submitted to a transverse high-frequency acoustic field. *J. Fluid Mech.*, 640:305–342, 2009. (Cited on page 184).

[132] F. Baillot, J.B. Blaisot, C. Richard, and M. Théron. Effects of acoustic radiation on air-assisted jets in a transverse high-frequency acoustic field. In *25th European Conference on Liquid Atomization and Spray Systems*, Chania, Greece, 1-4 September 2013. (Cited on page 184).

[133] L.P. Gor'kov. O silakh, deistvuyushchikh na maluyu chastitsu v akusticheskom pole v ideal'noi zhidkosti. *Dokl. Akad. nauk SSSR*, 140:88–91, 1961. (Cited on page 185).

[134] Benjamin D. Bellows, Mohan K. Bobba, Jerry M. Seitzman, and Tim Lieuwen. Nonlinear flame transfer function characteristics in a swirl-stabilized combustor. *Journal of Engineering for Gas Turbines and Power*, 129:954–961, 2006. (Cited on pages 204 & 208).

[135] WA Chishty, SD Lepera, and U Vandsburger. Spray combustion dynamics under thermoacoustic oscillations. *World Academy of Science, Engineering and Technology*, 5(1):837–842, 2011. (Cited on page 209).

[136] Jean-Marie Donnini and Lucien Quaranta. Modélisation électrique et acoustique du haut-parleur : impédance électrique et bande passante acoustique. *Bulletin de l'Union des Physicien*, 89(777):1627–1637, 1995. (Cited on page 217).